Fracture scaling of concrete under multiaxial compression

قَالُوا سُبْحَانَكَ لَا عِلْمَ لَنَا إِلَّا مَا عَلَّمْتَنَا إِنَّكَ أَنتَ الْعَلِيمُ الْحَكِيمُ

They (angels) said: "Glory be to You, we have no knowledge except what you have taught us. Verily, it is You, the All-Knower, the All-Wise." (The Quran 2:32)

dedicated to my parents
to my wife Buket
to my daughter Nur

Fracture scaling of concrete under multiaxial compression

Proefschrift

ter verkrijging van de graad van doctor
aan de Technische Universiteit Delft,
op gezag van de Rector Magnificus, prof. dr. ir. J.T. Fokkema,
voorzitter van het College voor Promoties,
in het openbaar te verdedigen

op dinsdag 20 december 2005 om 10:30 uur

door

Ahmed Said Kamal ELKADI

Master of Science in Engineering Geology,
ITC, Enschede

geboren te Tanzania

SUMMARY

Fracture scaling of concrete under multiaxial compression

The influence of specimen size on measured material properties in solid heterogeneous materials, such as concrete and rock, has been an issue of research and discussions for a few decades. A thorough understanding of the size effect phenomenon and the physical processes involved is imperative. An appreciable amount of experimental data on size effect can be found in literature, which mainly focuses on direct and in-direct tension, bending, and uniaxial compression. These data are used for developing and validating numerical material models of fracture and size effect. To date, however, only few and limited experimental data exists for size effect in the biaxial and multiaxial compressive regimes.

Size effect experiments under multiaxial stress conditions require three-dimensional scaling, which are experimentally challenging. For such experiments, the hollow-cylinder geometry lends itself for providing permutations of various multi-axial states of stress around its inner-hole depending on the stress path applied to its boundaries. Under external hydrostatic stress, it allows for a gradual and stable pre-peak failure development (in case of quasibrittle materials) across the wall thickness from the inner-hole outwards. Hollow-cylinder tests are commonly used in the oil and gas industry as model experiments for perforation and wellbore stability studies.

In this thesis, series of scaled hollow-cylinder tests were carried out on two model (cement-based) materials with varied maximum aggregate size. The objective of these tests was to enhance the knowledge about size effect and fracture processes in multi-axial compressive failure of quasibrittle materials. The focus was to get insight into the physical mechanisms underlying the observed size effect. In addition, the deformation behaviour and fracture characteristics were closely examined and analyzed.

For this purpose, a high-pressure test cell was developed that enables testing of hollow-cylinders with dimensions up to 200 mm outer-diameter and 300 mm length. The cell was equipped to accommodate smaller specimens in a size range 1:4. The set-up was supplemented with novel measuring device for monitoring the deformations taking place inside the inner-hole, both in radial and axial directions for all sizes. Impregnation experiments were performed on all tested specimens using fluorescent epoxy resin. Obtained crack patterns were examined using both optical microscopes and Environmental Scanning Electron Microscope (ESEM).

Numerical analyses using the distinct element program PFC2D were conducted in order to obtain a more thorough understanding of the phenomenon and experimental results. Modelling took place through firstly, developing a synthetic material that is calibrated for its (micro-) parameters using a set of laboratory mechanical tests. Afterwards, a model was developed to simulate the hollow-cylinder test in two-dimensions. Analyses of the hollow-cylinder test and its size dependence using the simulated model material and test procedure were performed. In addition, size effect simulations were performed for uniaxial compression and Brazilian splitting tests.

Size effect was observed in the strength of the hollow-cylinders with a consistent de-cease of strength with size. The experimental/numerical results and the performed analysis revealed the size effect in hollow-cylinder tests as a result of complex combination of structural factors (e.g. stress gradients), mechanical processes of failure including deformation, and material characteristics in terms of heterogeneity and fabric. Emphasizing only one factor in a model or hypothesis and neglecting others brings an error to the model, which could be significant. Observed size effect was dependent on aggregate size, being stronger for the mixture with smaller aggregate size.

The onset of size effect in the experiments was observed linked to the commencement of nonlinearity in the stress-strain response. Microscopic examination of fracture processes at this stage showed small boundary cracks to exist with barely any crack interaction or propagation activities. This implies that material related factors contributing to onset of size effect should be linked to processes taking place at crack initiation, which are largely due to heterogeneity and distribution of defects. The predicted size effect according to Weibull theory described with reasonable success the obtained size effect trends near crack initiation levels.

Delft, December 2005

Ahmed S.K. Elkadi

Samenvatting

Schaaleffecten bij breuk van beton onder meerassige druk

De invloed van de grootte van het proefstuk op gemeten materiaaleigenschappen in vaste heterogene materialen, zoals beton en rots, is reeds tientallen jaren onderwerp van onderzoek en discussie. Een diepgaand begrip van het fenomeen schaaleffect en van de bijbehorende fysische processen is noodzakelijk. In de literatuur is een aanzienlijke hoeveelheid aan experimentele gegevens te vinden. Deze spitsen zich vooral toe op directe en indirecte trek, buiging en eenassige druk. De gegevens worden gebruikt voor de ontwikkeling en validatie van numerieke modellen voor breuk en schaaleffecten.

Experimenten voor schaaleffecten bij meerassige spanningstoestanden vereisen een driedimensionale schaling; dit is experimenteel bezien een uitdaging. Experimenten met holle cilinders lenen zich voor dit doel; afhankelijk de van extern aangebrachte belastingen kunnen uiteenlopende meerassige spanningstoestanden rondom de holte verkregen worden. Een externe hydrostatische druk maakt een geleidelijke en stabiele breukontwikkeling tot falen mogelijk (voor het geval van quasi-brosse materialen). Deze breukontwikkeling begint aan de holtezijde van de cilinder en plant zich over dikte van de van de cilinderwand voort. Experimenten met holle cilinders zijn gebruikelijk in de olie- en gasindustrie. Ze dienen als experimentele modellen in studies omtrent de stabiliteit van boorgaten en perforaties.

In dit proefschrift worden verschillende series van schaalexperimenten met holle cilinders uitgevoerd. Hierbij zijn twee (cementgebonden) modelmaterialen gebruikt met een verschillende grootste korrelafmeting van het toeslagmateriaal. Het doel van deze experimenten was het versterken van de kennis over schaaleffecten bij breuk van quasi-brosse materialen bij meerassige druk. De nadruk lag op het inzicht krijgen van de fysische mechanismen die ten grondslag liggen aan de gemeten schaaleffecten. Bovendien wordt het vervormingsgedrag en de breukkarakteristieken nauwlettend onderzocht en geanalyseerd.

Met dit doel werd een drukcel ontwikkeld waarmee holle cilinders met een maximale diameter van 200 mm en een maximale lengte van 300 mm onder hoge druk getest kunnen worden. De drukcel was zodanig toegerust dat de grootte van proefstukken kan variëren van 1:4. De proefopstelling was aangevuld met een nieuwe meeteenheid om de vervormingen aan de binnenzijde van de cilinder te registreren; de vervormingen werden voor alle afmetingen van de proefstukken zowel in radiale als in axiale richting gemeten. Op alle proefstukken werden experimenten uitgevoerd met impregnatie van een fluorescerende epoxyhars. De verkregen scheurpatronen werden onderzocht met zowel optische microscopen als met een Environmental Scanning Electron Microscope (ESEM).

Voor een meer diepgaand begrip van het fenomeen en de experimentele resultaten zijn numerieke simulaties met het "distinct element"-programma PFC2D zijn uitgevoerd. Het modelleren vond plaats door eerst uitgaande van een synthetisch materiaal en een bijbehorende reeks mechanische laboratoriumexperimenten de (micro-)parameters te kalibreren. Hierna werd een numeriek model ontwikkeld om een experiment met een holle cilinder tweedimensionaal te simuleren. Er zijn numerieke analyses uitgevoerd voor de experimenten met de holle cilinders en het bijbehorende schaaleffect. Ook werden numerieke simulaties uitgevoerd voor het schaaleffect bij eenassige druktesten en de Braziliaanse splijttesten.

Voor de sterkte van de holle cilinders werd een schaaleffect waargenomen waarbij de sterkte consequent afnam met de grootte van het proefstuk. De experimenteel-numerieke resultaten en de uitgevoerde simulaties onthulden dat het schaaleffect in experimenten met holle cilinders het resultaat zijn van een complexe combinatie van structurele effecten (zoals bijvoorbeeld een verlopende spanning), mechanische breukprocessen, inclusief vervormingen, en materiaalkarakteristieken in termen van heterogeniteit en structuur. Het benadrukken van slechts een van deze factoren in een model of hypothese en het verwaarlozen van de andere factoren leidt tot fouten; deze fouten kunnen significant zijn. Het waargenomen schaaleffect was afhankelijk de korrelafmeting van het toeslagmateriaal, waarbij een kleinere korrelafmeting leidt tot een grotere sterkte.

Het is waargenomen dat de aanzet van schaaleffecten in de experimenten gekoppeld was met het begin van niet-lineariteit in het spannings-rekgedrag. Microscopisch onderzoek van het breukproces in dit stadium toonde het bestaan van kleine oppervlaktescheuren die nauwelijks interactie hebben of scheurgroei vertonen. Dit betekent dat de factoren die aan het materiaal gerelateerd en welke bijdrage aan de aanzet van schaaleffecten gekoppeld moeten worden aan processen rondom scheurinitiatie; deze worden voornamelijk bepaald door heterogeniteit en de verdeling van defecten. De voorspelling van het schaaleffect volgens de theorie van Weibull beschrijft met redelijk succes de waargenomen tendensen in het schaaleffect in het stadium van scheurinitiatie.

Delft, december 2005

Ahmed Said Kamal Elkadi

CONTENTS

Chapter 1

INTRODUCTION

1.1 GENERAL

The work reported in this thesis was formulated as a subproject in the research programme 'A Combined Experimental and Numerical Approach to Crack Propagation in Concrete and Rock'. The programme is primarily financed via grants form the Dutch Technology Foundation (STW-DCT3923) and the Research School Structural Engineering (OSBOUW). The goal of this research project is to develop a rational procedure for the determination of material parameters, which would enhance the predictive capabilities of numerical models concerned with cracking in quasibrittle materials such as concrete and rock. Phenomena like the size effect that is commonly observed in fracture experiments and strength tests ought to be inherent in these models as well. In this context, the development of accurate experimental procedures for providing the necessary material parameters undertakes an important role. The experiments are thought to consider realistically the complex and various loading conditions that exist in real concrete and rock structures. The current subproject was intended to experimentally study the size/scale effect in thick-walled hollow-cylinder tests.

Size effect is a salient property of fracture of quasibrittle heterogeneous materials such as concrete and rock. An appreciable amount of experimental data on size effect can be found in literature, which mainly focuses on direct and indirect tension, bending, and uniaxial compression. These data are used for developing and validating numerical material models of fracture and size effect. To date, only few and limited experimental data exists for size effect in multiaxial compressive fracture of concrete and rock. The effect of confining pressure on the size-strength relations and fracture propagation is missing substantial experimental background. Conversely, most of the loading states of concrete and rock structures lie in the biaxial and triaxial compressive domains, e.g. stresses around a wellbore, and therefore the importance for quantifying size effects in this loading range. In this perspective, a thorough understanding of the size effect phenomenon and the physical processes involved is imperative. Laboratory experiments using model openings such as scaled hollow cylinders are suited for such an investigation. The hollow cylinder geometry lends itself for providing permutations of various multiaxial states of stress around its inner-hole depending on the stress path applied to its external boundaries.

In the oil and gas industry, stress induced instabilities of wellbores are of great economic significance. The concern is due to the increase in drilling horizontal and deviated wells in unique geological environments as well as drilling intricate hydrocarbon reservoirs, which follow the quest for new energy resources. Difficult reservoirs include for instance, unconsolidated or poorly consolidated sediments, shales, complex geometries, and over-pressured or naturally fractured reservoirs. A wellbore is a particular type of excavation considering the various loads involved, including in-situ stresses, drilling fluid pressure, temperature induced forces, and mechanical work, which create conditions for rock failure that are different from those in other types of underground openings. Therefore, unlike other types of excavations, the state of stress in the rock adjacent to a wellbore is highly indeterminate. In terms of failure, quasi-brittle rocks, e.g. sandstones, at moderate or no drilling fluid pressure commonly fail in the form of an enlargement of the size of the wellbore. Furthermore, the failure mechanism and failure strength are observed to be size dependent in laboratory model tests, hollow-cylinders. This size/scale effect renders difficult the extrapolation of small-scale laboratory tests to large field-scale wellbores.

1.2   Research objectives

The purpose of this study is twofold. Firstly, to experimentally investigate the size/scale effect on strength in hollow-cylinder tests. The three-dimensional size effect experiments performed in this research are thought to enhance the knowledge about size effect in multiaxial compressive failure of quasibrittle materials. Moreover, the effect of material heterogeneity, represented by the maximum aggregate size, on size effect and fracture behaviour is examined. Structural effects from test geometry and set-up are to be evaluated and considered as well. Secondly, to gain more understanding of the mechanical and fracture behaviour of weak rock-like materials under simulated in-situ conditions as those encountered during drilling for oil and gas. It is intended that this understanding include the deformation and strength characteristics of those materials under non-uniform stress state; provided by the hollow-cylinder geometry, and the observation of their failure mechanisms under these conditions.

This research is a fundamental investigation into the size effect and fracture behaviour of weak quasibrittle materials subject to multiaxial compressive stresses. The results are believed of interest to many disciplines including, concrete fracture mechanics, petroleum engineering, and geomechanics. However, as inherent to any experimental investigation, certain boundary conditions are applied in the experimental design that ought to be considered in view of the applicability of results. Those employed in this research could be outlined as follows:

– Axisymmetric cylindrical openings are considered (thick-walled cylinders).
– Hydrostatic external pressure with zero inner-hole pressure is applied.
– Weak quasibrittle (cement-based) materials are tested.
– Tests are performed under normal temperature conditions ($\pm 20°$ C).

1.3 RESEARCH APPROACH

A combined experimental and numerical programme was introduced in order to achieve the abovementioned research goals. In view of that, two main aspects could be distinguished in the research methodology of this thesis:

1– Carefully designed laboratory experiments simulating as closely as possible the fundamental processes encountered in real structures.
2– Modelling and numerical simulation of the underlying mechanical processes with respect to size effect and failure.

The experiments are conducted on scaled thick-walled cylinders from tailored quasibrittle materials. Mixtures of similar qualities and differing maximum aggregate size (namely, 2 mm and 4 mm) were investigated. This is to account for the influence of the heterogeneity of the material on size effect and fracture behaviour. Next, the main characteristics of this experimental work are outlined:

– Development of synthetic quasibrittle model materials.
– Characterization of the developed materials through uniaxial compression, triaxial compression, and Brazilian splitting tests.
– Development and debugging of a high-pressure test cell for the size effect tests.
– Conducting size effect experiments on specimens from the designed mixtures.
– Performing verification experiments to clarify the influence of both structural effects and intrinsic material factors thought to affect the results of the size effect experiments.
– Impregnation experiments are then utilized to preserve the fracture patterns obtained after the size effect experiments.
– Finally, post-mortem examination of the fractured specimens took place using both optical microscopy and scanning electron microscopy techniques.

Numerical tools were employed in designing the experiments at different stages and in analyzing their outcome. Non-linear Finite Element (FEM) simulations were utilized in the experimental design phase to elucidate some possible effects from the test set-up and applied boundary conditions. Important factors considered were, end effects, load configuration, thickness of the rubber sleeve that separates the specimens from the pressurizing oil, and stress path. Moreover, Distinct Element (DEM) analyses were carried out using the Particle Flow Code (PFC2D) in order to improve the understanding and interpretation of the experimental results. This mesoscopic modelling approach was considered useful in explaining the experimental observations in terms of fracture processes due to its large-deformation capacity and unrestricted crack-nucleation capability. The modelling scheme pursued in this approach comprised the following main steps:

– Develop a numerical model-material with desired macro-parameters through an iterative calibration procedure using laboratory mechanical test results.
– Parameter study for the influence of model-parameters on the analysis outcome.
– Development of model assemblies in order to simulate the experimental tests; uniaxial and triaxial compression, splitting tensile, and hollow-cylinder.
– Interpretation of the results of simulations in comparison with experiments.

1.4 OUTLINE AND CONTENTS OF THE THESIS

This thesis comprises eight chapters, which describe the work and results carried out in this study. The structure of the thesis is shown graphically in Figure 1.1.

In Chapter 2, a literature survey is presented to establish the current state of understanding and theoretical background of the main aspects of this research. A comprehensive description of the compressive failure process in concrete and rock is given. The factors affecting this process are highlighted such as confinement, aggregate size of the material, and aggregate concentration. The size effect phenomenon is then introduced with a focus on the current state of knowledge regarding size effect in compressive failure. Finally, the wellbore stability problem is reviewed.

Chapter 3 presents the development process of the two model-materials used for testing. Moreover, a description of the materials and their behaviour are given. The description concerns the meso-structure of the materials as well as their physical and mechanical properties. The behaviour relates to mechanical performance and fracture behaviour under various loading conditions such as uniaxial compression, triaxial compression, and Brazilian splitting.

Chapter 4 describes in detail the experimental facilities and adapted experimental techniques. The construction of the hollow-cylinder test cell is explained. Furthermore, measurement devices, data acquisition, and test control are described. The sample manufacturing and preparation for testing is explained as well. Thereafter, the verification experiments are presented with emphasis on specimen homogeneity and isotropy, end effects and effect of test boundary conditions. Later, the size effect test procedure is described with focus on stress path, and testing scheme. Finally, the impregnation experiments and the adapted post-mortem techniques are highlighted.

In Chapter 5, the results of the scaled hollow-cylinder experiments are given. The stress-strain behaviour and size effect in the failure process of the two tested mixtures are accentuated. The other emphasis of the chapter is put on the failure mechanisms and fracture patterns during the hollow-cylinder tests for the different specimen sizes from both materials.

Chapter 6 deals with the numerical meso-mechanical modelling using the distinct element code PFC2D. First, the concept of the distinct element method and model used is introduced. The modelling procedure is then described with emphasis on model preparation, calibration processes, and parameter study. The hollow-cylinder test is then analyzed using the developed model. Moreover, the suitability of the model to predict size effects is thoroughly investigated.

Chapter 7 presents a synthesis for both the experimental observations and numerical outcome. A detailed interpretation of the various processes engaged in the experimental observations of size effect is illustrated. Attention is paid to both structural and statistical aspects as well as the onset of size effect. Moreover, a phenomenological model is developed and presented regarding the failure mechanism in hollow-cylinders, which accounts for the effect of specimen size and heterogeneity. The wellbore stability problem is analyzed in view of the hollow-cylinder test results. The results are interpreted using commonly used constitutive models and failure criteria to examine their validity against the experimental results. Furthermore, numerical results concerning failure mechanisms

and stress-strain response from the hollow-cylinder simulations are compared with data from experiments.

Finally, Chapter 8 summarizes the major results and findings obtained in this study. The need for further research into certain aspects of the problem is suggested.
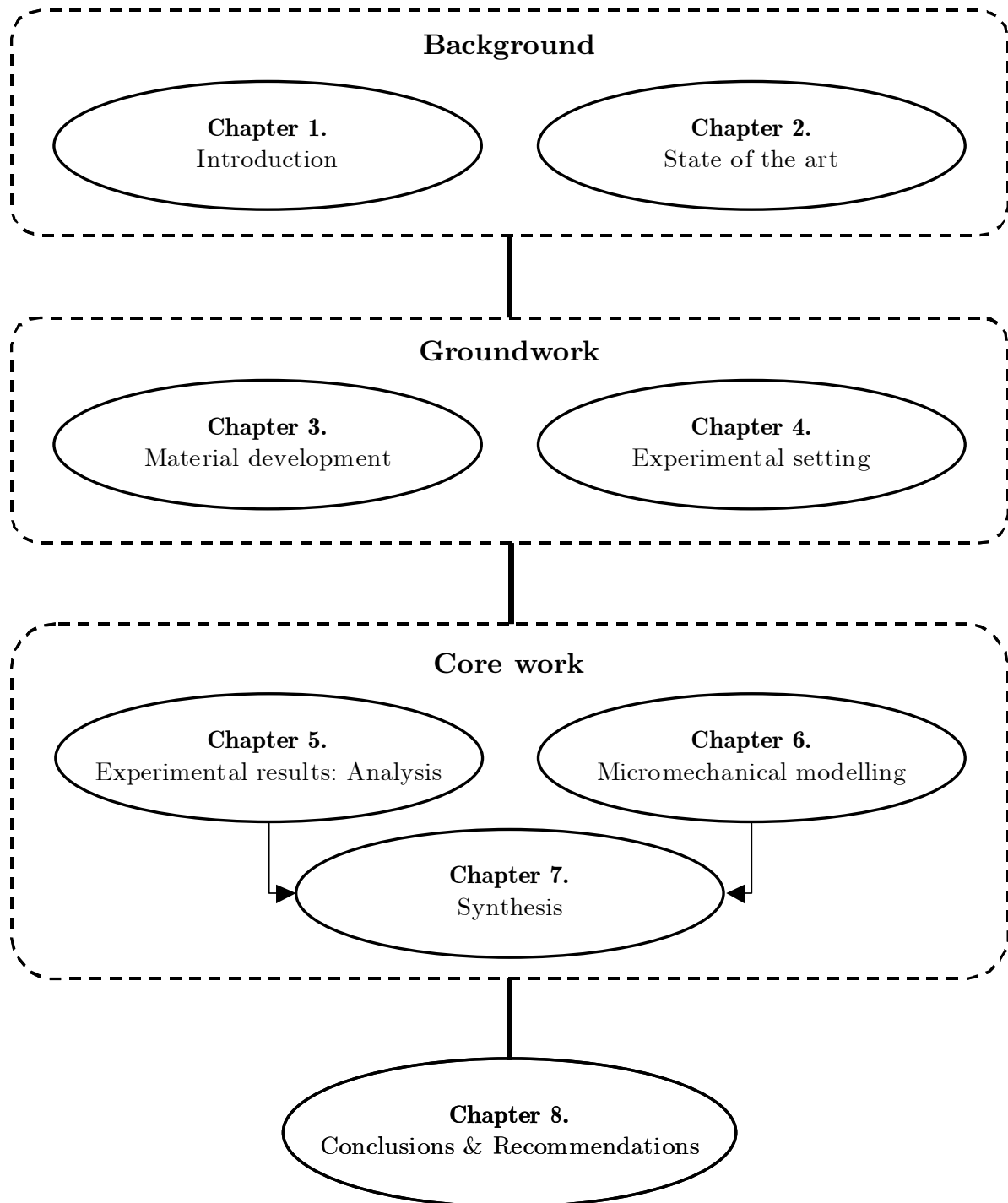
Figure 1.1: Outline representation of the structure of this thesis.

1.5 SIGN CONVENTION

Compressive stresses are reckoned positive throughout this thesis. Likewise, strains are regarded positive when they are contractile and negative when they are extensile. All parameters used are presented in SI units. A list of symbols with units and abbreviations is included at the end of this thesis.

Chapter 2

SCALING OF COMPRESSIVE FRACTURE

In this chapter, a brief review is attempted regarding size effect and compressive failure in quasibrittle materials such as concrete and rock. Attention is given to stress-strain response and cracking behaviour under uniaxial and multiaxial compressive loading. Some focus is provided for the influence of meso-scale material structure such as aggregate size and grain density on the overall behaviour. The size effect phenomenon in the compressive domain is discussed afterwards with outline of related theories and models. Finally, the hollow-cylinder test is presented regarding stress and strain distribution, failure behaviour, and observed size dependency.

2.1 MATERIAL STRUCTURE AND OBSERVATIONAL SCALE

In order to gain a better understanding and more realistic description of the complex behaviour of composite materials such as concrete and rock core, their heterogeneous structure should first be comprehended. It is thus sensible to classify the material structure based on a multi-scale observational level of heterogeneity. In contemporary concrete fracture research, it is common to adapt a three-level approach; presented first by Wittmann (1983), which distinctly defines micro-, meso-, and macro-scales. This concept promotes a multi-scale modelling approach of the material's constitutive behaviour. Moreover, the interaction between material constituents at one scale and its impact on observed material behaviour at one higher scale could be established. To illustrate this concept, a cascade plot is presented in Figure 2.1, which incorporate the three-scales and their mutual interaction. In the figure, it is indicated that knowledge about material structure and its interaction at one scale aggregates necessary information to explain observed material behaviour at one scale higher. In turn, the feedback from a higher-scale to one scale below would represent the imposed extrinsic factors or boundary conditions. The horizontal scale in Figure 2.1 represents the phenomena that takes place and could be either intrinsic or extrinsic processes of mechanical, chemical, physical, or combined nature, e.g. cement hydration and size effect. The vertical scale describes the spatial scale, which distinguishes the evolution of observational scale.
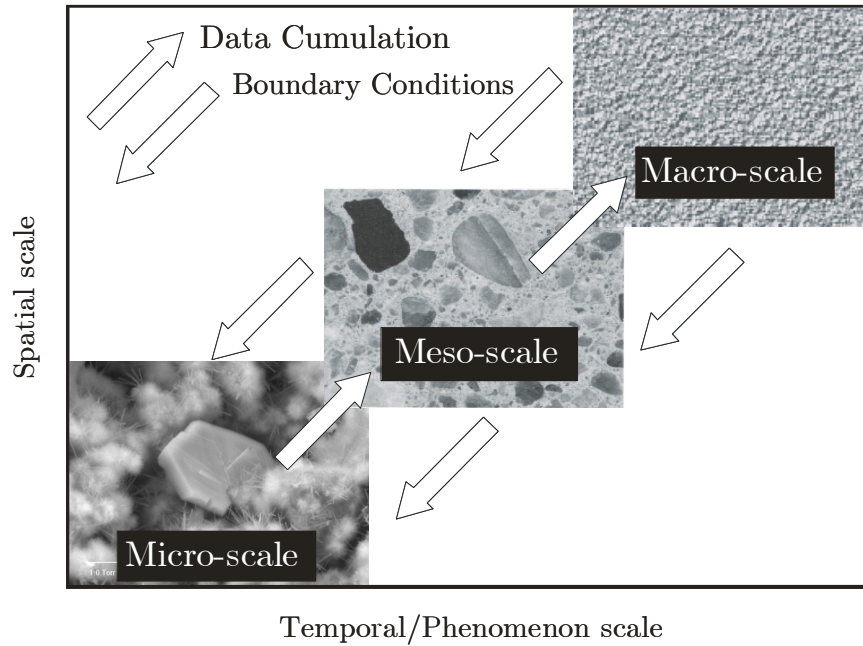
Figure 2.1: Cascade plot illustrating the three-levels of scale in concrete.

In this classification, the micro-scale covers the physical and chemical processes from the atomic level of cement and aggregate grains (10^{-8} m) to un-hydrated cement grains and portlandite (10^{-3} m). The meso-scale is that of individual fine and coarse aggregates as well as relatively large air voids (10^{-3}–10^{-1} m). The macro-scale assumes a homogenous-continuous material structure and ranges from the scale of laboratory specimens (10^{-1} m) to the scale of buildings and structures (10^{0}–10^{+3} m). This study focused mainly on processes at the meso- and macro-scales with links established to the micro-scale when necessary.

2.2 COMPRESSIVE STRENGTH

2.2.1 Stress-strain relation

When discussing mechanical strength of concrete or rock materials, structural and geomechanical engineers generally refer to the uniaxial compressive strength (f_c or UCS) measured through testing an intact rock or a plain concrete specimen. This attributes largely to a fact that the majority of concrete structures are subject to compressive stresses and that large compressive fields exist within the rock mass and around underground structures e.g. tunnels and deep boreholes. In addition, until recently it was thought easier to conduct uniaxial compression tests as compared with tensile or bending tests. Contemporary experimental research on compressive failure of concrete (Van Mier, 1984; Vonk, 1993), however, have elucidated that a stress-strain curve of concrete is not a material property, but a mix of structural and material behaviour. Much attention should be paid to factors such as end conditions, specimen size and shape effects when performing compression tests.
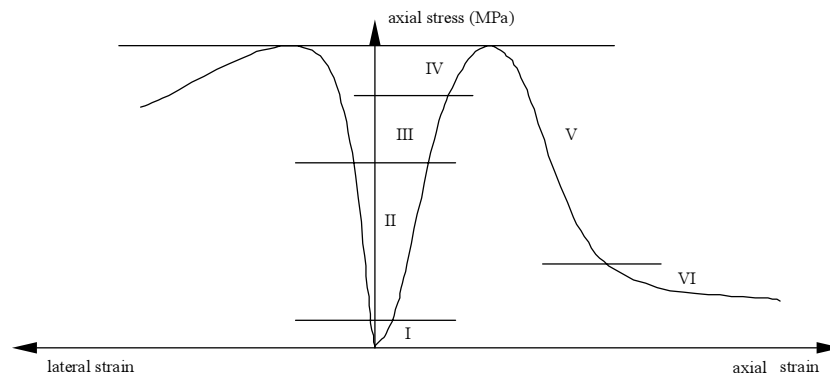
Figure 2.2: Schematised stress-strain response of concrete and rock in uniaxial compression

The uniaxial compressive strength is determined during a uniaxial compression test where a representative specimen, in terms of shape and size, is axially compressed while recording its load-axial deformation response. This observed load-deformation behaviour is then translated to a stress-strain curve, which is commonly considered as an essential input parameter in most of the current standards and design codes, e.g. Finite Element design packages. In Figure 2.2, a typical stress-strain curve for concrete and rock is schematised, which could be obtained from a deformation-controlled uniaxial compression test. Generally, it is well established that this stress-strain curve can be subdivided into several characteristic regions (I-VI in Figure 2.2). These regions represent the stages during the specimen's failure process. Those suggested stages (regions) could be summarized as follows (e.g. Bieniawski, 1967):

– Region I: closure of pre-existing cracks (in rocks) producing an inelastic, concave-upward stress-strain section. This region is observed in rock, whereas in concrete the stress-strain curve in this section is more or less straight. This could be due to the denser nature of normal strength concrete as compared to sedimentary rocks with probably less defects and flaws in the initial state prior to loading.

– Region II: a nearly linear elastic relation between the axial stress and both the axial and the lateral strains. The end of this region represents the initiation of new micro-cracks accompanied by an increase in the lateral strain rate relative to the axial strain rate (increase in Poisson's ratio).

– Region III: crack growth and sliding on existing crack interfaces. The crack propagation in this region is considered 'stable'. The end of this region indicates a rapid increase in the micro-crack density and the end-point corresponds to the onset of nonlinearity termed as "yield point" in rock literature.

– Region IV: unstable fcrack propagation where a system of intersecting, coalescing cracks is developed. Rapid increase in the micro-crack density up to many folds at a stress level 75-90% of the peak stress. The end of the region represents the peak stress corresponding to a strength failure.

– Region V: formation of a macroscopic fracture plane accompanied by a drop in the load bearing capacity. This process is known as softening.

– Region VI: sliding along macroscopic fracture planes with increasing deterioration and crushing accompanied by friction and interlocking between the cracked sections.

The material may still possess load-carrying capacity, referred to as the residual strength.

The stress-strain response in Figure 2.2 characterizes the macro-scale behaviour in laboratory scale specimens when subject to a uniaxial compressive stress. Processes occurring at the meso- and micro-scales are of significant impact on this behaviour. In addition, external factors such as type of loading, rate of loading, structural effects, temperature, and time dependency are of notable effect. This complexity and ambiguity of the stress-strain behaviour triggered many researchers to try understanding and clarifying these observations. To our interest, the effect of the type of loading together with meso-scale material structure and fracture processes are to be further discussed in the following sections. Extensive information on factors influencing stress-strain behaviour of concrete and rock under compressive loading and a more comprehensive review are referred to in the literature (e.g. Paterson, 1978; Jaeger and Cook, 1979; Hoek and Brown, 1982; Andreev, 1995; Van Mier, 1997).

Under compressive loading, elastic deformation is usually limited to the first 40% of the maximum applied load. Cracks develop progressively as the material is loaded above this level and at higher loads, time dependent crack interaction and coalescence become increasingly more important. Albeit the load carrying capacity may decrease considerably with deformation in the post-peak region (i.e. material softens), behaviour in this phase can be critical to the overall performance of rock or concrete structures in practice. If lateral deformations are inhibited through confinement, the peak load is increased and the rate of softening will be decreased. Under sufficient lateral constraint, softening may change to hardening and the load will continue to increase (higher bearing capacity) rather than decrease.

2.2.2   Influence of confinement

In general, compressive strength and strain capacity of concrete and rock materials increase under confinement. When confining pressure is applied simultaneously with axial pressure, the material becomes subject to a biaxial or multiaxial stress state and a division of these stresses into two parts is commonly considered useful (Goodman, 1980). First part is a mean stress (σ_m) known as the hydrostatic stress, which is equal compression applied in all directions. The other part is a deviatoric stress (σ_{dcv}), which is the normal and shear stress remaining after subtracting a hydrostatic stress from each normal stress component. A motivation for this is that deviatoric stresses produce destruction to the material with shape change, whereas non-deviatoric (hydrostatic) stresses generally result in volume change/compaction.

Under hydrostatic compression, first, bulk material compression consisting of pore deformation and grain compression takes place at an almost linear rate. The slope of the hydrostatic pressure-volumetric strain curve is known as the material's bulk modulus (see Figure 2.3a). Further, an increasing deformation occurs with hardly increasing the stress, which is generally explained by pore collapse. The level of pressure where pore collapse occurs is highly dependent on the structure of the material in terms of its porosity. Finally, when all of the pores are closed (locking), grain compressibility takes place
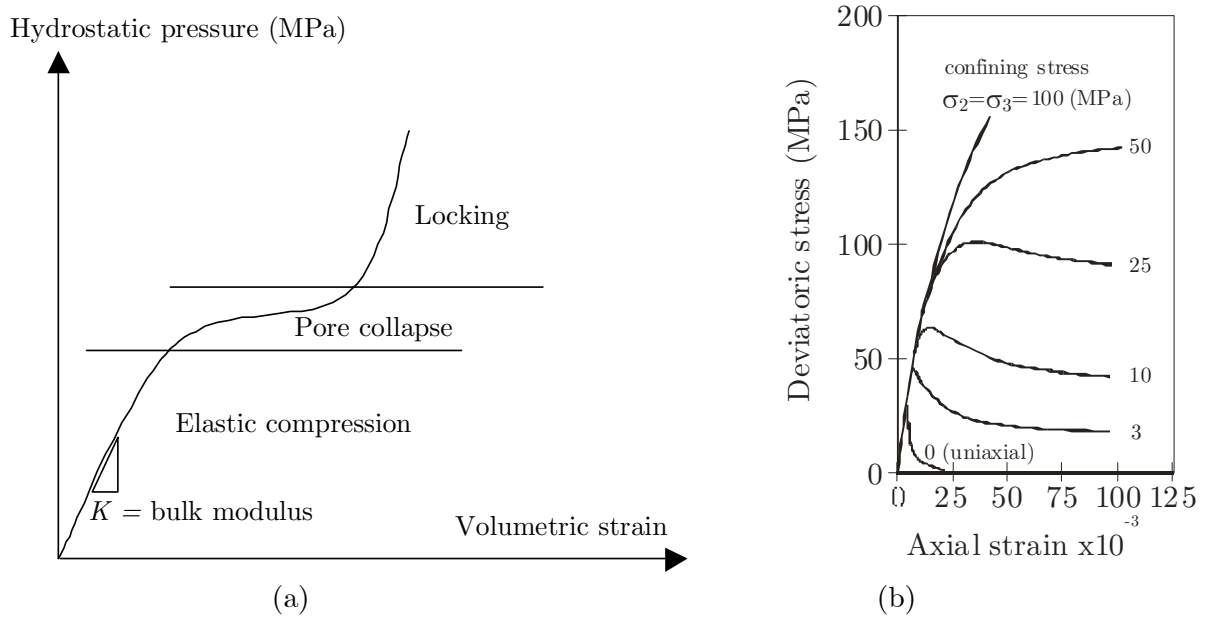
Figure 2.3. (a) Volumetric compressive response under increasing hydrostatic pressure. (b) Confined triaxial compression tests ($\sigma_2 = \sigma_3$) for concrete (After Jamet *et al.*, 1984).

and the bulk modulus becomes progressively higher. Burlion *et al.* (2001) performed compaction tests on mortar and reported a coupling between the hydrostatic and deviatoric responses with the former being largely influenced by the latter

Applying a deviatoric stress would generally produce the material response discussed in § 2.2.1, which is applicable for uniaxial compression and multiaxial compression under low confinement levels. As confinement increases, depending, among others, on the structure of the material (dense or porous), the strength and strain at peak stress substantially increases. This strengthening is accompanied by a transition in the behaviour of the material in a process known as the brittle-ductile transition. At certain pressure, the brittle-ductile transition pressure, the material behaves fully plastic with continued deformation without any increase in the stress (expected between 25 and 50 MPa in Figure 2.3b). Afterwards, hardening takes place with an increase in stress with increasing deformation. In rocks, the transition pressure is generally observed at σ_3 / σ_1 (σ_1=maximum principal stress and σ_3=minimum principal stress) approximately equals 0.30 depending on the rock type (Paterson, 1978). For normal strength concrete, a ratio equals 0.20–0.25 is commonly reported (Van Mier, 1997). For fine-grained dense materials, the transition is observed at higher pressures as compared to porous coarse-grained materials. For the majority of concrete structures and near surface rock constructions, reaching high levels of confinement close to the brittle-ductile transition and higher might not be feasible. However, other structures such as deep mines or deep boreholes are subject to high pressures, hence consideration of transition pressures and beyond would be of relevance.

In the above discussion, the effect of confinement is treated in a more general sense and largely based on experiments from standard triaxial experiments on cylinders. In such experiments, confinement is applied through pressurising a fluid around the cylinder's circumference with $\sigma_2 = \sigma_3$ (σ_2 =intermediate principal stress), which is in reality a biaxial state of stress. A true triaxial stress state, also known as the ployaxial stress state,

would be the case if $\sigma_1 \neq \sigma_2 \neq \sigma_3$ and is experimentally obtained by loading a rectangular parallelepiped or a cube across its three pairs of mutually perpendicular surfaces or in hollow-cylinder tests. True triaxial testing enables identifying the influence of intermediate and minor principal stress, load-path, and strength anisotropy on the stress-strain behaviour of the material. The influence of the intermediate principle stress has been a controversial matter in the field of rock mechanics for quite some time. Recently, it became obvious that σ_2 would influence the strength of the material under controlled test conditions with minimal end effects resulting, generally, in an increase in peak stress. Van Mier (1984), carried out stable displacement-controlled true triaxial tests on normal strength concrete cubes to investigate, among others, the influence of σ_2, σ_3, and strength anisotropy on the stress-strain behaviour. From his results, at a constant stress ratio $\sigma_3 / \sigma_1 = 0.05$, and varying ratio of σ_2 / σ_1, a clear strengthening effect was observed with increasing σ_2 in terms of peak stress and strain capacity. A strengthening of the peak stress of about 2 times was observed for a σ_2 / σ_1 ratio between 0 and 0.33 (Figure 2.4). More remarkable was the post peak response, where he observed that specimens tested under a stress configuration close to the compressive meridian, i.e. $\sigma_2 = \sigma_3$ (test with $\sigma_2 / \sigma_1 = 0.10$ in the figure), were behaving more ductile as compared to other stress configurations. Similarly, the effect of intermediate principal stress has been reported in rock mechanics (Mogi, 1967). Moreover, it is observed that under constant σ_3, increasing σ_2 increases the value of σ_1 at failure, but only up to a point. Further increase in σ_2 after this point results in either constant or slightly decreasing σ_1 with the latter more pronounced at low σ_3 levels (Takahashi and Koide, 1989). It is reported that the point where the effect of σ_2 diminishes or reverses occurs roughly at $\sigma_2 / \sigma_1 = 0.5$ for a wide variety of sedimentary rocks.
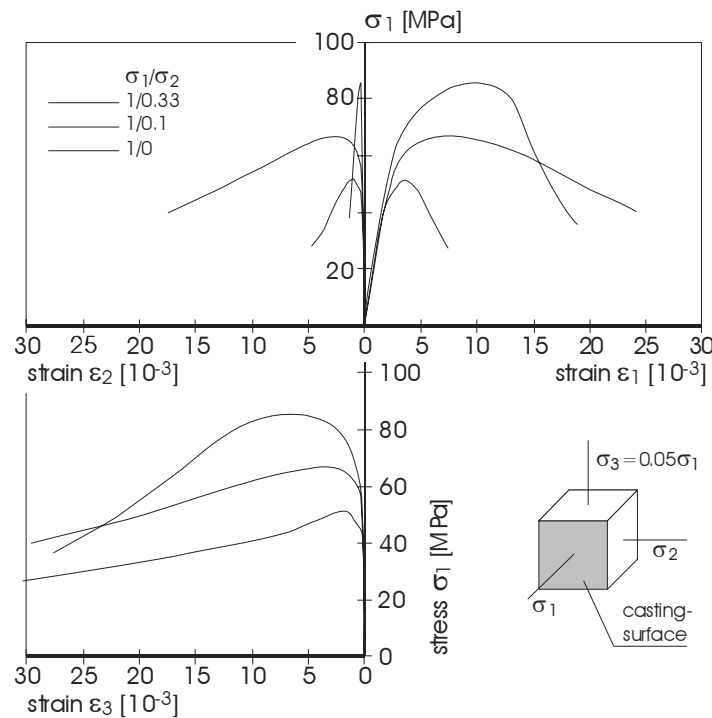

Figure 2.4: Effect of intermediate principal stress in triaxial constant stress-ratio tests on concrete with $\sigma_3/\sigma_1 = 0.05$ and $\sigma_2/\sigma_1 = 0$, 0.10, and 0.33. (After van Mier, 1984).

2.2.3   Influence of material structure

Heterogeneity of concrete constituents could possibly be best described in a three-phase system consisting of hardened cement-paste, aggregates, and interface between aggregates and cement-paste known as the Interfacial Transition Zone (ITZ). The hardened cement-paste and part of the fine aggregates constitute together what is termed as cement-matrix. The ITZ, established to be the weakest link in concrete, has a typical thickness of 20 to 60 μm, but depends largely on the aggregate type, among others. The ITZ is characterized by a clearly open structure with severe porosity gradient, being higher close to aggregate contacts. The influence of the ITZ on the compressive strength is less than on the tensile strength, but measurable effects still exist in the order of 10 to 15 % of the compressive strength. According to Mindess *et al.* (2003), the properties of the ITZ does affect the compressive response of concrete, but it is overshadowed by the properties of the cement paste and aggregate constituents of concrete and the heterogeneous nature of the composite.

Regarding the aggregate size, as the maximum aggregate size (d_{max}) increases, for given cement content and w/c ratio, the higher the localized stress concentrations leading eventually to strength decrease. Under compressive loading, localized stresses and strains around aggregates are observed, using photo-elastic coatings on the surface of concrete specimens, in the order of 2 and 4.5 times the average values from nominal applied stresses and strains, respectively (Mindess *et al.*, 2003). However, the w/c ratio has a measurable effect on the influence of d_{max} on compressive strength. Experimental results also suggest an increase in the elastic modulus of concrete under compression with increasing d_{max} (Issa *et al.*, 2000). With regard to material softening, the aggregate size influences the post-peak material behaviour in both tension and compression by altering the contribution of the various toughening mechanisms active in the region. This reflects in the value of the residual strength, which mainly depends on these mechanisms.

In rocks, much finer aggregates are available, yet a dependence on the grain size has been observed as well. Eberhardt *et al.* (1999), reported an inverse relation between grain size and strength and Young's modulus in three crystalline rocks under uniaxial compression. He reports also that increasing grain size reduces the crack coalescence and propagation threshold, whereas little or no influence on crack initiation thresholds. The decreasing strength of these rocks with grain size, therefore, seems due to lower coalescence stresses rather than inducing earlier crack initiation.

Aggregates make up 60–80% of the concrete volume and thus of noticeable contribution to its mechanical behaviour. Aggregate concentration by volume could be of an influence in determining concrete strength. This is shown for tensile loading by Prado and Van Mier (2003) in numerical lattice analyses of a three-phase particle model. Tasdemir and Karihaloo (2001), found the compressive strength of concrete to decrease with an increase in the aggregate volume fraction up to a ratio of 0.5 and remains practically constant afterwards. On the other hand, they showed the modulus of elasticity and the splitting tensile strength to increase with the aggregate volume fraction. Wittmann *et al.* (1993), however, showed experimentally that a critical threshold exists for aggregate content in mortars (2 mm maximum aggregate size), after which, sudden decrease in the elastic modulus arises. Most of the cited literature on the effect of aggregate volume tends to support the fact that strength decreases with an aggregate volume increase.

2.3 COMPRESSIVE FRACTURE IN CONCRETE AND ROCK

2.3.1 Crack initiation

It is rather established that the basic crack initiation mechanism in heterogeneous multi-phase systems such as concrete and rock is tensile or extensile (Slate and Hover, 1984; Einstein and Dershowitz, 1990). This is regardless of the macroscopically applied stress, whether being of compressive or tensile nature. In compression, the cracks nucleate at initial material defects, such as grain boundaries or crack-like low aspect-ratio cavities. When no lateral restraint is present, these (micro)cracks are observed almost parallel to the direction of maximum compression. The micro-mechanism responsible for the formation of these cracks is not fully understood. In concrete and rock, (micro)cracks or crack-like voids do exist in the material prior to the application of external load, which are primarily bond cracks (as shown by e.g. Hsu *et al.*, 1963). Several other processes are known that promote microcrack initiation by mechanical loading. Most recognized are stress concentrations in the neighbourhood of grain boundaries and cavities and the elastic mismatch between different material phases.

(a)   (b)   (c)
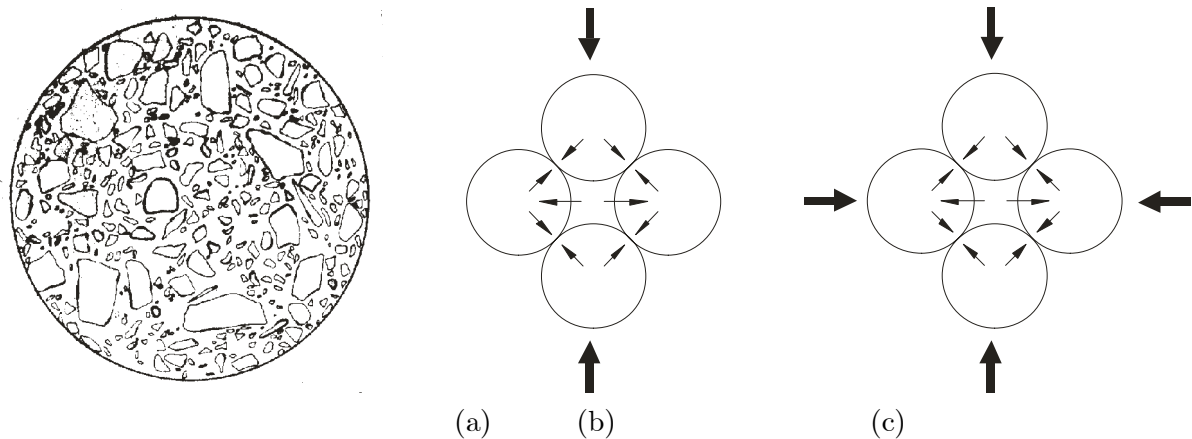
Figure 2.5: (a) Example of bond crack-pattern found in concrete from a polished specimen surface with cracks enhanced by thicker black line. The section is horizontal and perpendicular to compressive load on a 10 cm diameter cylinder at pre-load state (zero strain). (After Hsu *et al.* 1963). Particle interactions under (a) uniaxial and (b) biaxial compression.

2.3.2 Crack growth and interaction

Given the existence of microcracks in the material prior to loading, it is important to understand how they respond to stress changes. Crack growth, coalescence, and interaction with other cracks are responsible for failure. In compression, a distinction between hydrostatic and deviatoric stresses is convenient for their differing impact on crack processes. Hydrostatic compression likely decreases the magnitude of stress concentrations near crack tips and increase frictional resistance between contacting crack surfaces. This results in an increase in the stress requirements for crack propagation and makes crack interaction less favourable. It is generally considered that hydrostatic compression should have no significant effect on crack nucleation, yet will inhibit crack growth and interac-

tion activities (Kranz, 1983). Deviatoric stresses on the other hand are responsible for crack processes observed in compression tests. This is due to a microscopically complex stress state that result from the differential stress condition applied on specimen boundaries. Under these conditions crack coalescence and interaction mechanisms are more favourable.

Laboratory testing on rocks subjected to differential compression have revealed many different mechanisms for extensile crack growth, including pore crushing, sliding along preexisting cracks, elastic mismatch between grains, dislocation movement, and hertzian contact (Kemeny and Cook, 1991). They assert that because of the similarity in rock behaviour under compression in a wide range of rock types, it is not surprising that micromechanical models have many similarities and this may explain the success of models based on certain micro-mechanisms (such as the sliding crack and pore models) in spite of the lack of evidence for these mechanisms in microscopic studies. Einstein and Dershowitz (1990), in an experimental/theoretical study report that three types of cracks are associated with fracturing in compressive stress fields. Namely, individual tensile fractures, tensile fractures connecting to shear fracture, and directly created shear fractures. Tensile fractures upon stress increase coalesce to form shear fractures 'en echelon' or are connected by shear fractures.

In concrete, similar mechanisms are recognized and several studies have contributed to the understanding of fracture mechanisms of concrete under compression. In this, the structure of concrete is commonly assumed to resemble that of a particulate granular material, e.g. sands, with cohesion. The particles made to represent the various material phases like cement and aggregates (Figure 2.5b). Slate and Hover (1984), Vonk (1993), and Van Mier (1998), among others, discuss possible failure mechanisms under compression in view of this aforementioned particle representation of concrete. Characteristic for concrete is the relatively weak ITZ that acts as favourable site for crack nucleation. If a particle stack is assumed to represent a concrete structure subject to uniform compressive field, upon loading stress concentrations will appear and the weak bonding (ITZ) will lead to interfacial cracks. At higher stresses, more cracks are formed and existing cracks start to grow around aggregates. This is associated with region III in Figure 2.2, § 2.2.1. In region IV, new cracks appear through the mortar (cement-matrix), which are regarded as 'unstable' meaning that the energy release rate exceeds the crack resistance. At this stage, failure would proceed without load increase and crack interaction takes place. At further stress increase, more mortar cracks develop and further crack coalescence and interaction occur. At this stage dilation or increase of volumetric strain is recorded. In this case, crack propagation is hindered or completely prevented when the crack tip meets an aggregate, a void, or when cracks run into areas of lower stress or higher strength.

Under uniaxial compressive loading conditions with free (low-restraint) end-conditions, axial splitting cracks are expected that run parallel to the direction of the maximum stress. With the application of confinement (biaxial or triaxial), a counteracting force develops against the compression induced splitting mechanism. This results in higher local splitting strength of the material, which in turn reflects on the material's macroscopic strength. This simple mechanism could be applicable for crack initiation mechanisms observed in multiaxial compression. Crack growth and interaction, however, is more complex when compared with uniaxial compression. In this case, depending on the stress

path and stress ratio, failure mechanisms are observed that range from uniaxial splitting cracks to discrete inclined shear cracks. Van Mier (1984), discusses failure under multiaxial stresses from his experimental results and graphically presents an overview of different failure modes observed (Figure 2.6).
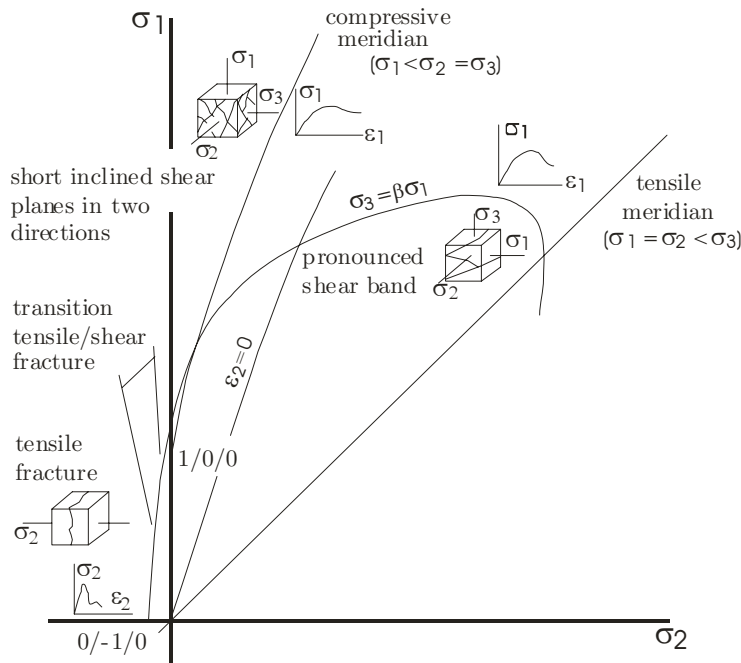
Figure 2.6: General overview of failure modes under multiaxial stress (After van Mier, 1984).

2.4 THE SIZE EFFECT PHENOMENON

A characteristic of quasibrittle materials is the dependence of their mechanical properties, stiffness and strength, on the size or volume of tested specimens. This phenomenon is known as scale or size effect. Differentiation between size and scale effects was introduced with developments in fracture mechanics with the former related to the representative volume element of material and supposed to vanish once this volume has been reached. In this context, scale effects describe the Weibull type statistical volume effect due to the fact that with increasing volume the number of weak spots in the material increases. For three-dimensional size effect investigations as pursued in this study it is realistic to define both scale and size effects in unison as the variation of material parameters with the material volume and is followed henceforth.

Curiosity about size effect could be traced back to work from Leonardo da Vinci in the sixteenth century and Galileo Galilei a century after (see Bazant, 2002, for more detailed historical review on size effect). Over the last three decades, numerous studies concerning size effect have been performed on concrete using various specimen geometries and loading configurations. Main focus of these tests was uniaxial tension and three-point and four-point bending testing. With less intensity, tests have been performed using Brazilian splitting tensile and uniaxial compression (centric and eccentric) tests (Rilem, 2004).

Much of these tests were conducted to try verifying size effect models such as the Size Effect Model (SEL) from Bažant and co-workers (Bazant, 1984, 1999) and the Multi-Fractal Scaling Law (MFSL) from Carpinteri and co-workers (Carpinteri and Chiaia, 1995; Carpinteri et al., 1995). These models are of phenomenological nature and must be fitted to experimental data for different material types, specimen geometry, and test type. Peculiarly, no test data are reported in literature regarding size effect under biaxial and multiaxial loading types despite their vital constitutive role for the behaviour of real structures. This is except few size effect tests on hollow-cylinder specimens of rock materials, which are representative for multi-axial compressive state of stress (§ 2.5).

Compression failure of quasibrittle materials, similar to tensile failure, exhibits size effect on strength and failure characteristics. However, the compression failure in general and its size effect in specific are more complex and less understood. In rock mechanics, the most investigated scale effects have been those in uniaxial compression tests using different types of rocks despite some emphasis on coal (Jaeger and Cook, 1979). The outcome of such tests has been commonly described using power laws or the Weibull statistical size effect with some debate on the applicability of the latter in compressive failure for its progressive nature (Brown and Gonano, 1975). Stress gradients due to non-uniform loading and stored strain energy were argued, among others, as causes for observed scale effects. Scaling in rock is more complex as compared with concrete and other geomaterials for the high uncertainty (e.g. stress history), heterogeneity, and anisotropy of rock structures on the rock mass scale. Despite some contradiction, most of the experimental data points out that a strength reduction occurs with the increase of specimen size and the same applies to the scattering of results (ISRM Commission on Scale Effects in Rock Mechanics, 1995).

Baecher and Einstein (1981), reported size effect test results on gypsum model material under uniaxial and biaxial compression. These are the only tests in literature, as known to the author, regarding size effect in biaxial tests. They examined the size effect on the deformation process represented by the inflection points in the stress-strain response (end-points for regions III and IV in Figure 2.2). They also examined size effect in uniaxial test results and showed the specimen size to affect all these stress levels, but differently. A strong size effect was observed at peak stress and a milder and constant size effect over region III. In the biaxial tests, they report no dependence of peak stress on specimen size, whereas stresses in region III showed a decrease in stress with size. However, both stresses showed no dependence on confining pressure. No explanation was provided for the disappearance of size effect on peak stress with confinement, but this observation could suggest an influence of the failure mechanism on size effect at this stage. The effect of confining pressure on failure mechanism is well known and is more tangible in region IV of unstable crack propagation.

Advancements and increased interest in fracture mechanics of concrete structures led to the development of size effect models of which the SEL and the MFSL are most common. In addition to these, the Weibull theory of statistical size effect is well considered and widely applied. This theory will be treated with more detail in § 7.1.3. Bažant (1984), presented the Size Effect Law (SEL) with energy balance considerations for stable crack growth in geometrically similar concrete members. Basically, the theory bridges between strength/plasticity limits used for small sizes and Linear Elastic Fracture Mechanics (LEFM) size effect used for large sizes. The SEL is found as,

$$\sigma_N = \frac{A_{SEL} f_t}{\sqrt{1 + \dfrac{D_c}{B_{SEL}}}} \tag{2.1}$$

where f_t is the tensile strength or a strength parameter, D_c is a characteristic dimension of the member, A_{SEL} and B_{SEL} are model constants to be determined by fitting of experimental data. Equation (2.1) was derived for quasibrittle structures failing after large stable crack growth and is referred to as a deterministic size effect. Bažant and co-workers carried out further refinements that led to the so-called Universal Size Effect Law (USEL) (see Bazant and Planas, 1998).

Another form of the SEL in Equation (2.1) was proposed for size effect in compressive fracture of quasibrittle materials (Bazant *et al.*, 1993). The model is centrally based on the assumption that compressive fracture proceeds through laterally propagating axial splitting cracks with a spacing between the cracks that is not dictated by material inhomogeneity leading to the form,

$$\sigma_N = C_{SEL} D_c^{-2/5} + D_{SEL} \tag{2.2}$$

where C_{SEL} and D_{SEL}=constants. In Equation (2.2), the spacing between splitting cracks is assumed to minimize σ_N and in the case of borehole breakout to increase with borehole size increase. If this spacing is dictated by material inhomogeneity and not varying, then the model reverts to the LEFM formulation with a power exponent of –1/2 (Bazant and Xiang, 1997). The equation was presented to describe size effect in the borehole breakout phenomenon for intermediate values of hole sizes.

Carpinteri presented the MFSL approach for size effect in 1992, which is based on the assumption of multifractility for the damaged material microstructure. The model is expressed as,

$$\sigma_N = \sqrt{A_{MFSL} + \frac{B_{MFSL}}{D_c}} = f_{MFSL} \sqrt{\left(1 + \frac{l_{ch}}{D_c}\right)} \tag{2.3}$$

where A_{MFSL} and B_{MFSL} are constants to be determined from a best fit to experimental data. The term $l_{ch} = B_{MFSL}/A_{MFSL}$ separates the disordered regime from the ordered homogeneous regime and is proportional to d_{max} in concrete. The strength term $f_{MFSL} = (A_{MFSL})^{1/2}$ represents the positive deviation from a limit nominal strength for infinitely large sizes. The concept could be compared with the variation of the fractal dimension with the scale of observation. The fractal dimension increases with increase of material disorder or material inhomogeneity and therefore it transforms from a high fractal dimension for small sizes/scales to a constant value for large sizes. Carpinteri *et al.* (1999), argued that the failure mode of compressed concrete specimens could be considered resulting from micro tensile mechanisms and therefore the model in Equation (2.3) could be used for size effect in compressive fracture.

In concrete, a boundary layer or wall effect is considered to be a contributing factor for observed size effects, which is due to the relatively smaller content of large aggregates adjacent to the surface layer (mould or formwork side) as compared with the interior. The layer has different elastic properties and its thickness is dependent on the maximum

aggregate size used and is independent of the member size. The size effect is expected in this case due to the fact that in smaller members, the boundary occupies a large portion of the cross section as compared with large members. Other factors such as particle distribution, shrinkage cracking, and differential hydration are recognized to contribute to size effect but have not been systematically studied. Global effects, including structural effects, such as stress and strain gradients and moisture gradients are identified as well for being an important factor (e.g. Van Vliet, 2000).

2.5 THICK-WALLED HOLLOW-CYLINDER TESTS

The hollow cylinder test is an important means of assessing the stability and failure of circular openings, which is a problem common to many disciplines, including geotechnical, mining, and petroleum engineering. For its economical significance, the problem of maintaining a stable wellbore during drilling and production of hydrocarbons received prominent interest over the last few decades. The fundamental developments for understanding the environment around a deep wellbore were established by Westergaard (1940). This classical theory postulates that when a hole is drilled in rock under triaxial stress, the horizontal stress is relieved and the load is transferred around the hole as hoop stress. If the hoop stress exceeds the elastic limit, the hole starts to collapse. Depending on the confining stresses and rock strength, the deformation behaves either brittle or ductile. In 1941, Biot extended these considerations and clearly explained the role of pore pressure and fluid flow. Since then, numerous authors have contributed to the state of the art and today, research and engineering efforts have been accelerated due to the need of drilling deviated and horizontal wellbores that are non-co-linear with the principle stress directions.

For the laboratory study of wellbore stability, it is more appropriate to perform experiments on model openings, such as hollow cylinders. The hollow cylinder geometry lends itself for providing permutations of various multiaxial states of stress around its inner-hole depending on the stress path applied to its external boundaries. Several studies are reported in literature with regard to hollow-cylinder tests for wellbore stability analysis purposes on different types of rocks (e.g. Santarelli, 1987; Perie and Goodman, 1989; Ewy and Cook, 1990a, b; Kooijman *et al.*, 1991; Van Den Hoek *et al.*, 1992; Ringstad *et al.*, 1993; Tronvoll and Fjaer, 1994). Investigations into the constitutive behaviour of materials have been performed as well (e.g. Robertson, 1955; Hoskins, 1969; Gay, 1973).

Robertson (1955) in a study of rock strength tested different types of rock, mainly limestone and marble. He performed experiments on hollow-cylinders mostly with different ratios of external to internal radii and loaded under hydrostatic compression up to failure. He observed that specimens with radius ratios of less than three failed by shear showing equiangular spiral fracture shape, what he termed "trap door" collapse. Those with ratios greater than three failed by spalling. Among his observations he noted that small samples were stronger than the larger ones. In the discussion he regarded this effect to either unrecognized differences in processing the cylinders or to fewer imperfections of gross dimensions than in larger cylinders but not to size effect on strength. Hoskins (1969) performed series of experiments on thick-walled hollow cylinders for dif-

ferent isotropic rocks. He used rock specimens of 50 mm outer diameter, 25 mm inner diameter and 120 mm long. All specimens were jacketed internally and externally with soft rubber tubing. He controlled the frictional restraints at the ends by using sheets of dry paper and a thin layer of graphite between the papers and the anvils. Internal, external, and axial pressures were applied and controlled separately with variable stress paths calculated using elastic theory. Hoskins showed that failure always started at the inner surface and propagated outward into the cylinder wall. Depending on the stress path used, he observed fractures occurring upon conical, spiral or helical surfaces.

Gay (1973) carried out a series of experiments to study the growth of fractures around holes (circular & elliptical) cut in isotropic, homogeneous sandstone and anisotropic quartzite under hydrostatic compression. He used samples of 76 mm outer-diameter, 22 mm inner-diameter, and 127 mm long. His examination suggested that initial fractures around all the openings have the same geometry and probably the same origin. He observed spalling to take place at two opposite ends of a diameter of the opening and having begun at these points, spalling then continued from this locus. He pointed that increasing the hydrostatic pressure or holding it for long sufficient time, a second set of conjugate shear fractures appear and extension cracks tend to form. In addition, the growth of the fracture zone depends both on the inhomogeneous stress distribution and on the relative size of the openings. Fracturing in specimens with circular holes continued along spiral surfaces until the fracture approached close enough to the outer surface with resultant collapse of the specimen.

Santarelli (1987) presented a closed form solution for the stresses and displacements induced around an axisymmetric wellbore with an elastic modulus function of the minimum principal stress. An experimental program accompanied the study using sandstone hollow-cylinders with 204 mm long, 25 mm inner-diameter, and 102 mm outer-diameter under various confining pressures. He showed that the tangential stresses at and near the inner-hole may be much lower than those predicted by constant modulus linear elasticity (§ 2.5.1). Also the maximum tangential stress could be induced some distance from the wellbore wall and strains at the wall will vary non-linearly with the normalized far field stress. Ewy et al. (1988; 1990a; 1990b) investigated the failure process around highly stressed holes in thick-walled hollow cylinders of Berea sandstone and Indiana limestone with a hole diameter of 25.4 mm, 89 mm outer-diameter, and 152 mm long, tested under axisymmetric stresses in plane strain loading. In what they described a first scenario, they showed that the fundamental fracture mechanism is the growth of small splitting cracks oriented parallel to the tangential stress around the hole, starting close to the hole and progressing deeper with increasing stress. The cracks coalesce to form macroscopic splitting fractures with en echelon patterns that meet the inner-hole's wall. They found out that the apparent strength of rock adjacent to unsupported holes is 2-3 times the uniaxial compressive strength and attributed this to a possible size effect.

2.5.1 Linear-elastic solution of stresses in hollow-cylinders

In order to examine the stresses surrounding an axisymmetric wellbore, the geometry of a hollow cylinder (Figure 2.7) is usually considered.

Considering a linear elastic stress-strain relationship, the stresses at a point identified in the cylindrical coordinates r, θ, and z are denoted σ_r, σ_θ, σ_z, $\tau_{r\theta}$, τ_{rz}, and $\tau_{\theta z}$ with σ_r=radial stress, σ_θ= tangential stress, σ_z=axial stress, $\tau_{r\theta}$, τ_{rz}, and $\tau_{\theta z}$ are shear stresses, and ρ is the material density. These stresses are calculated through solving three sets of equations (Jaeger and Cook, 1979),

–   The equations of equilibrium in cylindrical coordinates:

$$\frac{\partial \sigma_r}{\partial r} + \frac{1}{r}\frac{\partial \tau_{\theta r}}{\partial_\theta} + \frac{\partial \tau_{zr}}{\partial z} + \frac{\sigma_r - \sigma_\theta}{r} + \rho R = 0$$

$$\frac{1}{r}\frac{\partial \sigma_\theta}{\partial_\theta} + \frac{\partial \tau_{r\theta}}{\partial r} + \frac{\partial \tau_{z\theta}}{\partial z} + \frac{2\tau_{r\theta}}{r} + \rho\theta = 0 \qquad (2.4)$$

$$\frac{\partial \sigma_z}{\partial z} + \frac{\partial \tau_{rz}}{\partial r} + \frac{1}{r}\frac{\partial \tau_{\theta z}}{\partial\theta} + \frac{\tau_{rz}}{r} + \rho Z = 0$$

In case of a hollow cylinder with inner radius R_i, inner diameter D_i, outer radius R_o, outer diameter D_o, pressure on outer surface σ_o, and on the inner surface σ_i, with neglecting the body forces and assuming that all quantities in (2.4) are independent of θ and z, the three partial differential equations degenerate into one ordinary differential equation,

$$\frac{\partial \sigma_r}{\partial r} + \frac{\sigma_r - \sigma_\theta}{r} = 0 \qquad (2.5)$$
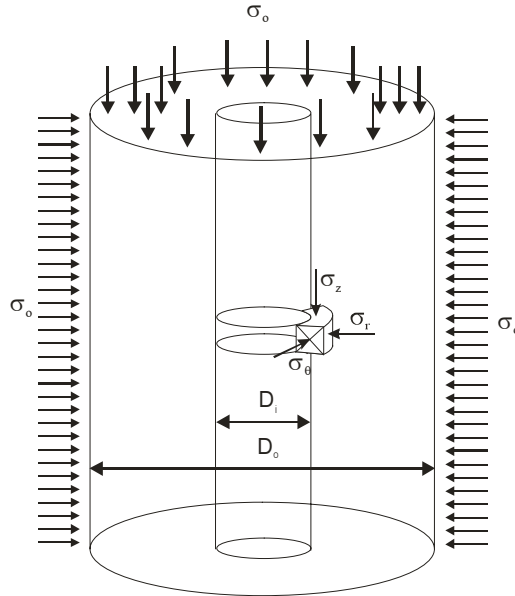

Figure 2.7: Geometry and boundary conditions of the axisymmetric hollow-cylinder geometry.

–   The compatibility equations that relate displacements and strains. If u and w are the radial and axial displacements, respectively,

$$\varepsilon_r = -\frac{du}{dr}$$

$$\varepsilon_\theta = -\frac{u}{r} \quad (2.6)$$

$$\varepsilon_z = -\frac{dw}{dz}$$

–   The constitutive material behaviour that is here assumed isotropic, linear elastic as described by Hook's law,

$$E\varepsilon_r = \sigma_r - \nu\sigma_\theta - \nu\sigma_z$$

$$E\varepsilon_\theta = \sigma_\theta - \nu\sigma_r - \nu\sigma_z \quad (2.7)$$

$$E\varepsilon_z = \sigma_z - \nu\sigma_r - \nu\sigma_\theta$$

Where E and ν are the Young's modulus and Poisson's ratio, respectively.

By solving equations (2.5), (2.6), and (2.7) with considering a plain strain condition (ε_z=0) and introducing the boundary conditions for the radial stress in case of a finite hollow-cylinder: σ_r=σ_o for r=R_o and σ_r=σ_i for r=R_i.

The stresses and radial displacement around the inner-hole in a hollow-cylinder with respect to the radius r from the cylinder axis could then be described as,

$$u = \frac{(1-2\nu)}{2E} \frac{\left(\sigma_o R_o^2 - \sigma_i R_i^2\right)r}{\left(R_o^2 - R_i^2\right)} + \frac{(1+\nu)}{E} \frac{\left(\sigma_o - \sigma_i\right)R_i^2 R_o^2}{\left(R_o^2 - R_i^2\right)r} \quad (2.8)$$

$$\sigma_r = \frac{\left(\sigma_o R_o^2 - \sigma_i R_i^2\right)}{\left(R_o^2 - R_i^2\right)} - \frac{\left(\sigma_o - \sigma_i\right)R_i^2 R_o^2}{\left(R_o^2 - R_i^2\right)r^2} \quad (2.9)$$

$$\sigma_\theta = \frac{\left(\sigma_o R_o^2 - \sigma_i R_i^2\right)}{\left(R_o^2 - R_i^2\right)} + \frac{\left(\sigma_o - \sigma_i\right)R_i^2 R_o^2}{\left(R_o^2 - R_i^2\right)r^2} \quad (2.10)$$

$$\sigma_z = 2\nu \frac{\left(\sigma_o R_o^2 - \sigma_i R_i^2\right)}{\left(R_o^2 - R_i^2\right)} \quad (2.11)$$

For the case of testing under external hydrostatic stress and zero inner-hole pressure (σ_i=0) and for cylinder with an outer-/inner-diameter ratio of 4, the equations (2.8)-(2.11) could be evaluated at the inner wall and further simplified to,

$$u = \frac{3}{2} \frac{\sigma_o R_i R_o^2}{\left(R_o^2 - R_i^2\right)E} \quad (2.12)$$

$$\sigma_\theta = \frac{2\sigma_o R_o^2}{\left(R_o^2 - R_i^2\right)} \quad (2.13)$$

$$\sigma_z = \nu \frac{2\sigma_o R_o{}^2}{\left(R_o{}^2 - R_i{}^2\right)} \qquad (2.14)$$

2.5.2 Hollow-cylinder stability and size dependence

Failure around wellbores and hollow-cylinder models from natural rocks has been well documented and studies have shown that final fracturing generally occurs on two opposite sides of the hole subject to the highest compressive stress concentration. The resulting failure then elongates the cross-section of the hole in a more or less elliptical shape, termed as wellbore/borehole breakout. Guenot (1989), in an analysis of the parameters involved in producing breakouts distinguishes four factors, which are:

–   In situ stresses that will be redistributed during the drilling of the borehole and concentrated in its vicinity.
–   The presence of a fluid in the voids of the rock that is usually different from the pressure in the borehole and there will be a pressure gradient.
–   Thermal gradients due to the cooling of the wall by the drilling fluid, which are able to generate additional stresses.
–   Chemical reactions between the drilling fluid and the rock surrounding the borehole.

Among these factors, the in situ stresses appear to be of utmost significance where most of the research activities on borehole failure have been directed. It is established that failure initiates around underground excavations inside the rock and not at the excavation wall, but the mechanism by which failure propagates is unclear and may be shearing or splitting tensile. In addition, a puzzling phenomenon for comprehending the behaviour of circular openings and their failure mechanism in laboratory tests is an observed size effect with definite strengthening when decreasing hole size (e.g. Haimson and Herrick, 1989; Carter, 1992; Van Den Hoek *et al.*, 1992; Ringstad *et al.*, 1993). These studies, however, did not apply inner-hole measurements, except for the study by Ringstad *et al.* (1993), and therefore little information is revealed on the deformation process and its link to the observed size effect. In these tests, generally, the collapse stress was used, which is a best estimate based on observing spalling activities or inner-hole observations using endoscopes. No studies are reported in the literature as well, to the best knowledge of the author, which tried to trace the fracture process in hollow-cylinder tests by e.g. testing to different levels of load and then unloading while freezing the fracture pattern and closely examining it afterwards. This procedure, rather than the final fracture pattern, could possibly shed light on the disputed failure mechanisms and its relevance to size dependence.

Quantification of the risk of failure during drilling or production requires the calculation of stress and/or deformation fields around the wellbore and a comparison with accepted criteria of failure. These calculations can be performed with varying degrees of sophistication and with varying prediction limitations. Most of the existing work on borehole stability is based on perfectly elastic/plastic models that are calibrated with test data taken from conventional triaxial compression experiments. In elastic analyses, failure is assumed to occur when the stresses reach the elastic limit that is usually set at the peak of the experimental stress-strain curve. Knowing the stress field associated with the well-

bore/hollow-cylinder configuration, various failure mechanisms can be assessed. The results of such analyses are frequently found conservative, which is probably due to their inability to account for pseudo-stable states associated with progressive failure and stress redistributions. In addition, such analyses ignore micromechanics of failure while focusing only on the strength of materials. Inelastic analyses take into account the existence of intact (elastic) and failed (plastic) zones, using appropriate constitutive relations. A major drawback of such procedure, and the elastic analysis as well, is its shortage to describe some observed failure modes such as cleavage fractures or splitting tensile failure.

Alternative solutions with higher sophistication and mathematical complexity based on the bifurcation theory were utilized as well (Vardoulakis and Papanastasiou, 1988; Vardoulakis and Sulem, 1995). The theory suggests that the critical bifurcation stress corresponds to the short wavelength limit that is affecting a vanishing narrow ring of material in the vicinity of the wellbore/hollow-cylinder wall. If surface instabilities are not possible, then the dominant failure mode is shear-band formation. Incorporating an internal length in the constitutive equations for such an approach enables modelling scale effects. This was done using a deformation theory for rigid-plastic material with microstructure (Cosserat material) by e.g. Mühlhaus and Vardoulakis (1987); Van Den Hoek *et al.* (2000). Zervos *et al.* (2001), used gradient elasto-plasticity to model the progressive failure and scale effect in hollow-cylinder tests. His simulations show a scale effect with strength increase as the hole radius decreases and that this effect is less pronounced for larger hole sizes.

Chapter 3

MODEL MATERIAL

3.1 INTRODUCTION

Two synthetic model-materials were developed in order to investigate the influence of micro-structural parameters such as aggregate size on the size effect and fracture behaviour in the hollow-cylinder tests. A synthetic material was chosen since natural rocks are highly heterogeneous in terms of their property distribution and it is hardly possible to obtain samples that are homogeneous and isotropic. The model material needed to be similar to weak reservoir rocks, mostly weak sandstones, where borehole instabilities often occur. Several methods exist for developing synthetic model materials, most of which are sophisticated, costly, and time consuming. The key to our work is that the method needed to be economic and simple enough for ease of control and reproducibility of results.

In this chapter, the model materials, their fabrication, and physical and mechanical properties are presented and discussed in detail. Afterwards, the material behaviour in terms of stress-strain response, failure, and fracture mechanisms is explained.

3.2 BACKGROUND

In this research, target characteristics for the model material were set as two fold, first, to generally represent a class of weak sedimentary rocks, e.g. weak sandstones such as Castlegate sandstones, exhibiting quasibrittle behaviour. Second, to accentuate the effect of microstructure, e.g. heterogeneity, on the material behaviour.

According to Stimpson (1970), suitability of a model material is often founded on the success with which one property only satisfies similitude since it is practically impossible to attain perfect similitude for a particular rock. When failure around boreholes is studied, this is often based on either the uniaxial compressive strength or the shear strength. It has been empirically demonstrated that a design criterion based on uniaxial compressive strength would broadly satisfy similitude conditions for triaxial strength in the compressive domain (Stimpson, 1970). A model material of this class can be fabricated from sand combined with a cementing agent, e.g. plaster, cement, clay, epoxy resin, oil or wax. Amongst, plaster and cement are the most advantageous binding agents for their cheapness and ease of fabrication. Cement-based materials are distinctive for their brittleness and therefore, cement was selected.

In the context of petroleum engineering and constructing models that simulate oil reservoirs, Wygal (1963), adapted a non-mixing approach through a particle distributor to produce a cement-sand pack that was subsequently consolidated by imbibing water. Heath (1965), modified the this technique through pouring the mixed sand and cement in a special distributor for producing a uniform mixture. Maloney and Kaiser (1989), developed an artificial sedimentary rock for borehole-breakout simulation tests using a mixture of sand/cement/water, which comprises 10% cement by weight and sand of the size 70-140 μm and 20-40 μm at a ratio 3:1 by weight respectively. The uniaxial compressive strength of their material is 3.14 MPa, Young's modulus of 1.35 GPa, porosity of 26%, and tensile strength of 1.2 MPa.

3.3 MATERIAL DEVELOPMENT

A trial and error procedure was employed for the mixture design and preparation of the model material. Considering the maximum safe capacity of our pressure test cell being 40 MPa and due to the often-observed strength enhancement during hollow-cylinder tests (§ 2.5) it was expected that if the material strength exceeds one-fourth the cell capacity, failure would not commence. Therefore, a target strength of 10 MPa uniaxial compressive strength was set for the model material, which is within the range of definition of weak sandstones (Dobereiner and De Freitas, 1986)

Commercially available river sand was used in a gap-graded sand mixture comprising two grain sizes at a grain diameter ratio approximately 6:1 and a ratio of large to small grains of about 3:1 by weight. Ordinary Portland Cement (OPC) of type CEM I 32.5 R (ENCI, Heidelberg Cement Group) was used at a content of about 200-330 kg.m^{-3} and a water/cement ratio ranging between 0.6-0.8. Several mixtures were developed with maximum grain sizes (d_{max}) of 1, 2, 4, and 8 mm. The absolute volume method was adapted in the design, while taking into account the assumed proportion values. In the

calculation, specific gravity values of 2.60 and 3.15 were used for the sand and cement, respectively. An overview of these mixtures, i.e. their proportions and compressive strengths, are given in Table 3.1. The presented compressive strength values were determined experimentally using portions of a beam, which is broken in flexure. This method was intended as a research tool for determining the relative compressive strength values of the various concrete mixtures. For each mixture, at least 3 beams of size 40x40x160 mm were cast and cured under water at room temperature for 28 days. At that age, the beams were tested for flexural strength using a three-point loading test. After visually confirming that fracturing occurred within the middle third of the beam span, the two broken portions were then tested in compression. In the compression test, the same set-up was used after changing the loading platens, so that the contact faces are basically square, with the same dimensions as the nominal width of the tested beam, i.e. 40 mm.

Table 3.1: Overview of mixing proportions for the trial mixtures

ID	Mix Proportions (kg.m^{-3})						Cement (kg)	w/c	$f_c \pm SD^*$ (MPa)
	River sand and gravel (mm)								
	4-8	2-4	1-2	0.5-1	0.25-0.5	0.125-0.25			
A_m	---	1071	---	187	170	---	200.0	0.60	13.9±1.2
B_m	---	1071	---	119	119	119	200.0	0.60	18.3±1.0
C_m	---	---	---	1353	---	451	220.0	0.80	2.10±0.7
D_m	---	---	---	1320	---	440	220.0	0.80	2.90±0.5
E_m	690	690	---	172.5	172.5	115	230.0	1.00	8.20±0.4
F_m	---	---	---	1265	---	460	230.0	1.50	3.00±0.3
G_m	---	1412.5	---	236	236	---	258.5	0.80	9.00±1.4
H_m	---	---	1412.5	236	236	---	258.5	0.80	6.30±0.7
I_m	709.6	709.6	---	173.5	173.5	173.5	236.5	0.80	11.7±0.6
J_m	---	---	---	1489	241	241	265.0	0.65	2.50±0.5
K_m	---	1175	---	376	376	---	235.0	0.80	9.20±0.4
L_m	---	---	1413.5	255	255	---	258.5	0.65	3.50±1.1
M_m	---	---	---	176.2	176.2	118.7	258.5	0.80	10.3±1.0
N_m	---	---	1412.5	236	236	---	258.5	0.80	6.50±0.8
O_m	---	---	1291.1	233	233	---	329.0	0.80	8.60±0.7
P_m	---	---	1409.5	216	216	---	282.0	0.80	7.50±0.6

*SD = standard deviation from tested samples (three samples minimum)

From Table 3.1, it is realized that only mixtures with a d_{max} greater than 2 mm could attain the target strength of 10 MPa. An aspect usually considered in concrete technology is the ratio between the smallest dimension of a structural element and d_{max}. Various standards specify this ratio to be at least 3-5 with a value of 5 being more widely considered. If we consider our smallest hollow-cylinder specimen (§ 4.2.1) of D_i=12.5 mm and D_o=50 mm, its least dimension is the wall-thickness (W) and is equal to (D_o–

$D_i)/2$=18.75 mm. This suggests d_{max} not to exceed 4 mm for which the ratio W/d_{max} for the smallest specimen is equal to 4.70.

Two materials were selected form the trial mixtures for use as model materials in the hollow-cylinder tests. The mixtures identified as G_m and O_m in Table 3.1 (outlined in the table) with d_{max} value of 4 mm and 2 mm respectively were chosen as they practically satisfy the design target strength. The difference in aggregate size, being double for G_m as compared with O_m, would serve in emphasizing the influence of microstructure on scaling and fracture properties. For convenience, in the remaining of this thesis the mixtures are named as M2 and M4 for mixtures O_m and G_m respectively. The grading size-distribution of the aggregates used in both mixtures is given in Table 3.2 and their grading curves are shown graphically in Figure 3.1.

Table 3.2: Grading size-distribution for the selected mixtures (% passing)

Sieve (mm)	4	2	1	0.50	0.25
M2	100.0	100.0	26.50	13.25	0
M4	100.0	25.00	25.00	12.50	0
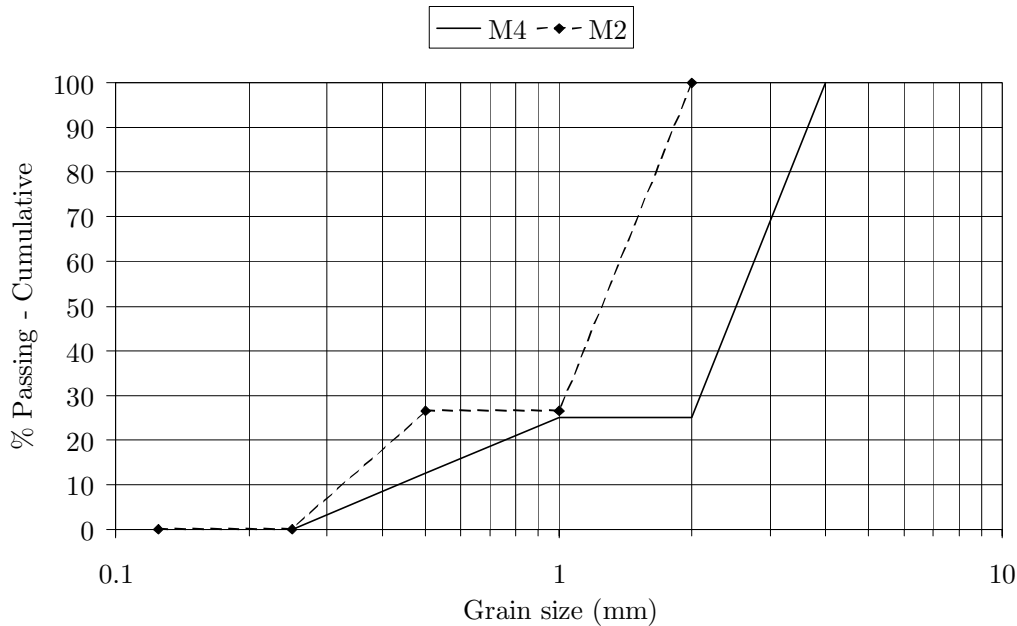
Figure 3.1: Grading curves of the two selected mixtures M2 and M4.

3.4 MATERIAL PROPERTIES

3.4.1 Physical properties and microstructure

For both mixtures, the density (skeletal and bulk) and effective porosity (interconnected pore space) were determined using Helium-pycnometry (Penta-pycnometer) and buoyancy techniques. The results from these tests are presented in Table 3.3.

Table 3.3: Physical properties of materials from laboratory experiments

Mixture	Penta-pycnometer				Buoyancy method		
	Bulk volume	Skeletal volume[*]	Skeletal density[*]	% Porosity[*]	Bulk density	Dry density	% Porosity
M2	55.48	44.24	2.62	20.25	2.22	2.06	16.32
M4	40.60	34.09	2.61	16.04	2.28	2.10	17.07

[*]Value based on average of three measurements

The results in Table 3.3 suggest that porosity determination using the Buoyancy method is reasonably accurate when compared to the gas-displacement method used in the Helium pycnometry. Therefore, the Buoyancy technique could suffice for applications where detailed information on pore structure is not a main concern.

It is eminent that the properties of any heterogeneous system, e.g. concrete, depend upon the mechanical and phyisco-chemical interactions between its different phases. In cementitious materials generally and OPC concrete particularly, the aggregate-matrix interface, (ITZ), is a weak zone and have shown to be the weakest-link in the system allowing for crack nucleation and propagation. In Figure 3.2, the morphology of aggregate-matrix interface in a fracture surface from M4 is revealed using the secondary electron (SE) technique in an Environmental Scan Electron Microscope (ESEM) model Philips XL30 ESEM. The interface bond with its porous nature is identifiable, which is not so surprising for this mixture with a $w/c=0.8$ and its scanty content of fines.

The backscattered electron (BSE) imaging technique was utilized for more insight on the composition and distribution of the microstructure. The basic principle of BSE technique is that electrons from the incident beam in ESEM are of higher energy as compared with secondary electrons and so are detected from greater depths. The intensity of the BSE signal is a function of the average atomic number of the investigated spot (Scrivener, 2004). A 400-day old specimen from M2 material was prepared for BSE examination with a size 33x17x10 mm. The specimen was vacuum dried, impregnated using a low-viscosity fluorescent epoxy-resin, and then cut to size. The specimen was then hand-ground on a lap-wheel with moderate-speed using p320, p500, and p1200 sand papers.
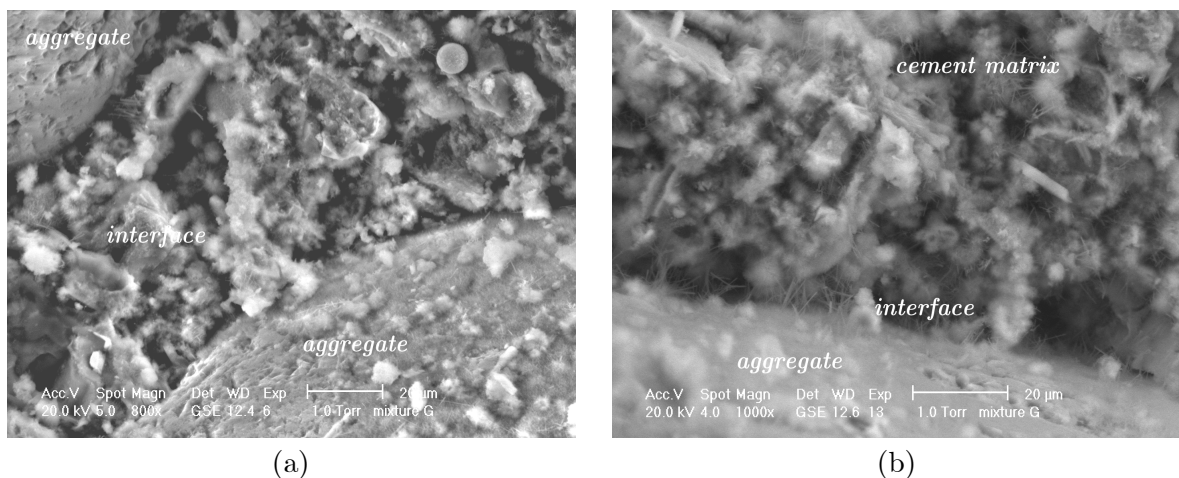

Figure 3.2: ESEM-micrographs showing (a) the morphology of aggregate-interface, and (b) the aggregate-interface bond.
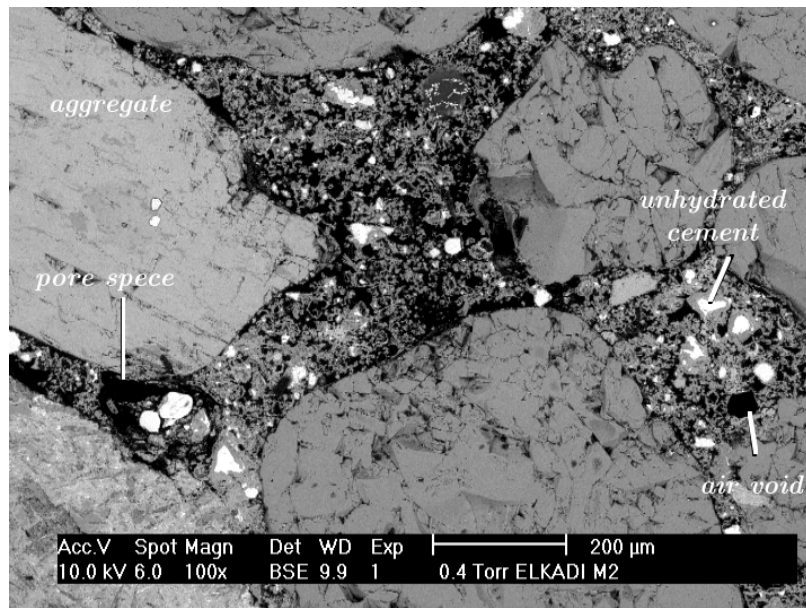
Figure 3.3: Micrograph from a 400-day old M2 specimen viewing an overview of aggregate layout and in-between the hydrated microstructure.

Diamond pastes were used afterwards for polishing the surface with a paste fineness of 6, 3, 1, and 0.25 µm correspondingly. The micrograph in Figure 3.3 was taken at a relatively low magnification to illustrate the different features of the hydrated microstructure of the M2. Shown are the sand grains, relatively large in the graphs 200-400 µm in size and labelled as aggregate, with the hydrated cement paste amid. Appreciable amount of pore space is visible in the graphs distinguished by its dark (black) appearance—labelled as pore space in Figure 3.3—due to the low atomic number of the epoxy resin filling those spaces. Air voids are differentiated from other pore space through their circular shape in two-dimensions (2D) as they are essentially spherical in three-dimensional (3D) space (Diamond, 2004), e.g. labelled as air void in Figure 3.3. In the same figure, unhydrated clinker particle is indicated, which is distinctive for their bright appearance in the BSE images. Darker hydration product-shells of different thicknesses closely surround these unhydrated cores. The particle layout in Figure 3.3 gives an impression of the high particle density used in the mixture (75%), which resulted in particles being of close proximity of one another (10-100 µm). The contact areas between the particles in these 2D views appear limited in size, but it should be mentioned that the 3D picture could differ from this. In BSE technique, the section through cement particles and aggregates is generally not equatorial—does not cut through the center—resulting in the thickness of features being overestimated (e.g. Scrivener, 2004).

In order to estimate the detected pore space in the cement paste, 9 micrographs were taken at higher magnification values (500X). In Figure 3.4a, an example from these images is shown. The image analysis program OPTIMAS 6.5 was used for this purpose. The image analysis started by image segmentation using threshold technique in grey level ranging from 0 to 255. A standardized contrast and brightness setting were used and pores were set from solid components at a grey level of 50 (Sahu *et al.*, 2004). The resulting image after the application of the threshold was binarized and afterwards filtered to remove pixels produced by noise. An automated procedure was employed in
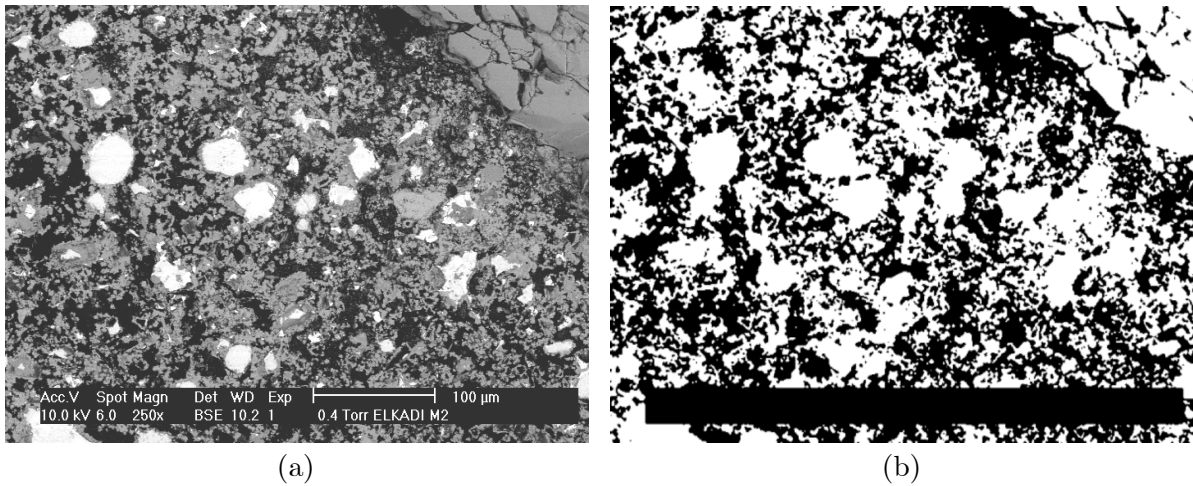
Figure 3.4: A typical BSE image used for porosity analysis (a), and its matched binary image with a 50/255 threshold (b). Black defines the pore (capillary) space in the image.

OPTIMAS to estimate the area occupied by the pore space. This resulted in an average estimate for this area equal to 55.3% with a standard deviation of 4.3%. Figure 3.4b compares the binary image obtained after applying the threshold 50/255 and filtering with its BSE image in Figure 3.4a. The high porosity obtained from the image analysis is in line with the premise that capillary porosity is primarily dependent on the w/c ratio.

3.4.2 Uniaxial compression tests

Two types of uniaxial compression tests were performed in this research. Firstly, a series of tests was performed on cylindrical specimens, for both mixtures, in a stiff testing machine with 500 kN load cell under a displacement-controlled mode. These were performed for material characterization purposes during its development phase. Secondly, routine cube tests were performed for quality control on casting and quality assurance for reproducibility of results. Results of these cube tests, which accompanied each series of size effect tests, are presented in § 5.3.1. In this paragraph, the uniaxial compression tests on cylindrical samples and their results are considered.

In all tests, cylindrical samples were used of height/diameter (h/d) ratio equals two. All samples were cored from 150 mm cubes, which were cast and then cured for 28 days in a climate room at 95-99% relative humidity (RH) and 20°C temperature (T). After the cores were drilled, they were cut to length, ground flat, and then dried in an oven at 105°C for two days, which were sufficient for equilibrium. For the M4, samples of 60 mm diameter were tested, whereas for the M2 samples of 54.1 mm diameter (NX size) were used. During testing, forces were measured by means of a calibrated load cell with 500 kN capacity. Two Linear Variable Differential Transducers LVDT of 5 mm stroke, which were mounted on the loading platens, were used for measuring the axial deformations. Lateral deformations were monitored as well with an MTS circumferential (chain) extensometer. A deformation control-rate of 4 μm.s^{-1} was used during all tests.

An overview of the tests performed for both mixtures and their outcome is given in Table A.1, Appendix A. In Table 3.4, the average mechanical properties calculated from the

individual results given in table A.1 are presented. These properties include the uniaxial compressive strength (f_c), the Young's modulus (E), and the Poisson's ratio (ν).

Table 3.4: Average properties from uniaxial-compression tests

Mixture	f_c MPa	E-modulus GPa	Poisson's ratio ν
M4	9.07±0.64	7.70±0.58	0.15±0.01
M2	12.56±2.52	6.77±0.85	0.12±0.02

The higher scatter in the strength value for the M2 as compared with the M4 could be explained owing to the extra difficulty in casting and compacting the 2 mm mixture as compared with the 4 mm. The finer structure of the mixture allows particles to float easier in the mix water recognizing the high w/c used. In addition, the standardized compaction style of vibrating on different layers, used in the cubes from which test results are shown in Table A.1, was not effective in our case with high w/c ratio. Interrupting the vibration during casting caused excess water and air to be trapped within the specimens causing the higher scatter and relatively large air voids after hardening. This aspect was later improved through adapting a continuous vibration style that forces excess water to travel to the surface while, however, observing not to lose much fines in the carried-away water.

3.4.3 Triaxial compression tests

Sets of triaxial tests were performed using the Hoek cell, which is a commercial triaxial cell designed to determine the triaxial strength of cylindrical cores of rock or concrete. In the Hoek cell, radial pressure is applied via a regular hydraulic pump through a thick (2.85 mm) urethane membrane. The axial load is applied directly to the flattened sample ends via a hydraulic ram through a pair of steel spherical seats. The tests were servo-controlled using the axial displacement whereas the confining stress ($\sigma_2 = \sigma_3$) was manually controlled with the help of a hydraulic jack.

Cylindrical core samples were used for testing, which were drilled form the same cubes used in the uniaxial compression tests (§ 3.4.2). The cylinders had a height/diameter ratio of $\cong$1.80 and a diameter of $\cong$55 mm (NX size). During testing, axial forces were measured by means of a calibrated 500 kN load cell. Two 5 mm stroke LVDTs were used for measuring the axial deformation and their average signal was used to control the tests at a deformation rate of 4 μm.s^{-1}.

Two sets of tests were performed for M4 and one set for M2. An overview of the tests and their results is provided in Tables 3.5-3.6 for M2 and M4 respectively, which include dimensions of specimens, confining pressure, biaxial strength f_{2c}, and the peak strain. The first set for M4 and the tests for M2 were performed at an age of 28 days, whereas the second set for M4 was performed at an age of 180 days. The values of f_{2c} in Tables 3.5 and 3.6 were calculated by dividing the maximum load carried by the specimen during the test by the original cross-sectional area. Complete stress-strain diagrams are presented and discussed in § 3.5.2.

Table 3.5: Mechanical properties of M2 from triaxial-compression test results

Diameter mm	Length mm	$\sigma_2 = \sigma_3$ MPa	$f_{2c} = \sigma_1$ MPa	Peak strain ε_1 x 10^{-3}
54.2	106.9	3.00	23.9	16.2
54.2	106.9	8.00	40.2	25.1
54.2	106.7	20.0	70.9	28.0
54.2	107.9	30.0	101.0	36.2

Table 3.6: Mechanical properties of M4 from triaxial-compression test results

Mixture	Diameter mm	Length mm	$\sigma_2 = \sigma_3$ MPa	$f_{2c} = \sigma_1$ MPa	Peak strain ε_1 x 10^{-3}
M4[1]	54.2	104.3	0.50	10.9	4.00
M4[1]	54.2	102.5	1.00	15.1	10.0
M4[1]	54.2	104.9	2.10	25.6	21.9
M4[1]	54.2	104.5	2.10	24.0	17.1
M4[1]	54.2	104.7	5.00	35.9	17.5
M4[2]	54.1	107.2	2.50	37.5	13.5
M4[2]	54.3	106.6	3.70	45.1	17.6
M4[2]	54.4	107.7	5.00	51.1	18.1
M4[2]	54.4	106.0	5.00	50.6	17.8
M4[2]	54.4	106.7	7.50	55.8	19.2
M4[2]	54.4	107.9	10.0	67.6	24.9

[1]tests performed at 28 days of age. [2]tests performed at 180 days of age.

3.4.4 Brazilian splitting tensile tests

In order to explore the strength properties of the material under indirect tensile-loading conditions, a series of Brazilian splitting tests was carried out. It was not considered viable to perform direct tensile tests in the material characterization phase due to its complexity in execution and interpretation. Besides, from pilot tests and literature, it was recognized that cracking in hollow-cylinders owes probably to an extensile failure mode driven by the compressive forces around the inner-hole. Therefore, information from splitting tests would suffice to supplement the results from cylinder compression tests.

A total of 20 disk-shaped specimens were tested for their Brazilian splitting strength (f_{spl}). The disks were sawn from cores, which were drilled from the same cubes used in uniaxial and triaxial compression tests. All disks were 60 mm diameter with a thickness of around 25 mm. The coring direction was parallel to the casting direction and the loading direction during testing was perpendicular to it, which resembles the situation in the cylinder tests. All tests were force controlled using a manual pump, which resulted in rapid crack growth accompanied by sudden failure at peak load.

The indirect tensile strength was calculated according to the following formula:

$$f_{sp} = \frac{2F_{spl}}{\pi\, t\, d}$$ (3.1)

where F_{spl}=load at failure, t=thickness of the specimen, and d=diameter of the specimen. The average splitting strength from these tests was 1.13±0.20 MPa for the M4. Accordingly, the ratio f_c/f_{spl} is around 8.0 after 28 days, which is close to the lower boundary of the range generally observed for concrete between 9-14 (Mindess *et al.*, 2003).

3.5   MATERIAL BEHAVIOUR

3.5.1   Strength-time relation

Due to the high w/c ratio used in the mixtures, it is expected that a notable increase in strength with age would occur. Figure 3.5 shows the relative gain of strength with time for both mixtures M2 and M4. The strength results have been determined from cube compressive tests on 15x15x15 cm cubes, which were cast and then cured until test date in a climate room at RH of 95-99% and T=20°C. As seen in the figure, the strength development rate form both mixtures is fairly constant up to 28 days with the strength measured at 7 days being approximately 57% of the strength at 28 days. Afterwards and up to 56 days, the M2 gains strength at higher rate as compared with M4. After that, the strengthening rate appears same for both mixtures and up to an age of 196 days for M4 and 308 days for M2.
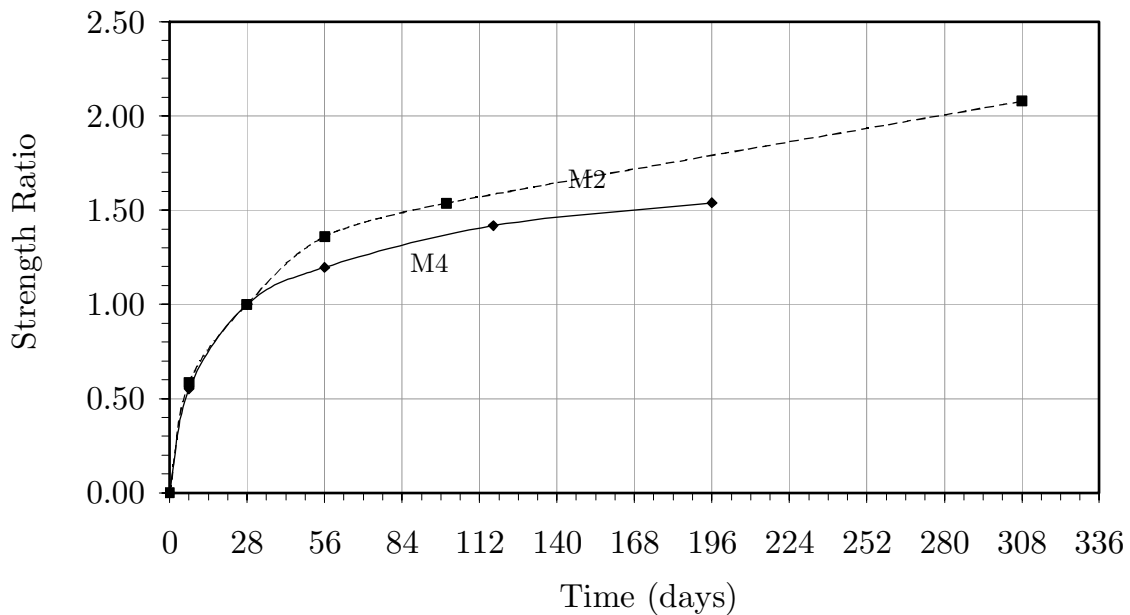
Figure 3.5: Relative gain in cube strength as compared to the 28 days strength with time for both M2 and M4 mixtures.

The reason for a higher rate in M2 during the period 28-56 days is not understood fully. For M2 the strength after 308 days is nearly two times that at 28 days, whereas for M4 the strength after 196 days is 1.5 times that at 28 days. The gain in strength with time is considered vital in connexion with the size-effect testing programme. The effect should be minimized to avoid introducing a fallacious factor that could produce an apparent size effect, which is not a true index of material behaviour. Also, the influence of d_{max} on size effect would be more factual if such effects are taken into account and prevented from affecting the experimental results. Accordingly, the time period up to 28 days appears optimum in this regard and is considered in the experimental design as discussed in § 4.3.1.

3.5.2   Stress-strain response

Uniaxial compression

As discussed in § 2.2.1 the stress-strain response is a combined structural and material behaviour and not a sole material response. However, the stress-strain curve reveals informative data and material indices, rather than properties, and is presented and discussed hereafter. Figure 3.6 shows the stress-strain diagram from uniaxial compression tests on cylinders from M4 (§ 3.4.2). The top graph in the figure represents the axial stress versus the axial and lateral strains, whereas the bottom graph shows their volumetric strain response.

In principal, all the stages schematized in Figure 2.2 (§ 2.2.1) concerning the stress-strain relation with failure development are recognized. When applying axial stress, an ascending branch is observed that is slightly curved indicating a non-linear response of the material. During this stage, the lateral strains are smaller than the axial strains with Poisson's ratio; the ratio of lateral to longitudinal strain, in the order of 0.15 at a stress level nearly 50% of the peak stress. At a stress level close to 80% of the peak, larger lateral deformations took place and the Poisson's ratio increased. By examining the volumetric strain curves, initial compaction is observed up to about 80% of the peak stress, after which volume increased since dilatancy took place. The dilatancy and rapid increase in lateral strains are generally attributed to unstable crack propagation and coalescence (see definition region IV, Figure 2.2). Similar behaviour is observed for the mixture M2, but with a higher scatter in the results (Figure 3.7). As seen in the figures, the mixtures show a high degree of stiffening during the initial loading, which is rather characteristic for porous materials such as sandstones due to their higher compressibility as compared with denser materials.
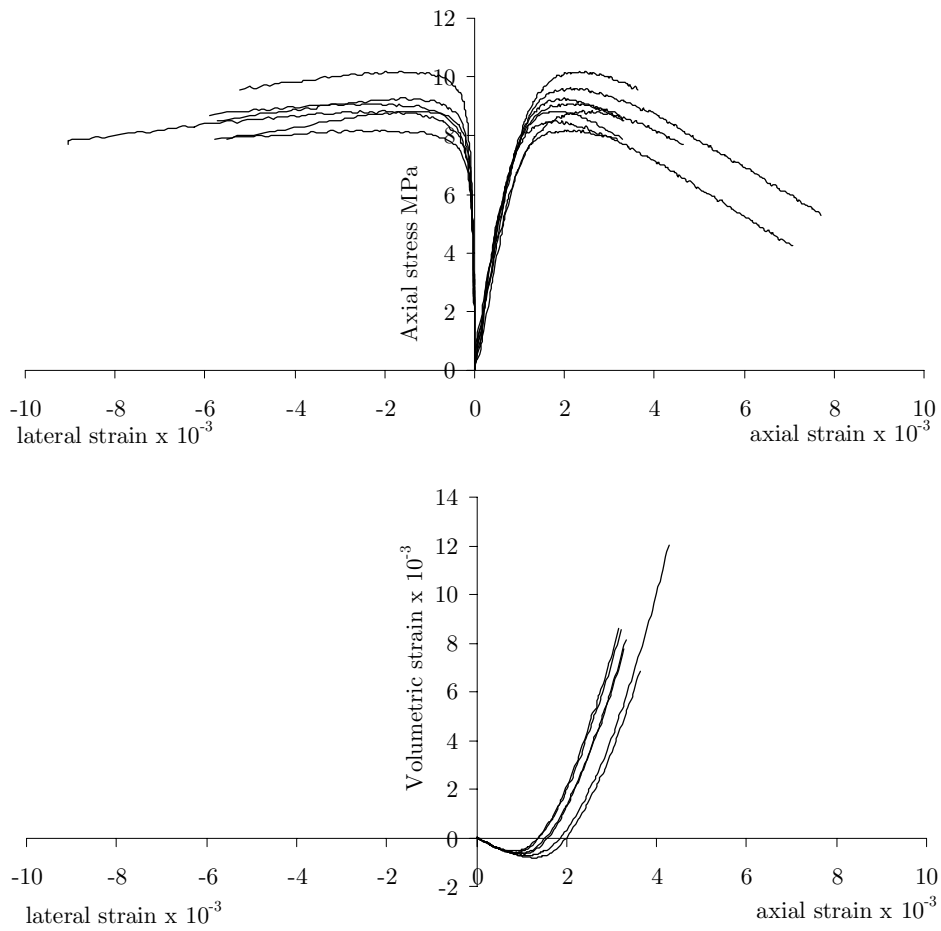
Figure 3.6: Axial stress (top) and volumetric strain (bottom) versus axial and lateral strains from uniaxial compression tests on mixture M4.
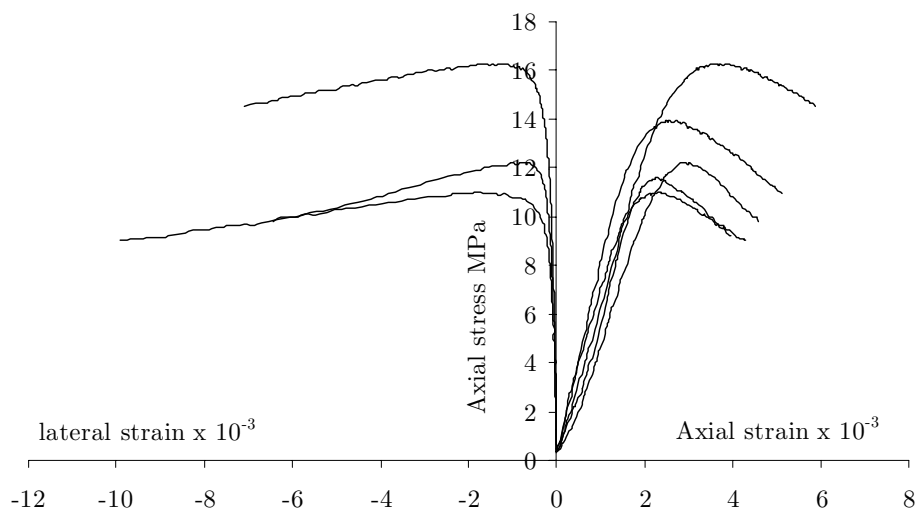

Figure 3.7: Axial stress versus axial and lateral strains from uniaxial compression tests on mixture M2.

Triaxial compression

During triaxial testing and due to the application of a small confinement, remarkable strengthening occurred for both mixtures. In Figures 3.8-3.9, the stress-strain relations are presented from tests on M4 at different levels of confinement. Results from two sets of experiments are included in the figures, which were performed at different age of the material (§ 3.4.3). The first set tested after 28 days was confined at 0.5, 1.0, 2.1, and 5.0 MPa (Figure 3.8), whereas the second set tested after 180 days was tested under confinement equal to 2.5, 3.7, 5.0, 7.5, and 10.0 MPa (Figure 3.9). The tests with a confining pressure of 2.10 MPa in the first set and 5.0 MPa in the second set were performed twice for checking reproducibility. In the figures, the axial stress includes the initially applied hydrostatic pressure; therefore, the stress values in the curves do not start from zero. By examining the results in Figure 3.8, an increase in the load carrying capacity of the material is observed. At a confining stress of 0.50 MPa, which is nearly 5% of the f_c value of the mixture, a peak could still be distinguished with a smooth descending post-peak response. As confinement slightly increased to about 1.0 MPa, a strength plateau is observed indicating apparent ductility of the material. This confinement appears to be close to the brittle-ductile transition since the peak is almost concealed, leaving a smooth elastic-plastic transition. At higher levels of confinement, 2.1 and 5.0 MPa, stress hardening is observed as the stress increases with increasing deformation.

The behaviour of the mixture M4 after 180 days is much alike after 28 days. A seeming difference between the two is a less stiffening effect in the tests after 180 days (Figure 3.9) as compared with those after 28 days (Figure 3.8), which is probably owing in part to a continued hydration process leading to a denser structure with time
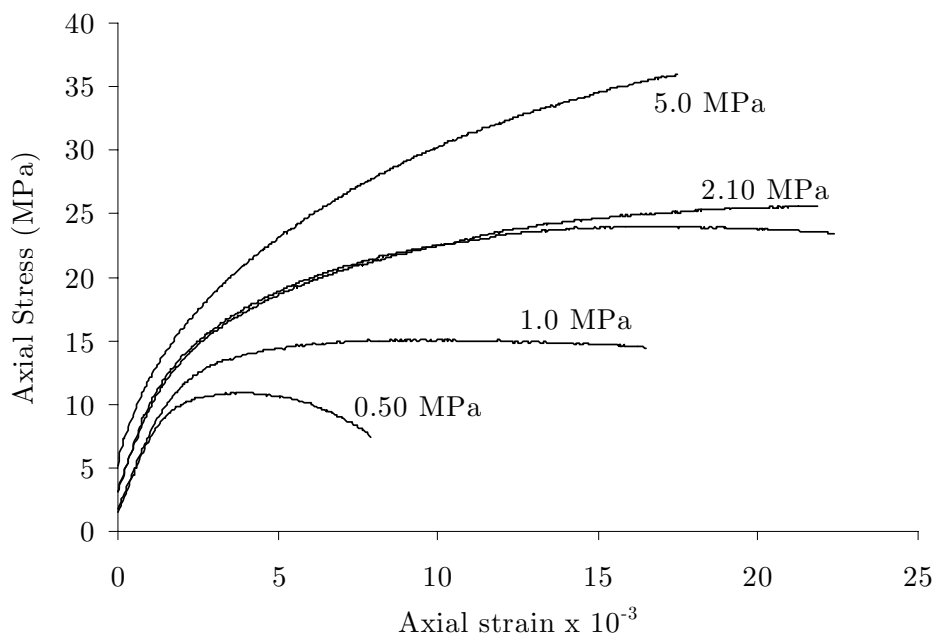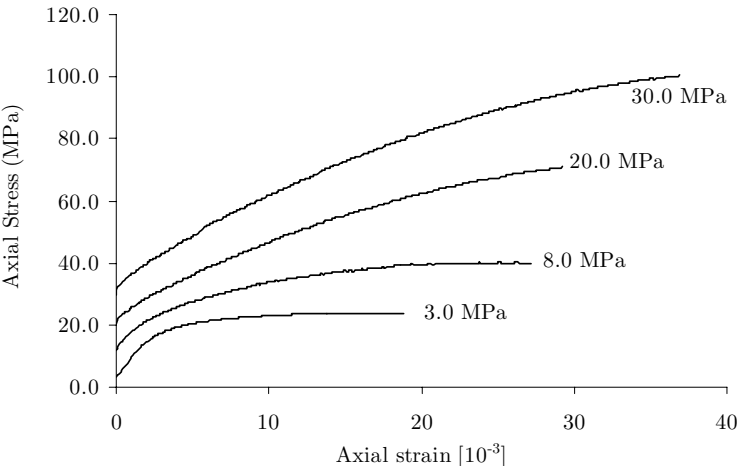

Figure 3.8: Axial stress versus axial strain curves recorded during triaxial tests on specimens of M4 mixture after 28 days. The numbers next to the curves are the confining pressure.
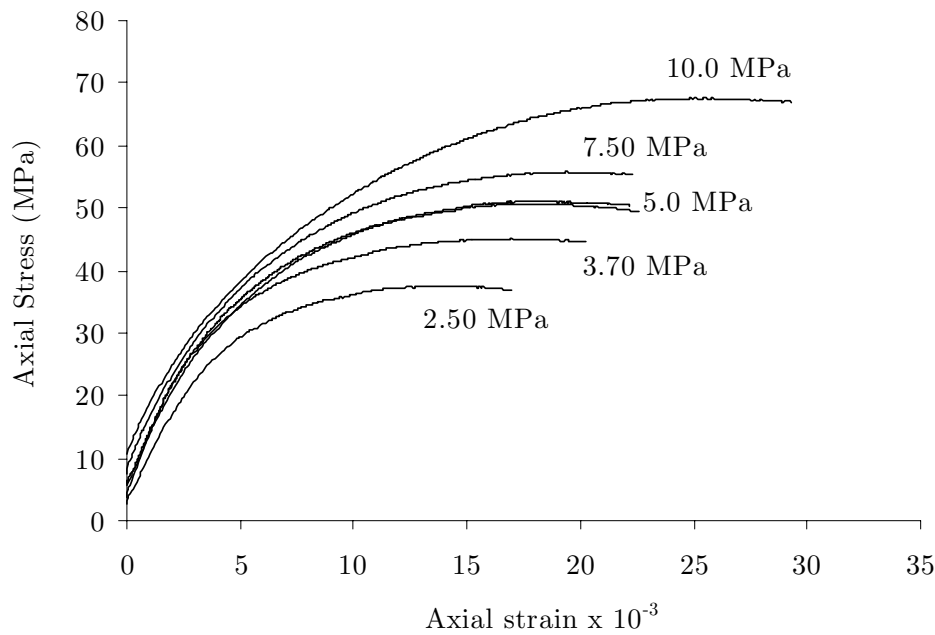
Figure 3.9: Axial stress versus axial strain curves recorded during triaxial tests on specimens of M4 mixture after 180 days. The numbers next to the curves are the confining pressure.

In Figure 3.8, the slope of the initial linear portion of the stress-strain curves increase with confinement suggesting that the specimens were compacting during hydrostatic loading prior to application of the deviatoric stress. The compaction and pore crushing will probably continue during deviatoric loading, as recently observed in uniaxial confined experiments on mortars with w/c=0.8 (Burlion *et al.*, 2001).

Noteworthy as well is a rather extended strain-hardening region in the curves, which is recognized as the part between the onset of nonlinearity (yield point) and the peak. Figure 3.10 shows a plot of the relation between the values of the ratio of the axial stress at onset of nonlinearity to peak stress versus confining pressure for the two sets of tests. It can be seen that this ratio decreases rapidly with confining pressure for tests after 28 days indicating an increase in the strain-hardening region with increase in confinement. As a result, the load applied in the strain-hardening region increases with confinement since the peak strength increases with confining pressure (Figure 3.8). For the tests after 180 days, the ratio appears initially constant up to 3.75 MPa and then decreases gradually. This shows less sensitivity at low confining pressures for the tests after 180 days as compared with the tests after 28 days.

Figure 3.11 shows the triaxial test results on M2 at confining pressures equal to 3.0, 8.0, 20.0, and 30.0 MPa. At a confining stress of 3.00 MPa, which is nearly 30% of f_c value, a plateau is observed indicating apparent ductility of the material. This confinement appears near the brittle-ductile transition since the peak is almost concealed, leaving a smooth elastic-plastic transition. At higher levels of confinement up to nearly 30 MPa, stress hardening is observed with increase in ductility.
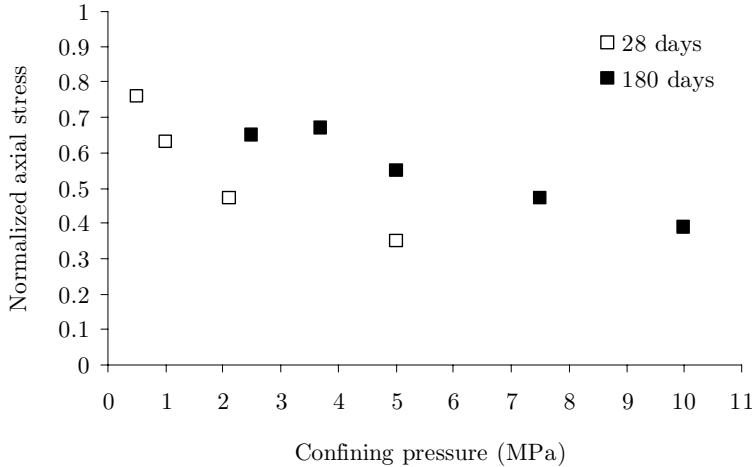
Figure 3.10: Variation of the normalized value of onset of nonlinearity with confining pressure measured during triaxial tests on mixture M4 after 28 days and 180 days.

Figure 3.11: Axial stress versus axial strain curves recorded during triaxial tests on specimens of M2 mixture after 28 days. The numbers next to the curves are the confining pressure.

3.5.3 Failure observations and fracture patterns

Uniaxial compression

In general, the specimens from both mixtures failed in a quasibrittle manner under uniaxial compression. The failure patterns revealed after completion of the tests, showed several distributed vertical cracks mostly intensified in the mid third of the specimens. The cracks were parallel to the direction of the maximum axial compressive stress with no distinct single macro crack (Figure 3.12).
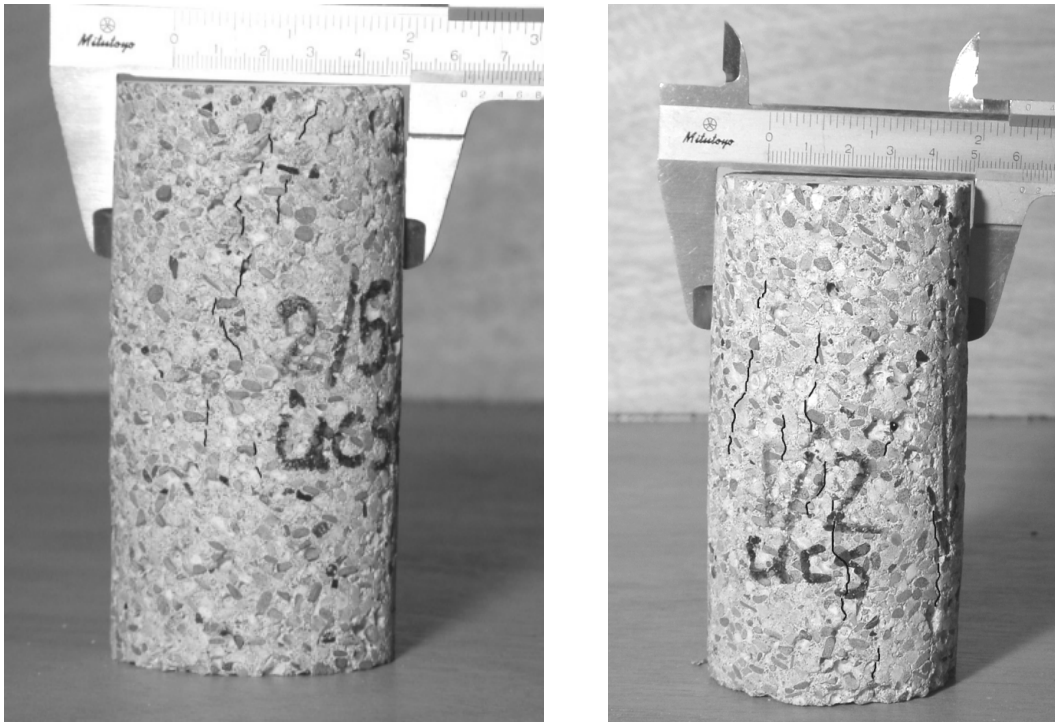
Figure 3.12: Example of fractures observed in M4 after uniaxial compressive tests. Fractures that were visible to naked eye are highlighted in black.

Triaxial compression

After each test, the specimens were carefully extracted and examined for failure pattern and cracking. Shear-like failure planes were observed in all of the performed tests and for all applied confining stresses. The failure was generally located within the mid-third of the specimens' height and with clear inter-granular cracking along the failure plane.

As discusses above (§ 3.5.2), the brittle-ductile transition for M4 was observed at a notably low stress, namely for $(\sigma_2=\sigma_3)/\sigma_1=0.07$. In normal strength concretes, this transition occurs commonly for $\sigma_3/\sigma_1\cong0.20$-$0.25$ (Van Mier, 1997), whereas for rock materials a value of $\cong0.30$ is expected, but depends on the type of rock. However, this low transition ratio appears to be in agreement with the observation that coarse-grained porous materials tend to have a lower transition ratio when compared with fine-grained materials (Paterson, 1978). This is also in accord when considering the result from the finer mixture M2 with its transition at a ratio of 0.14, which is higher than that of M4 but still lower than common values for normal concrete. More noteworthy is that the brittle-ductile transition for M4 appears to take place at a σ_3/σ_1 value, which is not affected by specimen age or strength. From

Table 3.6 and Figure 3.9, this transition takes place for specimens tested after 180 days at $\sigma_3/\sigma_1=0.07$, which is identical to the value obtained from specimens tested after 28 days. This indicates that the material structure is rather decisive for the brittle-ductile transition in relation to its strength.
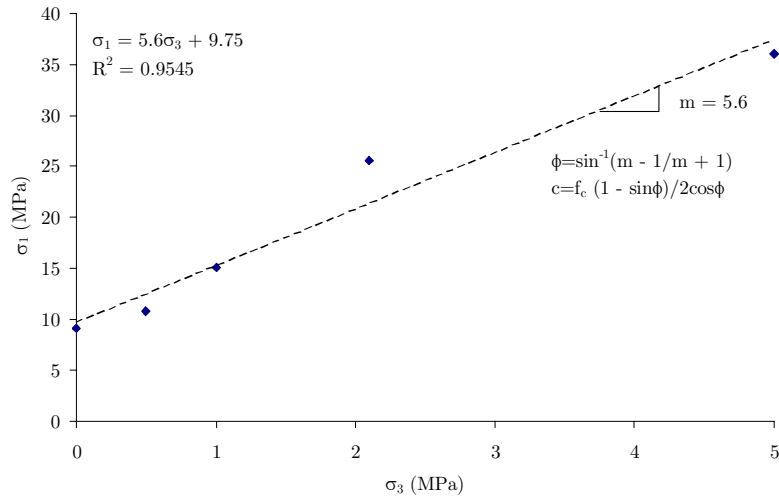
Figure 3.13: Linear Mohr-Coulomb failure criterion fitted to the triaxial test data after 28 days for M4

A linear Mohr-Coulomb (M-C) failure criterion was fitted to the M4 test data after 28 days (Figure 3.13), which could be expressed as:

$$\sigma_1 = 9.75 + 5.60\sigma_3 \tag{3.2}$$

and resulted in the values 1.9 MPa and 44° for the cohesion (c) and internal friction angle (φ), respectively. Based on these values and assuming shear failure during triaxial confinement, the expected orientation of the shear plane (β) with respect to the major principal stress can be predicted theoretically by the model of Mohr as: β=45 -φ/2, resulting in an orientation of the failure plane of 23°. From the tested specimens, failure bands ranging between 75° to 84° were measured for all specimens (Figure 3.15).
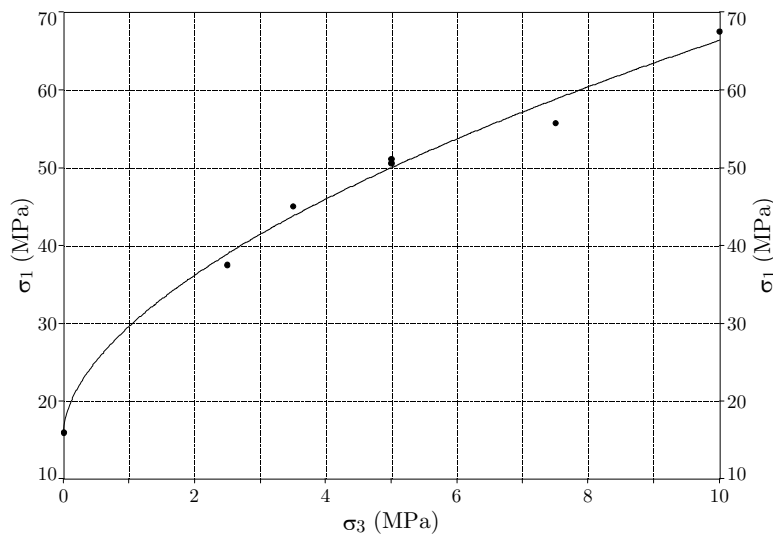
Figure 3.14: The Bieniawski failure criterion fitted to the triaxial data after 180 days for M4.

For the test data after 180 days, the linear M-C criterion could poorly represent the nonlinearity in the peak-strength data and instead a non-linear failure criterion proposed by Bieniawski (1974) was fitted by least squares linear-regression (Figure 3.14). The value of the coefficient of regression 0.98 and Figure 3.14 shows the good quality of the fit of the Bieniawski criterion, which could be expressed as:

$$\sigma_1 = 15.97 \left(1 + 4.12 \left(\sigma_3 / 15.97\right)\right)^{0.57} \tag{3.3}$$

Predominantly a single major crack was observed after the experiments regardless of the confinement level (see Figure 3.15). In triaxial testing on sedimentary rocks, a pair of conjugate shear-fractures rather than one is frequently observed under increasing confinement towards the brittle-ductile transition (Santarelli, 1987). However, according to Paterson (1978), this is influenced by end conditions, i.e. the type of end platens used in testing. In our testing, the use of Hoek cell with spherical seats on both ends seems to favour the formation of a single shear fracture as compared with tests reporting conjugate shear fractures performed using flat rigid steel-platens. The spherical seats seem capable of counter acting the bending forces associated with the formation of a shear fracture on one side of the specimen and hence allowing it to further develop. Similar mechanisms are observed in uniaxial tension tests with the initiation of secondary cracks when using fixed ends, which is largely reduced when using flexible (hinged) ends (Van Vliet and Van Mier, 2000).

The triaxial data for the M2 was fitted as well using the M-C failure criterion (Figure 3.16), which could be expressed as:

$$\sigma_1 = 16.0 + 2.97 \sigma_3 \tag{3.4}$$

and resulted in the values 3.4 MPa and 33° for c and φ, respectively. Based on these values and assuming shear failure during triaxial confinement, the expected orientation of the shear plane β with respect to the major principal stress can be predicted theoretically by the model of Mohr as: $\beta = 45 - \varphi/2$, resulting in an orientation of the failure plane equals 28.5°. The inclination of the failure planes as measured after testing was in the range 65-72° from the direction of σ_1.
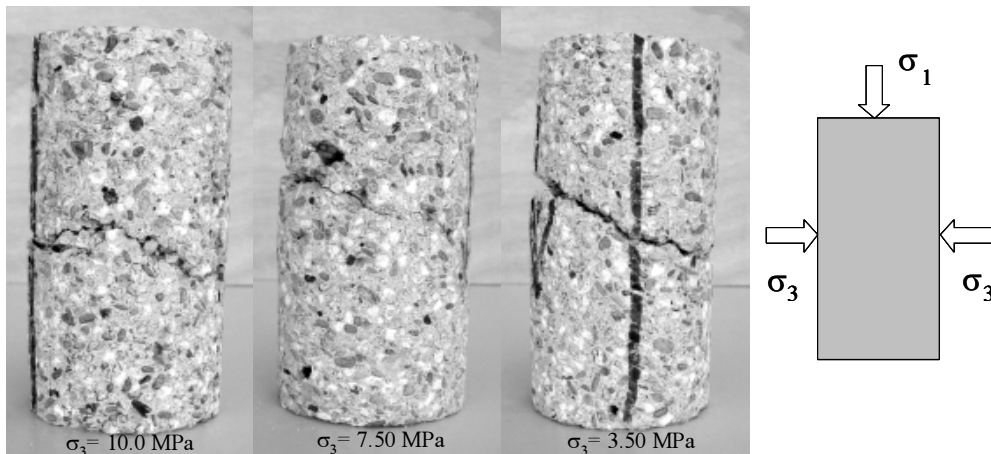
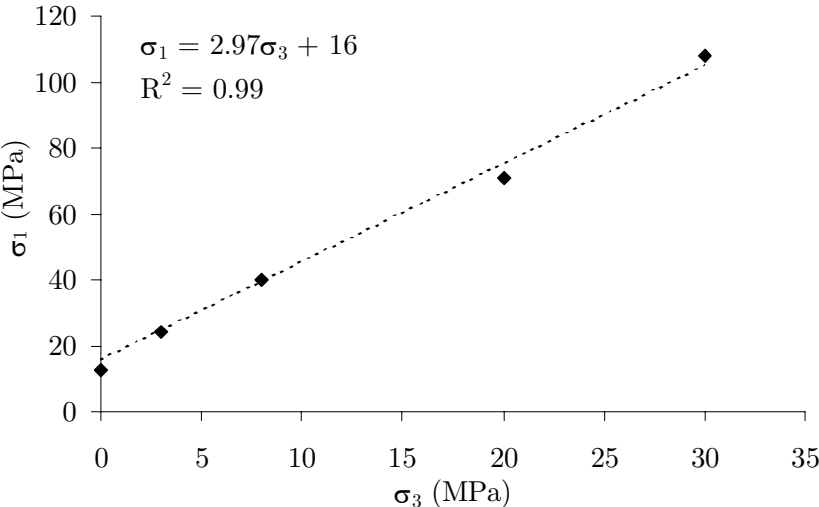Figure 3.15: Types of fractures in M4 seen after triaxial tests at various confining pressures

Figure 3.16: Linear Mohr-Coulomb failure criterion as fitted to the triaxial test data for M2.

Brazilian splitting test

The facture patterns and testing set-up are shown in Figure 3.17. Generally, the failure was rapid since tests were performed under force control. The visual detection of the failure mechanism indicated a longitudinal extensile crack traversing diametrically across the specimens. Occasionally, two cracks developed parallel to one another with crack-tip overlap near the centre of the specimen (Figure 3.17a).

(a)   (b)
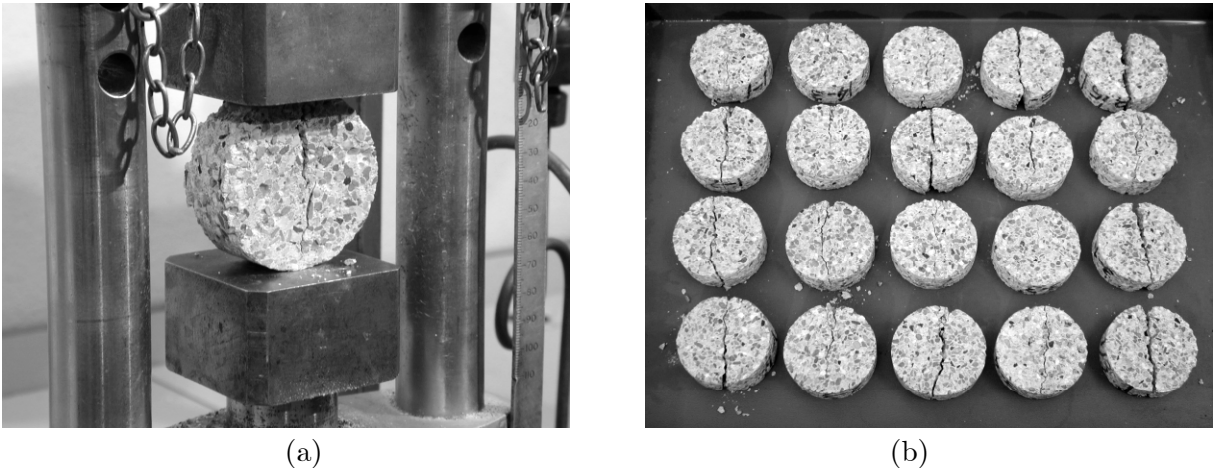
Figure 3.17: The Brazilian test set-up (a) and the types of fractures after testing in M4

3.6 SUMMARY

This study is concerned with fundamental aspects of size dependency and fracture be-
haviour of hollow-cylinders, and therefore any representative type of material, natural or
synthetic, could have been considered for the experimental work. An advantage of syn-
thetic material is in its isotropic and reproducible qualities as compared to most natural
rocks and in particular weak sandstones. Two cement-based mixtures were developed in
this work as model testing materials. Target characteristics for both mixtures were set to
firstly, generally represent weak sedimentary rocks, e.g. Castlegate sandstone, exhibiting
quasibrittle behaviour. Secondly, to accentuate the effect of microstructure, e.g. hetero-
geneity, on material behaviour under complex loading conditions and its size dependency.

Microscopic examination of the microstructure of the mixtures using ESEM revealed
their high capillary porosity and porous bond between the aggregates and mortar matrix.
The SE technique was used for identifying the morphology of the material and ITZ from
fractured surfaces. The BSE technique in combination with image analysis was employed
for investigating the microstructural details from flat fine-polished surfaces.

The overall behaviour of the mixtures, despite their low strength, observed in laboratory
experiments could be described as quasibrittle under uniaxial compressive loading and
plastic-strain-hardening when subjected to low or moderate confinement.

In uniaxial compression, the observed failure pattern was mainly axial splitting, with mi-
cro-cracks parallel to the direction of the maximum axial compressive stress and mostly
intensified in the middle part of the specimens. During triaxial testing, the brittle-ductile
transition was depicted at remarkably low confining stress, at approximately (σ_2
$=\sigma_3)/\sigma_1$=0.07 for the 4 mm mixture and 0.14 for the 2 mm mixture. Mainly a single ma-
jor crack was observed after the triaxial experiments with angles ranging from 75 to 84
degrees oblique to the maximum principle stress.

Chapter 4

EXPERIMENTAL PROCEDURES

4.1 INTRODUCTION

Hollow-cylinder test specimens are versatile in use and applications ranging from studying the behaviour of geomaterials under a variety of stress paths to simulating stress situation around underground openings in the laboratory. However, they are little utilized due to the lack of standard testing facilities and the considerable time and effort needed in building such test equipments and developing test procedures. A challenging aspect of the hollow-cylinder tests, used for studying the stability of circular openings, is the measurement of the deformations at the inner-hole using an accurate and reusable system.

In this research, a multi-scale high-pressure hollow-cylinder test cell was built, debugged, and intensively utilized in testing. In addition, a novel measuring device was developed for monitoring the radial deformations taking place at the inner-wall of the hollow-cylinders. Boundary conditions of the experiments were investigated and verification tests were performed to evaluate their effect on the results. Further, impregnation experiments were designed to investigate the fracture pattern after testing.

This chapter presents in detail the development and operation process for the test cell and measuring devices. Verification experiments and analyses performed to determine the influence of boundary conditions and test procedure on the results are discussed. Further, specimen preparation, stress path, test procedure and control, and test data processing are explained. Finally, the methods used in the impregnation experiments are described and an overview of the hollow-cylinder test scheme is given.

4.2 TEST FACILITIES

4.2.1 Multi-scale hollow-cylinder test cell

In order to experimentally investigate the size effect phenomena with least structural effects, great attention should be paid in making test conditions much alike for all sizes. This could be best achieved in testing hollow-cylinders by using one test cell, which could accommodate the size range of interest. A triaxial pressure-cell was therefore developed in this research that is capable of accommodating and testing hollow-cylinders of a size range 1:4.

The pressure cell is capable of simulating underground conditions comparable to a geostatic stress at depth of about 2200 m. The samples are hollow-cylinders with inner-diameters of 12.5, 25, and 50 mm and with a ratio of inner-diameter/outer-diameter/length equal to 1:4:6. In the remaining of this thesis, samples with inner-diameter of 12.5, 25, and 50 mm are referred to as A, B, and C, respectively. The axial and radial pressures could be applied independently on the samples and up to 40 MPa each (maximum safe pressure) under process temperature of ±20 C.

Figure 4.1 shows a cross-sectional view of the cell with its main components while containing a C type specimen. The main parts of the cell include: housing, top and bottom safety platens, specimen stack, and seals. The axial pressure is exerted by pumping oil into the cell through an upper connection in the top safety-platen. The resulting pressure is then transmitted onto the sample using the plunger. The radial pressure is applied by pumping oil via one of the two oil inlets in the housing wall of the cell. The oil pressure is transmitted as radial stress via a 2 mm NBR (Nitrile-Butadiene Rubber) sleeve on the sample's outer-circumference. A 90 mm hole in the lower safety-platen allows measuring devices to be installed for monitoring the axial displacement of the sample and radial deformation at the inner-wall during testing. The design and accreditation activities for the pressure-cell were carried-out by Ing. A. Hoving from the Dietz-laboratory of the department of Geotechnology, Delft University of Technology. The design followed the specifications for apparatus under pressure of the Dutch assessment and certification authority (Stoomwezen). The manufacturing took place at the central workshop of Delft University of Technology.

The housing of the pressure cell is constructed from massive heat-treatable steel (Böhler V155; German standards DIN code 34 CrNiMo6). Two radial holes with sealing NPT-thread are present in the housing for use as oil inlets/outlets. The housing is attached to the top and lower safety-platens using 8 safety-bolts M42 mm from heat-treatable steel (Böhler V320; DIN code 42 CrNiMo4). The top and lower safety-platens are manufactured from the same steel used for the housing. A hole with NPT-thread is present in the centre of the top safety-platen to allow the use of lifting eyebolt in transporting the platen and for transmitting the axial pressure during the tests. The plunger (heat-treatable steel Böhler V155) transfers the axial pressure onto the sample. An L-shaped hole exists in the plunger for enhancing the link of axial and radial pressures in case hydrostatic pressure is applied. If independent pressures are used, a thread at the top end of this hole is used to seal the connection with a bolt.
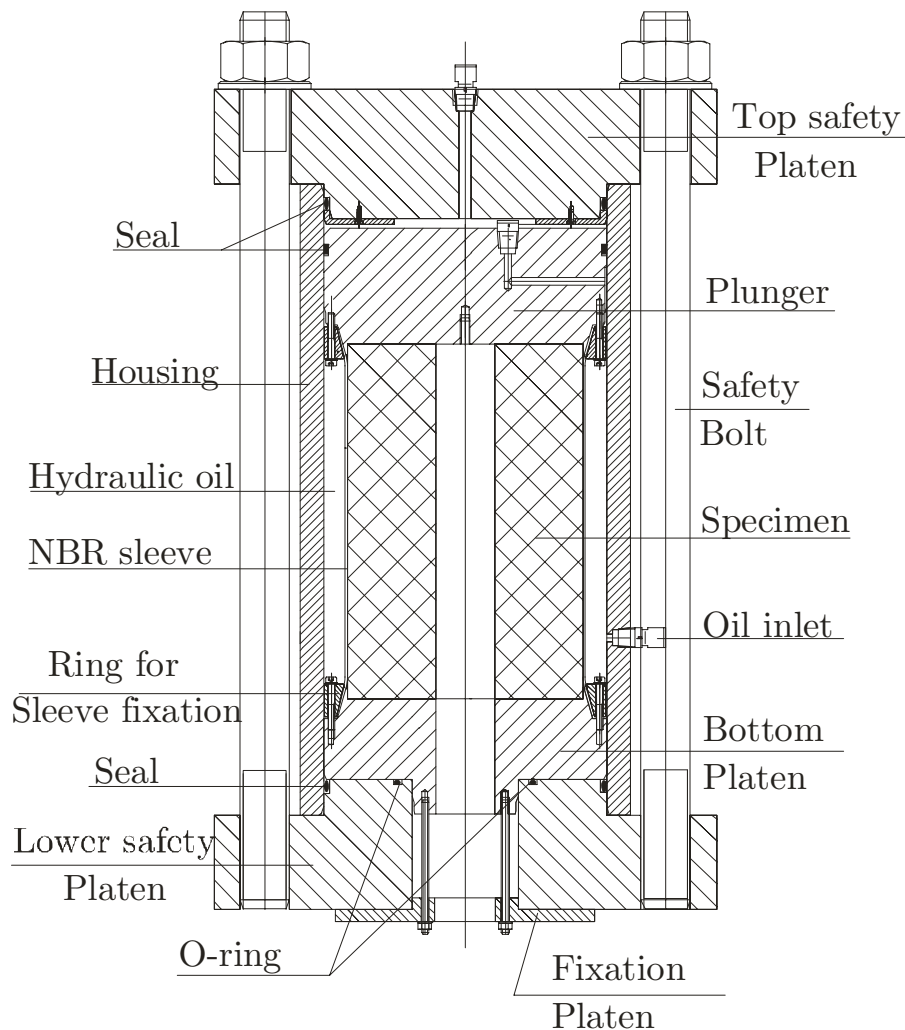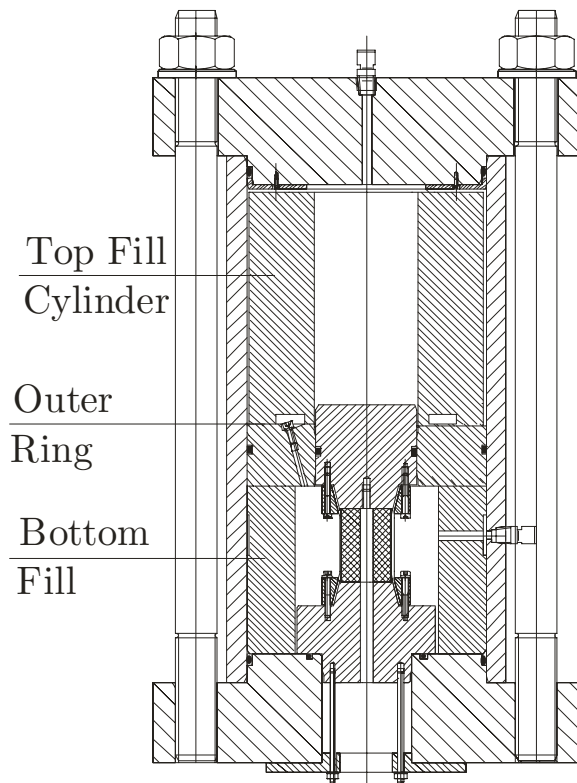
Figure 4.1: Sectional drawing of the developed triaxial pressure-cell including specimen C.

Almost all seals used in the pressure-cell are spring-energized polymeric EnerSeals™. The material offers low-friction characteristics and high degree of chemical inertness. The use of a high-grade internal spring ensures positive sealing under low pressure. Under high pressures, the internal hydrostatic pressure of the contained fluid energizes the seal and supplements the spring force, which increases contact pressure and eliminates potential leakage. Only one rubber O-ring is used at the contact between the lower safety-platen and bottom-platen near the central hole to prevent leaking of the radial pressurizing oil (Figure 4.1).

In order to place and test all three sizes in the cell, modifications in the specimen stack (plunger and bottom platen) are introduced. They were adapted to the size of each specimen to avoid any additional stress concentrations or unbalanced moments. For C type specimens, the assembly fits precisely in the housing of the cell with a controlled tolerance. For the A and B sizes, hollow aluminium-cylinders are used as fill blocks to compensate for the increase in volume of the pressurized oil in the cell. This volume increase is due to the decrease in specimen size. For safety reasons, the volume of pressurized oil is maintained at controlled levels as that used for size C.
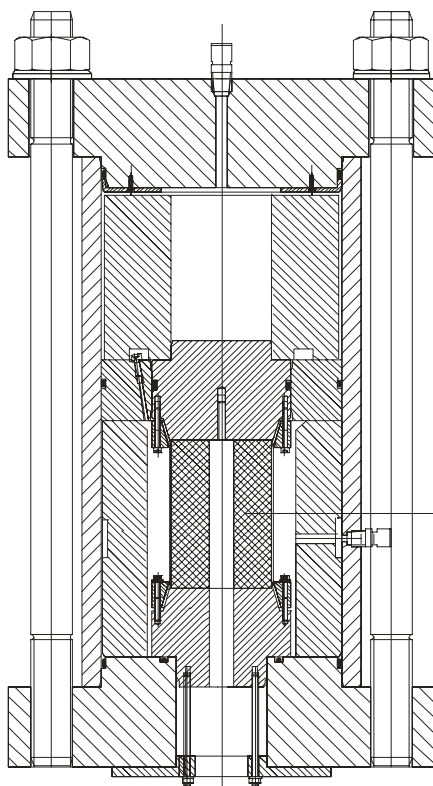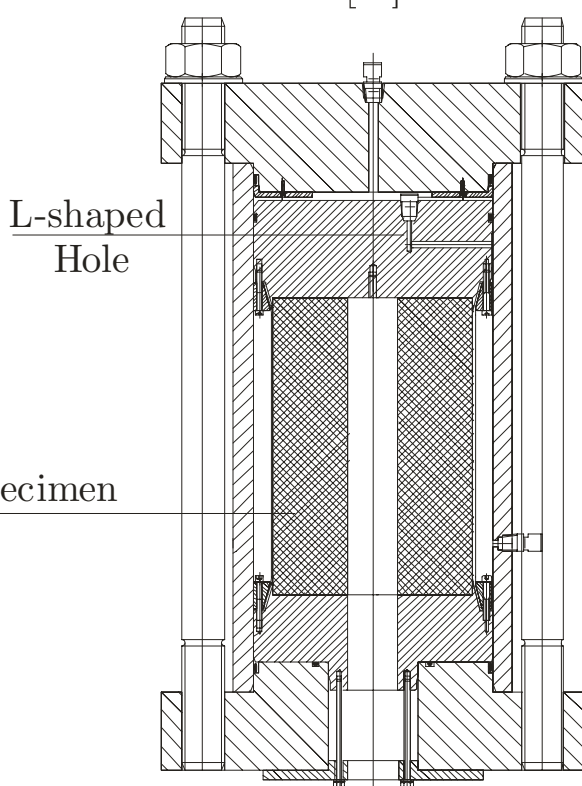
Figure 4.2: Image of the pressure-cell and three schematic cross-sectional views for the cell prepared with the three sizes A, B, and C.

In Figure 4.2, sectional views from all three sizes are shown together with an image for the pressure-cell. The plungers for sizes A and B are divided into inner-platen and outer-ring with an EnerSeal in-between. This is to allow the application of independent axial and radial pressures, while maintaining the size of the plunger proportional to the specimen size. In case hydrostatic pressure is applied, as in our tests, the outer-ring could be omitted or the inner- and outer-seals could be left out during testing. For specimen C, the plunger is designed as one piece.

As explained in § 5.2, a large borehole-simulator was used in pilot testing to possibly extend the size range to 1:8. The set-up is to a great extent similar to the test cell developed in this research and described above. The main difference is that the borehole-simulator is capable of testing cylindrical samples of outer-diameter equal to 400 mm and length of 600 mm (size D). Description of the design principles and operation procedure for this borehole-simulator are described elsewhere (i.e. Rouschop *et al.*, 1989). As it turned out not viable to prepare the specimens of size D in the same manner and time frame as for the other sizes (§ 4.3), its use was limited for pilot testing. The main obstacle was the unavailability of precise machinery within a close perimeter of the University (testing) premises, which is capable of delivering high quality end conditions for these large specimens in terms of flatness and paralleling of ends.

4.2.2 Inner-hole instrumentation

Generally, measurement of deformations in a hollow-cylinder is known to be experimentally challenging. A review by Santarelli (1987), describes most of the techniques used for such measurement as rudimentary. These varied from placing a steel disk of very low yield-strength in the hole after testing to measuring the volume of expelled oil from the hole during failure. The latter technique is used as indication for hole volume change that if combined with axial displacement measurement enables computing the radial displacement at the inner wall as used and reported by e.g. Ewy *et al.* (1988). Santarelli (1987), tried using a measuring device based on a cantilever principle where strain gauges measure the deflection of beams produced by the displacement of the wall. He abandoned using this device after some calibration tests that revealed a pressure and time dependence and suggested that it would be unrealistic to try to instrument a hole less than 50 mm in diameter with a reusable measuring device. Later, he used strain gauges that were glued onto the surface of the inner-hole (25 mm diameter), which he reported to provide satisfactory results.

Gluing strain gauges onto the surface of the inner-hole bears some problems including difficulty in positioning the gauges and the quality and effect of the gluing process. For a porous material as used in our tests with sizable air voids, the chance is high to fail in obtaining a good contact between the specimen and the gauge. In addition, the procedure would have been highly complicated for the size A with a hole-diameter of 12.5 mm. Alternative solutions were therefore investigated that could provide more reliable measurements and preferably reusable. The device should be extremely sensitive for measuring small deformations, few micrometers, and flexible enough at the same time to accommodate the variation in the diameter of the hole and its associated difference in maximum deformations that could be attained.

Tronvoll *et al.* (1992), reported using a two-arm calliper (cantilever) in measuring hole deformations for three different sizes, i.e. 10, 20, and 40 mm diameter. The principle used in their testing is similar to that initially tried by Santarelli (1987).

A novel measuring device was developed in this research that was used in measuring the radial deformation at the inner-wall. A single device was used for the three tested sizes with only a minor adaptation of minimal effect on accuracy and performance. In addition, a second device was developed to measure the axial displacement, but this was only limited to specimen size C due to lack of space in the two smaller sizes (A and B with 12.5 and 25 mm diameter, respectively). The preference was therefore made for the radial measurement as it leads to the tangential strain value, which is the maximum principal strain value under the chosen and applied stress path.

The basic operational principle of the measuring device used for radial deformation is a two-arm system that transmits the displacement at two opposite measuring points at the wall, positioned about mid height of the specimen, through a pivot to a Linear Variable Differential Transducer (LVDT) with ±1 mm stroke (Figure 4.3a). The arms contact the wall through semi-circular steel plates, which are glued to the arms. The device is mounted on the bottom fixation plate of the cell (detail A in Figure 4.3a).

(a)   (b)
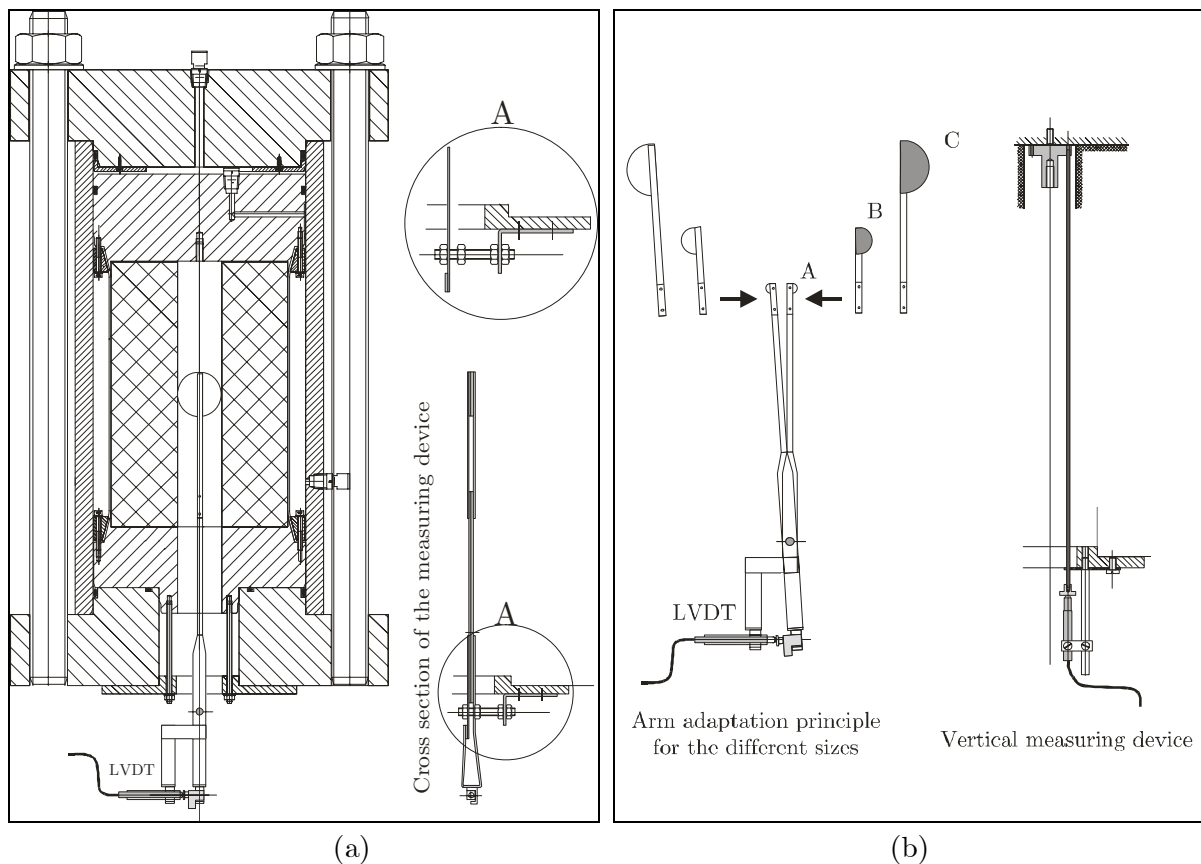
Figure 4.3: Overview of the measuring device developed for monitoring the radial displacement at the inner-wall. (a) Schematic for the device in operation inside the cell with a size C specimen. (b) Schematic for the adaptation procedure of the device for the three sizes and a schematic for the vertical measuring device.

The length of the arm is designed to fit at mid height of the specimens. Basically, the device is equipped for specimen type A plus two extra sets of arms that are used to extend it for use when testing specimens' type B and C (Figure 4.3b).

In Figure 4.3a, the schematic shows the measuring device during operation for a specimen size C. The two arms are hold in place using a rubber band placed above the LVDT, which acts as a low-stiffness spring. By this, measuring the radial deformation at the wall is possible in two directions (inward or outward) provided the capacity of the LVDT. The two arms are attached using bolt and nuts and with three rings of 1 mm thickness as a spacer in-between. All contacts between these connection pieces (detail A in Figure 4.3a) are separated using Teflon sheets of 100 μm thickness to minimize any contact frictional resistance during operation of the device.

Another feature of this design is it allowed using one LVDT for all sizes with their considerable difference in deformation range. The use of a pivot in transferring the deformation to the LVDT resulted in a scale factor for each size, which is the ratio of the length of the arms above and below the pivot. The measuring ranges for the different sizes based on this scale factor are: ±2.52, ±3.12, and ±3.68 mm for A, B, and C, respectively. These were sufficient to cover the deformations attained in the tests.

Measurement of the axial displacement was performed using a steel rod (3 mm diameter) screwed to the bottom-face of the plunger from inside the hole. The other end is fixed to a steel plate positioned at the bottom of the cell. An LVDT of ±5 mm stroke, mounted vertically outside the cell, is then attached to that steel plate (Figure 4.3b). During testing, the downward displacement of the plunger caused by the axial compression in the specimen is directly translated through the steel rod to the LVDT. The axial displacement measurement was performed for size C specimens only.
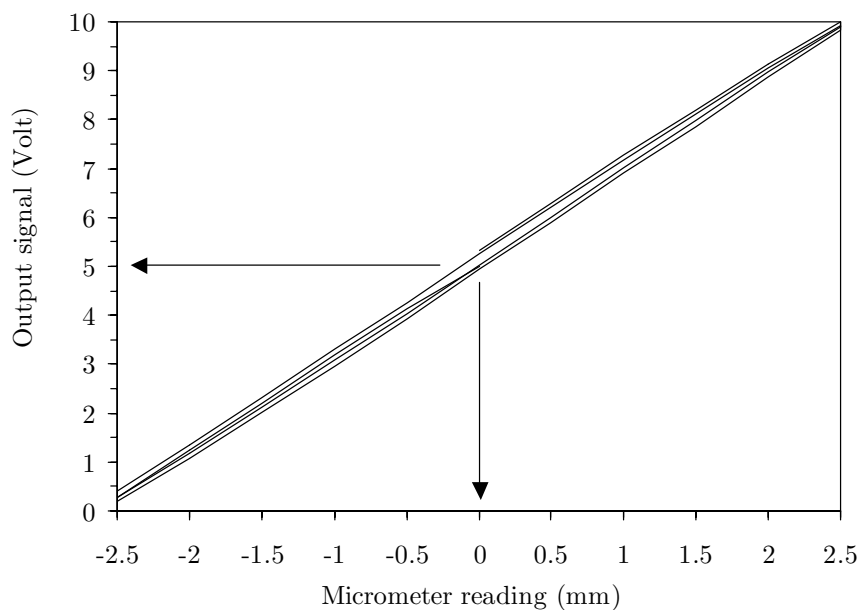
Figure 4.4: Calibration diagram for the radial displacement measuring-device using a manually operated micrometer calliper.

The calibration of the radial-deformation transducer took place by mounting its arms between the measuring rods of a screw micrometer-calliper with 2 μm accuracy. The calibration of the transducer was done simultaneously with the amplifier and data acquisition system. During calibration, the output signal was collected in a data scan by a measuring program running on a PC (see § 4.5.1 for overview on test control). The calibration took place for the complete measuring range of 10 Volt corresponding to ±1 mm of the LVDT. Initially, the system was set so that at zero micrometer reading, a signal of 5 Volt is obtained from the LVDT. The micrometer was then manually displaced in steps of 0.5 mm within the range ±2.5 mm and the procedure was repeated three times. The linearity was rather good (Figure 4.4) and minor nonlinearities were recorded close to the ends of the measurement range. The transducer has an accuracy of 20 μm over the full range. The calibration parameter obtained was used together with the scale factor of the measuring arms to calculate the final parameters for the three sizes, which were then used in calculating the deformations.

4.3   Specimen and test preparation

4.3.1   Casting and curing

A Zyklos mixer (forced-flow mixer) of capacity 120 litres was used for the preparation of the mixtures. The volume of the batch used for a test series with sizes A, B, and C was constant at 60 litres. In addition to the three specimens, 12 cubes of 150 mm were cast and used as control cubes. Six cubes were tested for uniaxial compression and splitting tensile (three cubes each) after 28 days. The other six cubes were tested similarly at the time of the hollow-cylinder experiments. This was fixed at 14 days of age for the principal test series as described in Chapter 5.

The gap-graded nature of the mixtures together with their high w/c ratio rendered difficult to obtain good repeatability of their characteristics. After hardening, sizable air voids were frequently observed at the outer surface of the cylinders causing notable strength heterogeneity and sleeve rupture during testing (if not treated). Several solutions were tried for solving this problem or at least bring it to a minimum. A major influence appeared to be the compaction style during casting. This was finally resolved to the use of a vibration needle in compacting specimen C and the cubes, whereas a small vibration table of low energy was used for specimens A and B. All specimens and cubes were cast and compacted simultaneously in a way to try forcing the excess water from the bottom to the cast surface without losing much cement slurry. The use of a vibration needle of any size in compacting the specimens A and B was practically impossible due to the limited size of their moulds. The effect of using two different compaction methods was investigated through comparing average strength of two sets of cubes. The first was compacted using a vibration needle only, whereas the second was partially compacted using a vibration needle and partially using a vibration table. In terms of average strength, the difference between the two sets was in the order of 4% and assumed minor.

After casting, all specimens and cubes were kept in the laboratory (20 C and 60% RH) for two days before they were de-moulded. During these two days, the top surface of the

cylinders and cubes (exposed surface) was sealed with Sullivan sheets. Afterwards, they were cured in a climate room (20 C and 99% RH) until five days before their testing date to allow for sample preparation. Special steel moulds were developed and used for the preparation of the hollow-cylinder specimens. A central steel-rod bolted to the bottom plate of the mould was utilized to create the inner-hole. The inner surface of the moulds and cubes were lubricated with de-moulding oil, except for the mould of specimen C and all central rods. These were lubricated using two layers of white Vaseline and a sheet of plastic foil (10 μm thickness) in-between. This was to minimize friction and facilitate extraction of the rod without disturbing the specimen around the inner-hole area.

4.3.2 Surface treatment

In order to apply the radial confining pressure to the specimen, the outer surface should be lined to prevent oil to penetrate into the specimen thus relieving the applied pressure and terminating the test. The lining should be rigid enough to withstand the applied stresses and flexible enough to accommodate the resulting deformations without rupture. A rubber sleeve is commonly used for this purpose and experience developed at the petroleum laboratory of Delft University suggested the use of NBR rubber for its resistance to oils and petrochemicals in addition to its suitable mechanical properties.
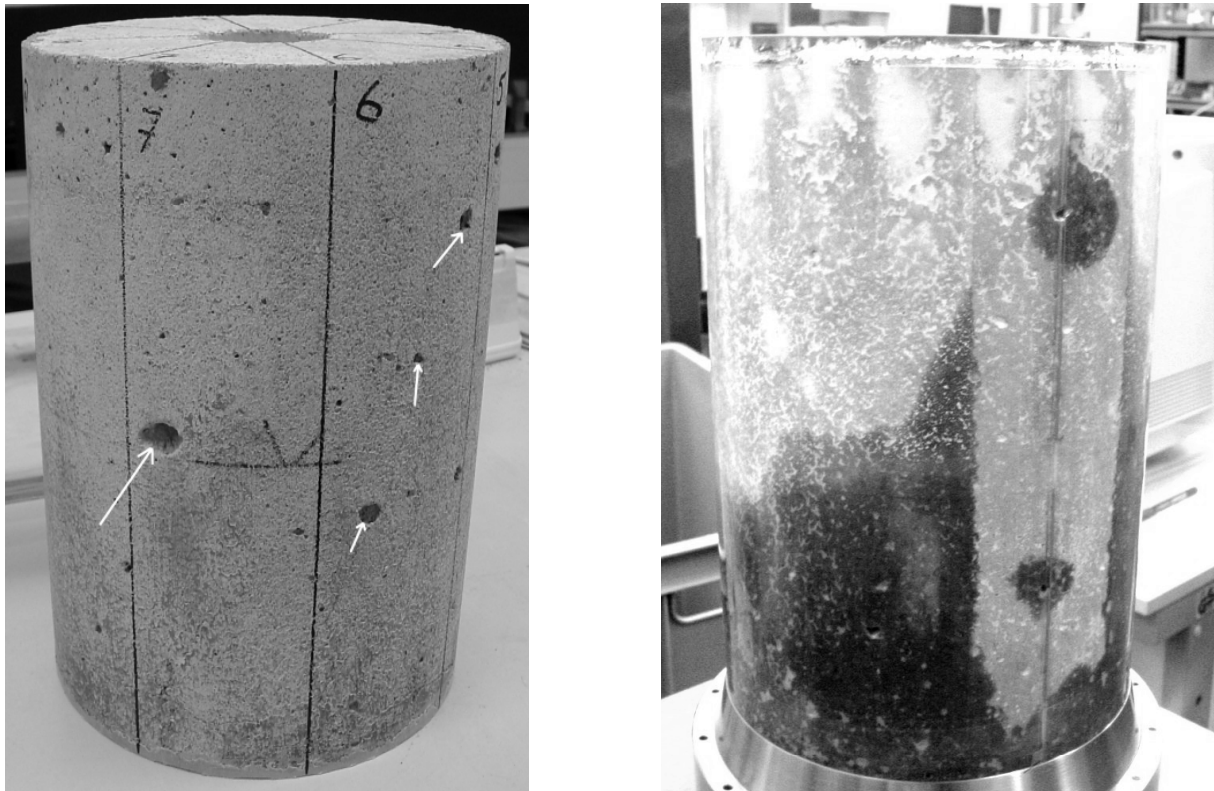
Figure 4.5: Images of specimen C with (left) air voids as found on specimen surface before surface treatment (some are indicated with white arrow) and (right) specimen contaminated with oil after sleeve rupture, even though was treated with gypsum paste.

A 2 mm NBR sleeve was used to enfold the specimens at their outer surface for protecting them from contact with the hydraulic pressurizing oil. The use of the sleeve gave several practical problems since it was easily ruptured under pressure at the locations of air voids on or adjacent to the surface of the specimens (Figure 4.5). This was costly in terms of time and planning since tests were stopped when sleeve ruptured and the whole size series had to be ignored. Much effort was therefore exerted in order to avoid such incidence. Firstly, a steel brush was used to scrub the surface of the specimens and try to reveal as possible from the air voids adjacent to the surface. All air voids were then carefully filled with a low-stiffness epoxy resin. Finally, the surface was smoothed using a fine sand paper. Before using the epoxy, several trials were performed using gypsum paste and poor cement-paste for filling the voids, but these mostly failed and rupture occurred (see Figure 4.5a).

Another important aspect of the surface treatment was the grinding and flatness of the top surface of the specimens. The ends of all specimens were ground flat and parallel to an accuracy of ± 100 µm to minimize end effects and to ensure good contact between loading platens and specimen. This was not possible using direct method for specimens type C for their large size with regard to the available facilities. A layer of castable two-part epoxy resin (epoxy gietmortel 2030, Masterbuilders) of $\cong 5$ mm thickness was used for capping the top surface of the C specimens. The bottom surface was considered flat and perpendicular to the longitudinal edges based on the accurate dimensions of the steel mould. A procedure was developed for this purpose by preparing a flat and levelled surface with an open cylindrical basin of 10 mm height fixed on top of the surface. At time of preparation, the specimen was hanged upturned right on top of the basin using a special support system and with its bottom surface levelled. The specimen basin was then filled with the epoxy compound and the specimen was directly placed inside under own weight ($\cong 21.0$ kg) and kept for at least 12 hours at laboratory conditions. This time was sufficient for hardening of the epoxy and the specimen was then ready to be placed in the specimen stack.

4.3.3   Specimen stack

A specimen stack consists of the specimen together with the top and bottom loading platens and the sleeve. Friction reducing pads were used at the contact between the platens and specimen (§ 4.4.2). Figure 4.6 shows an image of specimen stacks prepared for testing. The specimen assembly was prepared as follows:

–   A Teflon pad is placed on top of the bottom platen and then the specimen is positioned above.

–   The sleeve is pulled along the specimen from top to bottom using air pressure to ease its sliding. The sleeve is next fitted to the assembly using an external ring, which meets the bottom platen at an angle with the sleeve amid (Figure 4.1). The ring is fixed to the bottom platen using nuts and bolts.

–   The second Teflon pad is placed on top of the specimen and then the top platen.

–   The sleeve is fitted at the top similar to the way it is fixed to the bottom platen.
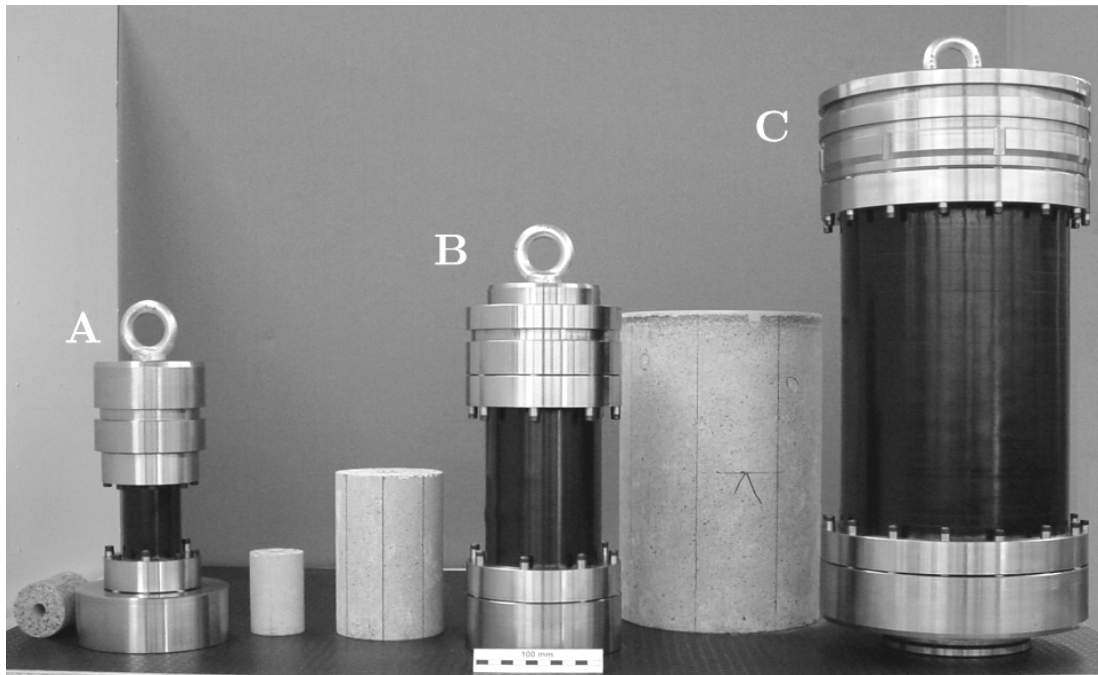
Figure 4.6: Image of specimen assemblies for sizes A, B, and C and a set of prepared specimens.

- The assembly is fastened together using a steel rod screwed to the top platen from within the inner-hole. The rod is tightened at the bottom using an external plate slightly larger than the central opening in the bottom platen.
- A lifting eyebolt is fitted to the top platen to allow transportation of the assembly and for placing or extracting the assembly in and out of the pressure cell.

4.4 VERIFICATION EXPERIMENTS AND TEST CONDITIONS

4.4.1 Strength (in)homogeneity in test specimens

In order to obtain an accurate interpretation of the fracture mechanism(s) around the hole, it is essential that all of the factors contributing in such a process to be identified and quantified. One of the important factors possibly associated with size effect in hollow-cylinder tests is the stress gradient along the cylinder wall. Anisotropy of strength inside the specimens could be a logical explanation for the commonly observed borehole elongation (breakout) along two opposite directions of the hole even if the cylinder is subject to an isotropic stress (further discussion in § 5.4). Therefore, it was decided to try minimizing the uncertainty associated with the specimens' manufacturing procedure, in terms of internal strength distribution, that might be misleading when interpreting the experimental results. A specimen size D was used for providing quantitative values over the strength distribution inside the hollow cylinder. The specimen was cast and cured for 28 days under controlled temperature and humidity conditions (20°C and 99% RH). The sample was then air-dried for nearly six weeks in normal laboratory conditions. Afterwards, the sample was cut into three equal parts perpendicular to its longitudinal hole-axis. Cylindrical cores of 60 mm diameter and 150 mm length were then drilled out

of each part parallel to the direction of casting and according to the schematic drawing shown in Figure 4.7. Four cores were drilled from each part along one horizontal axis, two adjacent to the hole and two behind closer to the outer edge. In addition, two extra cores were drilled in the middle part adjacent to the hole and perpendicular to the first axis.

All cores were tested for evaluating their uniaxial compressive strength f_c and elastic parameters E and ν using the test set-up and procedure as discussed in § 3.4.2. In Appendix B, summary of the results obtained from these tests is given. Observations could be stated about the strength (an)isotropy and gradient inside the hollow-cylinder from these results. In the middle part, the average of results for specimens 6-7 were calculated and compared to those of specimens 9-10 as they were considered to describe the situation of strength (an)isotropy.
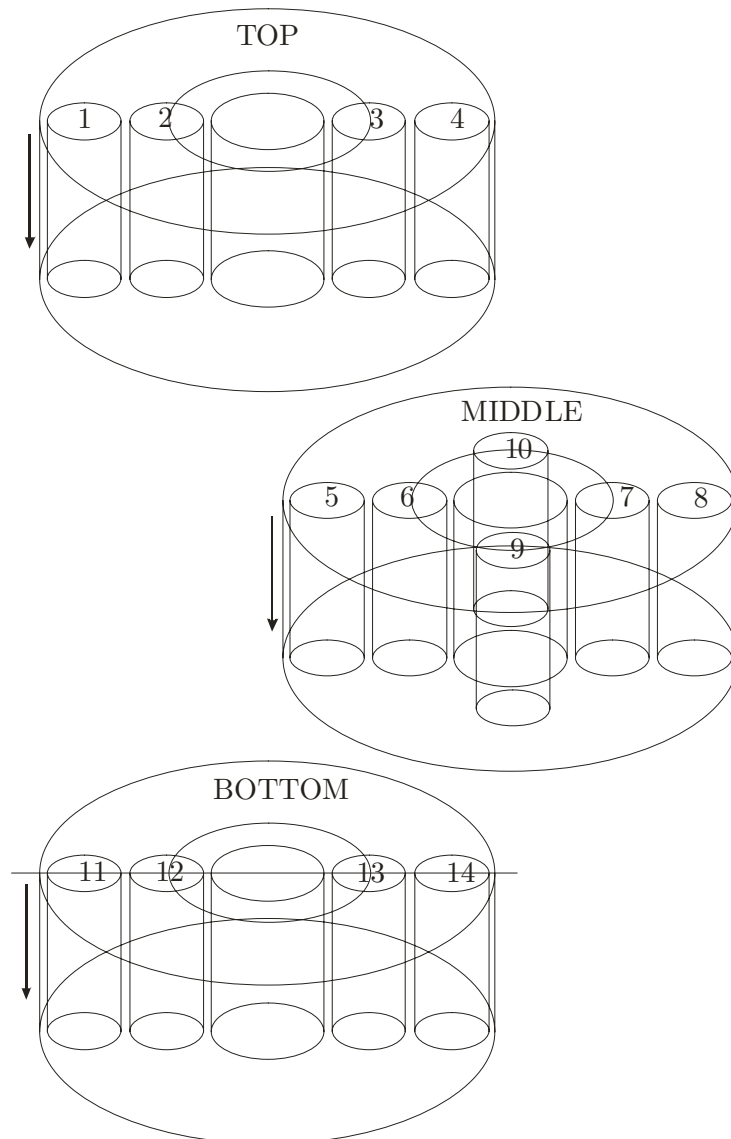
Figure 4.7: Schematic for the location of the drilled cores used in verification tests.

Table 4.1: Test results from the verification series for strength homogeneity

Core No.	Location	E (GPa)	ν (--)	f_c (MPa)
1	Top	14.30	---	18.10
2	Top	15.10	0.11	17.80
3	Top	14.10	0.11	19.50
4	Top	16.10	---	18.60
5	Middle	15.80	0.10	16.40
6	Middle	16.60	0.13	19.50
7	Middle	15.80	0.13	18.30
8	Middle	16.90	0.14	18.00
9	Middle	15.20	0.12	18.80
10	Middle	15.70	0.14	18.40
11	Bottom	11.60	---	14.50
12	Bottom	13.90	0.12	15.42
13	Bottom	13.30	0.09	16.10
14	Bottom	14.00	---	13.70

The average value of f_c, E, and ν for the specimens 6-7 was 18.9 MPa, 16.2 GPa, and 0.13, respectively. For specimens 9-10 the results were 18.6 MPa, 15.5 GPa, and 0.13, respectively. These results show an insignificant variation regarding the strength and elastic properties in two perpendicular directions around the hole. Therefore, considering an isotropic state around the hole is a valid assumption for the design and interpretation of the experiments.

Regarding the strength gradient along the wall of the cylinder, the results from the tested cores adjacent to the hole were averaged and compared to those from the cores close to the outer edge. Near the hole, the average results were 18.0 MPa, 14.9 GPa, and 0.12 for f_c, E, and ν, respectively. Near the outer edge, the results were 16.5 MPa, 14.8 GPa, and 0.12, respectively. These results as well show a minor variation and recommend that prior to loading and for design purposes, the sample could be considered homogeneous in terms of strength and elastic properties.

In addition, comparing the average results from the three different parts (top, middle, and bottom) could reveal information about the casting quality. In this case, the bottom part (lower during casting) appeared of less strength and stiffness qualities when compared with the middle and top parts. This seemed not in agreement with the conception that closer to the bottom of casting, the material should be denser and stiffer than above due to extra compaction and increased overhead weight. A tentative explanation is that the design of the moulds is firmly water tight at the bottom and considering the high w/c ratio used in the mixture, it is possible that after the completion of hydration more free water remained trapped in the bottom part leading finally to higher porosity/lower-strength. The problem could be less noticeable in the smaller sizes (A, B, and C) due to their shorter lengths as compared to size D as tested here. Alternatively, it could be that the compaction process for the bottom layer was not performed properly in comparison with the above layers for this specimen.

4.4.2 Specimen end conditions

Frictional restraint at the contact between the platens and the specimen and its conse-
quences are classical problems that have been subjected to numerous researches. A direct
contact between the steel platens and the specimen, assuming a full frictional restraint, is
expected to develop shear stresses causing a triaxial compression state of stress near the
specimen ends. This situation completely changes when using lower stiffness platens or
low-friction interlayer between the specimen and the platens. Van Mier (1997), discusses
the topic comprehensively and concludes that the ductility of the specimen (slope of the
post-peak stress-strain curve) changes when different end conditions are applied with a
notable effect from the loading system on the stress-post peak deformation relation.

In an attempt for defining a standardized test method for measuring the softening be-
haviour of concrete under uniaxial compressive loading, RILEM TC 148 SSC (2000), rec-
ommends the use of a friction reducing pad from two Teflon (Polytetrafluorethylene)
sheets 100 μm thickness each and 50 μm of bearing grease in-between. This method was
developed and in application with success at the Stevin laboratory of Delft University
since 1995. Van Vliet and van Mier (1995), reports on results from uniaxial compression
tests on normal strength concrete when using this friction reducing interlayer. They con-
clude that the use of this interlayer could diminish effects from frictional restraint on
peak stress and pre-peak response. They also discuss experimental results, which show
how this interlayer could effectively reduce slenderness effects from testing prisms of dif-
ferent height.

The same technique with Teflon-grease sandwich was used in our tests and the pads were
prepared and inserted between the loading platens and the specimens. This is to assure
as possible eliminating any effect from frictional restraints that could develop at these
contacts. It should be noted, however, that frictional stresses are expected to diminish at
high confinement levels, as confining pressures negate the developing shear forces.

4.4.3 Effect of sleeve thickness

A 2 mm thick NBR sleeve was used in the experiments to enfold the specimens' outer
surface (§ 4.3). This was to allow the application of the radial pressure using hydraulic
oil without direct contact with the specimens. It was not feasible to scale the sleeve
thickness in the same manner as the specimens were scaled i.e. 1:4, for its importance in
resisting against rupture under the high pressures applied. Therefore, it was decided to
investigate the influence of the sleeve thickness on the stress situation around the hole
for the different sizes and to try quantifying this effect. This was done analytically and
using the principles of linear elasticity (Appendix B).

The tangential stress at the inner wall was calculated for all of the different sizes (A, B,
and C) with a fixed thickness for the sleeve equal to 2 mm. The outer radial stress σ_o has
been selected as 40 MPa, which is the maximum safe stress applied in the experiments.
Consequently, the following stresses (σ_θ) have been calculated to be, 83.10 MPa,
82.9 MPa, and 82.7 MPa for sizes A, B, and C, respectively.

These results indicate a slight stress concentration ($\cong 1\%$) at the wall of size A when compared to that of size C. Accordingly, the effect of not scaling the sleeve thickness is of considered of minor influence on the experimental results and is therefore neglected.

4.5 TEST PROCEDURE

4.5.1 Operation and test control

In order to perform the hollow-cylinder test; firstly, the specimen stack was carefully placed inside the cell using a crane (for specimens A and B, the lower fill-block was placed before the specimen stack). The specimen was then fastened to the bottom of the cell using the fixation platen (see Figure 4.1) to secure the functioning of the lower O-ring. Next, the cell was filled with hydraulic-oil (Tellus T22) and measures were taken to ensure all air was expelled from the oil circulation. Afterwards, the top safety platen was placed and firmly fixed using eight safety bolts and nuts. After that, two high-pressure connections were hooked-up between the top and side oil-inlets in the cell and two hydraulic-oil pumps (Holmatro, HTW8800B). The measuring devices were installed inside the inner-hole after extracting the steel rod, which was used for holding the specimen stack, and were then regulated closest possible to their zero reference using a digital Voltmeter.

For performing tests under hydrostatic loading condition, the pressure was manually applied using one of the two pressure pumps. For this, the stop valve between the pumps was set on open position to ensure applying the same pressure in the axial and radial directions simultaneously (Figure 4.8). The pressures were visually controlled using two pressure gauges and scanned using two pressure-transducers (MSI, model MSP-600). The analogue signals from the LVDTs were amplified and then digitally collected on a PC through a 12-bit A/D converter. The converter was also used for digitizing the signals from the pressure transducers. An interface program was written to monitor and record the pressures and displacements during the tests. All tests were performed under slowly building-up the hydrostatic pressure to either a maximum pressure of 35-40 MPa or to a prescribed tangential strain level.

4.5.2 Stress path

Linear-elastic solutions for stresses and deformations in a hollow-cylinder subject to external boundary pressures can be found in many textbooks on rock mechanics or solid mechanics, e.g. Jaeger and Cook (1979). This solution suggests a maximum stress concentration to develop at the wall of the inner-hole with $\sigma_\theta > \sigma_z > \sigma_r$ (compressive stresses are positive) and hence failure is expected to initiate around the inner-wall and propagate outwards under increased stress. Figure 4.9 schematically illustrates the stress path applied in the experiments and its calculated resultant stress-state around the hole.

In all tests, the inner-hole pressure was kept at atmospheric, whereas specimens were loaded hydrostatically on their external boundaries up to a maximum pressure of
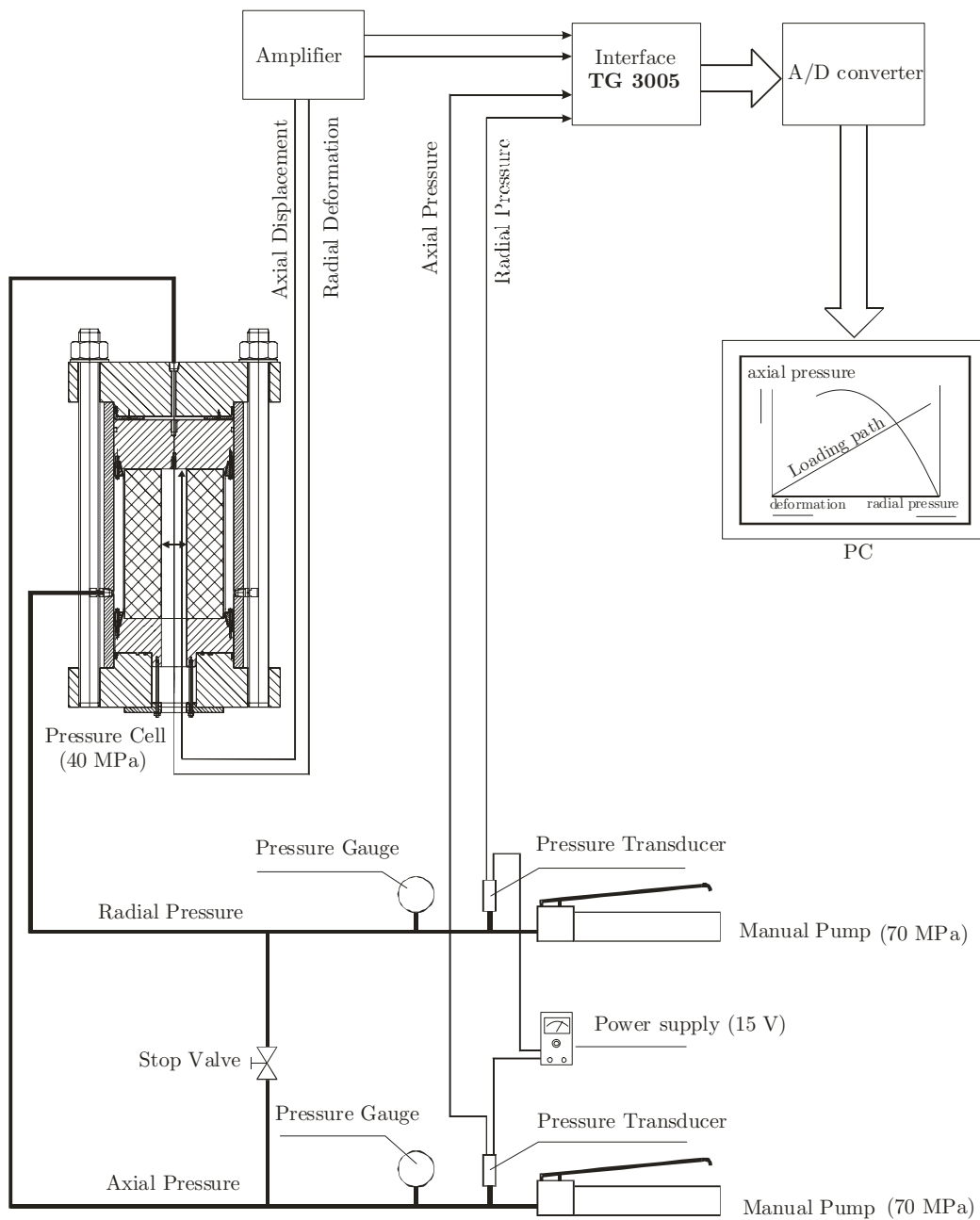
Figure 4.8: Schematic of the operation, control, and data acquisition of the pressure-cell.

40 MPa. This stress path is most common in simulating deep underground conditions around wellbores. The external hydrostatic pressure (σ_o) would translate into a triaxial stress gradient over the thickness of the cylinder's wall with a maximum principal stress σ_1=tangential stress σ_θ, intermediate principal stress σ_2=axial stress σ_z, and minimum principal stress σ_3=radial stress σ_r. For the hollow-cylinders tested in this research with an outer-diameter/inner-diameter ratio of 4, the expected maximum principal stress σ_1 equals 2.13 σ_o at the inner-wall.

Despite the fact that an elastic approach is common in the design of circular openings, it is widely viewed as being insufficient to quantitatively predict failure or describing the
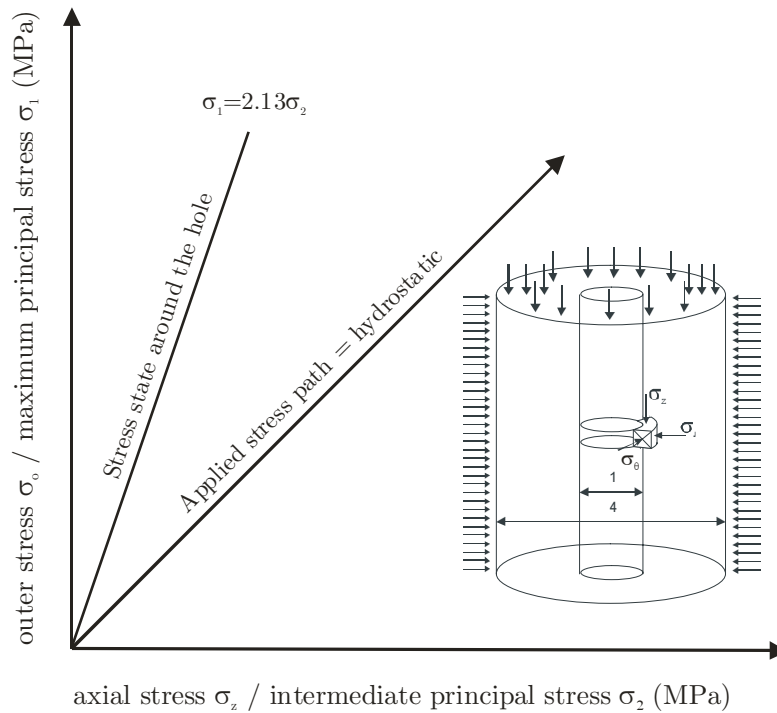
Figure 4.9: Stress path applied in the experiments and its resulting stress state at the hole.

various failure modes observed in underground excavations as well as in hollow cylinder tests (Santarelli, 1987). Elasto-plastic analyses have been performed by several researchers to determine the stress and displacement fields around a circular opening taking into account the existence of intact (elastic) and failed (plastic) zones. To model quasibrittle materials, a constitutive behaviour characterized by tensile cracking and compression crushing can be implemented. In a multi-axial stress state, a crack model can be combined with a plasticity model such as the Mohr-Coulomb and Drucker-Prager. According to Sluys and de Borst (1999), use of the latter model is not recommended for analyses of materials with a relatively high internal friction angle due to a pronounced difference between the results of biaxial compressive strength and uniaxial compressive strength analyses.

A combined crack-elasto-plastic analysis was performed using a Mohr-Coulomb failure criterion with associated plasticity supplemented by a smeared-cracking model that is described by a linear tension cut-off. These nonlinear simulations were performed using the finite element program DIANA (TNO DIANA BV) to analyze the effect of the stress path on the behaviour of the hollow-cylinders. The purpose was to examine the influence of the chosen stress path on the behaviour of the hollow-cylinders. The problem was modelled as 2D axisymmetric with symmetry around the longitudinal axis of the hollow-cylinder. A hollow-cylinder with a wall thickness of 15 cm was considered for the analyses. Both, the top plunger and bottom platen were incorporated in the model together with the Teflon friction-reducing interlayer. The Teflon interlayer was modelled using interface elements. A quadrilateral fine mesh (Figure 4.10a) was used for the analysis. The input data and material properties used in analysis are presented in Table 4.2.

Table 4.2: Model parameters used in the DIANA simulations

Property	Value
Uniaxial compressive strength (MPa)	10.0
Tensile strength (MPa)	0.80
Young's Modulus (GPa)	6.80
Poisson's ratio	0.15
Cohesion (MPa)	4.50
Friction angle	34.0
Dilatancy angle	34.0
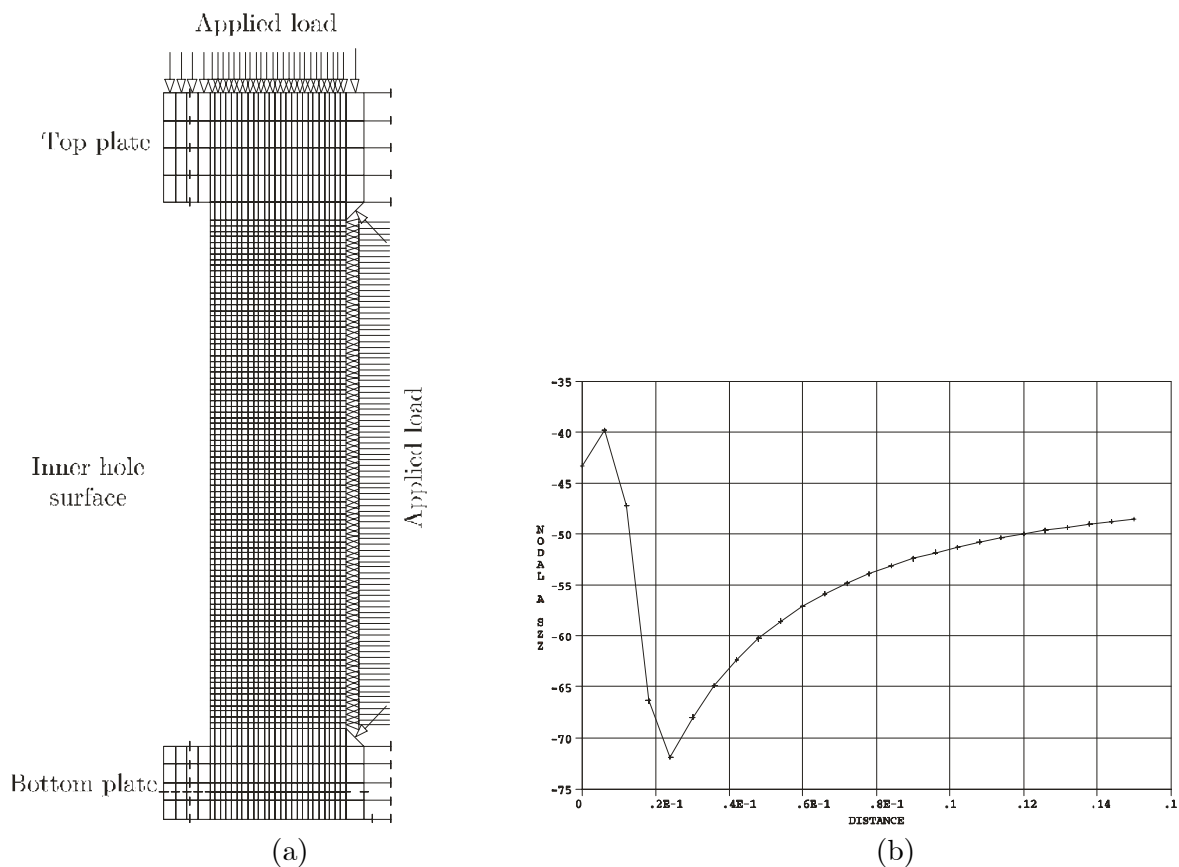
Figure 4.10: (a) schematic diagram of the mesh, loading, and boundary constraints. (b) tangential stress distribution along the wall at outer stress equals 40 MPa.

The simulation results showed a plastic zone to start developing around the inner hole at a hydrostatic outer-pressure of 8 MPa and continued till the end of the simulation. At maximum load, the thickness of the plastic zone was 2 cm inside the hollow-cylinder wall. A pronounced reduction in the tangential stress (stress relief) at the inner wall took place (Figure 4.10b) as a result of the plastic state achieved combined with the assumption of brittle behaviour. With regard to cracking, the analysis showed cracks to initiate next to the inner-wall at an outer-pressure of 18.50 MPa. The cracks started from mid-height of the specimen and propagated vertically and laterally with load increase in a uniform manner (see Figure 4.11).
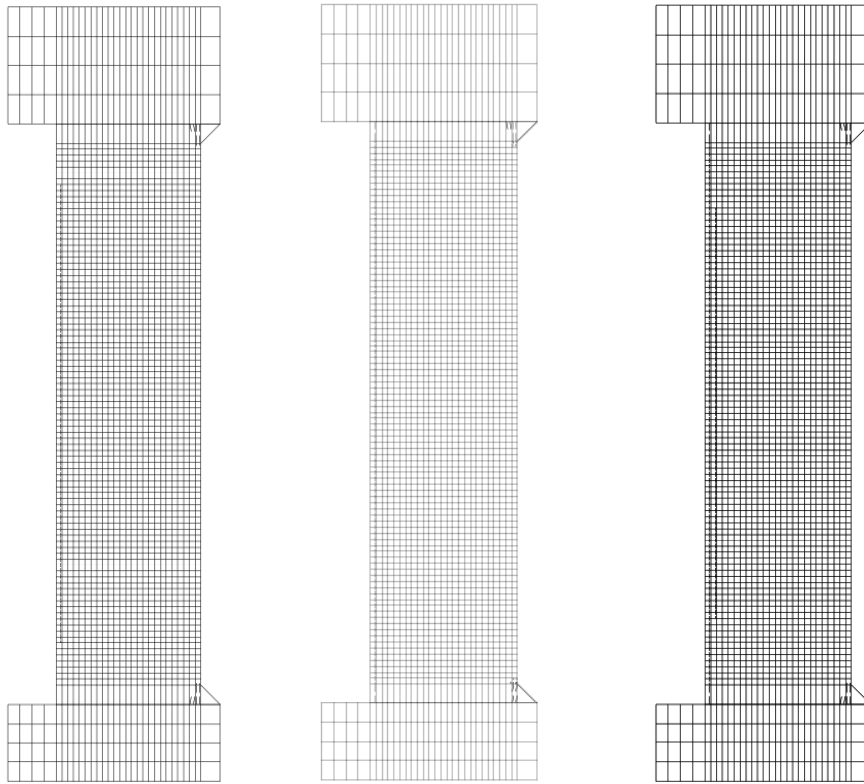
Figure 4.11: Crack propagation sequence in DIANA simulations at different load steps, from left to right the outer stress is 20, 40, and 50 MPa. The short dashed lines symbolize the cracks.

4.5.3 Data handling and presentation of results

The processing of hollow-cylinder test data comprised several steps; firstly, the recorded stresses (axial and radial at the outer boundaries) and displacements (axial and radial inside the hole) were converted using calibration parameters from an electrical signal with units of Volt to their equivalent mechanical units in MPa and millimetre, respectively. The second step involved the calculation of axial, tangential, and volumetric strains using the calibrated displacement measurements. The calculation of strains followed the linear-elastic principles as discussed in § 2.5.1. Subsequently, the outer-stress values corresponding to a tangential strain of 0.5% were determined and utilized afterwards in the size effect analysis.

As mentioned in the previous section, no full collapse or peak stress was obtained in the performed tests. Therefore, a criterion needed to be defined for use in the analysis of size effect test results. As will be comprehensively discussed in Chapter 5, it was reasonable to assume that failure initiated where the stress-strain curve showed deviation from linearity. The high nonlinearity of the response hindered the definition of one point as reference for failure initiation in the tests. Therefore, for assessment of size effects, stress levels at a prescribed tangential strain level of 0.5%, calculated from the deformations measured at the inner-wall, were considered and compared (Figure 4.12). This arbitrary strain value is chosen being as close as possible to the point where deviation from
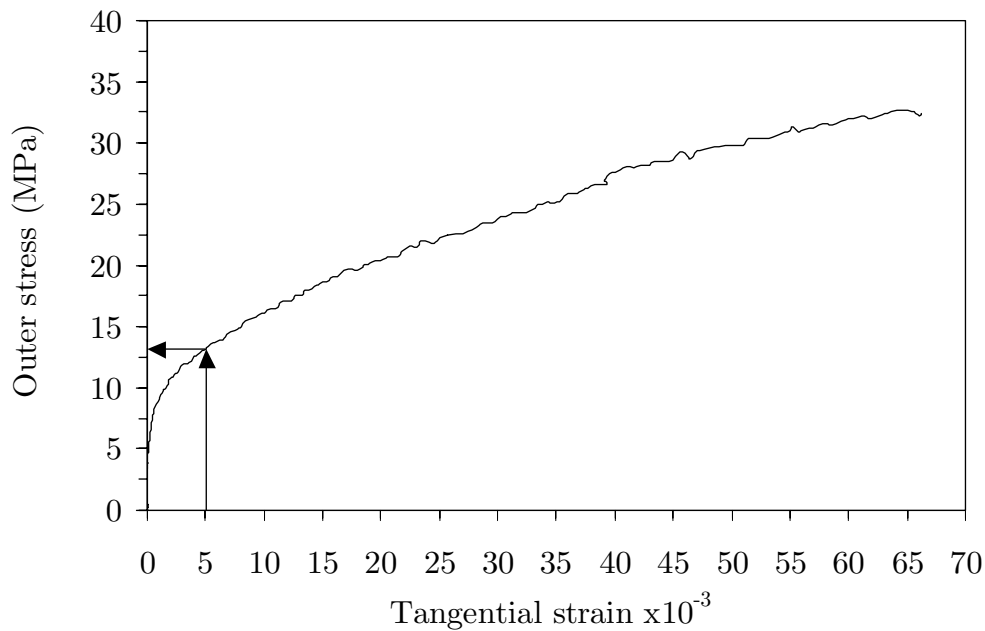
Figure 4.12: Outer stress-tangential strain curve for C specimen from the mixture M2 with indication for the procedure of stress determination corresponding to 0.5% tangential strain.

linearity occurred along the inner-hole surface and deformation rates were accelerated (see Figures 5.2 and 5.5 for complete stress-strain curves). Size effect relations from using other strain values than the 0.5% are presented and discussed in § 7.1.1 as part of the discussion on onset of size effect.

4.6 IMPREGNATION EXPERIMENTS

The detection of crack and fracture mechanisms was of vital importance in this study in order to try exploring its physical behaviour and possible effect on size effect. Various techniques are available to date, each with its own cons and pros and can be divided into direct and indirect methods as described by Shah *et al.* (1991). Indirect methods include amongst, acoustic emission, ultrasonic pulse-velocity, interferometry techniques, and stereo-photogrammetry. Whereas direct measurements include optical and scanning microscopy accompanied by enhancing techniques such as dyeing and impregnation. In compression, stereo-photogrammetry is seen as a suitable indirect surface-measurement method with the limitation of plane stress loading condition besides cumbersome and time-consuming data processing. As a surface method the fracture process in the interior of the specimen is not depicted and thus a complete fracture process is not characterized (Van Mier, 1997). Acoustic emission techniques can be regarded as a suitable tool for revealing interior crack processes and the shortcoming of clarifying the physical mechanism. In rock and petroleum sciences, the acoustic techniques and acoustic related material properties acquired a great deal of attention and are widely applied. Using direct or defective methods, microscopy; optical, Scanning Electron Microscopes (SEM), and re-

cently Environmental Scanning Electron Microscopes (ESEM) are the most applicable in scanning surface crack processes with high resolution.

An insight in crack growth process can be obtained by applying a step-wise procedure at different levels of the loading process. Impregnation and dyeing methods enhance the visibility of cracks with the possibility to visualize internal cracking after cutting a specimen into slices. Impregnation is done under vacuum since moisture must be removed to allow for saturation with epoxy or dye and it is favourable to impregnate under load. Appropriate material for impregnation includes, dye, fluorescent epoxy, and molten Wood's metal (solid at room temperature and melts at temperatures between 70-88° C). In hollow-cylinder tests, Ewy et al. (1988), used molten Wood's metal applied under 5 MPa of pressure for preserving crack patterns during their experiments on Berea sandstone and Indiana limestone.

In this study, bearing in mind the low strength of the tested materials, it was contemplated that specimens could crumble after failure and therefore would not allow a proper investigation of the facture process. In similar hollow cylinder experiments reported in the literature, stronger materials are usually investigated (5-9 times higher strength) and crack patterns are visually examined either after testing or during testing using an endoscope placed inside the hole. From the results of pilot testing, however, it appeared that failure process of the used mixtures is rather stable with no signs of major collapse allowing for post-test impregnation.

An impregnation procedure using low-viscosity fluorescent epoxy was therefore implemented after testing, which took place under medium-vacuum pressure. After carefully extracting the specimen out of its stack following completion of the test, it was placed in a cylindrical vacuum chamber. Depending on the specimen size, they were subject to medium-vacuum pressure for a time period in the range of 2 to 12 hours. The fluorescent epoxy was prepared at the end of the vacuuming period using a mixture of epoxy resin, yellow dye, and hardener (EpoFix resin, EpoFix hardener, and EpoDye, STRUERS, Denmark).

The resulting fluorescent epoxy was then slowly poured into the space of the inner-hole through a flexible tube with flow valve. The epoxy was left to rest inside the hole for few minutes to ensure that nearly all air inside the hole and in open pores around it was replaced with epoxy. Atmospheric pressure was then slowly restored inside the chamber and the epoxy was left to harden under laboratory conditions for 48 hours. Afterwards, the specimens were cut into slices using diamond saws (Figure 4.13).
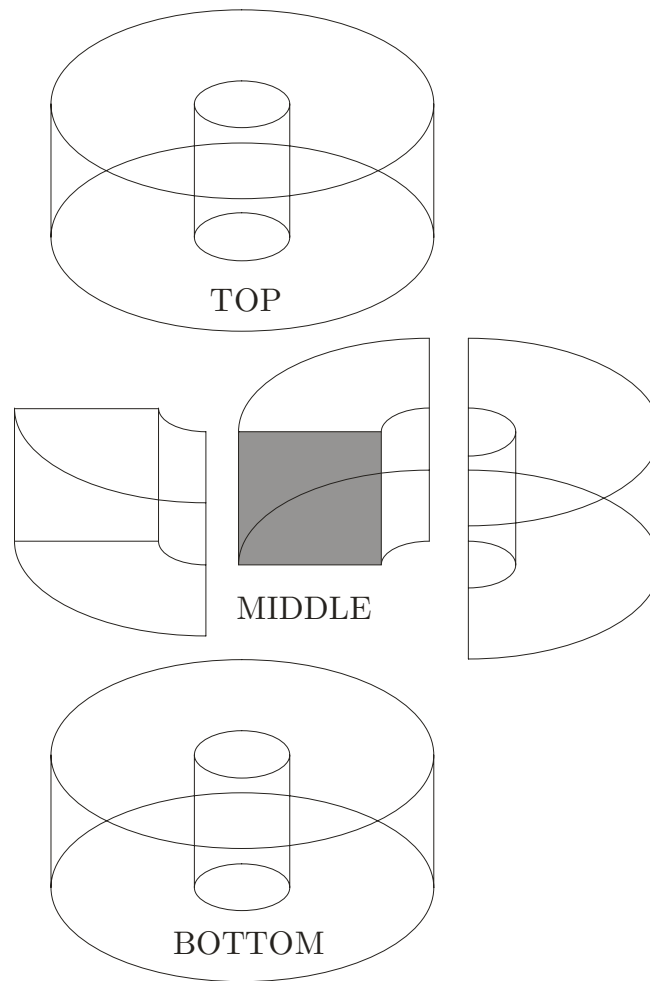
Figure 4.13: Schematic for a typical cut of an impregnated hollow-cylinder specimen.

4.7   TESTING SCHEME

In total, twenty-one test series were conducted with a sum of sixty-four hollow-cylinder experiments. Eight test series were performed for the M2 and thirteen test series for the M4. Unfortunately, results of four principal test series for the M4 were dismissed due to their abnormal high strength values as compared to the other series, which was revealed from the control cube strength. The reason for this anomalous strength results is not clear, but as discussed in § 4.3.1 the control on the casting procedure was rather difficult for these low-strength mixtures. For the principal test series (Chapter 5) with sizes A, B, and C, all tests were conducted at 14 days of age. Mostly, the tests were performed on two consecutive days and occasionally it was possible to test all three sizes on the same day. This was to try eliminating the effect of strengthening of the materials with time. The tests were carried-out in an alternating scheme between the mixtures M2 and M4. An overall view is given in Table 4.3 for all hollow-cylinder experiments, including the pilot tests, which were used in analysis and interpretation of experimental results (Chapters 5 and 7).

Table 4.3: Overview of the complete hollow-cylinder experimental programme

Test series	Type	Mixture	Size range	Age at test (days)	f_c at test (MPa)	f_c after 28 days (MPa)	f_{spl} at test (MPa)
01M4I	Pilot	M4	1:8	181	16.8	11.9	1.40
02M4II	Pilot	M4	1:4	243	22.1	12.3	2.10
03M2I	Pilot	M2	1:4	48	14.0	11.5	1.80
04M4III	Principal	M4	1:4	14	9.70	11.3	1.10
05M2II	Principal	M2	1:4	14	9.00	10.7	1.00
06M4IV	Principal	M4	1:4	14	8.30	9.50	0.90
07M2III	Principal	M2	1:4	14	6.50	8.70	0.80
08M4V	Principal	M4	1:4	14	8.10	10.8	1.00
09M2IV	Principal	M2	1:4	14	8.30	10.5	0.95
10M2V	Principal	M2	1:4	14	7.90	10.3	0.90
11M4VI	Principal	M4	1:4	14	10.0	13.9*	1.00
12M2VI	Principal	M2	1:4	14	7.30	10.3	1.10
14M4VIII	Principal	M4	1:4	14	9.50	12.9	1.30
15M2VII	Principal	M2	1:4	14	11.9	16.4	1.15
17M2VIII	Principal	M2	1:4	14	9.10	12.4	1.18
20M4XII	Principal	M4	1:4	14	9.00	11.5	1.10
21M4XIII	Principal	M4	1:4	14	9.50	14.1	1.17

Chapter 5

HOLLOW-CYLINDER EXPERIMENTAL RESULTS

5.1 INTRODUCTION

An experimental program using thick-walled hollow-cylinder specimens was conducted to study size effect on strength of the two mixtures developed in this research (Chapter 3). In addition, (in)elastic deformations, cyclic behaviour, fracture, and failure development in the hollow-cylinder tests were investigated. The tests were performed under externally applied hydrostatic pressure, while maintaining the inner-hole pressure at atmospheric. Inner-wall radial deformations and axial displacements were monitored during the tests. Fracture patterns were preserved after testing through impregnating a fluorescent epoxy resin under vacuum into the vicinity of the inner-hole. Slices from the impregnated specimens were investigated afterwards under high magnifications using both optical microscopy and ESEM.

In this chapter, results of the scaled hollow-cylinder experiments are presented. First, the stress-tangential strain responses are discussed for each mixture with emphasis on the deformation process and onset of failure. Then, results from the cyclic tests are discussed. Afterwards, the size effect results are presented. Subsequently, the volumetric response during the hollow-cylinder tests is explored. Finally, fracture mechanisms and failure development in the tests are investigated and their results are presented with emphasis on microscopic failure mechanisms.

5.2   RESULTS OF PILOT TEST SERIES

As discussed in Chapter 4, it was considered in the experimental design phase to extend the size range to 1:8 (§ 4.2.1). A large pressure vessel similar to the one developed in this project was used in testing the largest size D with inner-hole diameter of 100 mm. One test series was performed including four sizes in a size range 1:8. The sizes A, B, and C were tested in the small test cell and size D was tested in the large test cell. Inner-hole deformations during testing and impregnation experiments after testing were carried out for all sizes. Hereafter, the result of this series is summarized in terms of stress-strain response and size effect.
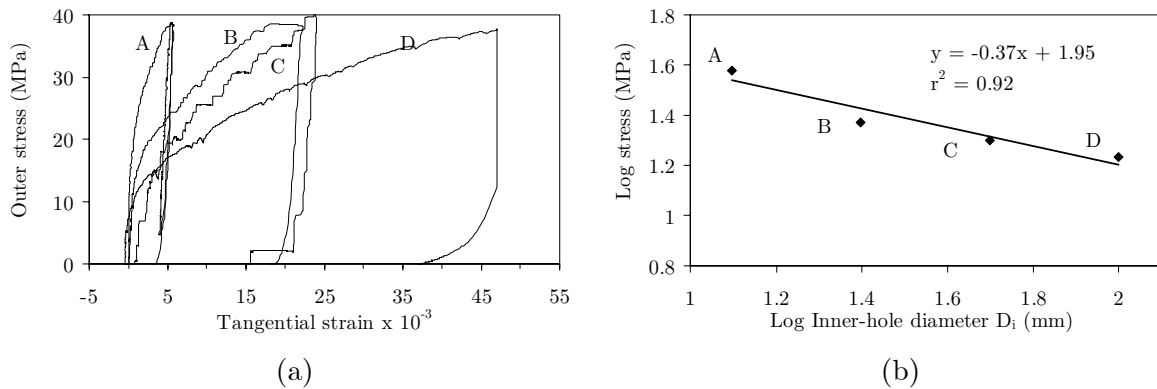
Figure 5.1: (a) Stress-strain curves for specimens A, B, C, and D of the mixture M4 at 180 days of age. (b) A log stress-log size relation with stresses taken at 5‰ strain.

In Figure 5.1a, the stress-tangential strain curves from the four tests are presented. The tests were performed using the mixture M4 at 180 days of age. In the figure, the material is shown to behave in a plastic-strain-hardening manner. The uniaxial compressive strength for the specimens from accompanying control cubes was 16 MPa. The specimens sustained external pressures up to 40 MPa without collapse. Spalling of small flakes from around the inner-hole took place during testing of specimens C and D for stresses above 25 MPa. The total tangential strains attained at the end of the tests suggested a size effect. In other words, the larger the specimen size the larger was its total strain. For an outer stress of $\cong$37 MPa, the total strain of specimen D was found 9.50 times that of specimen A. For all sizes, an initial stiff response is observed up to an outer stress value in the range of 11 to 15 MPa. Afterwards, the strain (deformation) rate increased with varying magnitudes, respectively with size from gentle for specimen A to rapid for specimen D.

In Figure 5.1b, the log σ_o–log D_i is plotted for the four sizes together with a best-fit relation using linear-regression. A good linear relation is observed on the log-log scale as indicated by the correlation factor of 0.92. A power relation with an exponent of –0.37 exists therefore on a normal scale between the three sizes. In this pilot series, final adjustments in the measuring device were not yet introduced and could have caused a measurement error of not more than 5%. This series, however, was conclusive on the aspects of performing scaled hollow-cylinder tests with reliable inner-hole deformation measurements and indicated a hollow-cylinder size dependency.

5.3 RESULTS OF PRINCIPAL TEST SERIES

In this section, results from scaled hollow-cylinder tests, which were performed on the M2 and M4 mixtures at 14 days of age are presented. In these series, a size range of 1:4 was considered, i.e. only specimens of type A, B, and C were tested.

5.3.1 Stress-strain behaviour

Stress-strain response for 4 mm mixture (M4)

Individual stress-strain curves from the tests performed on the mixture M4 are presented in Figure 5.2. The stress in the graphs represents the outer hydrostatic-pressure applied onto the specimens, whereas the strain is the tangential strain ε_θ. To examine the process of failure development and associated mechanisms, some tests were terminated at prescribed strain levels (§ 5.5). Namely, strain levels of 0.5, 1.5, and 2.5% were used. The stress-strain responses from these tests are included in Figure 5.2 as well. From the responses, the material shows a plastic-strain-hardening behaviour up to the end of tests. The specimens sustained outer pressures up to $\cong 40.0$ MPa without collapse. The final computed strains ε_θ were notably high in the order of few percents. Tangential strains up to 3.1%, 5.1%, and 6.4% were observed for the specimens' type A, B, and C, respectively.

In Figure 5.3, the average total tangential-strains are plotted with their standard deviations against the inner-hole diameter D_i for all sizes. Only total strains from complete tests with no prescribed strain levels are considered. The figure illustrates the increase in average total strain with specimen size. The scatter in strain values is notably higher for size B as compared with A and C. The higher scatter owes probably to the limited number of samples used in calculating the average and scatter; namely, 3 values for A and B. For the C specimen, no scatter value was calculated since only two data points existed. However, the relation from the average calculated values strongly suggest an increasing trend with size.

Stress-strain curves obtained from all sizes showed a smooth transition from an initial slightly curved to a subsequent softer response (see Figure 5.2). Overall, the response could be described as bilinear from the firstly short portion with stiff behaviour to a less stiff afterwards with an increased rate of deformation. Noteworthy is where this transition more or less takes place. Examining the stress-strain curves indicate that it occurs at an outer stress (σ_o) around 7-10 MPa. This value appears qualitatively independent of the specimen size and more remarkable is its proximity to the average value of the compressive strength of the mixture.

The unloading path is included in the graphs as well. The amount of permanent (irrecoverable) deformation remained after unloading indicates the ductile characteristic of the material under this loading state. Generally, not more than 25% of the total exerted strain in the specimens was restored after unloading. This was also observed for tests terminated at relatively low strain levels (less than 1% strain) conforming the sensitivity of the material to confinement as observed in the triaxial compression tests (§ 3.5.2). The occurrence of irrecoverable strains at low stresses suggests that the use of classical linear-elastic models to analyze and explain the phenomenon observed in these hollow-cylinder

tests would be doubtful. The percentile ratio between the permanent strain and the total
strain from all performed tests, a ductility index, is presented graphically in Figure 5.4.
An increasing trend in ductility with size is generally observed with size B particularly
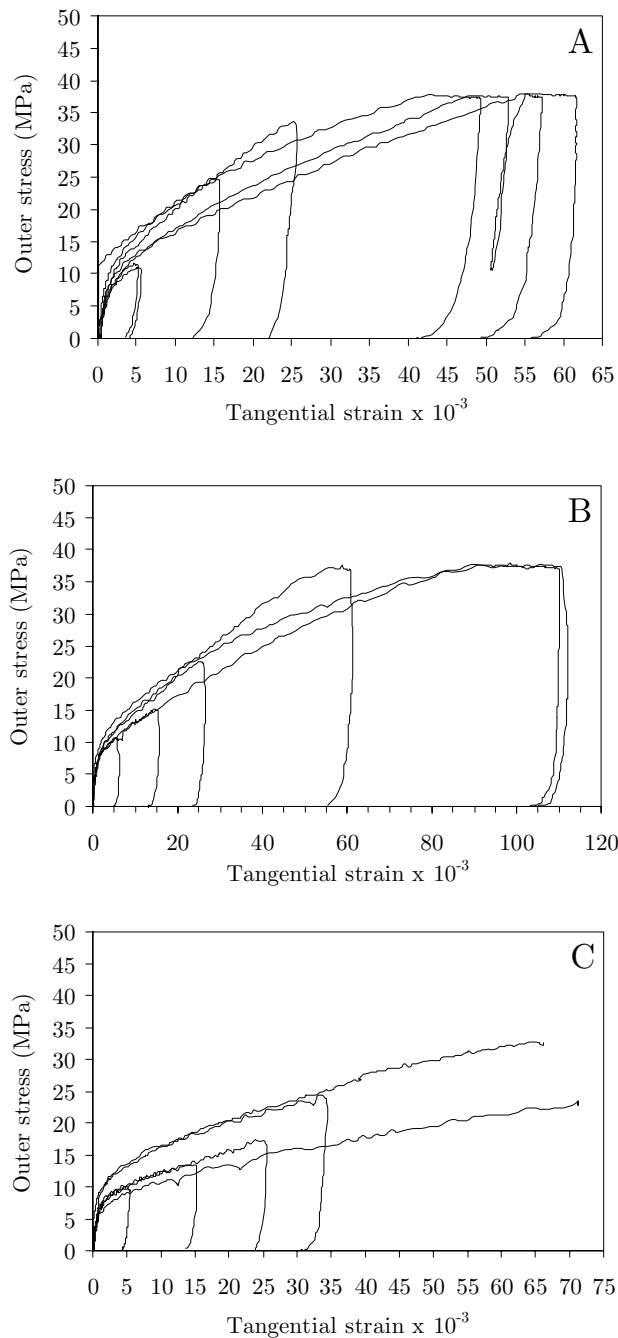higher than A and C.
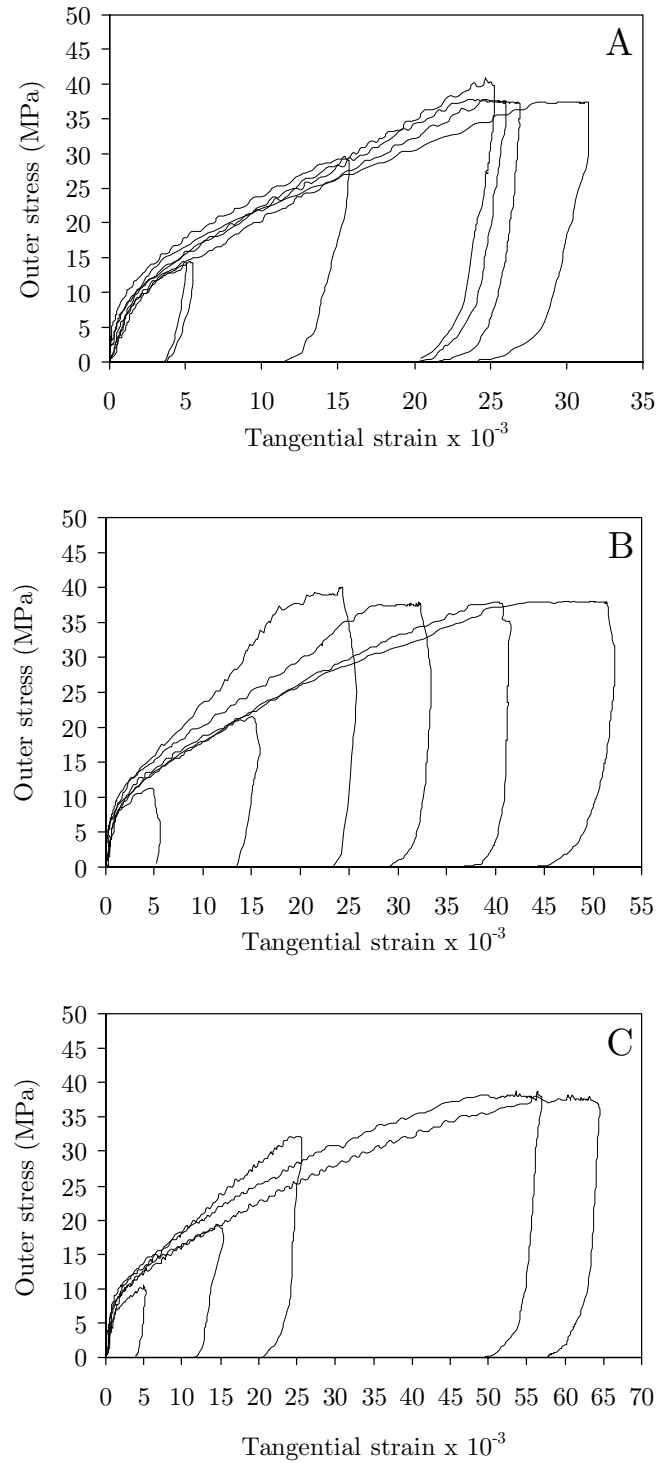
Figure 5.2: Overview of all stress-strain curves obtained for hollow-cylinder specimens type A, B,
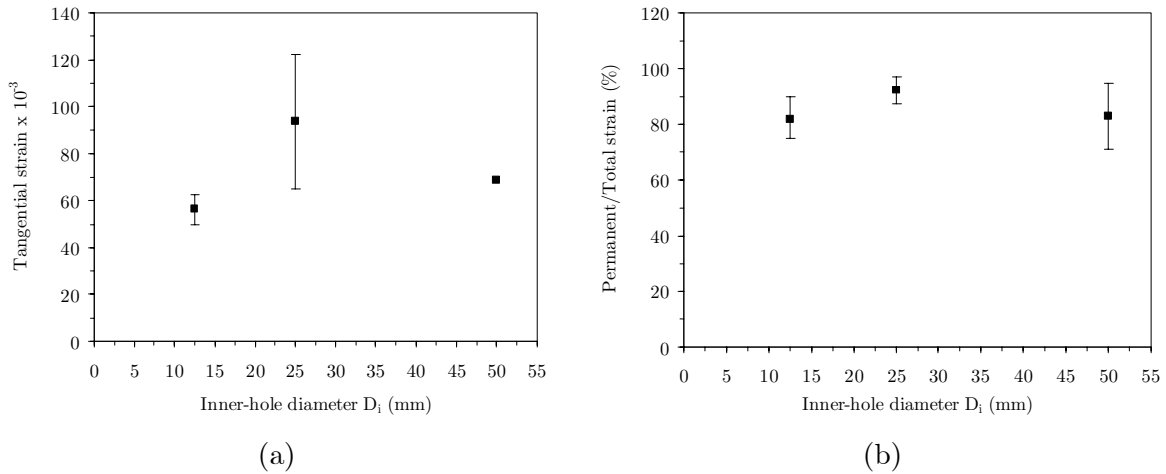and C for the mixture M4.
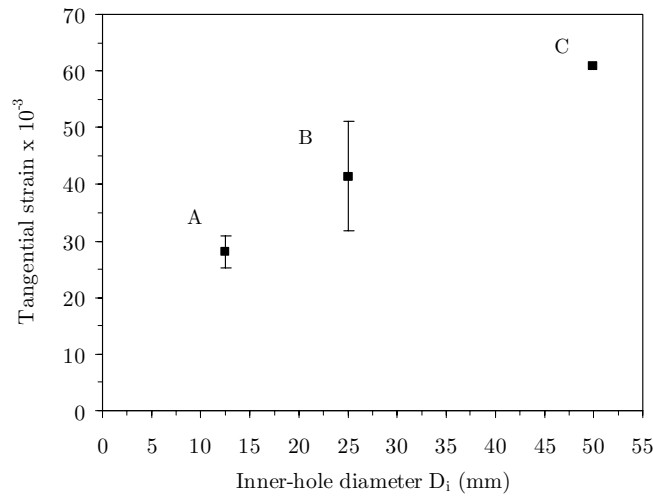
Figure 5.3: Total tangential strain calculated at end of tests on M4 for sizes A, B, and C. Scatter of results for sizes A and B included together with the mean values.
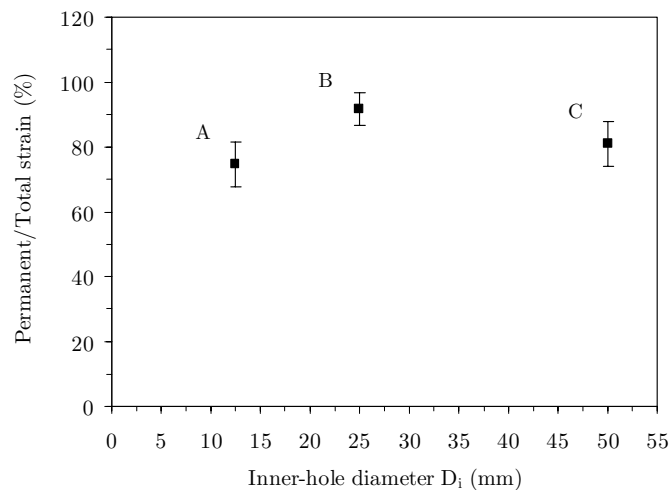
Figure 5.4: Percentile ratio between the permanent and total tangential strains with their standard deviation for sizes A, B, and C.

Stress-strain response for 2 mm mixture (M2)

In Figure 5.5, the individual stress-strain curves are presented from tests performed on the mixture M2. Mostly, the stress-strain responses of the mixture are comparable to those of the mixture M4. A noticeable difference is the higher ductility and strain capacity of the specimens from the M2. Tangential strains up to 6.1%, 11%, and 7.1% were observed for the specimens' type A, B, and C, respectively. In Figure 5.6a, the average total tangential-strains are plotted with their standard deviation versus D_i. Generally, an increasing trend with size is observed, but both the average and standard deviation for size B are remarkably high in comparison with A and C. The reason for this higher scatter is probably the use of limited data in calculations, 3 measurements, raising an influential weight for each measurement.

For size C, two tests were stopped at stress levels lower than the 40 MPa pressure-capacity of the test cell (the responses without unloading path in Figure 5.5 type C). This was due to an accelerated failure and spalling that took place around the inner-hole in those tests hindering the deformation measurement to continue functioning effectively. The tests were stopped and the measurement device was de-mounted to save it from possible damage. It is doubted, however, that those tests could have continued up to the stress levels obtained in sizes A and B, viz. 35-40 MPa, without their collapse. This explains the lower average strain value for size C in Figure 5.6a in comparison with B and why no unloading response was recorded for those two tests.

Figure 5.5: Overview of all stress-strain curves obtained for hollow-cylinder specimens type A, B, and C for the mixture M2.

Figure 5.6: (a) Total tangential strain calculated at end of tests on M2 for sizes A, B, and C. Scatter of results for sizes A and B is included. (b) Percentile ratio between the permanent and total tangential strains with standard deviation for sizes A, B, and C.

Similar to the mixture M4, a smooth transition was observed from an initial slightly curved to a subsequent softer response (see Figure 5.5). This transition curiously seems to occur at an outer stress σ_o around 7-10 MPa as with the M4. The value appears also independent of the specimen size and in proximity to the average value of the compressive strength of the mixture. In rock mechanics, the point of transition or onset of nonlinearity is generally associated with the onset of failure or damage. After onset of failure, one common mode of rock behaviour afterwards is brittle fracture and another mode is plastic behaviour. In Figure 5.6b, the ductility index for M2 is presented.

Onset of failure in the hollow-cylinder tests

In the abovementioned discussion, the transition in the stress-strain response is mentioned to occur at σ_o of about 7-10 MPa. According to linear-elastic calculations, this stress would give a tangential stress at the hole-wall equal to $\cong$15-21 MPa. This transition connotes a clear change in the deformation rate of the hole-wall and is seen as an indication of the onset of failure. Remarkably, this transition was observed to take place independent of specimen size and maximum aggregate size in the mixture.

Figure 5.7 shows the individual stress-strain curves for the mixtures M2 and M4 in the range 0 to 7‰ strain for all sizes. This range generally covers the transition zone and is used to emphasize the transition process and onset of failure. The smooth transition that takes place in the curves renders difficult the identification of a specific transition point. However, a bilinear model could be assumed to reasonably represent the stress-strain responses. The transition could then be approximated as the kink point in the assumed bilinear behaviour. In the figure, the bounded areas correspond to the range where transition seemed to take place from the various curves. The transition range is 7 to 10 MPa for the M4 and 5 to 10 MPa for the M2. The lower limit in the range for the M2 is due mainly to type C specimens, which were generally weaker than the rest and is believed due to more difficulty witnessed during their casting and compaction process.
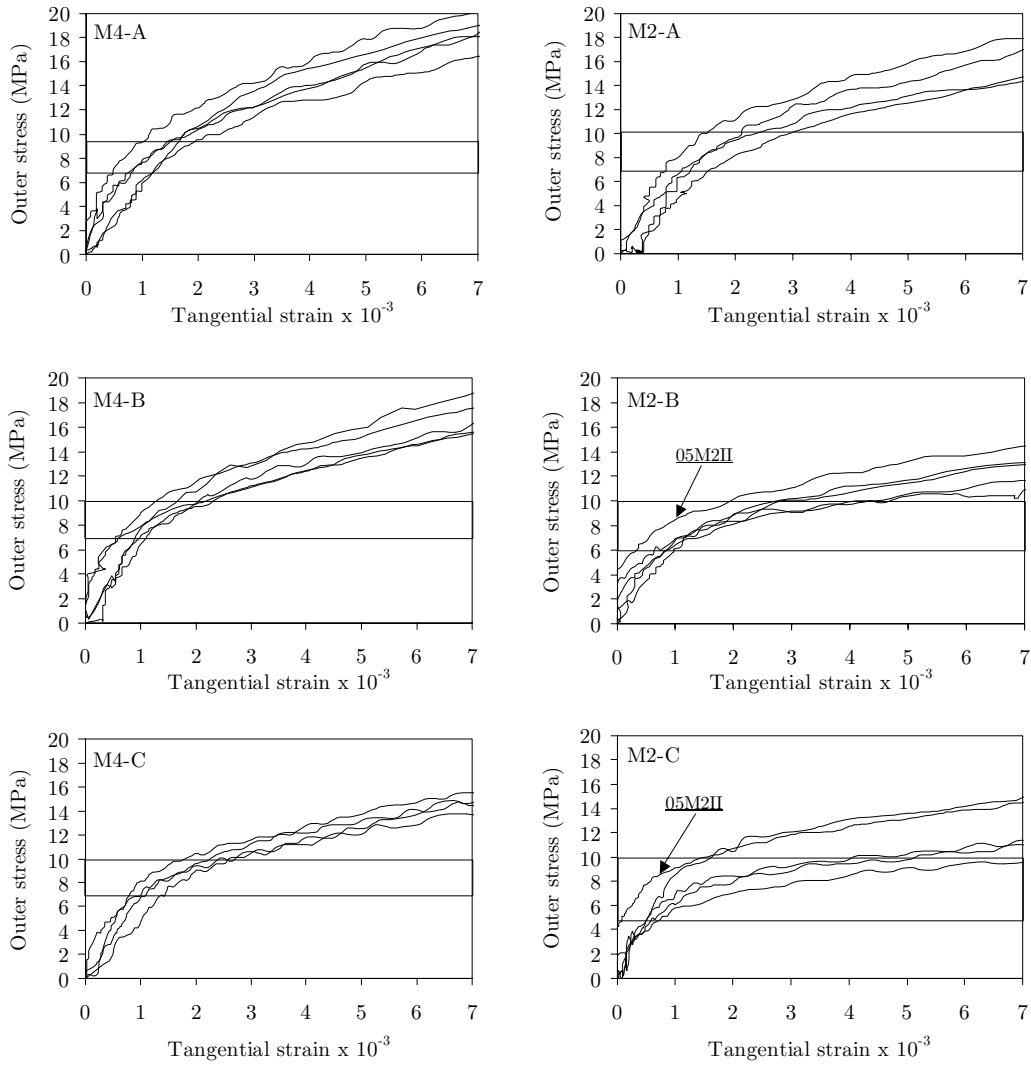
Figure 5.7: Outer stress-tangential strain curves for mixtures M2 and M4 in the range 0 to 7‰ strain for specimens A, B, and C. Bounded areas highlight the transition zones.
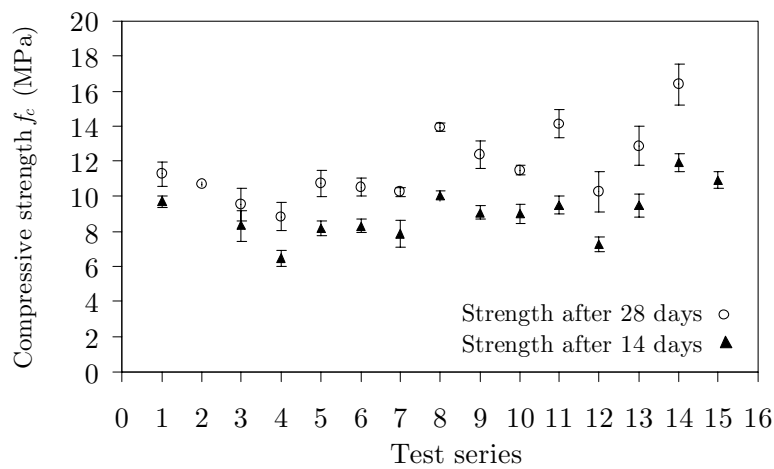
Figure 5.8: Cube strength values after 14 and 28 days of age for all M2 and M4 mixtures from the principal test series performed at 14 days.

To examine the relation, if any, between the observed transition and the f_c value of the tested mixtures, the mean and standard deviation for all tested series are plotted in Figure 5.8. The cube strength values are presented for test results after 14 and 28 days of age. The average cube strength for the M2 after 14 days was 8.0 ± 0.9 MPa and was after 28 days 11.0 ± 1.5 MPa. The average cube strength for the M4 after 14 days was 10.0 ± 1.2 MPa and was after 28 days 12.6 ± 2.4 MPa. The scatter in the strength after 28 days was higher than that after 14 days. The average strength after 14 days achieved 70-80% of the strength value after 28 days. The average strength after 14 days for the M4 was 1.25 times that of the M2 with a comparable scatter (11.25% and 12% for the M2 and M4, respectively). Considering once more the average transition or onset of failure in the stress-strain curves (7-10 MPa), their concurrence with the average strength value at the age of testing for both mixtures is then distinguishable.

The correspondence of the external stress where onset of failure took place with the average compressive strength of the tested mixtures is noteworthy. This is for its potential importance in stability studies of deep wellbores under similar conditions as those in the conducted hollow-cylinder tests. Accordingly, it is tentatively suggested that onset of failure is to be expected at around the f_c value of the concerned rock. However, the uncertain and rather complex state of stress deep in the underground as compared to laboratory test conditions should be considered. In terms of local failure at the hole-wall, the onset of failure is observed at a tangential stress σ_θ in the range 15 to 21 MPa (from linear elasticity). This stress is nearly two times the f_c and is active just behind the inner-wall. However, there exists as well the axial stress σ_z component of value in the range 7-10 MPa. The onset of failure therefore commenced at a deviatoric stress σ_1-σ_3=σ_θ-σ_z=8-11 MPa. This deviatoric stress value is in proximity as well of the average strength of the mixtures after 14 days.

In Figure 5.7, specimens B and C of the test series 05M2II (indicated by arrows in the figure) show a delayed stress-strain response with a zero strain value to an outer-stress value of about 4 to 5 MPa. This was due to a technical problem in the measuring device during these tests, which was resolved in all the remaining performed tests.

5.3.2   Stress-strain response under cyclic loading

An important aspect of the behaviour of concrete and rock materials is their stress-strain response under cyclic loading. Two test series were conducted (one series per mixture) wherein unloading/reloading cycles took place at prescribed strains. In each test, two cycles were applied at tangential strain values of 5 and 15‰ strain. Afterwards, the tests were continued to a stress of 35-40 MPa before stop and unloading. The results of these two series are shown graphically in Figure 5.9

The results suggest a general characteristic for both mixtures and for all sizes under load cycling except for specimens A from the M4 and C from the M2 (M4-A showed peculiar large hysteresis and M2-C was abnormally weak). Both mixtures showed a ductile response with the capacity to sustain large permanent deformations while maintaining the ability to resist additional outer stresses. The total tangential strains attained in the cyclic tests (Figure 5.9) were smaller in magnitude when compared with those from monotonic tests (Figures 5.3 and 5.6) with nearly 25% for M4 and 35% for M2. This is in line

with observations from rock testing where higher stresses are attained for cycles taking place in the ductile region (Jaeger and Cook, 1979).

In Figure 5.9, the reloading branches of the cycles at 5‰ strain reached and joined the original stress-strain path close to the point of initial unloading. For the second cycles at 15‰ strain, the reloading branches bend away and pass below the point of unloading and seem to reach the original stress-strain path afterwards. The unloading/reloading branches demonstrated nonlinearity resulting in hysteresis. The existence of hysteresis means more work is done on the body during loading than is done during unloading (Jaeger and Cook, 1979). In other words, energy is dissipated in the specimen's body during a cycle of loading and unloading.
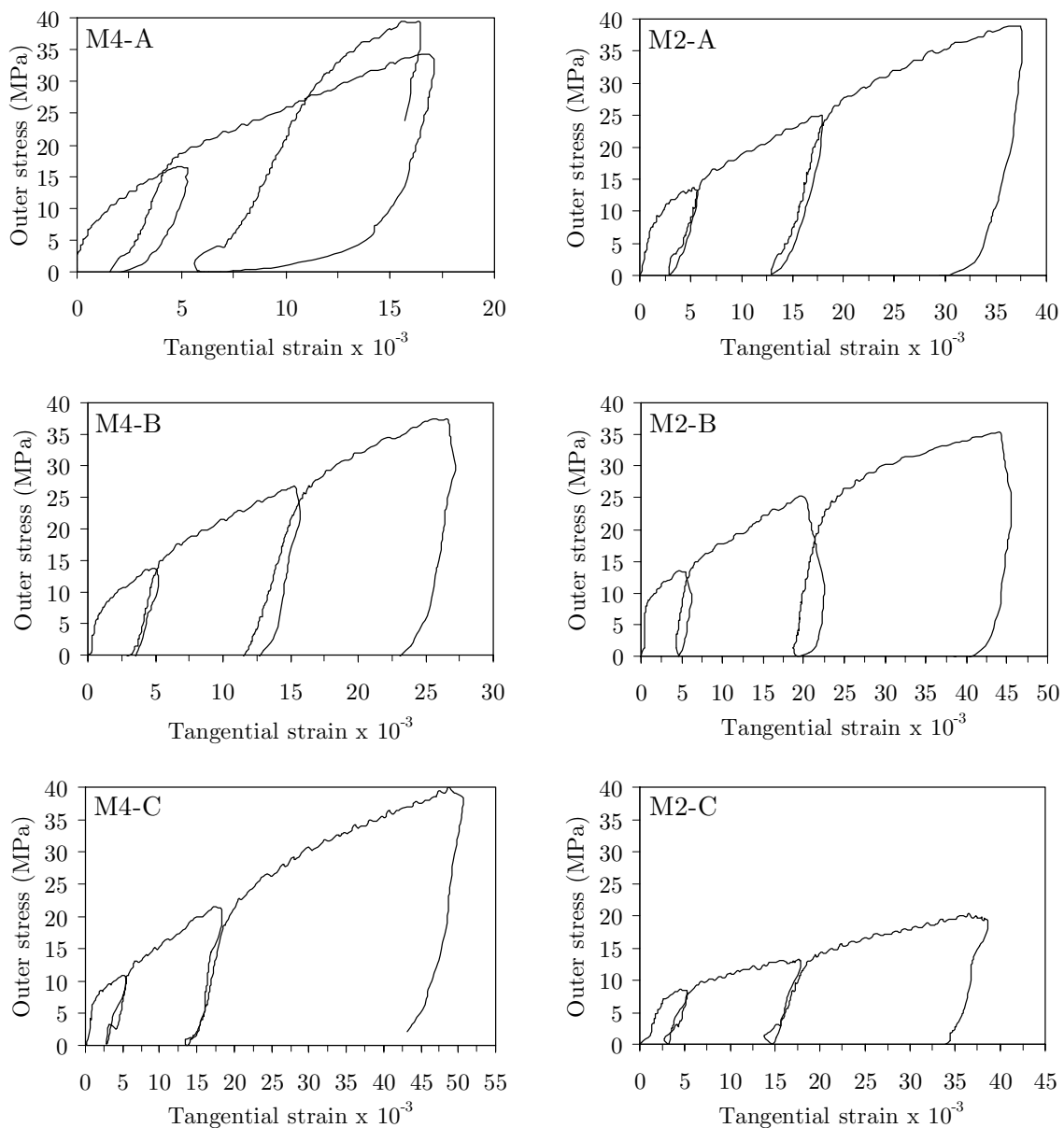
Figure 5.9: Outer stress-tangential strain curves for mixtures M2 and M4 under cyclic loading for specimens' type A, B, and C.

According to Spooner *et al.* (1976), the dissipated energy comprises three components. These are energy generated in damage, in damping, and the elastic strain energy. They quantify the energy dissipated in damage as the area between the initial stress-strain curve and the reloading curve of following cycle. Following this assumption and qualitatively examining the results in Figure 5.9 indicates that damage was effective at low strain levels in the order of 5‰ strain, which is also characterized by the high irrecoverable deformations in the specimens.

A characteristic of damage in cyclic tests is a degradation in the slope of the loading curves with increased strain in tests under cyclic loading (Sinha *et al.*, 1964; Spooner *et al.*, 1976). In our tests, the slopes of all ascending and descending branches are qualitatively parallel (see Figure 5.9) with stiffness in the range 6.7 to 8.5 GPa. This stiffness value is roughly equal to the modulus values obtained from the uniaxial compressive tests (Table 3.4, § 3.4.2). The reason for this is thought due to a densification of the cement-paste, considering its porous nature, which takes place during loading. This precedes the damage characterized by cracking and spalling that occurs later in the loading process. It is expected if loading cycles were performed at strain levels where more 'destructive' damage is proceeding (>15‰ strain), then degradation in the re-loading modulus might have been observed. It should be noted that few grain-boundary microcracks were observed in specimens unloaded at 5‰ strain and relatively more cracks at 15‰ strain (§ 5.4). The intensity of these micro-cracks, however, seems not large enough yet to cause degradation in the stiffness modulus.

5.3.3   Size effect

The size effect on strength in the hollow-cylinder tests was calculated according to the procedure described in § 4.5.3. In Figure 5.10, the size-stress relation $\log \sigma_o$–$\log D_i$ is presented for all individual test results from both mixtures. At least six tests were conducted for each size from each mixture and are all included in the figure. Mean stress values at 5‰ strain and their standard deviations are included in the $\log \sigma_o$–$\log D_i$ plots of Figure 5.11 and are summarized in Table 5.1.

Table 5.1: Mean stress values at 5‰ strain and their standard deviations used for size effect

Mixture/Size		A	B	C
M4	σ_o (MPa) at 5‰ strain	16.1	13.9	12.2
	Standard deviation (MPa)	1.34 (8.3%)	1.69 (12.2%)	1.28 (10.5%)
	Number of tests	6	6	6
M2	σ_o (MPa) at 5‰ strain	14.5	11.6	10.1
	Standard deviation (MPa)	2.10 (14.5%)	1.20 (10.3%)	1.62 (16.0%)
	Number of tests	7	7	6

The results presented in Figures 5.10-5.11 illustrate a size effect on strength of the tested hollow-cylinders. The difference in mean stress values between specimen A and specimen C is 32% and 44% for the M4 and M2, respectively. A scatter in the stress results is marked for all sizes from both mixtures. For the M2, the scatter for A and C is larger

than that for B. Carefully examining the individual values for stress in Figure 5.10 (bottom) shows one value for size C that is notably higher than the rest. If this data point would be considered as an outlier, the largest scatter would be for the smallest size A. For the M4 data, the scatter is observed for the three sizes with that of B being slightly higher than A and C.

The scatter for size A in the M4 could have been expected larger than B and C as observed in tensile size-effect tests by van Vliet and van Mier (2000). In their tests, the scatter for the smallest specimen was much larger as compared with the other larger sizes. This was ascribed largely to the relative small aspect ratio D_c/d_{max} of the specimen (equal to 3.75) as compared with the representative volume. The aspect ratio W/d_{max} for size A in the hollow-cylinder tests is 4.69 and 9.38 for the M4 and M2, respectively. The scatter for size A, however, was not the largest when compared with other sizes. The reason for this is thought due to the difficulty met in casting the mixtures, for their gab-grading and high w/c ratio, causing air voids of varied sizes to be trapped inside the specimens. This led to higher heterogeneity and higher stress concentration around these air voids. The larger the specimen size, the larger the chance was for these voids to develop and cause therefore a higher scatter.
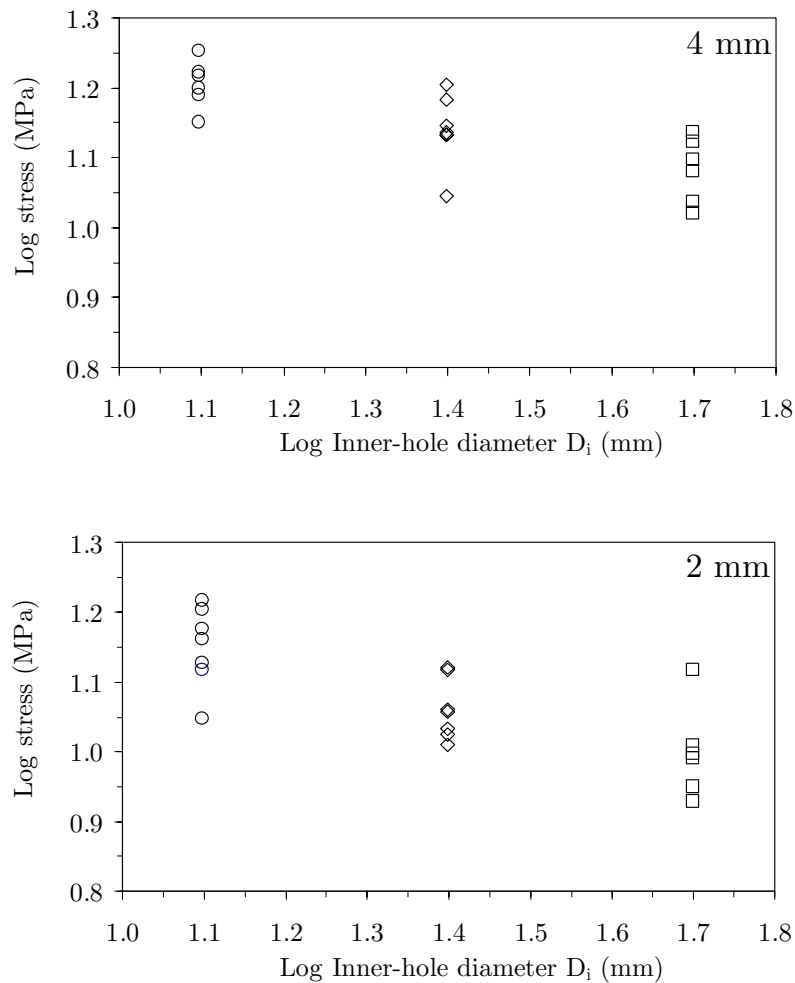
Figure 5.10: Individual values for log outer-stress σ_o versus log inner-hole diameter D_i.

In Figure 5.12, mean values are plotted for the stresses at 5‰ strain for both mixtures with their best-fit using linear-regression. Both mixtures show a nearly perfect linear relation on a log-log scale as indicated by the high correlation factor. A power relation, therefore, exists between the three sizes on a normal scale. The exponent of this power relation is -0.19 and -0.26 for the M4 and M2, respectively. The size effect trend for both mixtures is comparable, but that for M2 showed slightly stronger size effect.
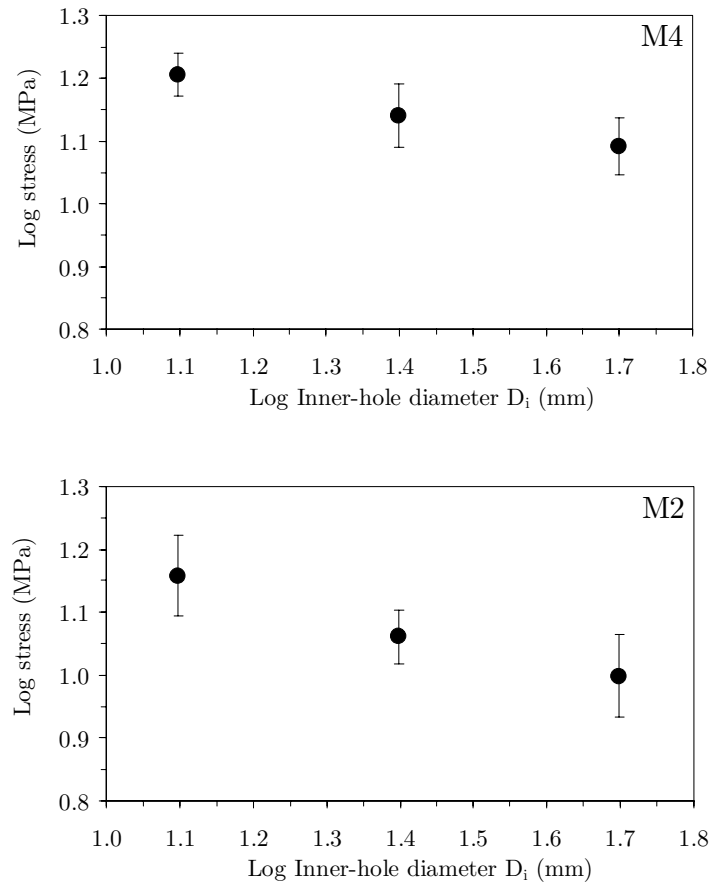
Figure 5.11: Mean values and standard deviations for log σ_o versus log D_i.
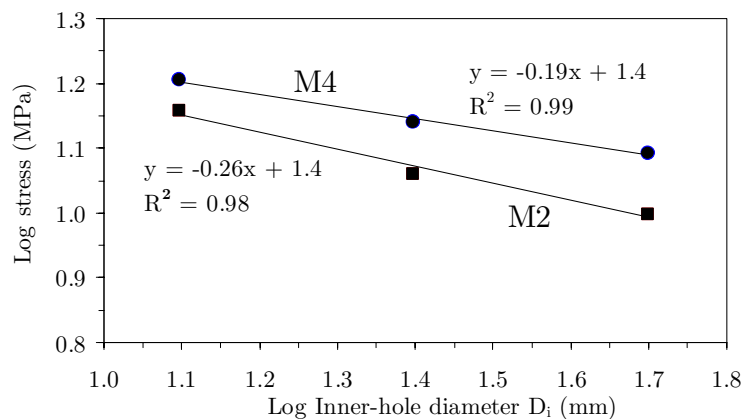
Figure 5.12: Plot of log σ_o versus log D_i for M2 and M4, and their fit with linear regression.

The overall strength of the M4 was higher than that of the M2 for all sizes (Figure 5.12). The mean stress at 5‰ strain for sizes A, B, and C from the M4 were 1.1 to 1.2 times those from the M2. As discussed in § 5.3.1, the average cube strength for the M4 was 1.25 times that for the M2 and this could therefore be the cause for the observed difference in stress values in Figure 5.12. This difference in strength could be largely ascribed to the effect of d_{max} suggesting a higher strength for mixtures with larger d_{max} in uniaxial compression and hollow cylinder tests. As discussed in § 2.2.3, mixtures with relatively low cement content (poor mixtures) tend to show an increase in strength with aggregate size. The cement content for the M4 is $\cong$260 kg.m^{-3} and for the M2 is $\cong$330 kg.m^{-3}. The effect of d_{max} was pronounced as well during fracture and spalling that was observed in the tests (see Figure 5.16 for effect on spalling).

5.3.4   Volumetric response

In addition to the measurement of radial deformations at the inner-hole, measurement of axial deformations was performed for a number of specimens of type C. It was not feasible to perform simultaneously both axial and radial measurements inside specimens of type A and B due to the limited inner-hole space (§ 4.2.3). The measured axial deformations, although limited, have yielded useful information concerning the volumetric strain response and the stress situation inside the hollow-cylinder.

Classical solutions for the problem of thick-walled cylinders, discussed in § 2.5.1, describe the stress and strain in the axial direction as the intermediate principal stress and strain, whereas the stress and strain in the tangential direction as the maximum principal stress and strain. In Figure 5.13, axial and tangential strains are plotted versus the hydrostatic stress applied in tests on specimens type C from two test series for the mixtures M2 and M4. For both mixtures, the axial strain is observed much stiffer with notably less total strain value relative to the tangential strain.
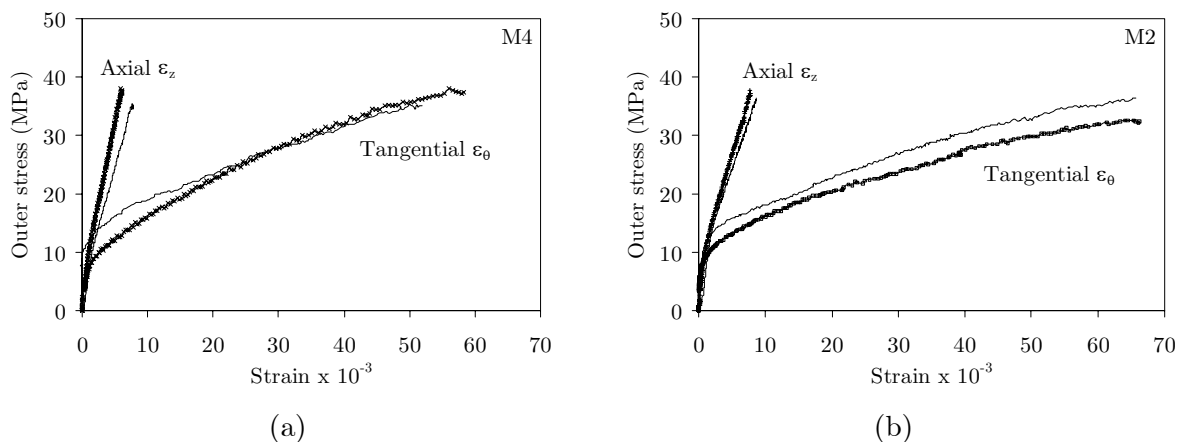
Figure 5.13: Outer stress (MPa) versus both the axial and tangential strains (x10^{-3}) for specimens type C from (a) the M4 and (b) the M2 mixtures.
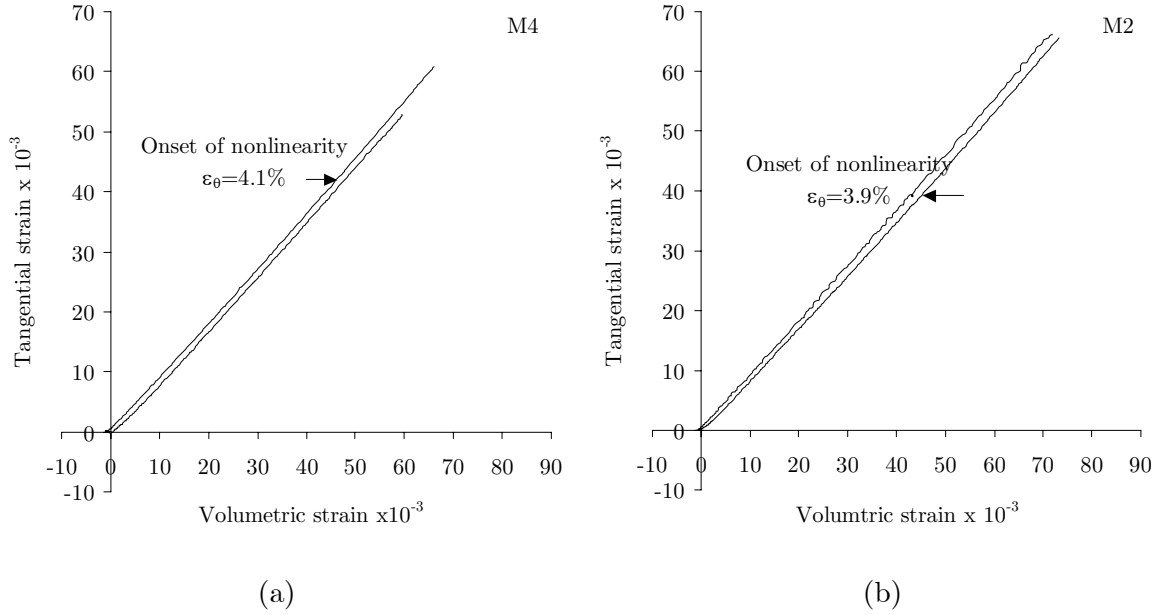
Figure 5.14: Volumetric strain versus tangential strain for specimens type C from (a) the mixture M4, and (b) the mixture M2.

This implies that the tangential stress and strain at the inner-wall in a thick-walled cylinder subject to an external hydrostatic pressure are the maximum principal components. This is considering the radial stress equals zero at the inner-wall in this case due to absence of inner-hole pressure. The radial stress and strain therefore are the minimum principal stress and strain.

The volumetric strain at the surface of the inner-wall was calculated for specimens type C, which included axial deformation measurements during its testing. The volumetric strain is calculated as the sum of the three principal strain components, i.e. $\varepsilon_v = \varepsilon_\theta + \varepsilon_z + \varepsilon_r$. In Figure 5.14, the volumetric strain is plotted against the tangential strain; the major principal strain, for the specimens included in Figure 5.13. Initially, the axial displacement is activated before the commencement of the radial deformation at the inner-hole. Afterwards, volumetric compaction (decrease in volume) took place and continued in a mild non-linear behaviour against the tangential strain until end of tests. The contracting behaviour of the specimens is governed mainly by the tangential deformation component and then the axial compression.

The nonlinearity in the volumetric strain response took place at a tangential strain of about 4.1% for the M4 and 3.9% for the M2. At these points, an increased rate in the closure of the inner-hole was detected with volume increase instead of decrease. As presented in the next section, at these levels of tangential strain ε_θ for specimens of type C, opening of cracks and spalling activities have already advanced. The reason for a delayed onset of nonlinearity in the volumetric response, as compared for example with tests under ployaxial compressive stress conditions (as in e.g. Newman, 1979; van Mier, 1984), owes probably to the stress condition applied during the tests.
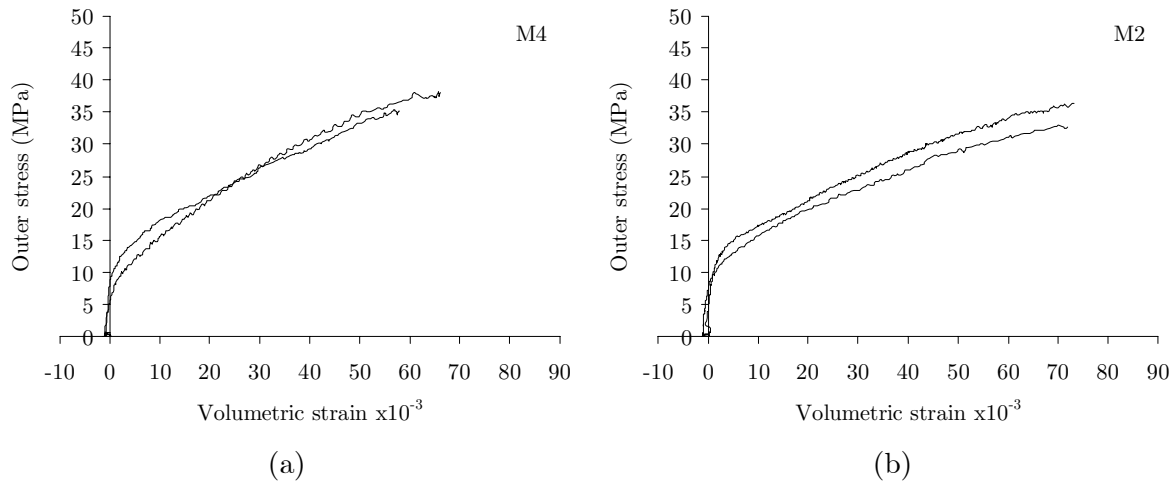
Figure 5.15: Volumetric strain versus outer-stress σ_o for specimens type C from (a) the mixture M4, and (b) the mixture M2.

Van Mier (1984), reported a continuous non-linear behaviour for the volumetric strain against the axial strain in ployaxial compressive tests under conditions of σ_3=0.05 and 0.10 σ_1. In his tests and similar ployaxial compressive tests, the deviatoric stress $(\sigma_1\text{-}\sigma_3)$ is non-constant and fairly uniform within the specimen during the whole test and until localization starts. In hollow cylinders under external hydrostatic stress and zero inner-pressure, the deviatoric stress is generally constant during the tests except at the surface of the inner-hole where the radial stress is equal to zero. The deviatoric stress, however, is non-uniformly distributed inside the hollow-cylinder due to its geometrical boundary condition. A major difference between a constant and non-constant deviatoric stress situation is that the latter is known responsible for a non-linear brittle failure with crack nucleation, propagation, and coalescence. Whereas the former is accountable more for volume decrease with fissure closing, bulk compression, and plastic failure (Goodman, 1980). This could explain the rather linear compacting response of the volumetric strain with delayed non-linearity and onset of dilation in the hollow-cylinder tests, but more insight is needed regarding the failure mechanism, which is examined closely in the next section.

Figure 5.15 shows the volumetric contraction of the inner-hole in the specimens discussed above under increasing outer-stress σ_o and zero inner-pressure. After a short linear segment, the response turns into a strain-hardening behaviour. The transition in the volumetric strain could be a mark for onset of failure or damage. This occurred at $\sigma_o\cong10$ MPa for both mixtures, which is associated with a volumetric strain of 2.0 to 2.5‰ strain for the M4 and 2.5 to 3.0‰ strain for the M2. According to linear-elastic calculations, an outer-stress of 10 MPa would give a tangential stress at the hole-wall equal to 21.3 MPa. As reported in Chapter 3 and discussed earlier (§ 5.3.1), the f_c for both mixtures ranged from 9 to 12.5 MPa. The apparent strength of the hole is therefore 2 to 2.5 times as high (see discussions on onset of failure in § 5.3.1). This is in quantitative agreement with the experimental results of Daemen and Fairhurst (1971), Santarelli (1987) and others as documented by Guenot (1987).

5.4 FAILURE CHARACTERESTICS AND FRACTURE MECHANISMS

Hollow cylinder test results over the past two decades on rock and concrete materials have established that failure taking-place around the inner-hole is governed by either an extensile/splitting or shear type failure mechanisms. Tendency of a certain material to follow one of these mechanisms in hollow cylinders is yet poorly understood and contradictory observations have been reported (Hoek *et al.*, 1994). Shear failure is macroscopically described by spiralling shear bands that originate at the surface of the inner-wall. Microscopically, unresolved debates exist over the shear fracture initiation mechanism whether micro-tensile cracks linkup in a macro-shear crack or do initiate in shear. Generally, in terms of micro-mechanisms of failure under compressive stresses, it is rather established that the basic failure mechanism for brittle and quasibrittle heterogeneous systems is tension and due to tensile stress concentrations (Hsu *et al.*, 1963; Bieniawski, 1967; Hallbauer *et al.*, 1973; Gramberg, 1989; Kemeny and Cook, 1991). How these micro-cracks further develop to an either shear or splitting macro-crack is a complex process, which is influenced by parameters such as, material characteristics, boundary conditions, and stress path.

Macroscopically, no major signs of failure were recorded during testing and up to an outer-stress level of 25-30 MPa when spalling activities occasionally took place. These were characterized by detachment and fall of flakes from the cementitious cover at the wall surface. At higher stress levels near end of tests, especially in the M2, spalling of loose grains and some larger slivers took place. Pictures taken inside open inner-holes just after testing (Figure 5.16) show the difference in spalling activities for specimen type C from the two mixtures. In the M4, small slivers are detached and intact material remains, whereas the M2 shows much more spall regions with hardly any intact material left. Failure in the M2 shows warping of the surface in an undulating way. Both mixtures, however, showed damage over the whole sample length and all around the inner-hole in an axisymmetric fashion.

$$(a) \qquad\qquad\qquad\qquad\qquad (b)$$
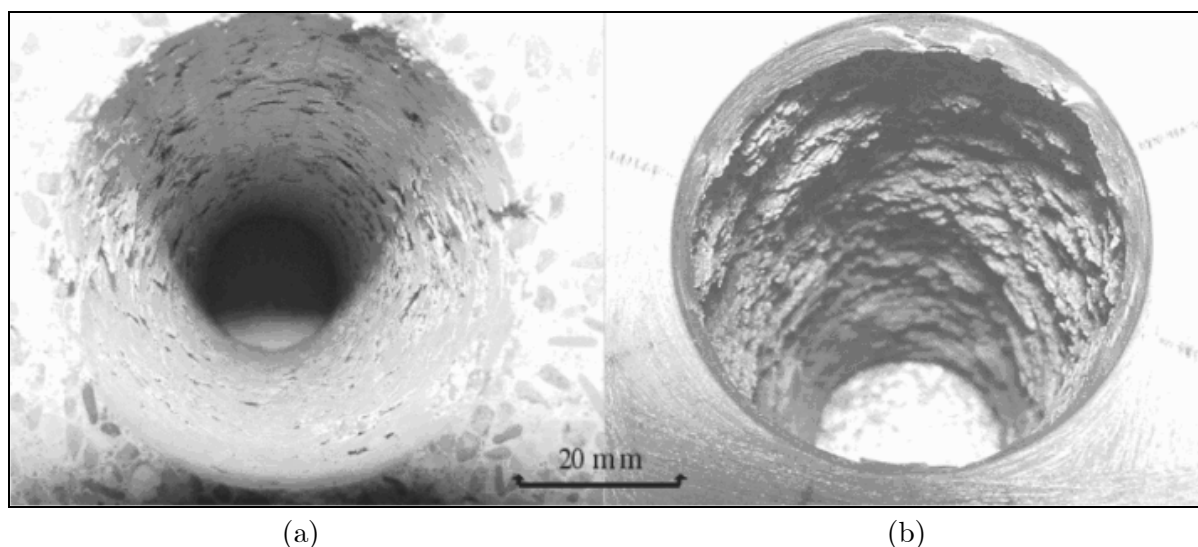
Figure 5.16: Photo images of open-hole appearance for specimens type C at completion of the tests (35-37 MPa) for (a) M4, and (b) M2.
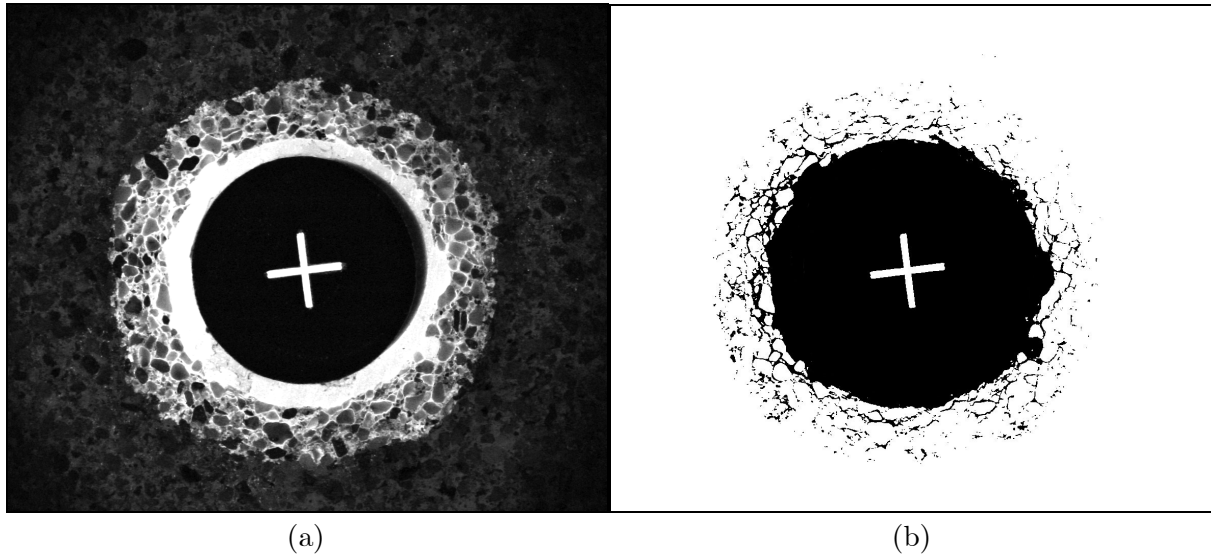
Figure 5.17: Failure pattern for specimen type B from M2. (a) Damage zone and fracture pattern highlighted under ultraviolet light and (b) the same after filtering the crack pattern.

Mesoscopically, at the aggregate scale, cuts from impregnated specimens were investigated using optical microscopy. Smaller slices were scanned under higher magnification using both optical microscopy and the BSE detector in ESEM. This enabled visualization of cracks with widths >1.0 µm.

Examining the slices cut from the various impregnated specimens of the different sizes revealed that damage is fairly distributed all round the inner-wall in a concentric pattern. The cracks in this damage zone are generally located parallel to the inner-wall, which coincides with the direction of maximum principal stress σ_θ. The thickness of the damage zone was calculated using the average of four measurements done visually using a scale at 90° intervals under ultraviolet light. The average depth of the damage zone for the M4 measured at end of tests was 3.5, 6, and 10 mm for specimens of type A, B, and C, respectively. For the M2, the average depth of the damage zone was 3.5, 4.5, and 9 mm for specimens of type A, B, and C, respectively. Thus, the type of mixture, with their different d_{max}, did not in effect influence the depth of the damage zone. Notable, however, is the increase in damage zone with size.

In Figure 5.17, a typical result from an impregnation experiment (specimen type B in this case) is presented. The highlighted zone in Figure 5.17a indicates the impregnation zone that also characterizes the damage zone in this test. As failure considered progressing from around the inner-wall outwards under increasing stress, the depth of the impregnation zone is assumed to represent the depth of the damage zone. The crack pattern in Figure 5.17b is obtained through filtering using a grey level threshold. Fracturing is characterized by cracks that are distributed all round the inner-wall in a symmetric fashion. These cracks are roughly parallel to the inner-wall and seem to form intact slabs of fairly uniform thickness, which is approximately equal to d_{max}. Both inter- and intra-granular cracks are formed (Figure 5.17a and more visible in Figure 5.19), which possibly depends on the grain mineralogy and/or grain orientation relative to the direction of σ_θ (maximum principal stress).
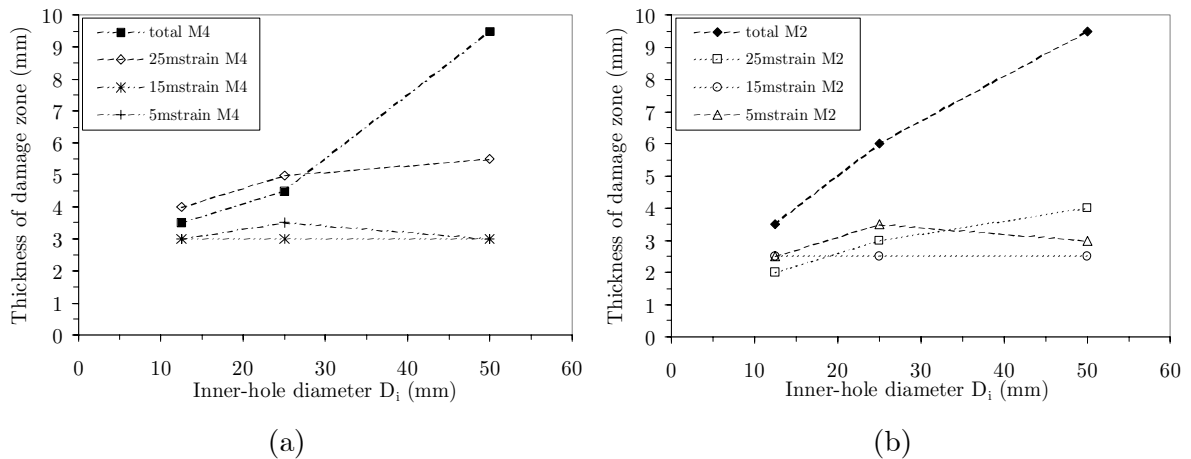
Figure 5.18: Thickness of damage zone as observed in tests at different strain levels on sizes A, B, and C from (a) the mixture M4 and (b) the mixture M2.

The symmetry of damage around the inner-hole is visible, which is different from observations by other researchers from tests using natural rocks (Gay, 1973; Guenot, 1989; Haimson and Herrick, 1989; Maloney and Kaiser, 1989). They generally observed failure zones of diametrically opposite, symmetric regions and mostly consistently oriented along the length of the sample (known as borehole breakouts).

As regards the damage thickness with respect to specimen size, a size dependence of the thickness of the damage zone was observed for complete tests (performed to the highest possible pressure of $\cong$35-40 MPa). The tests conducted to a prescribed strain level showed no dependence on specimen size for strain levels in the range 5 to 15‰ strain and a mild dependence for tests stopped at 25‰ strain. In Figure 5.18, these observations are presented graphically. The size independence of the damage propagation at these levels of strain does not comply with the size dependence of strength in these tests (§ 5.3.3), which was evaluated at 5‰ strain. This implies that size effect in strength of the hollow-cylinders is triggered early in the stress-strain response and prior to propagation of cracking and damage. More in-depth discussion on the activation of size effect in hollow-cylinder tests is in § 7.1.1. Experimental artefacts related to the impregnation and measurement procedure of damage depth could play a role and should not be overlooked.

In Figure 5.19, mesoscopic images of impregnated slices for specimens type C taken under ultra-violet light are presented. The images demonstrate that damage took place generally through short boundary cracks (associated with the grain boundary) in a direction parallel to the inner-wall. These cracks seem to propagate inter-granularly, in their plane or towards the inner-wall being a stress-free surface, and intra-granularly. The cracks, in many areas around the hole, connect and line up at nearly constant distance from the inner-wall. A typical depth of these lineaments is d_{max} of the concerned mixture and extends for a length of 8-12 mm parallel to the inner-wall. They often end by intersecting the circumference of inner-wall or close to it. These features are recognized in both the longitudinal and cross-sectional directions and thus possibly forming three-dimensional slabs that could detach and finally spall.
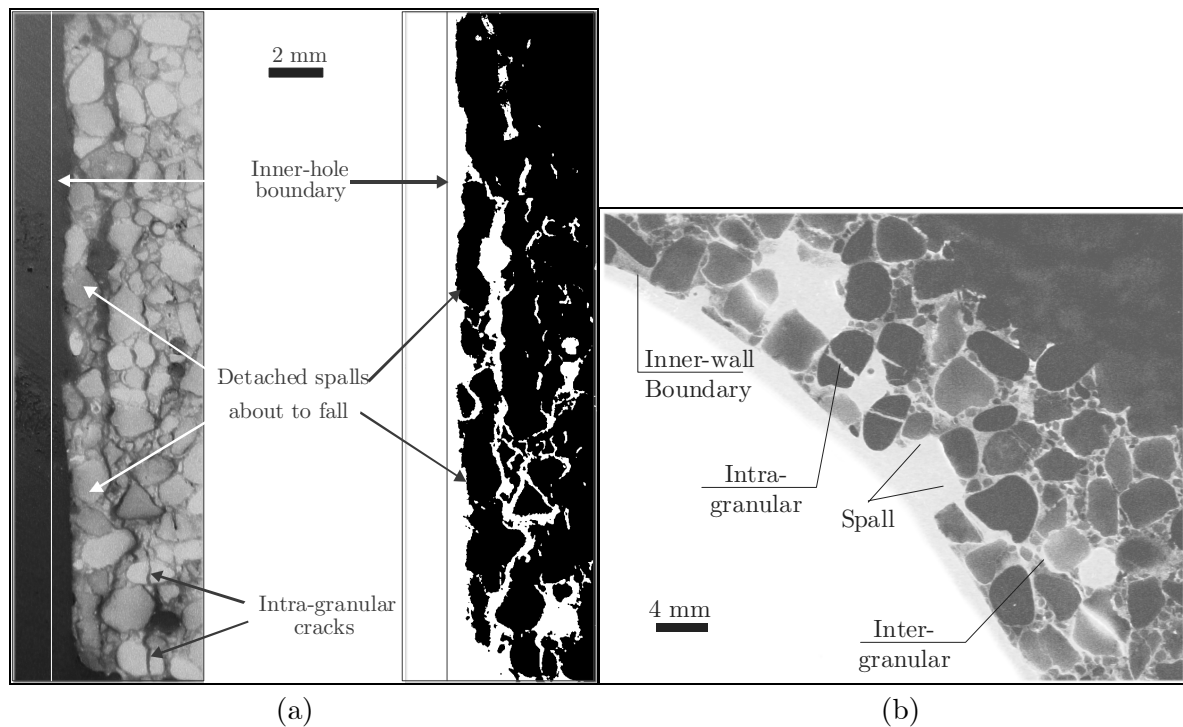
Figure 5.19: Cracking mechanisms at end of tests from impregnated specimens. (a) Vertical section in specimen C from the M2. (b) Cross section in specimen C from the M4.

5.5 FAILURE DEVELOPMENT IN HOLLOW-CYLINDER TESTS

Analysis of the fracture process on both mixtures revealed an insight into the damage mechanisms taking place during the tests. The process was observed in stepped experiments where loading was stopped at prescribed strains of 5, 15, and 25‰ strain. Different specimens from different series were utilized since it is, unfortunately, practically impossible to visually observe the process in real time during one test using the impregnation technique. The results are described next for both mixtures with focus on micro-mechanisms of failure as observed in representative samples (see § 7.3 for interpretation of the results). These were cut to size and then hand-ground on a lap-wheel using silicon-carbide paper of grit size 320, 500, and 1200, respectively. Mono-crystalline diamond paste and poly-crystalline diamond spray were used afterwards for polishing the surface with a fineness of 6, 3, 1, and 0.25 µm correspondingly.

5.5.1 Fracture growth in the 2 mm mixture

The fracture process in hollow-cylinder tests on the M2 as depicted from the micrographs shown in Figure 5.20a-d, could be summarized in the following steps:

–   Specimens unloaded at tangential strain level of 5‰ strain showed no signs of major fracturing or spalling activities. The surface of the inner-wall was intact as from visual inspection prior to impregnation and microscopy analysis. Using the ESEM with a BSE detector revealed initial micro-grain boundary cracks to exist around few individual grains. These cracks were (ex)tensile (de-bonding) cracks within the ITZ

and their width did not exceed 20 μm. They were generally located at a depth around d_{max} from the hole in direction parallel to the inner-wall and principal stress direction. Occasionally, these cracks extended intra-granularly between grains in direction parallel to the inner-wall (Figure 5.20a).

– Figure 5.20b shows a micrograph from specimen unloaded at 15‰ strain. Damage increased in the form of more grain-boundary cracks, which linked occasionally to form thin slabs close to the inner-wall. This caused minor spalling activities to occur during tests. Slight damage was observed deeper in from the hole as individual grain-boundary cracks parallel to the inner-wall.

– At 25‰ strain, crack openings notably increased and new cracks were observed deeper in from the hole. In addition to grain-boundary cracks and intra-granular cracks, few cracks were detected running through the cement-paste in direction parallel to the inner-wall (Figure 5.20c).

– Extensive and considerable damage with crack coalescence, detachment and spalling were evident in specimens unloaded at strain level of 70‰ strain (σ_o=35 MPa). The cracks continued to grow inter- and intra-granularly along the spring lines of the hole (Figure 5.20d). Crack widths increased close to the hole to around 100 μm and were
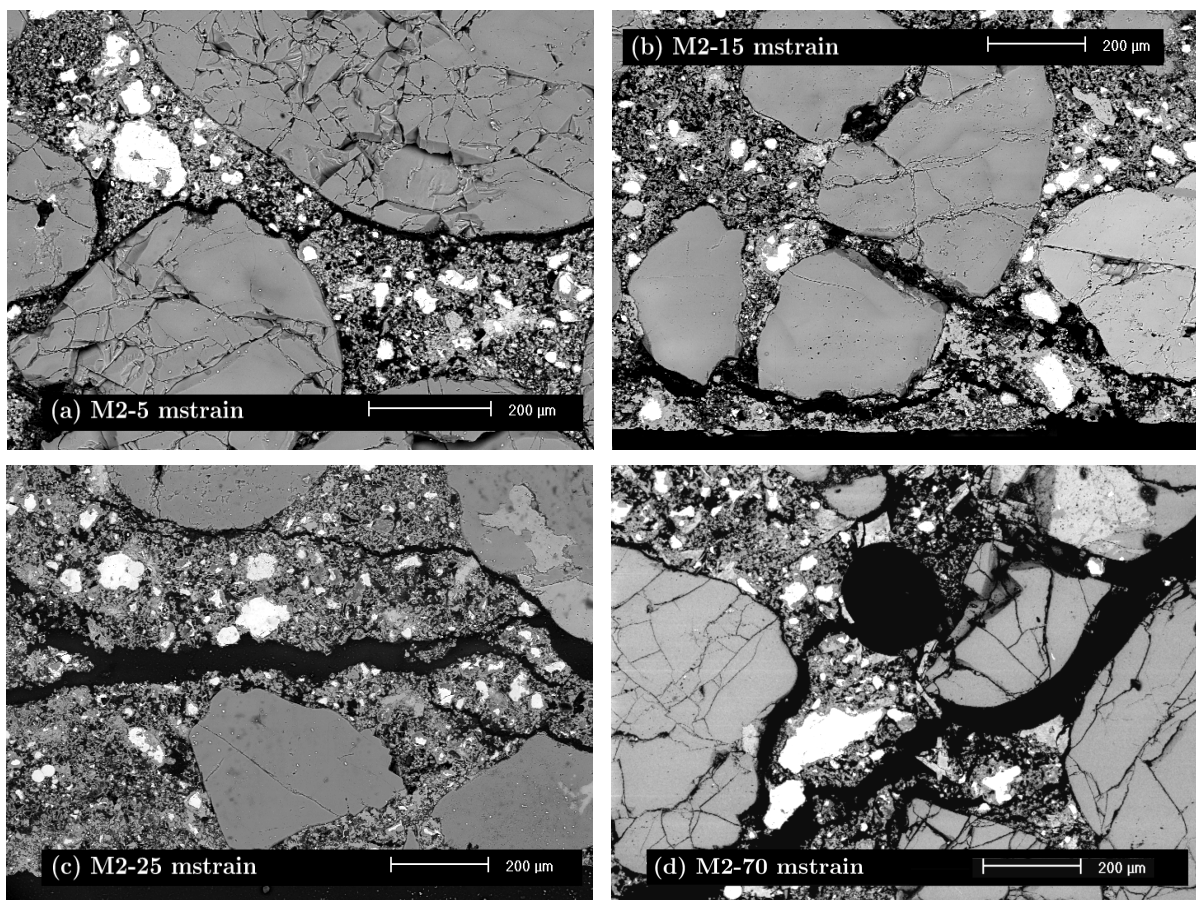
Figure 5.20: Selected photomicrographs showing sequence of failure in the M2 from C specimens at (a) 5‰ strain, (b) 15‰ strain, (c) 25‰ strain, and (d) 70‰ strain. Direction of applied major principal stress is horizontal and parallel to the long dimension of the images. Cracks are distinguishable in the images by their black lineal shape.

observed to frequently intersect the inner-wall. The fracture process seemed to repeat itself gradually with new extensional cracks of small width forming behind spall zones, which are expected to extend later on forming new slabs of spalling potential. Close to the hole, severe grain damage is evident with occasionally complete disintegration of grains. However, grain damage was observed in unloaded specimens (Figure 3.3) and its damage is therefore not solely introduced by the induced stress change. The existence of sizable air-voids ($\cong$200 µm in Figure 5.20d) in the mixture acted as stress concentrator in attracting grain-boundary cracks.

5.5.2 Fracture growth in the 4 mm mixture

The fracture process in hollow-cylinder tests on the M4 as depicted from the micrographs shown in Figure 5.21a-d was found closely resembling that for the M2 (described above) and therefore only observed differences are outlined hereafter.
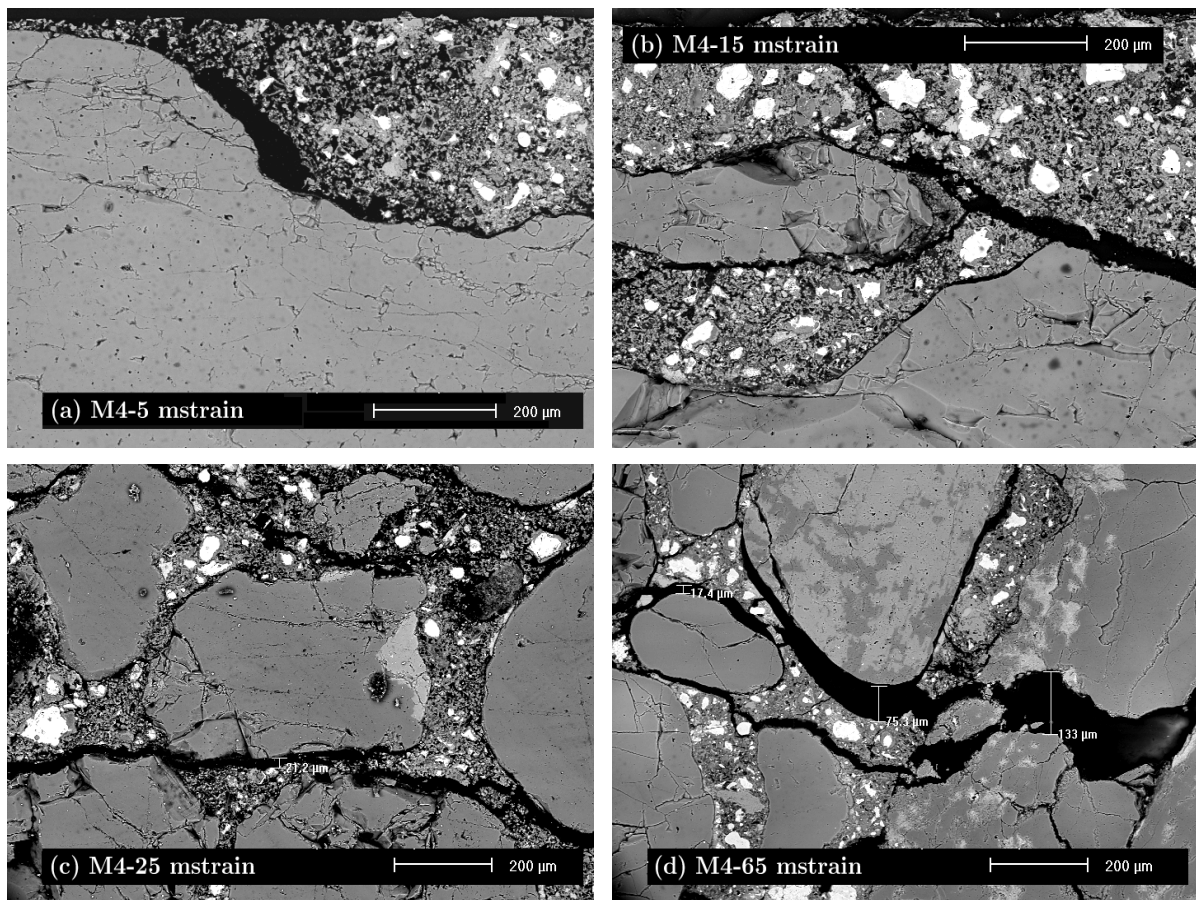
Figure 5.21: Selected photomicrographs showing sequence of failure in the M4 from C specimens at (a) 5‰ strain, (b) 15‰ strain, (c) 25‰ strain, and (d) 65‰ strain (d). Direction of applied major principal stress is horizontal and parallel to the long dimension of the images. Cracks are distinguished in the images by their black lineal shape.

At 5‰ strain, limited number of grain-boundary cracks was detected, which were generally around individual grains and mostly limited to a short length of the grain-boundary (Figure 5.21a). Cracks were observed very close to hole along grain-boundaries next to the inner-wall at typical depth 300-500 μm. The fracture process and cracking patterns observed at higher strains (15, 25, and 65‰ strain) were basically comparable to those for the M2 (steps 2-4 in 5.5.1). A difference noted during tests is that less spalling occurred in the M4, which is thought due to its larger d_{max} making complete grain detachment more difficult as compared with the M2, especially for smaller specimen sizes. Crack arrest was more pronounced in the M4 probably due to its larger grain size. In this case, hindrance of crack propagation by a 4 mm aggregate is relatively easier than with a 2 mm aggregate. Depending on the grain size, mineralogical strength, and grain position with respect to the orientation of crack propagation, cracks could propagate either inter- or intra-granularly parallel to the principal stress direction (Figure 5.21c-d).

Relevant to the aforementioned mechanisms is the direction of loading with respect to direction of casting. In compression, van Mier (1997) reported that loading parallel to casting direction shows delayed crack growth as compared with perpendicular loading since in the latter orientation of initial defects or micro-cracks is more favourable for crack propagation. Under the loading path and test setting applied in this study (for all sizes), the major (deviatoric) principal stresses were always in direction perpendicular to casting direction, which should be considered if the results are to be utilized.

5.6 SUMMARY AND CONCLUDING REMARKS

Three-dimensional size effect experiments were performed using scaled thick-walled cylinders in a range 1:4. The mixtures developed in this research, M4 and M2, were utilized in these tests. Radial deformations at the inner-wall together with axial displacements were instrumented and monitored during all tests. At least six tests per size and for each mixture were conducted to account for scatter in the results. Microscopic examinations on slices from impregnated specimens were carried out to get insight into fracture mechanisms and evolution of damage in the hollow-cylinder tests.

The shape of the stress-strain response from the recorded curves of outer pressure versus tangential strain at the inner-wall was concave up indicating the non-linear characteristic of the materials. Their constitutive behaviour could be approximated using a bilinear model with initial short stiff segment followed by a plastic-strain-hardening part to the end of tests. The kink point, at which the gesture of the curvature changes, can be approximated to correspond to outer pressures of about 7 to 10 MPa for both mixtures. This transition point could be reasonably assumed to represent the onset of failure in the tests as confirmed experimentally from the irrecoverable strains recorded near these levels and the development of micro-cracks next to the wall. The transition range, onset of failure, was remarkably observed corresponding to the average uniaxial compressive strength of the mixtures. In addition, this onset of failure was observed at $\cong 0.5\%$ strain, which is typical for quasibrittle materials under low or no confinement. However, the non-linearity and large amount of irrecoverable deformations at this point indicate a ductile behaviour.

A significant size effect was observed in the strength of the hollow-cylinders from the two mixtures. A consistent decrease of hollow-cylinder strength with size (at tangential strain of 5‰ strain) was recorded up to 32% and 44% for the M4 and M2, respectively. A scatter in the size effect results was marked for all sizes from both mixtures. A power relation could reasonably describe the observed size effect trends with an exponent of –0.19 and –0.26 for the M4 and M2, respectively. The overall strength of the M4, from the size effect trends, was higher than that of the M2 with a value comparable to the difference in their compressive strength (20-25%).

Failure around hollow cylinders of the two mixtures used was observed to initiate through small splitting, opening-mode, cracks along grain-boundaries oriented parallel to the maximum principal stress. These cracks develop firstly close to the hole and under increase of load could develop further deep in from the wall in a concentric pattern. The cracks were observed to propagate either inter- or intra-granularly parallel to the principal stress direction. Cracks were observed to preferably grow along the spring-lines of the hole; however, occasionally they turn to meet the surface of the inner-wall. Coalescence of these micro-cracks sub-parallel to the inner-wall resulted in the formation of thin slabs, which then detached and started spalling into the hole. The fracture process seemed to sequentially repeat itself with new extensional cracks of small width forming behind spall zones, which are expected to extend later on forming new slabs of spalling potential. Typical crack openings close to the hole at low outer-stress levels (8-11 MPa) were about 20 μm, which gradually increased to about 200 μm (10 folds) near end of tests (35-38 MPa).

Chapter 6

DISTINCT PARTICLE MODELLING

6.1 INTRODUCTION

This chapter is concerned with the application of the distinct element approach in modelling the size effect and fracture behaviour in hollow-cylinder tests. The numerical program PFC2D (Particle Flow Code in Two Dimensions) was utilized for this purpose. The PFC2D belongs to the class of mesoscopic discrete models, which incorporate an internal length scale in their formulation. In addition, the model offers large strain capacity and unrestricted crack formation capabilities. The procedure followed in modelling the hollow-cylinder test was similar to that followed during the experiments. Firstly, a model material is developed and calibrated for its mechanical properties using uniaxial and biaxial compression and Brazilian splitting tensile simulations. Afterwards, analyses of the hollow-cylinder test and its size dependence were performed.

In this Chapter, essentials of the PFC2D are briefly introduced followed by specimen preparation and model calibration procedures. Numerical results are presented and analysed in terms of model robustness in reproducing macro-mechanical behaviour and failure mechanisms. Experimental results from the uniaxial and biaxial compression, the Brazilian splitting tensile (Chapter 3), and the hollow-cylinder tests (Chapter 5) were used for comparing with numerical output. Thereafter, the capabilities of the model in predicting size effects in these tests are carefully investigated and discussed.

6.2   The Distinct Element Method

In the field of geomechanics and mechanics of materials, discrete particle modelling is known as the Distinct or Discrete Element Method (DEM). Development of the DEM has progressed over the last three decades after being initially presented by Cundall (1971) for analysis of rock mechanics problems and applied after to soils by Cundall and Strack (1979). Thorough description of the method could be found in e.g. Cundall (1988). In the DEM, finite displacements and rotations of discrete bodies (termed as particles) are allowed, including complete detachment, with automatic recognition of new contacts as calculation progresses.

Interaction of the particles in the DEM is treated in an explicit dynamic process. The calculations performed alternate between the application of Newton's second law to the particles and a force-displacement law at the contacts. Newton's second law gives the translational and rotational motion of the particles based on their contact forces, whereas the force-displacement law is used to update the contact forces based on the displacements. The numerical representation of the dynamic behaviour is through a time-stepping algorithm over which velocities and accelerations are assumed constant. The time step is chosen so that, during a single time step, perturbations cannot propagate from any particle further than its immediate proximity.

6.3   Material Modelling Using PFC2D

6.3.1   Theoretical background and constitutive models

The numerical program PFC2D simulates the mechanical behaviour of a system comprising a collection of rigid disks or circles referred to as particles (Itasca Consulting Group, 2003). Numerical behaviour of these particles is modelled in a fully dynamic manner based on the Distinct Element Method (§ 6.2). Motion of the particles obeys Newton's law of motion, whereas the interaction between them is defined through constitutive models associated with each contact. At a particular contact, the constitutive model consists of three parts: a contact-stiffness model, a slip and separation model, and a bonding model (contact-bond and/or parallel-bond). At the contact level (micro-scale), particles and their interaction are characterized by the following parameters:

- Geometric and physical parameters

$\tilde{R}$	Average particle radius	ρ	Particle density
ϕ	Porosity of particle assembly		

- Parameters for the constitutive contact models

k_n	Normal stiffness	T_n	Normal strength (stress units)
k_s	Shear stiffness	T_s	Shear strength (stress units)
k_n/k_s	Stiffness ratio	μ	Friction coefficient

Quasi-static analyses using PFC2D are achieved through applying a local mechanical damping procedure. In this procedure, a damping force with magnitude proportional to the unbalanced force is applied to each ball through a damping coefficient. A damping coefficient of 0.7 is used by default in the program and was used in all analyses in this study. This value was shown adequate for producing a quasi-static condition when simulating cracking and failure of brittle rocks by Hazzard *et al.*(2000). They performed uniaxial compression simulations for different material models (granite and chalk) with different damping coefficients and found that the energy released by crack events (i.e. bond breakage) may significantly influence the behaviour in the simulations. The waves emanating from cracks are capable of inducing more cracks if nearby bonds are close to failure. They also showed that the effect of these dynamically induced cracking was to decrease the compressive strength in granite models by up to 15%.

Contact-stiffness model

The contact-stiffness model describes the elastic force-displacement relation of the contact either linearly or nonlinearly (Hertz-Mindlin model). The normal and shear stiffness assigned at each contact (particle-particle or particle-wall) relate the normal and shear components of force to their corresponding relative displacements. In the linear model, forces and relative displacements are linearly related by a constant contact stiffness at each contact, which is expressed as:

$$F_n^i = k_n U_n^i n_i' \tag{6.1}$$

$$\triangle F_s^i = k_s \triangle U_s^i \tag{6.2}$$

where F_n^i and F_s^i are the normal and shear component of the contact force, U_n^i and U_s^i are the relative displacements between the contacting bodies in normal and shear directions, respectively. The force-displacement law operates at a contact and can be described in terms of a contact point lying on a contact plane that is defined by a unit normal vector n_i'. The contact point is within the overlap volume of the two entities. For particle-particle contact, the normal vector is directed along the line between particle centres and for particle-wall contact, the normal vector is directed along the line defining the shortest distance between the particle centre and the wall. Contact between a particle with the linear model and a particle with the Hertz model is not allowed, since the behaviour is undefined. Also, since the Hertz model is not defined for tensile forces, it is incompatible with any type of bonding and therefore cannot be used for modelling cohesive materials. Throughout this study, the linear contact-stiffness model is applied.

Slip and separation model

The slip model allows sliding at the contact level (particle-particle or particle-wall) and separation if no contact-bond exists. Slip occurs when the shear component of force F_s reaches the maximum allowable shear contact force (F_s^{max}), which is the product of multiplying the minimum friction coefficient of the two contacting bodies μ by the
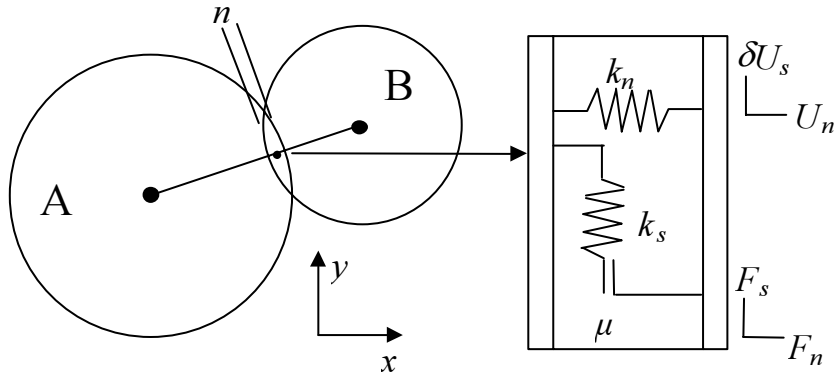
Figure 6.1: Schematic of two particles at contact (overlapping) with their associated linear contact-stiffness and slip models at the contact point.

compressive normal component of force F_n. The slip condition enforces no-tension criterion by checking whether the contact overlap n is less than or equal to zero. The overlap distance n (shown in Figure 6.1) describes the normal displacement between two contacting bodies following the *soft contact approach* employed in PFC2D where deformations between contacting bodies are represented by small overlaps over vanishing small contact areas, i.e. a point. The slip criterion could be expressed as

$$F_s^{\mathrm{max}} = \mu \left| F_n^i \right| \tag{6.3}$$

if $\left| F_s^i \right| > F_s^{\mathrm{max}}$, then slip is to occur and

$$\text{if } n \leq 0, \text{ then } F_n^i = 0 \text{ and } F_s^i = 0 \tag{6.4}$$

Contact-bond model

In order to simulate the behaviour of cohesive-granular materials such as concrete and rock, a bonding model simulating the adhesion between the particles is required. In PFC2D, two basic bonding models are supported: a contact-bond model and a parallel-bond model. The contact-bond acts only at the contact point between two particles, whereas the parallel-bond assumes particle contact over a finite-size area positioned between the particles. In this study, the contact-bond model is used and is described hereafter. A detailed description of the parallel-bond model can be found in the documentation of PFC2D (Itasca Consulting Group, 2003).

The contact-bond model can be envisaged as a pair of elastic springs of specified constant normal and shear stiffness and specified normal and shear strengths (see Figure 6.1). Contact-bonds allow tensile forces to develop at a contact when $n<0$, while precluding the slip possibility unless failed in shear. The failure criterion for the contact bond can be expressed as:

$$F_n^i = 0 \,\&\, F_s^i = 0 \qquad \text{if } F_n^i \geq T_n \tag{6.5}$$

$$\left|F_s^i\right| = \mu \left|F_n^i\right| \qquad \text{if } F_s^i \geq T_s \qquad (6.6)$$

Breakage of a contact-bond occurs when either the normal or shear component of the contact force exceeds its corresponding contact-bond strength. If breakage takes place in shear, the contact forces are not altered and the residual shear contact force obeys a frictional law characterized by μ and the normal compressive force F_n. If new contacts are created after breakage of contact-bonds, then the slip model only is activated at those contacts. In other words, at each particle-particle contact point either the slip model or the contact-bond model is active at any given time during calculation.

Calculation cycle

The calculation cycle in PFC2D consists of the repeated application of the law of motion to each particle, a force-displacement law to each contact with a constant updating of boundary (walls or string of particles) positions. At the start of each time step, all contacts are updated from the known particle and wall positions. Then, the force-displacement law is applied to each contact to update the contact forces based on the relative motion of the two contacting bodies (particle-particle or particle-wall) and the applied contact constitutive model. Next, the law of motion is applied to each particle to update its position and velocity according to the contact forces and/or any body forces (Itasca Consulting Group, 2003).

Assumptions and justification of use

The analysis performed in this study using PFC2D involved three simplifications with regard to simulating the structure and behaviour of concrete-like materials. Firstly, two-dimensional simulations were considered instead of three-dimensional. This is for the high computational demand of three-dimensional simulations, especially for size effect analyses. Besides, two-dimensional modelling provides more insight into mechanisms and obtained results because of its relatively straightforward visualization features.

Secondly, a simplification is made to the shape of the aggregate grains, which are considered as circles or cylinders in this study. Actual grains are much more complex and their description involves intricate geometrical shapes that could lead to substantial increase in computational cost and efficiency. A characteristic for circular grains as compared with more complex shapes is their ability to roll easier (Baars, 1996), which will not probably cause deviations in this analysis since cemented grains could barely roll.

The third simplification is in the description of contact behaviour between grains, which is expressed in the model through a contact point or small contact area that are defined through simple constitutive models. In discrete modelling of concrete on microscopic and mesoscopic levels, the structure could be best described as two-phase composite or possibly more detailed as three-phase composite to distinguish between the aggregate grains, the mortar matrix, and possibly the ITZ (Vonk, 1993; Van Vliet and Van Mier, 2000). For this, a circular grain shape does not suffice and extra material parameters and constitutive relations should be defined to describe the additional material phases and their behaviour. Applying this to the analysis of the hollow-cylinder problem and its size dependence is not straightforward and would require huge computational capacity. This is

seeing that it is considered important to include the complete hollow-cylinder geometry in the simulations for its structural contribution to the fracture and size effect behaviour in hollow-cylinder tests. Considering this for size effect analysis with size range as in the experiments and that could be extended beyond this range would accordingly be computationally very demanding.

The assumptions and simplifications discussed above would inevitably lead to some discrepancies between experimental measurements and model results and would therefore affect the model prediction capabilities. However, it has been shown that much of the characteristics from these materials could be reproduced with reasonable success using PFC2D type approach in DEM analyses (e.g. Baars, 1996; Hazzard *et al.*, 2000; Potyondy and Cundall, 2004). This is to consider the particle system in the PFC as an independent system in its own right, which is capable of simulating the behaviour of the more complex material systems with a rather satisfactory analogy. The following excerpt from the PFC2D manual regarding numerical modelling should be considered as well, "It should be borne in mind, however, that it is impossible to fully verify and validate any numerical model of a natural system, as discussed by Oreskes et al. (1994). A model is an unprovable representation, useful for such things as: 1) corroborating hypotheses; 2) elucidating discrepancies in other models; 3) performing sensitivity analyses to determine which aspects of a system need more study and what additional data is needed; 4) supporting design decisions; and 5) guiding further study. However, if confirming observations agree with a model's predictions, the likelihood that the model is correct increases and thus warrants acceptance". With this in mind, the following modelling is conducted.

6.3.2   Preparation of model specimen

In order to simulate disordered granular materials such as rock or concrete using PFC2D, irregular particle assemblies are generated and packed. Preparing a well-connected, densely packed irregular assembly is the key to a successful simulation and is by no means an easy task compared with the discretization procedure in finite element or finite difference modelling (Huang, 1999). In this study, assemblies of arbitrary particle (disks of unit thickness) packing are generated using a radius expansion algorithm offered in PFC2D. The objective of it is to fill the given space with particles of a given radii at given porosity and ensure their equilibrium.

Particle generation is accomplished using a random particle generator that places a specified number of non-overlapping particles at random coordinate locations in a given space. The particles are placed at smaller particle radii than their final values to facilitate their placing. They are expanded afterwards in a trial and error manner till the desired porosity is obtained. The number of particles is determined using the prescribed porosity and particle size distribution. At this level, no bonding between the particles exists and low friction is specified (μ=0.05-0.10) to enable packing of the assembly at a reasonable number of time steps. The prescribed porosity value affects both the packing of the assembly and initial mean stress. A value in the range 15% to 18% is recommended and found to produce an assembly with relatively small initial mean stress ($\leq 10\%$ f_c) and good packing density in PFC2D (Huang, 1999; Itasca Consulting Group, 2003). A prescribed porosity of 16% is used in all simulations in this study.

After the initial assembly is generated and packed, hydrostatic compaction using controlled boundary conditions is employed to obtain a dense state. Then a friction coefficient is applied to all particle contacts and the assembly is equilibrated under a specified isotropic stress. It should be noted, however, that it is impossible to create an irregular assembly with a simultaneous specified porosity and specified initial stress. The initial stresses in an assembly are partly inherited from the generation and compaction phases. A specified isotropic stress is typically set at low value relative to the material strength. The radii of all particles are changed uniformly to achieve the specified isotropic stress defined as the mean of two direct stresses. This is to reduce the magnitude of the locked-in stresses that will develop after the subsequent bond-installation, since the magnitude of the locked-in forces (both tensile and compressive) will be comparable to the value of the compressive forces at the time of bond installation (Itasca Consulting Group, 2003).

In order to ensure having a well-connected assembly, a procedure to eliminate the so-called *floaters* (particles with fewer or zero contacts) is applied. The floater algorithm expands and moves floaters until every particle has a specified minimum number of contacts. In this process, all particles except floaters are fixed and given zero velocities. Floaters are then expanded by a large amount (30%), sufficient to ensure contact with all of their immediate neighbours. After being cycled to local equilibrium, the floaters are contracted by an amount that is calculated to reduce their mean contact normal force below a target force (one-tenth of the mean contact normal force for the assembly). If the mean contact normal force for a particle is below the target force, then it is declared *inactive* and is not contracted further at this stage. The contraction step is applied repeatedly until all floaters become inactive. The complete procedure is repeated until all floaters have been removed. In this study, the minimum number of contacts set during the floater procedure is three. The assembly is now ready for test simulation.

6.3.3   Calibration of the model

To create a PFC2D synthetic material that simulates the mechanical behaviour of our concrete, numerical calibration was necessary. Calibration is the term used to describe an iterative procedure of determining and modifying the micro-mechanical parameters for a PFC2D model. The micro-mechanical parameters are those that govern the particle contact and bonding properties and cannot be determined directly from laboratory tests. The material properties determined from laboratory tests on the other hand are termed macro-mechanical parameters in this process.

Several researchers attempted to establish micro-macro relations, e.g. Bathurst and Rothenburg (1992); Potyondy and Cundall (1999), but no complete theory yet exists. During calibration, responses of the model are compared to those of laboratory samples and the micro-parameters are iteratively modified to achieve good agreement with their corresponding macro-parameters of the material. This inverse procedure adapts a trial and error method to try relating these two sets of parameters for irregular bonded-assemblies. In this analysis, the macro-parameters in the calibration simulations were the Young's modulus E and the uniaxial compressive strength f_c from uniaxial compression tests. In addition, fracture patterns and crack behaviour from Brazilian splitting tests were incorporated as well.
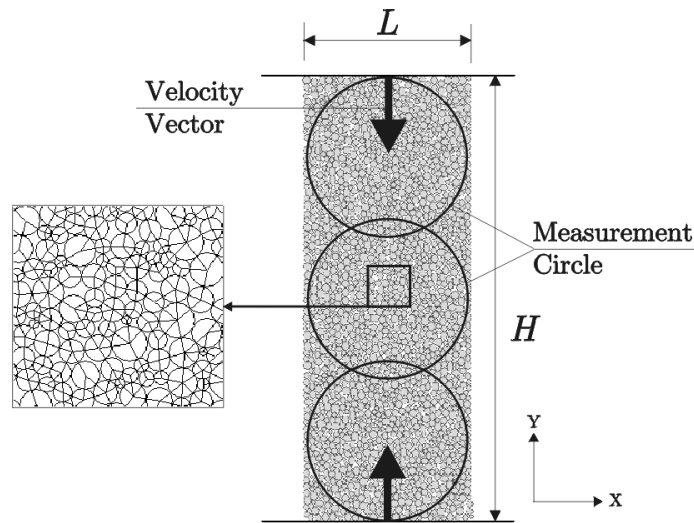
Figure 6.2: PFC2D model used in uniaxial compression simulations with direction of applied velocities (stress) and zoom-in that shows the connectivity between the discs.

For calibration purposes, a rectangular disk assembly of width L and length H was used in the uniaxial compression simulations (Figure 6.2). Ratios of $H/L=2.50$ and $L/\tilde{R}=38$ were used, where $\tilde{R}$ is the average particle radius. The radii R ranged from 0.33 mm to 0.66 mm according to a normal particle-size distribution. This irregular assembly contained about 1000 bonded particles contacting at $\cong 1700$ contact points. Four walls bounded the assembly during the specimen preparation process. Afterwards and during testing, the lateral walls were removed and the top and bottom walls acted as loading platens with their velocities being servo-controlled by a servomechanism that maintains a specified strain rate similar to laboratory experiments. The normal stiffness of the top and bottom walls were set equal to 1.1 times the average normal stiffness of the assembly to ensure that the particle-wall overlap remains small. If too much overlap occurs, the model could become unstable. On the other hand, excessively stiff walls will be too sensitive to small particle displacements. Stresses and strains were computed based on the forces acting up on the walls and the relative positions of the walls. In addition, measurement circles distributed inside the specimens (Figure 6.2) were used for calculating average stress and strain values. Each measurement circle can be used to measure quantities such as porosity, average stress, and strain rate. The size and location of a measurement circle is freely chosen.

In addition to the uniaxial compression simulations, Brazilian splitting test simulations were carried out. The Brazilian test was performed using a cylindrical specimen, which was trimmed from the same rectangular particle assembly used in uniaxial compression test simulations. The diameter of a Brazilian specimen is equal to the width of the uniaxial specimen and therefore, for simplicity, the term L will be used for both hereafter. The specimen genesis procedure is the same for both simulations as was the case with laboratory tests since samples for Brazilian and uniaxial compression laboratory tests were prepared from the same batch (Chapter 3). In the laboratory, however, particle packing is not the same for the Brazilian and compression tests as performed in PFC2D.

The results of these simulations were used for confirming the calibration process in terms of crack pattern and fracture behaviour. This due to the fact that the fracture process in a Brazilian test is relatively well understood and predictable when compared with that in a uniaxial compression test. Generally, experimental observations for concrete materials indicate that cracks initiate in the centre of specimens and then extend towards their ends parallel to the loading direction (Lilliu and Van Mier, 1999).

As an input for the numerical simulations with the contact-bond model, five micro-parameters are needed; namely, k_n, k_s, T_n, T_s, and μ. The effect of these parameters is studied individually in addition to the influence of some of their dimensionless combinations. Their effect is evaluated as part of the calibration process before arriving at a set of micro-parameters that is able to replicate (in a best-fit sense) our test concrete. The results of this parameter study are discussed in the next section. After several trial simulations using both the uniaxial compression and Brazilian splitting assemblies, a best-fit PFC2D material was created with mechanical behaviour comparable to that from laboratory tests. The calibrated micro-mechanical parameters are listed in Table 6.1.

Table 6.1: PFC2D micro-parameters used for calibration

Parameter	value
k_n (GPa)	11.5
k_n/k_s	3.00
T_n (MPa)	5.00
T_s/T_n	3.00
μ	0.80

In Table 6.2, results from the calibration procedure are presented in terms of f_c and E as obtained from both the PFC2D simulations and laboratory experiments.

Table 6.2: Comparison of calibration results with laboratory values

Parameter	PFC2D	Laboratory
f_c (MPa)	9.20	9.10
E (GPa)	7.30	7.70

In Figure 6.3, the assembly and fracture pattern form a calibrated Brazilian simulation is given. The resemblance of the fracture pattern from the simulation with that from laboratory test (shown in the figure) is evident. In Figure 6.4, the test assembly and fracture pattern from a uniaxial compressive simulation are shown. The cracks obtained in the uniaxial simulations are all bond cracks, which follow from the contact tensile strength being exceeded. The majority of those cracks are oriented in a nearly vertical direction parallel to the maximum principal stress as was observed experimentally. A typical axial stress versus axial strain curve from the uniaxial compression simulations is shown in Figure 6.5. The stress-strain curve shows the characteristic damage initiation at about 0.4 of the peak strength and rapid increase in crack density during strain softening.
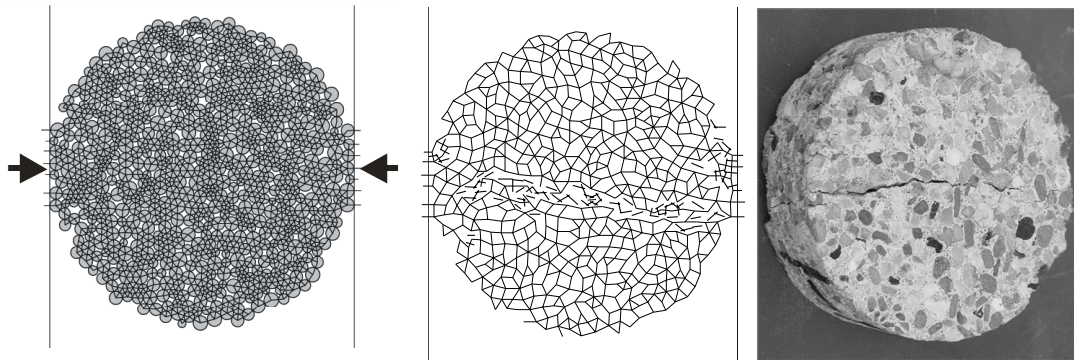
Figure 6.3: Brazilian test assembly with (left) particle configuration and contacts, (middle) contacts and fracture pattern, and (right) fractured specimen from Brazilian laboratory test.
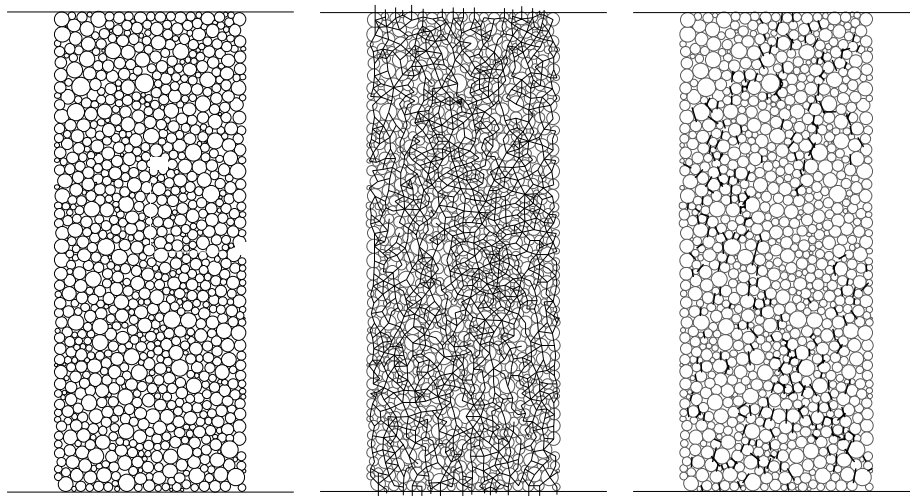
Figure 6.4: Uniaxial compression test assembly with (left) particle configuration, (middle) particles and contacts network, and (right) particles and fracture pattern.
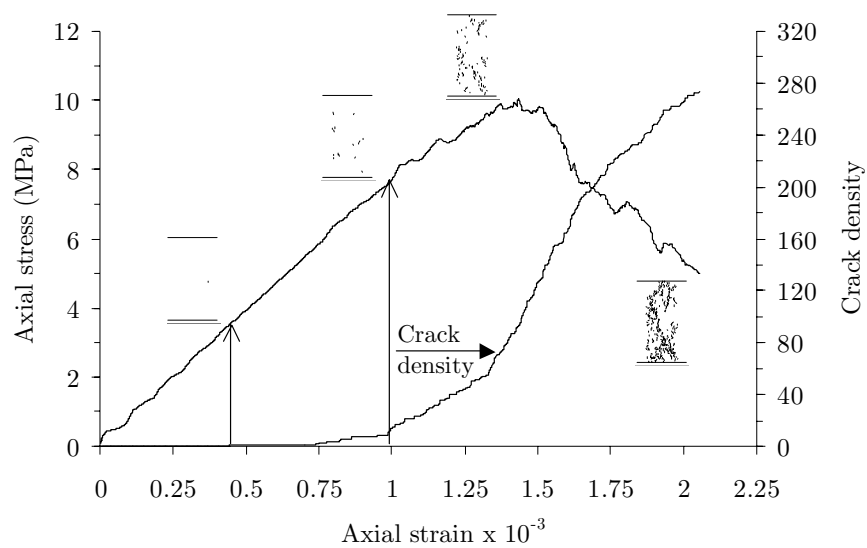
Figure 6.5: Axial stress-strain response from PFC2D simulation. Shown as well are the accumulation of crack density with stress and the development of damage in terms of fracture patterns.

6.3.4 Model micro-parameter study

Huang (1999), using a dimensionless analysis has shown that in contact-bonded models, the scaled ratios k_n/k_s and T_s/T_n are dominant parameters in the procedure, whereas μ is of minor importance. Figure 6.6a shows the calibration curves for the effect of particle stiffness ratio k_n/k_s on E and f_c values for the calibrated particle assembly. The trend in the curves is approximately a descending power relation for E and a linear relation for f_c. Similarly, Figure 6.6b shows the curves for the effect of particle strength ratio T_s/T_n on E and f_c values. Both E and f_c showed an initial dependence on the strength ratio up to a certain threshold, i.e. T_s/T_n=1.0 and 2.0 for E and f_c, respectively, followed by a horizontal plateau. Unlike the stiffness ratio, the strength ratio had a clear influence on the failure mode and crack pattern. For values smaller than 1.0, the failure mode was dominantly shear. In the range 1.0 to 2.0, mixed tensile and shear failures were observed and for values larger than 2.0, tensile failure prevailed. This is following the convention that if a bond's shear strength is exceeded, then the crack will be called a shear crack and when the bond's normal strength is exceeded, a tensile crack is the result.

Another important parameter during specimen preparation is the value of the initial isotropic stress. As mentioned above, it is recommended to specify a low value for this initial stress relative to the material strength. This is to reduce the magnitude of the locked-in stresses that develop after the subsequent bond-installation. The calibrated particle assembly was used to examine the effect of initial isotropic stress on the values of E and f_c and for initial stresses of 0.1, 0.5, 1.0, 5.0, and 10.0 MPa. These stresses correspond to 1, 5, 10, 50, and 100% of the f_c of the assembly (see Table 6.2). The results of this calibration analysis are given in Figure 6.7, which show a minor effect for stress levels below 1.0 MPa (10% of the specimen's compressive strength) followed by a rapid decrease for both the E and f_c values. Therefore, the results suggest a minor influence for initial stress that is $\leq 10\%$ of the assembly's compressive strength. The value of the initial stress did not affect the failure mode or failure sequence in the simulations. In this study, an initial isotropic stress of 1 MPa ($\cong$10% of the material's compressive strength) was used throughout the analyses.

(a)   (b)
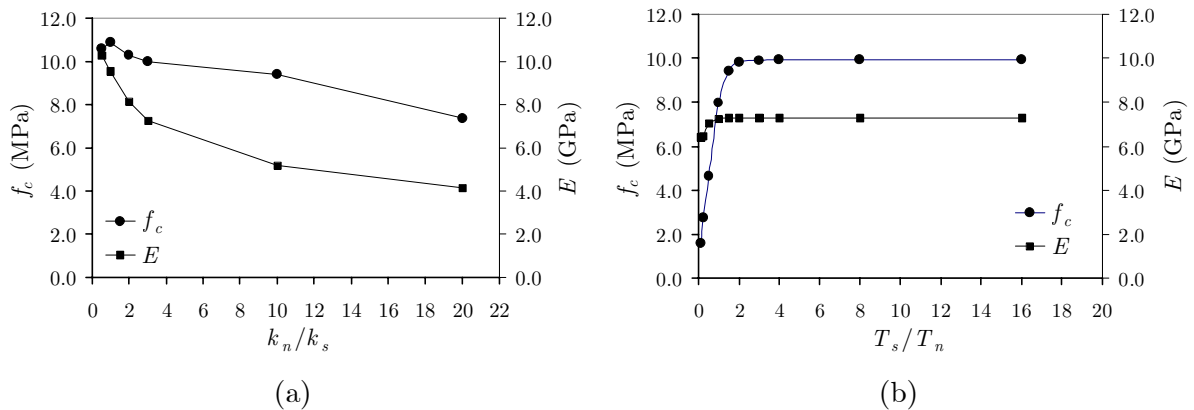
Figure 6.6: Variation of uniaxial compressive strength f_c and Young's modulus E with (a) the contact stiffness ratio k_n/k_s and (b) the contact strength ratio T_s/T_n for the bonded assembly used in the calibration simulations.
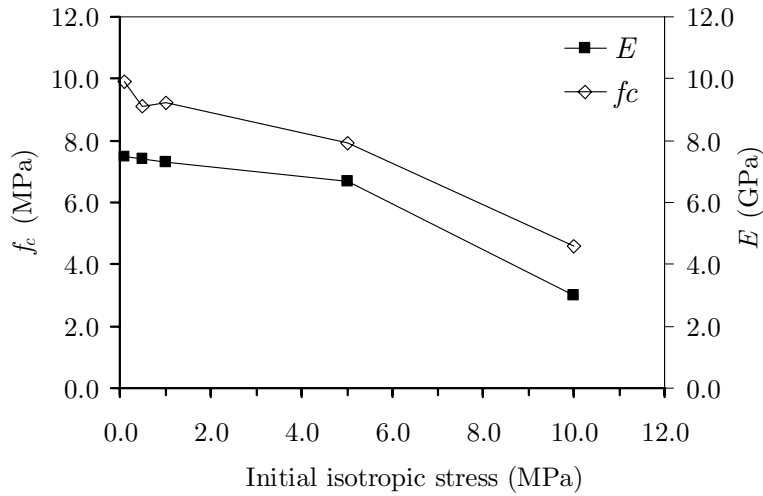
Figure 6.7: Variation of uniaxial compressive strength f_c and Young's modulus E with the initial isotropic stress.
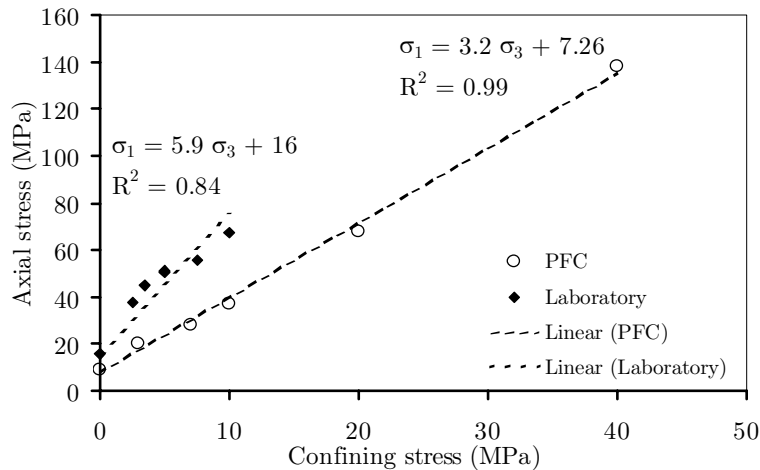
Figure 6.8: Biaxial strength envelope from PFC simulations using calibrated configuration and from the triaxial laboratory tests for the M4.

Before simulating the hollow-cylinder test, it is worthy to analyze the biaxial behaviour of the calibrated PFC2D assembly. This is the stress state that exists in the 2D hollow-cylinder simulations to be considered. A series of biaxial compression simulations was performed using the calibrated configuration. First, the particle assembly was isotropically compressed to a predefined confining pressure. Then, the lateral confinement was maintained constant whereas the vertical axial compression continued to increase monotonically. Confining pressures of 3, 7, 10, 20, and 40 MPa were used in these simulations.

Figure 6.8 plots the failure envelope from the biaxial compression simulations in the $\sigma_1 - \sigma_3$ plane. A linear Mohr-Coulomb failure criterion is fitted to the failure envelope. The friction angle φ evaluated from the failure criterion was around 25°. This value is much less than the value obtained form laboratory experiments of 45° (Chapter 3), which is also shown in Figure 6.8. The biaxial simulations, therefore, underestimate the

internal friction angle and consequently could miscalculate or underpredict the biaxial strength. In addition, the failure envelope for the PFC2D simulations is best fitted using a linear criterion, whereas the experimental envelope showed a rather nonlinear response. Potyondy and Cundall (1999), investigated the factors influencing the biaxial strength envelope produced by PFC2D and conclude that the bond-strength ratio T_s/T_n is most important. They observe essentially a linear envelope with a slope that increases with increasing the strength ratio. Other factors they investigated such as particle clusters, and type of bond (parallel-bond instead of contact bond) did not show an effect on the envelope. In the simulations above, a bond-strength ratio of 3.0 was used, which was shown (Figure 6.6b) to deliver minimal effect on the strength and stiffness of the model.

6.4 ANALYSIS OF HOLLOW-CYLINDER TEST

In order to model the hollow-cylinder geometry, the option of general walls, which is introduced in PFC2D-V.3.0 and later, was utilized. This enables full circular or arc walls to be created, but does not, however, support force or velocity applications for full circles. This is due to the fact that wall velocities in PFC2D are defined in a Cartesian coordinate system and could be applied in $\pm x,y$ directions only. This also applies to the built-in data acquisition and servomechanism algorithms for walls, which are all configured for straight walls and Cartesian coordinate system.

6.4.1 Geometry and loading procedure

The external and internal wall boundaries consisted of 4 arcs each representing a quadrant from a closed circle (Figure 6.9). The external 4 arcs (1-4) serve as an outer boundary for creating the assembly and for loading it during testing. Initially, a particle assembly is generated between the two sets of internal and external walls and then isotropically compacted. Next, initial stresses are installed, floaters are removed, and finally the assembly is bonded using contact-bonds and being prepared for analysis. In PFC2D, forces could not be applied to walls, but velocities could be specified that drive the walls in a certain direction while monitoring their reaction forces. This procedure was followed here for simulating the pressures applied on the outer cylinder walls.

For performing a hollow-cylinder simulation, the internal walls were removed and load was applied at the external walls. Loading was applied by moving the external walls at a constant prescribed velocity, which ensures a quasi-static test to be simulated. Each wall (arc) moved under two equal and constant velocities in the x,y directions (Figure 6.9) so that their resultant velocity vector was directed to the centre of the assembly. Equal Movement of the walls exerted forces on the particles and built up a symmetric radial pressure that replicates the pressure applied in laboratory experiments. While loading, reaction forces on the external walls and the radial displacement between sets of prescribed particle gauges on opposite sides around the inner-hole were monitored. These data were used further in calculating and plotting stress-strain responses.
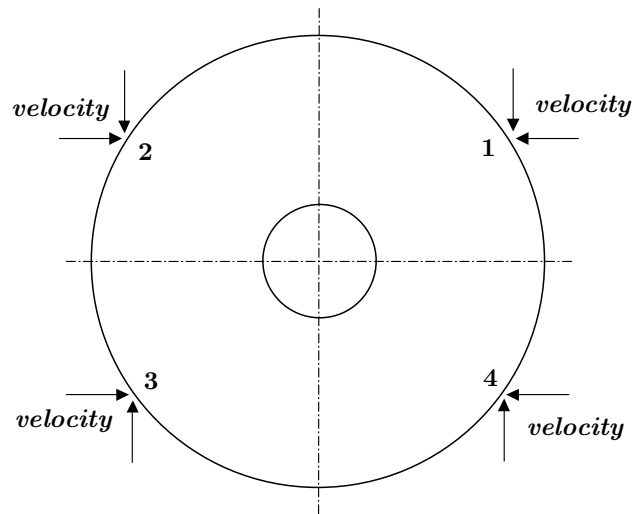
Figure 6.9: Schematic representation of the PFC2D model used in hollow-cylinder simulations.

6.4.2   Simulation of the hollow-cylinder test

Numerical calibration of the hollow-cylinder test was performed using an assembly of 875 particles (discs), D_o=50 mm, D_i=12.5 mm, R_{min}=0.50 mm, and R_{max}/R_{min}=2.00. This assembly simulates a hollow-cylinder specimen of size A. The ratio between the cylinder's wall-thickness to average particle size $W/\tilde{R}$ was 25. Initially, the hollow-cylinder simulation was performed using the calibrated material in § 6.3.3 and with the micro-parameters listed in Table 6.1. The result of such analysis produced a dissimilar crack pattern when compared with those observed in the laboratory (Figure 6.10a). A rather diffuse crack pattern with mainly shear cracks was produced, which is different from the phenomena seen in experiments (§ 5.4 and Figure 5.17). The deformation behaviour, however, was comparable to experiments from a hollow-cylinder test size A, in terms of strain values, but the behaviour of the model was somewhat linear (Figure 6.10b).

(a)   (b)
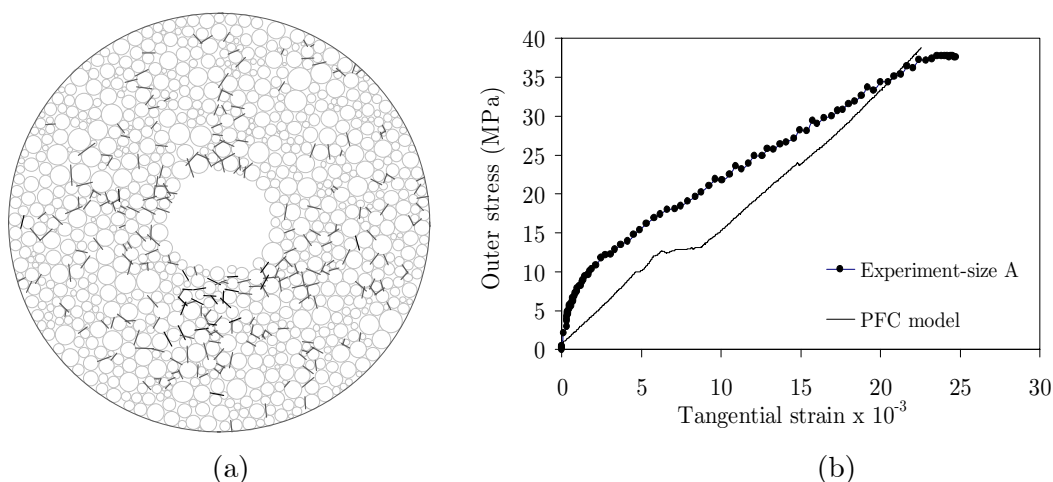
Figure 6.10: (a) Damage pattern from simulated hollow-cylinder test at 2.3% tangential strain and (b) stress-strain response from both simulation and laboratory experiment on size A.

Accordingly a separate calibration process was invoked for the cylinder test with the calibration macro-parameter being the experimental tangential strain ε_θ at the inner-hole. Additionally, the crack pattern and fracture behaviour observed in experiments was used to judge the objectivity of the calibration process. After several simulations, a set of parameters was obtained that could comparably simulate the deformation and failure behaviour as in the experiments (see Figure 6.11). The final set of micro-parameters is presented in Table 6.3. The main improvement appeared in the crack pattern as the strain and stiffness values were not much affected.

Table 6.3: Calibrated parameters for hollow-cylinder simulations

Parameter	PFC2D
k_n (GPa)	11.0
k_n/k_s	2.00
T_n (MPa)	15.0
T_s/T_n	2.00
μ	0.80

Comparing the values in Table 6.1 and Table 6.3, it is seen that mainly the strength value was modified with a factor of three stronger in the calibrated cylinder model. Accordingly, it seems that calibrating on simpler test configurations, i.e. uniaxial and biaxial compression tests, and using the corresponding parameters on more complex configurations such as the cylinder test might be misleading with regard to fracture behaviour. It is therefore recommended to include fracture mechanisms and crack patterns in the calibration procedure. The extra strength needed in calibrating the cylinder model could be partly explained through the commonly observed strengthening phenomena during hollow-cylinder experiments. This phenomenon, known as abnormal stability, is a state where no sign of distress is observed although the level of straining has exceeded the predicted capacity of the tested material. Guenot (1987), summarizes test results, mainly on rock, where the ratio between the actual load at failure and the theoretical load, based on elastic limit models, was between 1.5 and 4 with extremes as high as 8.

As mentioned above, the stress-strain behaviour of the PFC2D model is somewhat linear and could not reproduce the nonlinearity seen in the experiments. The experimental curve could be practically approximated by a bi-linear relation with two different stiffness and deformation rate values (§ 5.3.1). In the experiments, a kink was observed for all sizes in all performed tests within the range 8 to 13 MPa. The model inability to clearly represent this bilinear behaviour could be tentatively explained through the absence of a cementitious-matrix phase in the numerical material. It is hypothesized that in the experiments, initial deformation and compaction of the porous paste, prior to crack initiation, is a non-linear process responsible for the nonlinearity and kinking observed. In addition, the use of a linear contact-stiffness model, which states the relation between forces and contact deformation, is possibly an additional factor. Diederichs *et al.* (2004), owes the linearity in PFC2D to inability of cracks to propagate more than an additional particle diameter and it is therefore necessary for a critical crack density to be reached for nonlinearity to arise.

| (a) | (b) |
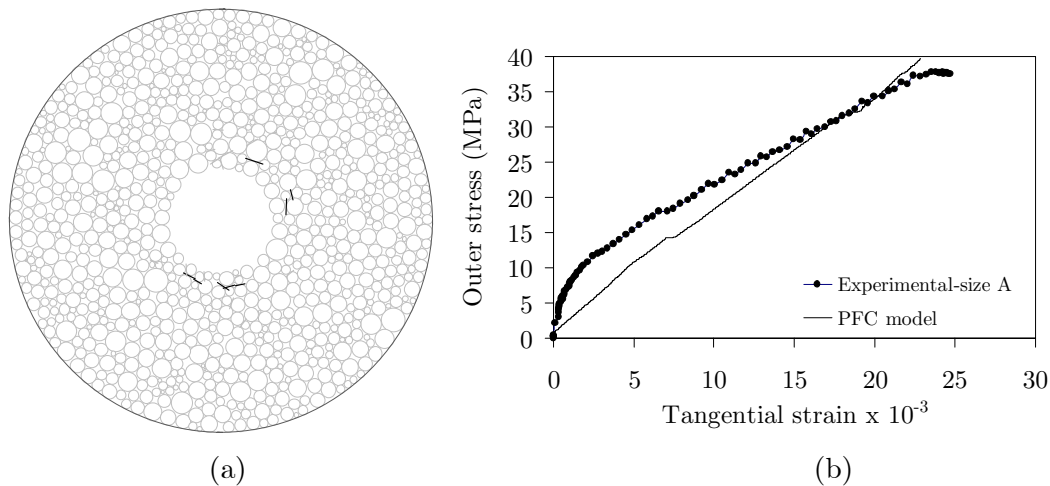
Figure 6.11: (a) Damage pattern from simulated hollow-cylinder test after re-calibration at 2.3% tangential strain ε_θ and (b) stress-strain response from both simulation and laboratory experiment on size A.

A comparison of damage patterns between the improved cylinder model and that from an impregnated laboratory specimen is presented in Figure 6.12, which shows comparable crack patterns. The model in Figure 6.12 consisted of 4451 particles and utilized the same micro-parameters listed in Table 6.3, while the impregnated laboratory specimen is from a specimen size B. In the model, tensile cracks initiated parallel to the inner wall and developed further inwards under increasing stress. This simulates the failure mechanism observed in laboratory experiments and discussed earlier in Chapter 5. Both damage patterns from the simulation and experiment are obtained at a tangential strain level of 3.5%. In the simulation, crack initiation took place at a tangential strain of $\cong 0.50\%$ that was equivalent to about 10 MPa. In the tests, few micro boundary cracks where observed in the ESEM, but their exact initiation levels were not determined.

| (a) | (b) |
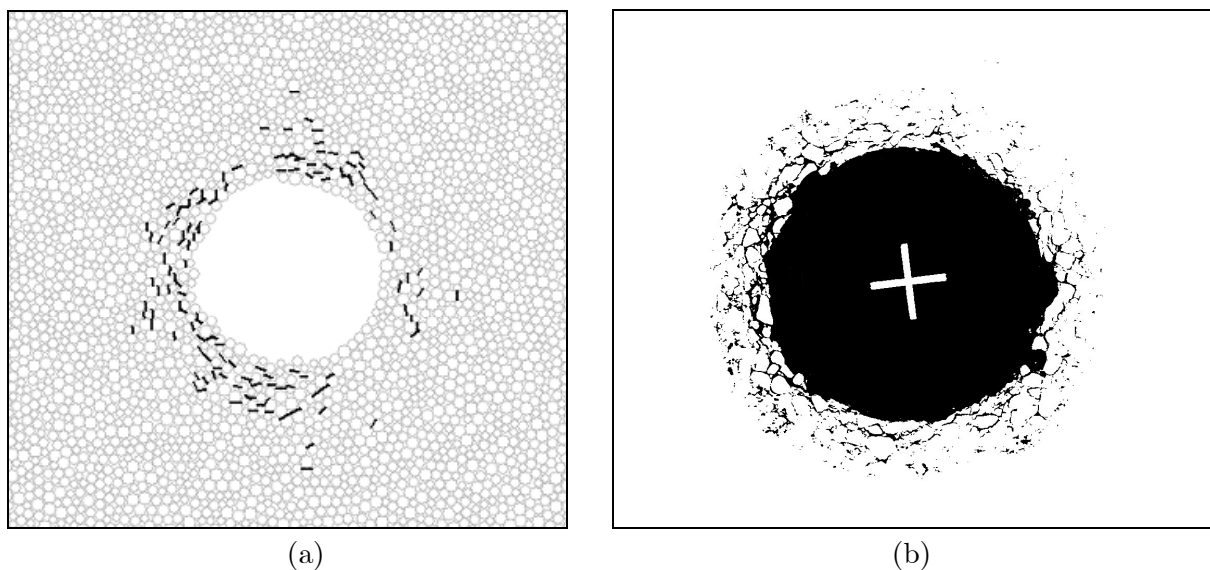
Figure 6.12: (a) Crack pattern from PFC2D simulation and at 3.5% tangential strain ε_θ and (b) damage zone and filtered fracture pattern from hollow-cylinder experiment on size B at 3.5% tangential strain ε_θ.

6.5 SCALING AND SIZE EFFECT IN PFC2D
6.5.1 Introduction and analysis approach

After the PFC2D model has shown reasonable success in simulating fracture processes taking place in the hollow-cylinder test, its ability to capture observed size effects was investigated. Generally, in PFC2D, the particle size is seen as a discretization length indicative of the model resolution. Linear scaling relations for elastic properties and contact strength (with stress units) are implemented in the augmented Fish formulation in order to make its response independent of particle size (Hazzard *et al.*, 2000; Itasca Consulting Group, 2003; Cundall and Carranza-Torres, 2004). The strength scaling relation applied in PFC2D, at each contact, for a model of unit thickness is:

$$F_{n,s} \propto \tilde{R} * T_{n,s} \tag{6.7}$$

According to (6.7), the particle size could in principle be chosen freely as long as the model contains a sufficient number of particles for being representative. This was shown, however, not to be always the case as discussed next. Results from the simulations presented hereafter showed the PFC2D model as particle size dependent with respect to f_c, f_{spl}, and f_{2c} (1 MPa confining pressure). Similar results are observed by Potyondy and Cundall (2004) for particle size dependence in PFC2D with respect to f_{spl}, but they report no obvious trend for E, f_c, and f_{2c}. They suggest that if failure mechanisms involve processes similar to those in a Brazilian test (extensile failure), an additional parameter should then be included in the calibration procedure such as fracture toughness. In their simulations, however, parallel-bonds are used and not the contact-bond model. Their results also suggest no particle size dependence for the elastic constants E and ν.

To further recognize the suitability of PFC2D models in studying size effects, a series of simulations were performed for uniaxial compression, Brazilian splitting tensile, and hollow-cylinder tests. Two types of simulations were carried out (except for the hollow-cylinder analysis), firstly, a series was performed using geometrically self-similar models and different values for $\tilde{R}$, namely: 1.00, 0.50, 0.25, 0.125, and 0.0625 mm (termed hereafter as *particle scaling*). Secondly, simulations were conducted while keeping $\tilde{R}$ constant and scaling the geometry instead (termed hereafter as *geometry scaling*). For comparison, the ratio $L / \tilde{R}$ in both series was taken the same for the different sizes, namely: 11.36, 22.7, 45.4, 90.9, and 181.8. Additionally, biaxial compression simulations under 1.0 MPa confinement were conducted for size effect using the geometry scaling approach.

For each of the series mentioned above, five rectangular assemblies were prepared in a size range 1:16 and with H/L=2.50. For each size, five different samples were produced with different packing arrangement through varying the seed for the random number-generator in the material genesis procedure. This is to include both packing and strength heterogeneities in the analyses. Each sample was subjected to uniaxial compression and Brazilian splitting loading under displacement control mode. The smallest specimen with $L / \tilde{R}$=11.36 consisted of 86 particles, whereas the largest specimen with $L / \tilde{R}$=181.8 consisted of 22097 particles. The simulation procedure for uniaxial compression and Brazilian tests was the same followed in calibration analysis, which utilizes the built-in algorithms for performing these tests in the augmented Fish tank of PFC2D-V.3.0.

6.5.2   Simulation of size effect in uniaxial compression and Brazilian tests

In Figure 6.13, a bi-logarithmic plot is given of the peak strength values f_c and f_{spl} versus specimen size from both series. As illustrated in the figure, size effect trends in PFC2D for f_c and f_{spl} are alike for the same $L/\tilde{R}$ ratio regardless to the scaling procedure applied (particle or geometry scaling). The compressive strength showed an increasing trend with size, whereas the splitting strength showed a decreasing trend. The analysis of these responses is subsequently discussed further.

Accordingly, PFC2D models with typical $L/\tilde{R}$ values will have the same strength (compressive or tensile) except from slight scatter due to heterogeneity effects. This means that size effect analysis using PFC should consider the discretization parameter $L/\tilde{R}$ for its influence on the analysis output. Additionally, the result implies that the scaling relation in (6.7) does not suffice to make the model particle size independent and that other parameters should be incorporated in the dimensionless analysis. Potyondy and Cundall (2004), report similar observations from their Brazilian test simulations, which they termed dual-model similarity, and put forward a scaling relation for the Brazilian splitting-tensile strength in the form:

$$f_{spl} \propto \bar{T}_{n,s}\sqrt{\frac{\tilde{R}}{L}} \tag{6.8}$$

where $\bar{T}_{n,s}$ is the mean bond strength. This relation incorporates the parameter $L/\tilde{R}$ as a scaling factor. Based on the results above (Figure 6.13), for analysis of compressive strength in PFC2D, a relation similar to that in (6.8) could be adapted as well and may supplement the scaling relation in (6.7). Such relation could hold the general form:

$$f_c \propto \bar{T}_{n,s} \times \frac{L}{\tilde{R}} \tag{6.9}$$

The results, therefore, suggest that particle size in PFC2D is not a free parameter and should be selected in consideration with the ratio $L/\tilde{R}$ and type of problem to be analysed. Results from all simulations for both series are given in Table 6.4 in terms of peak strength for uniaxial compression, Brazilian splitting, and biaxial compression tests.
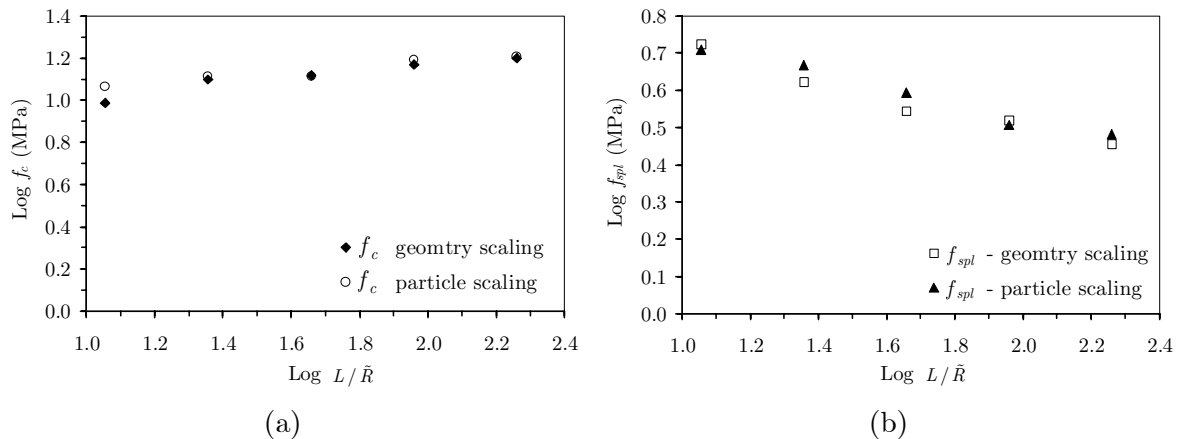
Figure 6.13: Size dependence of (a) uniaxial compressive and (b) Brazilian splitting tensile strengths on the discretization parameter $L/\tilde{R}$ in PFC2D.

Table 6.4: Size effect simulation results in PFC2D

	Geometry scaling			Particle scaling	
$L / \tilde{R}$	f_c (MPa)	f_{2c} (MPa)	f_{spl} (MPa)	f_c (MPa)	f_{spl} (MPa)
11.36	9.72±0.92	14.9±2.40	5.29±0.44	11.6±4.38	5.11±0.38
22.73	13.2±2.06	18.1±1.30	4.20±0.66	13.0±2.03	4.66±0.28
45.45	13.2±2.40	19.4±0.42	3.50±0.66	13.0±0.57	3.93±0.44
90.90	14.8±2.02	20.0±0.49	3.31±0.49	15.6±0.25	3.21±0.08
181.8[1]	15.8±0.92	20.2±0.21	2.86±0.20	16.2±0.01	2.86±0.14

[1]three simulations were performed per analysis type instead of five used for remaining sizes.

In an attempt to analyze the obtained size effect trends and their physical grounds, the results from the geometry scaling approach were further considered. This scaling approach was preferred since it resembles more closely the commonly applied test procedures for studying size effects in the laboratory. In addition, in this way a constant microstructure is assumed for all sizes in order to avoid confusing meso-level behaviours with particle size effects.

For Brazilian splitting strength, the size effect trend obtained in PFC2D is comparable to findings from laboratory experiments (Rocco *et al.*, 1999). Generally, it is observed that f_{spl} is size dependent and with failure characteristics similar in all sizes; namely, a major failure plane traversing across the specimens. The Brazilian simulations mostly reproduced these failure characteristics. In Figure 6.14, typical crack patterns obtained at peak load for specimens from the five sizes are shown. For the smallest specimen in Figure 6.14, the cracks did not form a discrete-like failure plane and only two cracks are formed at peak load. Crack propagation was arrested by the presence of the relatively large particles in the crack path and therefore hindering a continuous failure plane to develop. This might have enhanced the ductility of the specimens by allowing stress redistributions to take place, which in turn could increase their strength contributing to the apparent size effect. On the contrary, larger specimens have more chance for relatively smaller particles to position in the crack path and crack propagation is therefore more favourable. This would accelerate the failure process at probably lower peak loads. These observations generally apply for the five simulations performed per size.

In compression, the failure process is fundamentally different and rather complex. The size effect trend from the PFC2D simulations showed an increasing strength with size (see Figure 6.13), which is a reversed trend as compared with the commonly observed size effect trend in uniaxial compressive and tensile strength. For concrete materials, experimental investigation of size effect in compression received little attention and hence less data exists for comparison. Burtscher (2002), observed size effect in uniaxial compressive tests and reported a reduction in strength with size increase. The scatter in his results, however, makes it somewhat inconclusive with regard to the final trend. Generally, it could be stated that due to the substantial influence of boundary condition effects in compression tests, there is no clear sight on how the scaling should go under compression (Van Mier, 1997).
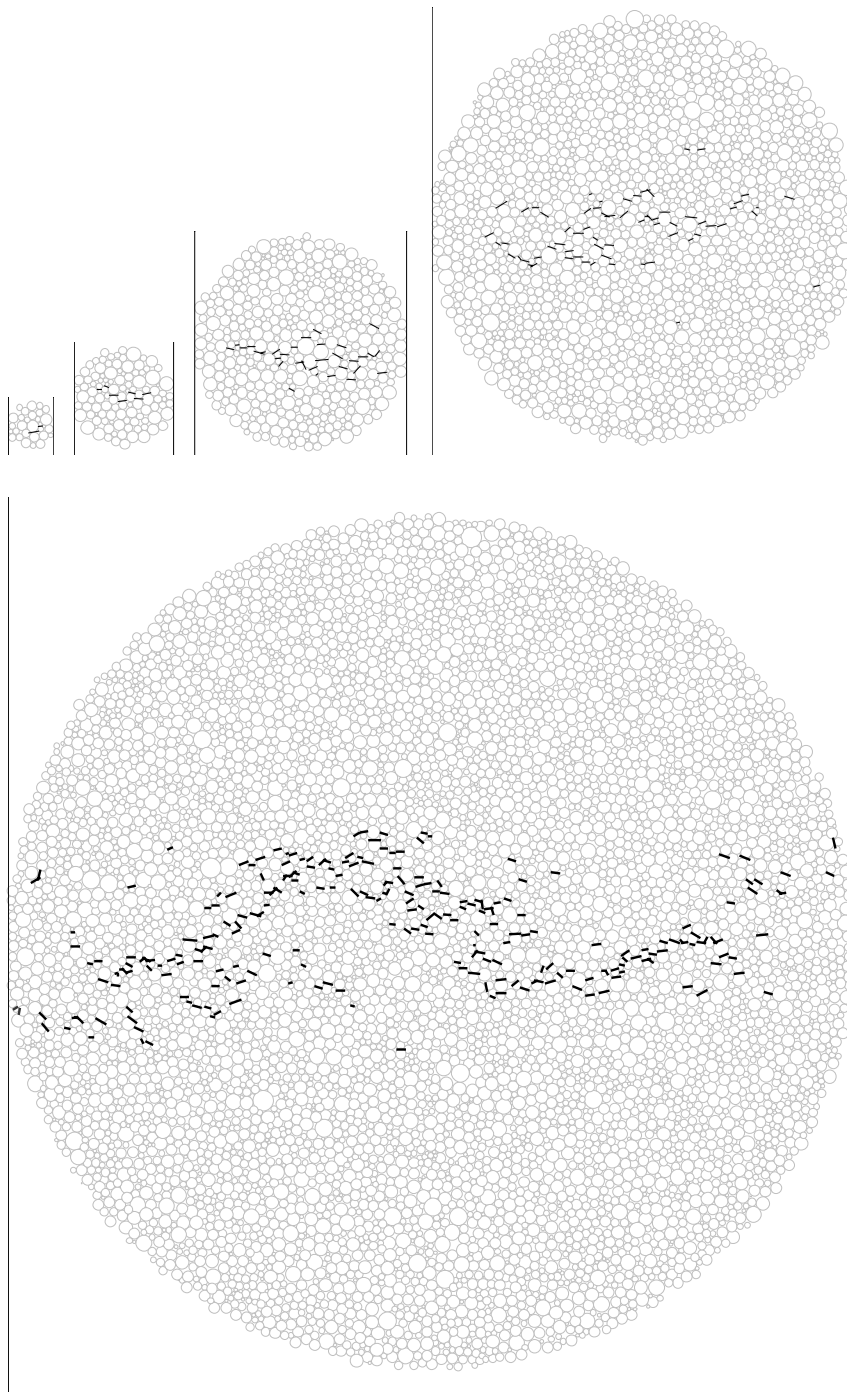
Figure 6.14: Damage pattern at peak stress in Brazilian splitting test simulations for specimens of a size range 1:16.

A close investigation of fracture behaviour during unconfined compressive failure for all sizes revealed that localization in finite inclined bands takes place in the pre-peak region. This is shown in Figure 6.15 where crack patterns obtained at peak load for all five sizes are presented. The larger the size, the more obvious the localized failure planes are observed and overall more than one plane could be distinguished. The broken contacts were generally horizontal resulting in cracks that are chiefly in the vertical direction, which is the direction of maximum principal stress.
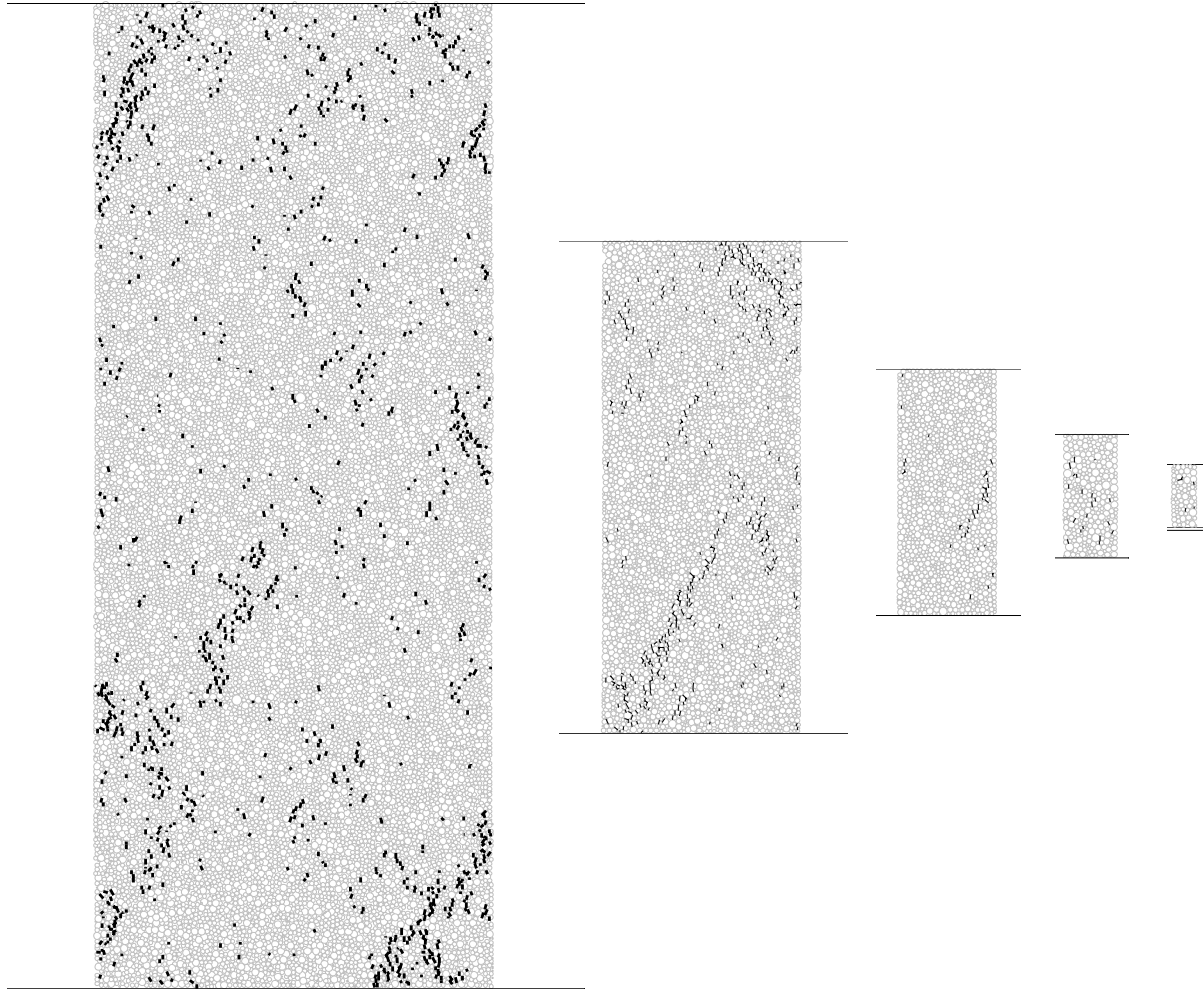
Figure 6.15: Damage pattern at peak stress in uniaxial compressive test simulations for specimens of a size range 1:16.

For both the f_c and f_{spl} analyses, the number of cracks (broken contacts) obtained at peak loads showed a nearly perfect linear relation on a log-log scale with the number of particles used in the simulations (Figure 6.16). The number of cracks was calculated as the average value from the five performed simulations for each size. The number of particles is directly proportional to the surface area of the specimen with both increasing in a quadratic mode with size. Accordingly, the size effect in strength for both the uniaxial compression and Brazilian splitting simulations could be correlated with the number of particles and hence the number of cracks.

The size effect in Brazilian strength exhibited an inverse relation with the number of cracks/particles. The existence of cracks in a specimen is known to negatively affect the elastic properties of the material and its strength. Hence, the obtained size effect trend in Brazilian simulations could be attributed representative to behaviour of real concrete-like materials. Van Vliet and Van Mier (2000), show from size effect experiments on concrete under uniaxial tensile loading that the obtained size effect could be fairly
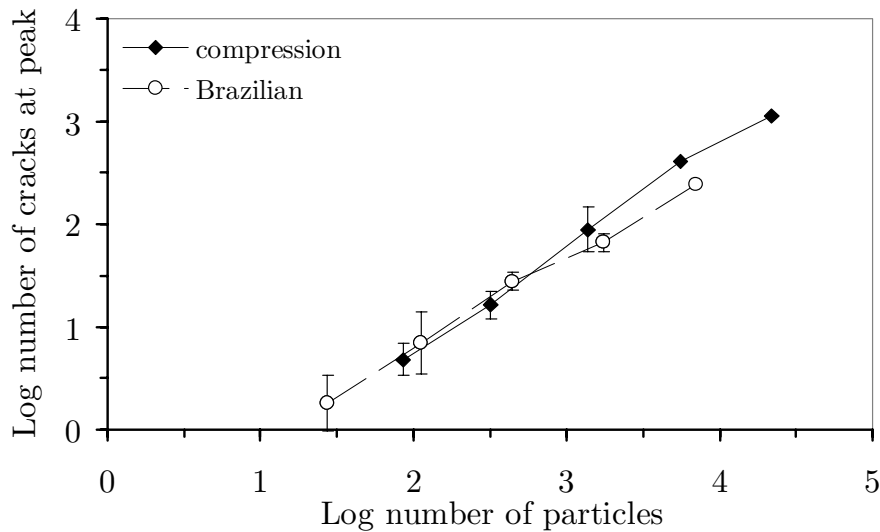
Figure 6.16: Number of particles versus number of cracks (mean values plus scatter) at peak stress in PFC2D simulations for uniaxial compressive and Brazilian splitting tensile tests.

represented using the classical statistical theory of Weibull. Accordingly, it was tested if Weibull's weakest link model could represent the size effect trend from the Brazilian PFC2D simulations. This is examined as we plot the Brazilian size effect trend in a log-log graph against the Weibull's statistical relation stating that:

$$\sigma_N \propto L^{-1/6} \tag{6.10}$$

This relation is adapted from the Weibull theory in its simplest form, the weakest link model, and for the case of two-dimensional scaling (Bazant and Planas, 1998). In Figure 6.17, the size effect in Brazilian splitting strength is plotted together with the graphical representation of relation (6.10). A good agreement between the simulation results and the size effect as predicted by the Weibull model is evident. Obvious from the figure as well is the large scatter band for the smallest size, which covers and exceeds the strength and scatter band from all other sizes. This is similar to findings by Van Vliet and Van Mier (2000), and for which they suggested that the RVE for uniaxial tensilt tests should be taken as large as 6-7 d_{max}. From our Brazilian test simulations (Figure 6.17), it seems that a reasonable discretization factor would be $L / \tilde{R} = 22.7$. It should be noted, however, and as mentioned earlier that a particle in PFC2D does not necessarily represent an aggregate or grain in real concretes.

With regard to compression simulations, the increasing strength with size indicates a direct relation with crack density and number of particles. The reason for this relation is not fully understood. It is expected for larger sizes with more particles to have more chance for stress redistributions, hence allowing for more ductility and higher strength. The scatter observed for the tested sizes showed a rather limited and some-what constant band for all sizes (Figure 6.18). Furthermore, for the simulations performed with 1.0 MPa confinement, an increase in strength with size was obtained (Figure 6.18), which closely resembles the trend from the uniaxial compression simulations. This was a rather
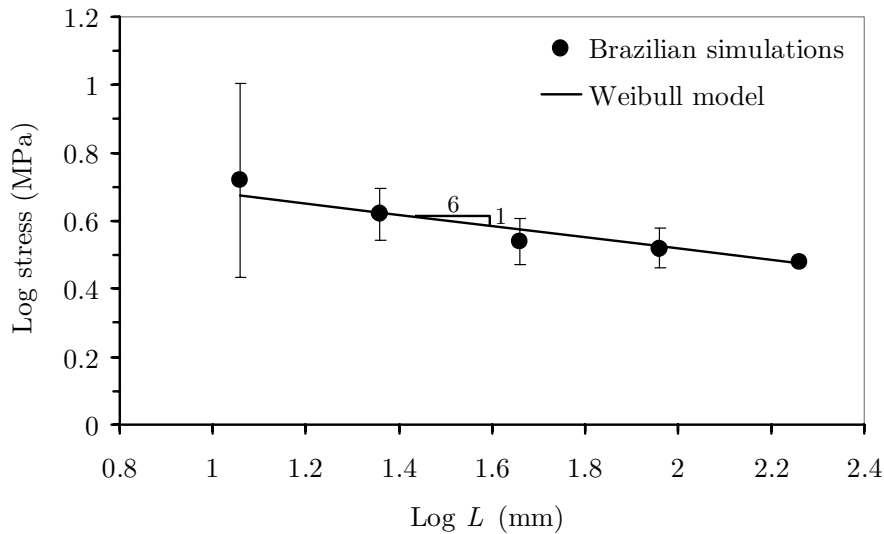
Figure 6.17: Size effect in Brazilian splitting tensile simulations. Shown are mean values and scatter plotted against the predicted size effect from Weibull's model.

curious result as compared to experimental observations on rocks that suggest a reduction in size effect and scatter in triaxial tests due to application of confining pressure (Paterson, 1978). The reduced scatter in triaxial tests is commonly attributed to a reduced end- and surface-effects due to confinement. The end-effects in uniaxial compression experiments are known to be a major hindrance for establishing a conclusive statement on size effect trend. Van Vliet and Van Mier (1995), show a reduction of scatter in uniaxial compression test results when end friction is eliminated. Rilem TC-148 (2000) recommends the application of proper end conditions, since the test results become more conclusive. In the performed PFC2D simulations, a reduced scatter of the results was attained. The boundary conditions used in the models were designed to closely resemble the experimental boundary conditions with no contact friction and with H/L=2.5, which are expected to bring the end-effects to a minimum.

6.5.3   Simulation of size effect in hollow-cylinder test

In this section, distinct particle modelling of the hollow-cylinder size effect experiments (Chapter 5) is discussed. In this analysis, the calibrated cylinder model presented in § 6.4 (Table 6.3) was utilized. Three hollow-cylinder assemblies were prepared to simulate the experimental specimens A, B, and C. The assembly that simulates size A was described earlier in § 6.4.2. For the larger two sizes, the cylinder dimensions were scaled and all other particle and model parameters were maintained constant. The number of particles used in the analyses were 875, 3497, and 13999 for the assemblies A, B, and C, respectively. The output of the simulations was interpreted in terms of the stress-strain response and fracture behaviour. The stress was calculated from the force exerted upon the external cylinder walls, while the strain represents the tangential strain ε_θ at the surface of the inner-wall.
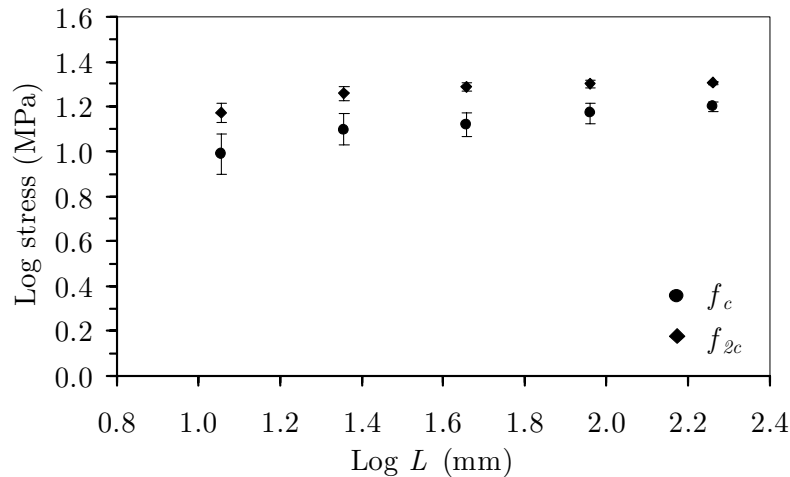
Figure 6.18: Size effect in uniaxial and biaxial (1.0 MPa confining pressure) compressive simulations in a range 1:16. Shown are mean values and scatter of results.

In Figure 6.19, a typical plot is given for the obtained stress-strain responses from the three assembly sizes. The results in the figure indicate a size effect after certain degree of strain was attained. For strain values less than 10‰ strain, there is no obvious size effect and stress-strain responses are linear. After that, for higher strain levels, the assemblies B and C started to show nonlinearity with strain hardening response followed by a plastic plateau. Assembly A did not show strain hardening and continued in somewhat linear response to the end of simulations. For size effect analysis, the criteria of 5‰ strain, followed in the analysis of experimental results (Chapter 5), was applied. In addition, the size effect was investigated at higher strain levels, i.e. 10, 15, and 20‰ strain. The size effect trends from hollow-cylinder simulations at these strain values are given in Figure 6.20. Consistent decrease of strength with size is observed for strain levels above 15‰ strain, whereas below this value, the size effect trend is unclear.
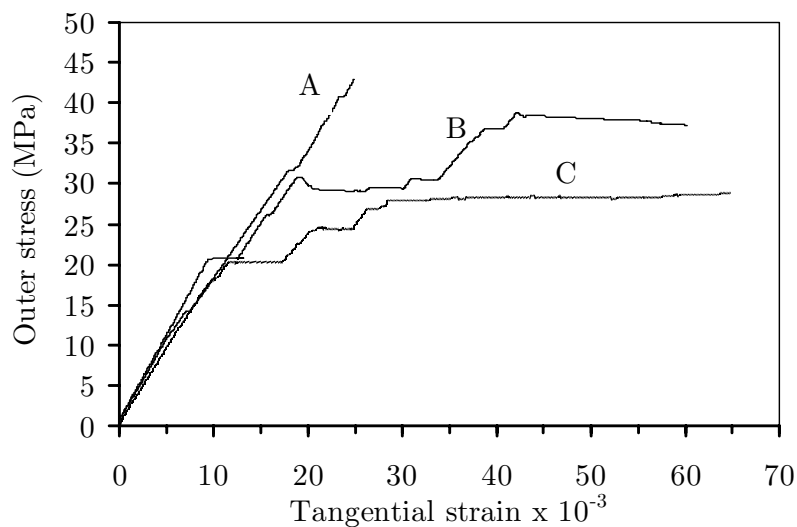
Figure 6.19: Stress-strain responses from PFC2D simulations for size effect in hollow-cylinder specimens size A, B, and C.
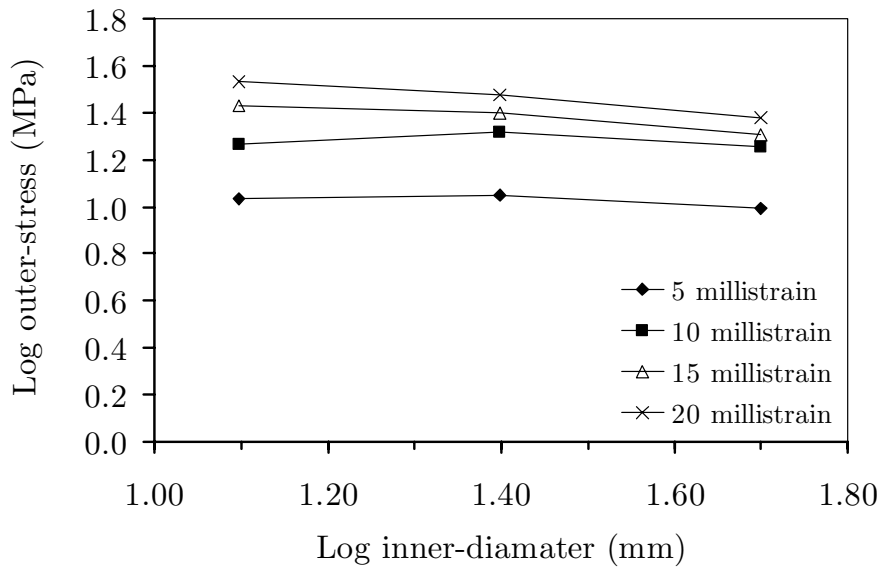
Figure 6.20: Log outer stress versus log inner-diameter at various tangential strain values from hollow-cylinder simulations of specimens size A, B, and C.

The results above indicate the capability of the distinct particle model in producing size effect with a trend comparable to that in the experimental hollow-cylinder tests. The model, however, could not reproduce the experimental stress-strain responses in terms of onset of nonlinearity. The resulting size effect is therefore quantitatively different from the experimental one, which hinders the model's prediction capabilities. The reason for this is thought to be the simplifications made for modelling. Amongst, the 3D effect and level of detail and heterogeneity to be modelled seem most relevant. Nevertheless, the model qualitatively showed a size effect trend with strength decrease as size increases.

Further, fracture patterns from the different sizes were evaluated and compared. Figure 6.21, shows plots from the different sizes with their fracture pattern obtained at a tangential strain value of 15‰ strain. This strain level showed a size effect trend comparable to the experiments (Figure 6.20). The results suggest a size dependent damage in the hollow-cylinder simulations. The number of cracks and extent of damage increased with specimen size, which is similar to experimental observations. In addition, the symmetry of fracture appears to increase with size. In size C, the cracks seem to better encircle the inner-hole as compared with those in A and B.

B (8 cracks)   **A (2 cracks)**

C (82 cracks)
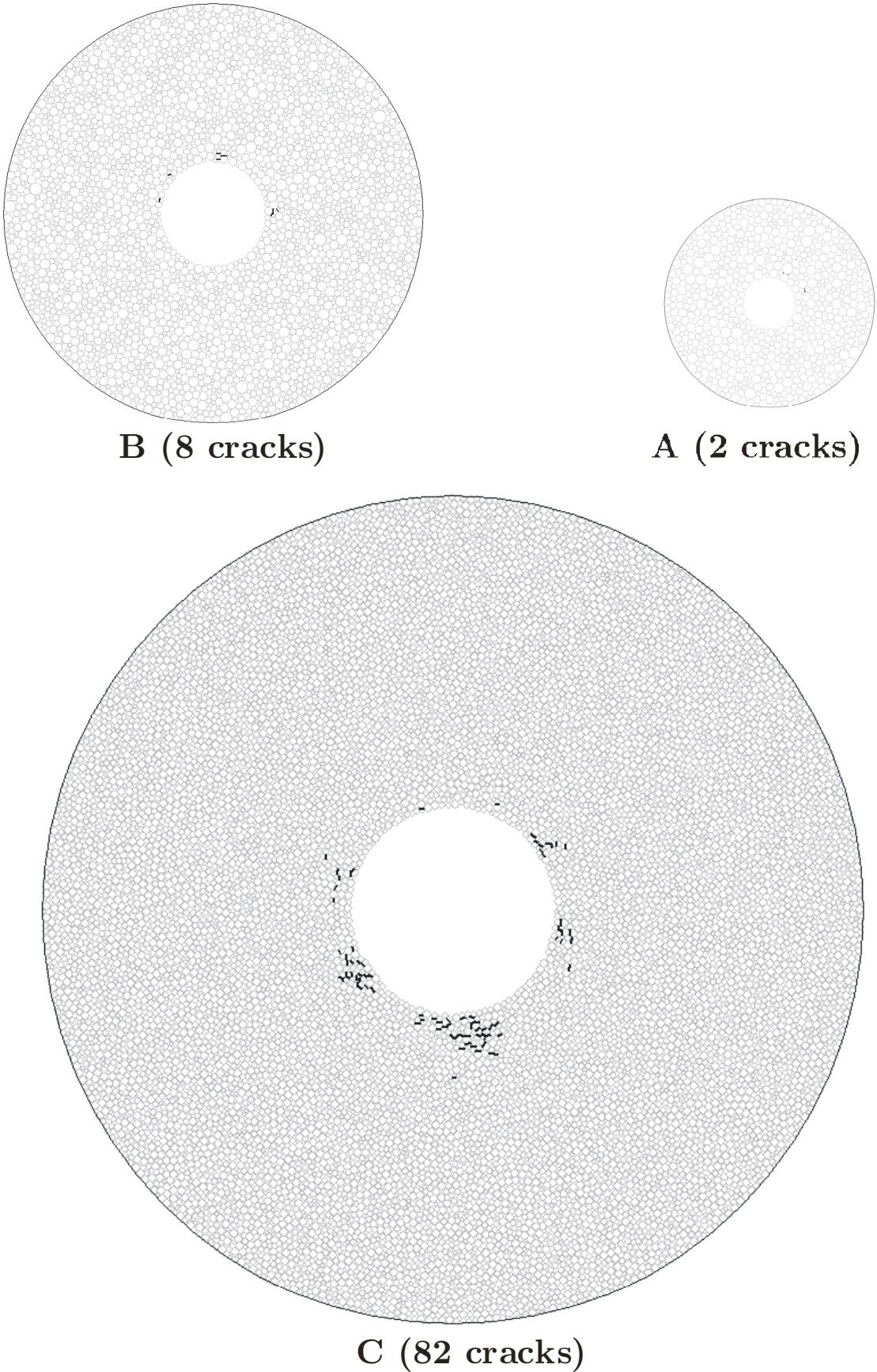
Figure 6.21: Fracture pattern in hollow-cylinders size A, B, and C from PFC2D simulations. The presented results are obtained at a tangential strain level of 15‰ strain

6.6 SUMMARY AND CONCLUDING REMARKS

Computations using PFC2D were performed, which revealed its ability in reproducing comparable macroscopic material behaviour observed in the hollow-cylinder experiments. This discrete meso-mechanical model was able to yield realistic fracture patterns and damage development. The calibration process, however, is not fully understood since a set of micro-parameters that satisfy for instance uniaxial compressive strength and Young's modulus would result in a higher Brazilian splitting strength and misleading fracture behaviour during hollow-cylinder simulations. It was necessary to increase the bond-strength with a factor three to obtain a more realistic fracture pattern in the hollow-cylinder simulations, which is comparable to those obtained in the experiments. On the other hand, the stress-strain response was not much affected and in both cases strain levels were attained, which were comparable to the experiments despite a somewhat linear behaviour from the model. It is therefore recommended to account for crack patterns during the calibration procedure of bonded assemblies in addition to macro-mechanical parameters such as peak stress, peak strain, and E-modulus.

Size effect simulations in PFC2D for both compressive and splitting tensile loadings showed the model to be dependent on the discretization parameter $L / \tilde{R}$. For the same $L / \tilde{R}$ value, similar strengths were obtained whether geometric or particle size scaling was employed. This suggested that the particle size in PFC2D is not a free parameter and should be selected with respect to the specimen dimension in a way to satisfy the macro-strength used for calibration (compressive or splitting tensile). Using the geometric scaling approach, a size effect trend in Brazilian test simulations was found, which is comparable to experimental findings reported in literature and with analogous failure mechanisms. The decreasing size effect trend showed a good agreement with predictions from the Weibull weakest-link theory. On the other hand, the compressive test simulations resulted in an increased strength with size for both uniaxial and biaxial compressive load conditions. The cause for this behaviour is not identified, but it should be realized, however, that due to the substantial influence of boundary condition in laboratory compression tests, there is no clear sight yet on how the scaling should develop (whether an increasing, decreasing trend, or no size effect).

Modelling of size effect in hollow-cylinder tests was carried out. Generally, no peak load was observed in the simulations and a plastic strain hardening took place instead, similar to the experiments. The model was able to produce a consistently decreasing size effect trend for tangential strain levels above 15‰ strain, which is more than twofold the experimentally observed value. This is probably associated with the inability of the model to capture the point of onset of nonlinearity observed in the experiments that took place in all sizes at a more or less equivalent stress levels. In addition, the pseudo-linearity and underprediction of the biaxial strength envelope in the PFC2D results could reflect on the stress-tangential strain behaviour in the hollow-cylinder simulations. However, the simplified bond model and discrete nature of the analysis were able to qualitatively reproduce the size effect in hollow-cylinder experiments and with comparable crack patterns.

Chapter 7

SYNTHESIS: ANALYSIS AND DISCUSSION

7.1 SIZE EFFECT IN HOLLOW-CYLINDER STRENGTH

In the preceding chapters, both experimental and numerical results were presented and discussed with regard to failure and size effect in hollow-cylinder tests. In order to try gaining more insight into these phenomena, a better and more comprehensive understanding of the results was deemed. In the following sections, the results are carefully examined and an analysis is presented of factors, processes, and hypotheses with regard to size effect in hollow-cylinder tests and its underlying causative mechanisms.

7.1.1 Onset of size effect in hollow-cylinder tests

As discussed in Chapter 5, the size effect analysis was conducted by comparing the outer-stress values from the three tested sizes that correspond to a tangential strain value of 5‰ strain. Since this strain value was selected rather arbitrarily, a comparison between size effect trends obtained at other strain values was carried out. Tangential strain values of magnitude 1, 10, 15, and 25‰ strain were selected for this purpose. No values were examined larger than 25‰ strain as it approaches the maximum attained strain for the smallest size A. the comparison was done for both the M2 and M4 mixtures. The results of this comparison are presented in Figure 7.1.

As the results in Figure 7.1 indicate, the size effect trends were much alike for strain values larger than 5‰ strain and they appeared qualitatively parallel. Therefore, the use of a 5‰ strain value in the experimental size effect analysis seems justified. Moreover, this suggests that if a peak stress was achieved in the experiments and its value was used for size effect analysis, a similar size effect trend would has been obtained as that from the 5‰ strain. This is due to the rather steady deformation rate in the strain-hardening phase for all sizes. On the other hand, the trends obtained at 1‰ strain were somewhat inconclusive and showed high scatter for all sizes from both mixtures (Figure 7.2)
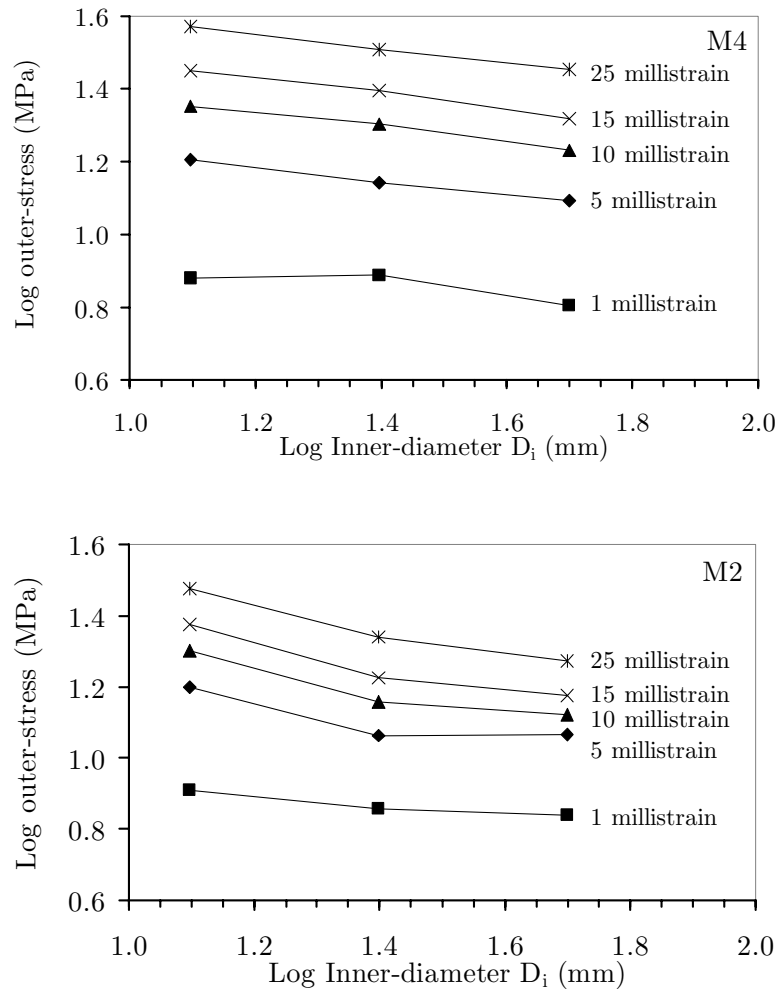
Figure 7.1: Bi-logarithmic plots of size effect trends obtained at various tangential strains in hollow-cylinder tests on the mixture (top) M4 and (bottom) M2. Shown are mean values.

At this strain level, nonlinearity in the $\sigma_o - \varepsilon_\theta$ curves was not generally commenced (Figures 5.2 and 5.5) and the response was in the linear phase. If the onset of material size effect is argued to be linked to fracture processes and therefore nonlinear stress-strain behaviour, then the trends at 1‰ strain might have been due to stress gradient effects (§ 7.1.2), which exist during the whole hollow-cylinder test.

In terms of onset of size effect, the results in Figure 7.1 imply that a nearly steady size effect trend was set off in the experiments at tangential strain levels of about 5‰ strain. At this level of strain, microscopic examination of fracture processes (Chapter 5) showed small boundary cracks to exist with not much crack interaction or propagation activities. In addition, there were no signs of spalling at this level of strain from the different sizes during the experiments. Accordingly, factors such as crack growth and coalescence, crack localization, and softening material damage could be apparently excluded as causing factors as they were not detected or attained experimentally at this stage. Size effect models assuming these factors as source for size effect would then fail to explain the size effect in these experiments for their conflicting underlying physical assumption. This is discussed further in the next sections.
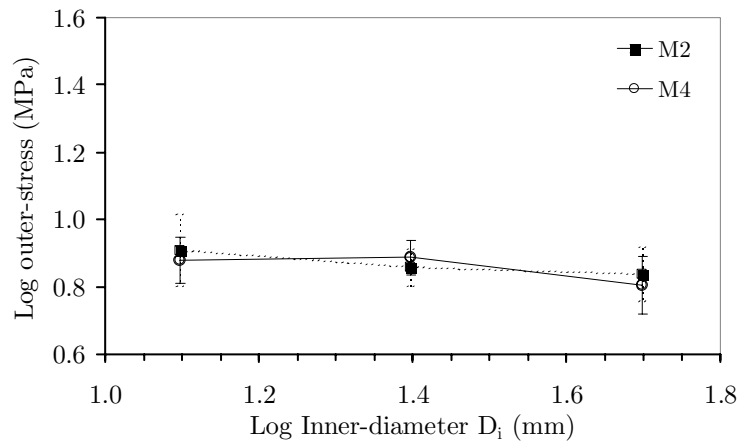
Figure 7.2: Bi-logarithmic plot of size effect trends obtained at 1‰ strain in hollow-cylinder tests on the M4 and M2 mixtures. Shown are mean values and scatter.

Material related factors contributing to size effect at this strain level are therefore linked to processes taking place at crack initiation. These are largely due to heterogeneity and distribution of defects in the material, which are of a rather statistical/probabilistic nature. This raises the curiosity if the statistical size effect theory of Weibull would be justified for use and could describe the experimental results. In § 7.1.3, the Weibull model is adapted to predict the size effect in hollow-cylinder experiments and its suitability and results are discussed. The aforementioned agrees as well with the modelling results (Chapter 6), where heterogeneity in the model was capable of producing size effects in the hollow-cylinder simulations.

7.1.2   Stress gradient as source for size effect
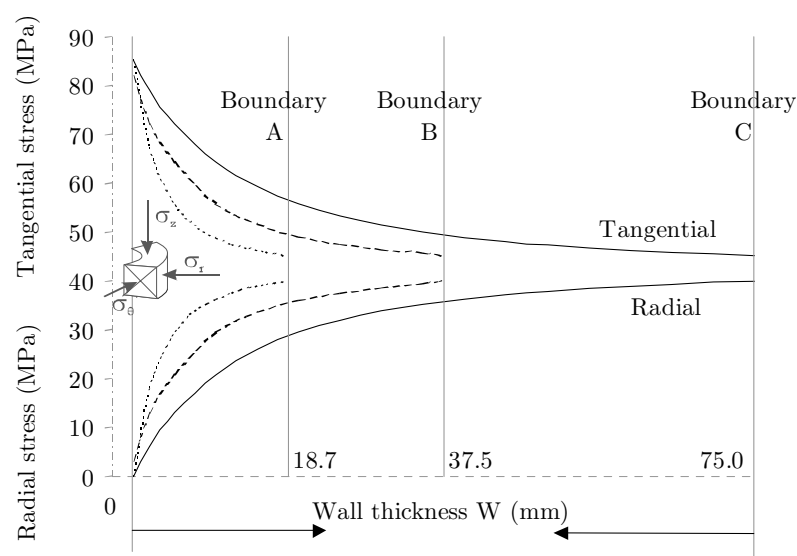
Figure 7.3: Schematic showing the tangential and radial stress distribution according to a linear-elasticity over the wall of hollow-cylinders size A, B, and C.

In order to check a possible contribution from stress gradients on the observed size effect in hollow-cylinder tests, an averaging procedure was applied by integrating the stresses, calculated form linear-elasticity, over various averaging distance (A_d) values and for each of the three tested sizes. A schematic for stress distribution according to linear-elasticity is presented in Figure 7.3 for the three different sizes (A, B, and C), which shows their difference in stress gradient intensity along the wall.

The maximum principal stress (tangential stress) in a hollow-cylinder subject to a hydrostatic pressure and zero inner-pressure is defined as follows (Kirsch solution),

$$\sigma_\theta = \frac{\left(\sigma_o R_o^{\,2} - \sigma_i R_i^{\,2}\right)}{\left(R_o^{\,2} - R_i^{\,2}\right)} + \frac{\left(\sigma_o - \sigma_i\right) R_i^{\,2} R_o^{\,2}}{\left(R_o^{\,2} - R_i^{\,2}\right) r^2} \tag{7.1}$$

for the special case of zero inner-pressure ($\sigma_i = 0$), the relation simplifies to,

$$\sigma_\theta = \frac{\left(\sigma_o R_o^{\,2}\right)}{\left(R_o^{\,2} - R_i^{\,2}\right)} \times \left(1 + \frac{R_i^{\,2}}{r^2}\right) \tag{7.2}$$

where σ_o is the pressure at the external boundary (applied pressure), R_o is the outer-cylinder radius, and R_i is the inner-cylinder radius. This relation represents the maximum principal stress σ_θ at any radius r for the range R_i to R_o. The average tangential stress over a distance A_d is described by the integral,

$$\overline{\sigma}_\theta . A_d = \int_{r=R_i}^{r=R_i+A_d} \frac{\left(\sigma_o R_o^{\,2}\right)}{\left(R_o^{\,2} - R_i^{\,2}\right)} \times \left(1 + \frac{R_i^{\,2}}{r^2}\right) . dr \tag{7.3}$$

Integration (7.3) and simplifying, results in the following relation for the average tangential stress,

$$\sigma_\theta = \frac{-\sigma_o R_o^{\,2} A_d (2R_i + A_d)}{(R_i^{\,2} - R_o^{\,2})(R_i + A_d)} \tag{7.4}$$

In terms of failure, a straightforward method for representing failure around the inner-hole is to assume this failure to initiate at a maximum principal stress level $\sigma_1 = \sigma_\theta$ equal to the uniaxial compressive strength value. Two values were examined, viz. 10 and 12 MPa, as an average from the available laboratory cube strength tests (see Figure 5.8). The Equation (7.4) was solved for the external stress at various A_d values, viz. 2, 4, 7, 10, and 15 mm. This procedure was applied for the three sizes (A, B, and C) through varying R_o and R_i, resulting in a stress gradient relation. The relation is represented graphically in Figure 7.4, which is a function of the specimen size, represented by the cylinder dimensions, the averaging depth A_d, and the outer stress σ_o.

The relation in Figure 7.4 shows a decrease in stress with size, which is a function of A_d value. In other words, a decrease in hollow-cylinder strength with size is obtained due to considering the maximum principal stress gradient along the cylinder wall. The larger the averaging distance A_d used, the stronger was the calculated size effect. Accordingly, the existence of compressive stress gradients in the hollow-cylinder contribute to the
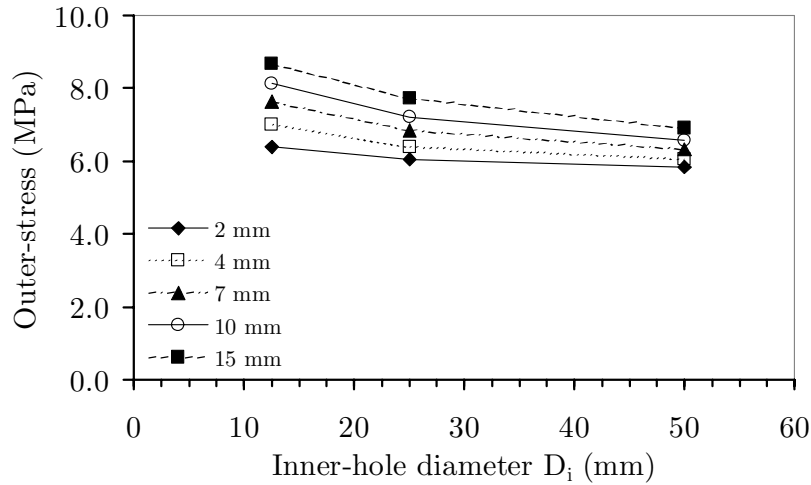
Figure 7.4: The outer stress σ_o as a function of the inner-radius D_i for the different sizes as obtained from the stress averaging analysis for different averaging distances A_d.

overall observed size effect in the experiments. Similar stress gradients, with diverse intensities, exist around in-situ excavations (tunnels or deep-boreholes) and therefore are expected to produce similar size effects. The analysis, however, does not consider the effect of the radial stress gradient acting on the wall thickness. Due to absence of confinement at the inner-wall, the assumption of failure under uniaxial compressive stresses is seen valid. In addition, possible deformation or strain gradients are not discussed. Such analysis requires more information with regard to deformation at the outer-surface of the cylinder, which was not performed experimentally.

In Figure 7.5, the size effect test results for the M2 and M4 mixtures, in terms of mean values at 5‰ strain, are plotted together with stress values from the stress gradient analyses for A_d=7 cm. Apparent is the contribution of stress gradient to size effect.
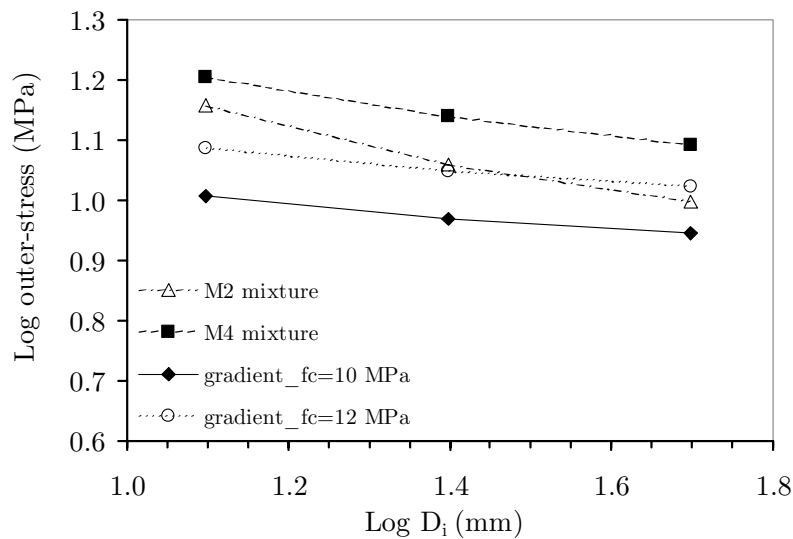
Figure 7.5: Bi-logarithmic plot of size effect from experiments on M2 and M4 mixtures and calculated size effect from the averaging of stress gradients at 7 mm distance from inner-wall.

7.1.3   Comparison of results with the Weibull weakest-link model

As discussed in § 7.1.1, the results showed a possible statistical factor to contribute in the obtained size effect. This factor is investigated using Weibull's theory for size effect. In Weibull's weakest-link theory (1939) on the statistics of strength of materials, a specimen is assumed as an assembly of series arrangement of elements. Failure of any of the elements causes failure of the specimen. The basic equation of this model for the probability of failure P_f of a specimen of volume V subjected to stress σ is,

$$P_f = 1 - \exp\left\{-\int_V \left(\frac{\sigma - \sigma_u}{\sigma_y}\right)^m dV\right\} \tag{7.5}$$

where σ_u, σ_y and m are constants and with σ_u representing the smallest tensile strength that any element can have in the assembly. For mathematical simplicity σ_u is usually assumed zero. The value for the Weibull modulus m for concrete from direct tensile tests by Zech and Wittmann (1978) is 12.

To account for non-uniform stress distribution, an assumption is made that σ depends on position $\sigma(x)$ and integrating (7.5) over the volume. Furthermore, a triaxial stress state could be considered as well for a principle stress situation $\sigma_i(x)$, $(i=1, 2, 3)$ that yields the following relation for the probability of failure P_f (Bazant and Planas, 1998),

$$P_f = 1 - \exp\left\{-\int_V \sum_{i=1}^{n} \left(\frac{\sigma_i(x)}{\sigma_y}\right)^m .dV\right\} \tag{7.6}$$

Equation (7.6) could be further simplified by using the notation $n(\sigma)$ so that:

$$P_f = 1 - \exp\left\{-\int_V n(\sigma).dV\right\} \tag{7.7}$$

where $n(\sigma) = \left[\sigma(x)/\sigma_y\right]^m$ that can reduce further to $n(\sigma) = \sigma^m / \sigma_y^{\,m} = k\sigma^m$.

The mean stress at failure, $\bar{\sigma}$, is given by,

$$\bar{\sigma} = \int_0^{\infty} \exp\left\{-\int_V n(\sigma).dV\right\}.d\sigma \tag{7.8}$$

For the case of a hollow-cylinder of length l and considering a cylindrical coordinate system (r, θ, z), the following relation is obtained (Jaeger and Cook, 1979),

$$\int_0^V n(\sigma)dV = \int_{R_i}^{R_o}\int_0^{2\pi}\int_0^l dr d\theta dz = 2\pi l \int_{R_i}^{R_o} n(\sigma).dr \tag{7.9}$$

Substituting for $n(\sigma) = k\sigma^m$ in (7.9) and for $\sigma = \sigma_\theta$ with σ_θ as given in (7.2),

$$\int_V n(\sigma).dV = 2\pi l k \frac{\sigma_o^{\,m}(R_o^{\,2})^m}{(R_o^{\,2} - R_i^{\,2})^m} \int_{R_i}^{R_o} \left(1 + \frac{R_i^{\,2}}{r^2}\right) r.dr \tag{7.10}$$
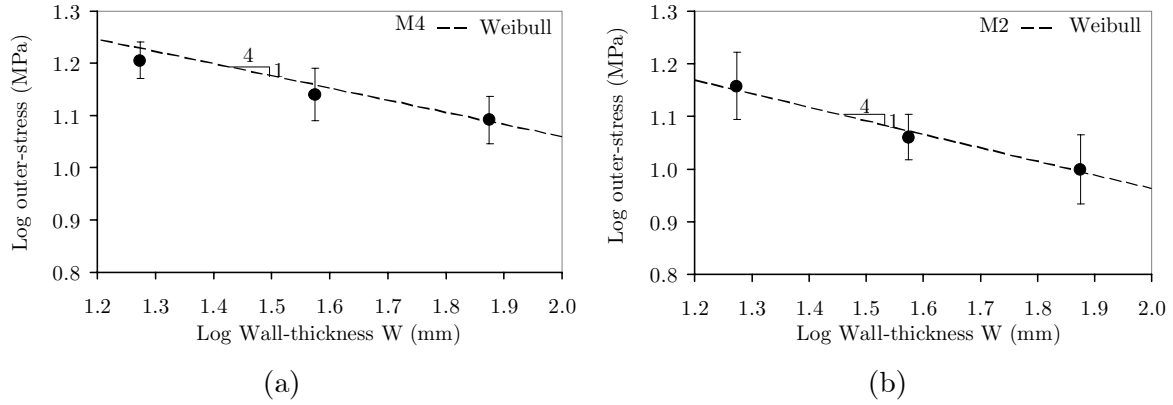
Figure 7.6: Bi-logarithmic plots of the outer-stress versus wall-thickness from the hollow-cylinder tests for sizes A, B, and C of (a) the mixture M4 and (b) the mixture M2. The size effect relation calculated by the Weibull model is included in the plots for comparison.

from (7.8) and (7.10) after integrating with $m=12$ for the three specimen sizes A, B, and C (substituting for R_i and R_o values in the equations), we obtain the following average stress for the three sizes consecutively,

$$\overline{\sigma}_A = 1.33k^{-1/12} = 1.33\sigma_o \qquad (7.11)$$

$$\overline{\sigma}_B = 1.12k^{-1/12} = 1.12\sigma_o \qquad (7.12)$$

$$\overline{\sigma}_C = 0.94k^{-1/12} = 0.94\sigma_o \qquad (7.13)$$

The above stress values obtained for each size typically obey a power size relation with an exponent of –1/4 where $\overline{\sigma} \propto D_c^{-1/4}$, and D_c is a characteristic dimension.

In the field of concrete fracture, the following form of the weakest-link model (Bazant and Cedolin, 1991) is commonly applied, $\sigma_N \propto D_c^{-n_d/m}$, where σ_N=nominal material strength, D_c=characteristic dimension, n_d=scale number, and m=Weibull modulus. In the case of hollow-cylinders, n_d=3 for three-dimensional scaling and m=12 (see above). This results in the following equation for three-dimensional similarity,

$$\sigma_N \propto D_c^{-1/4} \qquad (7.14)$$

The relation in (7.14) is evident to conform to the relation obtained after (7.16-18) for the special case of hollow-cylinder with external hydrostatic pressure. In Figure 7.6, bi-logarithmic plots of the size-stress relation from the performed test series are presented together with the graphical representation of equation (7.14). In the plot, the characteristic dimension D_c is represented by the wall-thickness W in the hollow-cylinders. A good agreement with the test results is observed. This does not, however, fully satisfy the nature of progressive failures in compression and mobilization of friction, which is different from the Weibull assumption of chain type failure. As discussed earlier in § 7.1.1, the trigger of size effect in the conducted hollow-cylinder tests, which was at low strain levels around crack initiation stage, appears to bear a statistical component. This component is tentatively described above using Weibull's model.

7.1.4 Comparison of results with SEL and MFSL

As discussed in Chapter 2, in the field of fracture of concrete and similar quasibrittle materials, three models are frequently used to describe size effect observed in laboratory experiments. In addition to the Weibull model, which is discussed separately above in § 7.1.3, the SEL presented by Bažant (1984) and the MFSL proposed by Carpinteri and Chiaia (1995) are considered. The latter two phenomenological models were basically proposed for fracture under tensile loading and adapted afterwards for compressive stress fields. Noteworthy here is that these models consider peak loads in their formulation, which is a state that was not attained in the conducted hollow-cylinder tests.

In particular, the SEL for compression was utilized to describe size effect in borehole breakout (Bazant *et al.*, 1993) based on fracture energy arguments using LEFM. One of the assumptions in this approach is failure through development of equally spaced axial splitting cracks and buckling of slabs that form amid these cracks. Spacing between the cracks is assumed to negatively correlate with borehole radius and is responsible for the model gradient of (-2/5) as compared with the gradient of (-1/2) from LEFM. This assumption contradicts the experimental results in this thesis (Chapter 5), since spacing of the obtained cracks was predominately function of the aggregates size and their distribution across the major stress field.
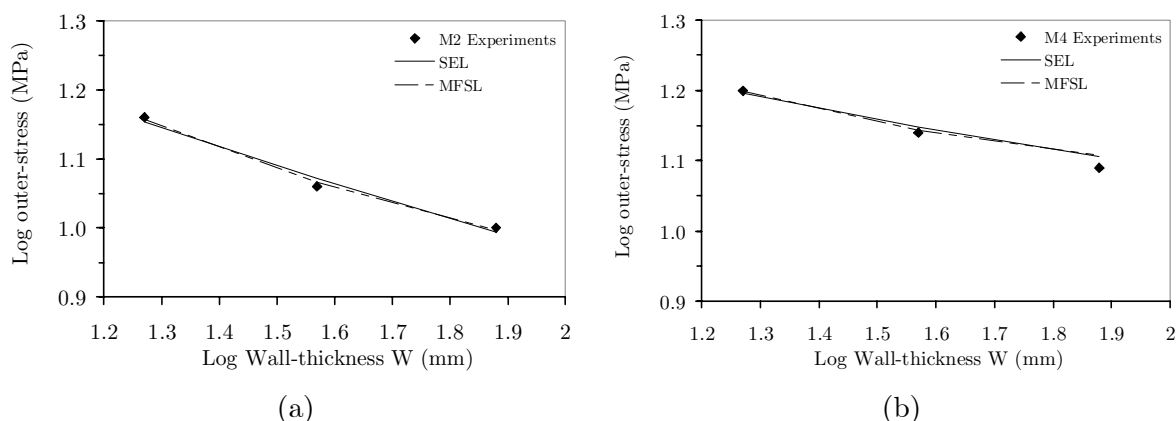
Figure 7.7: Fitting of the SEL and MFSL to the experimental size effect results for (a) the M4 and (b) the M2 mixtures. Shown are the mean experimental values at 5‰ strain.

In Figure 7.7, the best-fit using nonlinear least-squared algorithm from both models is presented for the experimental results on both the M4 and M2 mixtures. In the size range of performed experiments, both models showed a nearly perfect fit. The models' parameters from the fitting exercises are summarized in Table 7.1, together with their goodness of fit. The characteristic dimension in the models is considered equal to *W* of the cylinders. As seen form these fitting results, both models could represent well the experimental results with correlation coefficients equal to nearly one. This is despite the physical contradiction of SEL with the experiments as discussed above. Furthermore, the use of these models for predicting size effects beyond the tested size range is uncertain for their differing asymptotical description at small and large sizes (Van Mier, 1997). Bažant and Xiang (1997), further comment on the assumption of size-dependent spacing in the SEL model and suggest that it is only applicable for homogeneous materials. In

the case of heterogeneous materials such as concrete, they suggest that the spacing will be fixed and dictated by the material heterogeneity. In this latter case, the stress negatively correlates with size as $D_c^{-1/2}$ for small to intermediate sizes, similar to size effect from LEFM, and levels off with a zero exponent for very large sizes.

Table 7.1: Model fitting parameters for SEL-compression and MFSL

SEL (compression) $$\sigma_N = C_{SEL} D_c^{-2/5} + D_{SEL}$$	MFSL $$\sigma_N = \sqrt{A_{MFSL} + \frac{B_{MFSL}}{D_c}}$$	
Fitting parameters for the mixture M4		
C_{SEL}=8.86	A_{MFSL}=136.9	l_{ch}=15.2 mm
D_{SEL}=22.1	B_{MFSL}=2097.3	f_c=11.7 MPa
R^2=0.98	R^2=0.99	
Fitting parameters for the mixture M2		
C_{SEL}=4.10	A_{MFSL}=63.8	l_{ch}=41.6 mm
D_{SEL}=32.8	B_{MFSL}=2651.3	f_c=7.98 MPa
R^2=0.98	R^2=0.99	

Now if the size effect relation given by $D_c^{-1/2}$ is used to describe the experimental results, the outcome in Figure 7.8 is obtained. The fitting parameters for the relation in the figure are given in Table 7.2. The capability of the model is reduced drastically, as seen from the results. This applies as well for analysis using LEFM. It should be noted that for rock materials (for which the SEL-compression was utilized in borehole breakout analysis), size effect experiments using sandstone hollow-cylinder specimens (e.g. Kooijman *et al.*, 1991; Van Den Hoek *et al.*, 1992) show that the spacing or spall thickness remains approximately constant with increasing cylinder size.
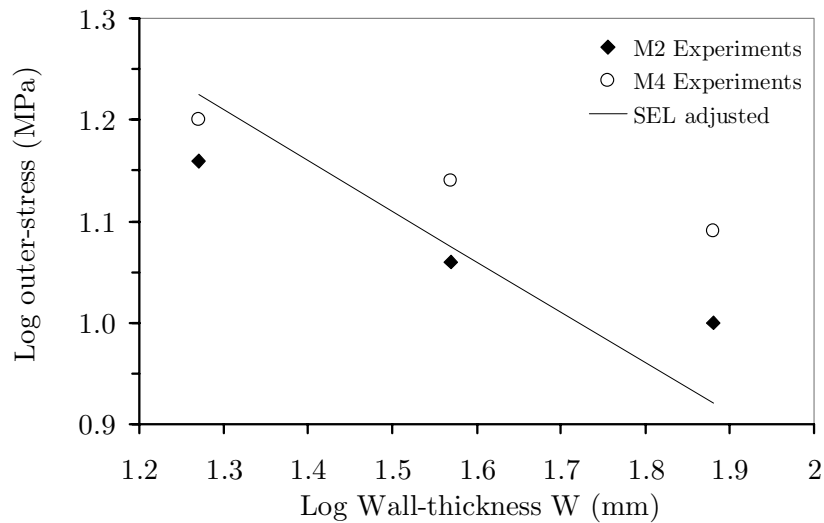
Figure 7.8: Fitting of the adjusted SEL-compression to the experimental size effect results after accounting for constant spacing between splitting cracks in the model assumption.

Table 7.2: Parameters for adjusted SEL

SEL-compression (adjusted)
$\sigma_N = C_{SEL} * D_c^{-0.5}$
C_{SEL}=72.42 (M2)
C_{SEL}=86.38 (M4)

Similar modelling approach, which is based on splitting failure as a combination of spall buckling and Griffith crack propagation with energy arguments, to estimate size dependency of the hollow-cylinder initial failure load were discussed by Ewy and Cook (1990a) and van den Hoek *et al.* (1994). The latter proposed an improvement to the approach by including elasto-plastic material deformation for perfectly plastic materials with large plastic zone and infinite outer hollow-cylinder boundary. Their modification results in the following relation for size effect,

$$\sigma \propto D_c^{\frac{\sin\varphi}{1+\sin\varphi}} \tag{7.15}$$

for M4 and M2 with φ =44° and 33°, respectively, and constant spall thickness this results in $\sigma \propto D_c^{-0.40}$ and $D_c^{-0.35}$, respectively. This size effect is stronger than the experimentally observed size effect, which behaves roughly as $D_c^{-0.20}$ for the M4 and $D_c^{-0.25}$ for the M2. The main variable in (7.15) is the friction angle φ, which is thought to only slightly contribute to size effect at early failure stages as observed here.

7.1.5 Synoptic view of size effect

Size effect in hollow-cylinder tests, as observed in the experiments conducted in this study and from the analysis presented above, is a phenomenon and a process resulting from mutually and commensurate occurring processes and mechanisms. It could be stated that this size effect is a result of complex combination of structural factors (e.g. geometry imposed effects such as stress gradient and surface area and volumetric effects), mechanical processes of failure including deformation, and material characteristics in terms of heterogeneity and fabric. Existing theories, hypothesis, and concepts to explain size effect (statistical, energetic, or related to violation of similarity laws) are reasonable but each has a different weight for the diversity and heterogeneity of materials, loading schemes, and test conditions as assumed by them a source for size effect (Andreev, 1995). No theory seems to exist that encompasses these various factors for its obscurity and since it is not clear which of the processes or mechanisms has a prevailing influence, if any. This is more pronounced in compressive failure processes, being more complex, with most of the factors often act combined and hence emphasizing only one factor in a model or hypothesis and neglecting others brings an error to the model, which could be significant. The isolation of one of the factors to be independently studied is a difficult task experimentally and numerical simulations based on physical hypothesis could form a favourable supplement. Brown and Gonano (1975), analysed the factors that are likely to produce size effect in rock under uniaxial compression. The result of their analysis agrees largely with the aforementioned discussion and is given in Figure 7.9.

Other factors contributing to size effect (Bazant, 2002), and was not explicitly examined in this study, are moisture gradients due to drying out of concrete, boundary layer effect for concrete surfaces adjacent to moulds and formwork, and time-dependent length scale. The contribution of these factors depends on the concerned problem and its application. Their effect could tentatively be described through fracture homogeneity and uniformity of stress distribution in Figure 7.9, except probably for time-dependence of the material constitutive law. Effect of moisture gradients, for example, is reported to mask strength fluctuations due to material heterogeneity in uniaxial tensile tests (Van Vliet, 2000) or may influence the fracture mechanism taking place in hollow-cylinder tests (Hoek *et al.*, 2000). The importance of these should not be overlooked and requires further efforts.
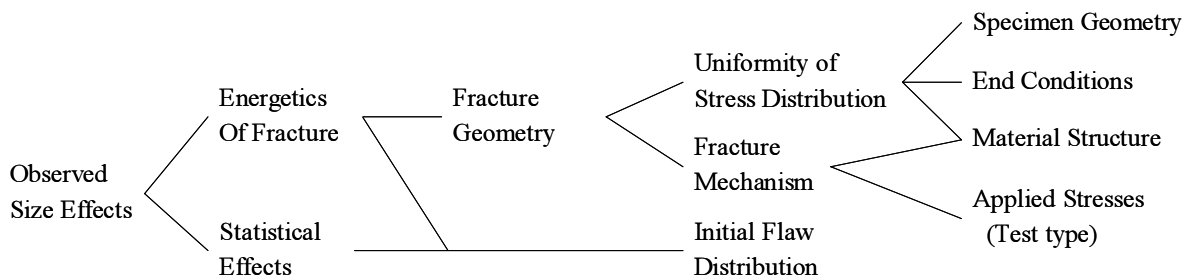
Figure 7.9: General relationship between causative factors and observed size effects (adapted after Brown and Gonano, 1975).

7.2   HOLLOW-CYLINDER STABILITY ANALYSIS

Assessment of hollow-cylinder stability is of practical interest for its common use as model test in simulating wellbore failure—was first used on a routine basis in the petroleum industry by Shell (Antheunis *et al.*, 1976). Field wellbore stability refers to phenomena related to the degradation of the rock adjacent to the walls of a borehole or cylinder as a result of the tangential stress concentration. Predictions of stability require the comparison of stresses and material strength using a failure criterion. The two most commonly used failure criteria in wellbore analyses are the M-C and the D-P criteria (Ewy, 1999). Stability assessments based on these models with linear-elastic behaviour assumptions were demonstrated not able to predict accurately the level of loading at which failure occurs for different types of rocks. Guenot (1987), summarized a series of tests where the ratio between the actual load at rupture and the theoretical (predicted) load, determined using classical theory, was between 1.5 and 8. This latter state is referred to in the geomechanical and oil literature as abnormal stability where no signs of failure are observed, while the level of straining has exceeded the predicted capacity of the material.

According to linear-elastic analysis (Chapter 2), tangential stress concentration at the hole wall, for hollow-cylinders with dimensions as tested in this thesis, is predicted to be 2.13 times the outer-stress. Considering this with a M-C criterion, then failure could be predicted according to the following expression (Jaeger and Cook, 1979),

$$\sigma_1 = \sigma_\theta = \frac{2\cos\varphi}{1-\sin\varphi} \times c \qquad (7.16)$$

According to (7.16) and the triaxial test results (Chapter 3), failure is predicted to initiate at an outer-stress equal to 4.2 and 5.8 MPa for the M4 and M2, respectively. From the results discussed in Chapter 5, it is seen that there was no collapse attained in the experiments, for any size, up to outer-stresses of 35-40 MPa, which is about 8-9 times the predicted values. If the initial failure of hollow-cylinders is considered, which is assumed represented by the onset of nonlinearity in the experiments, then values of 8-10 MPa outer-stress could be used. In this case, the test stresses are nearly 2 times the predicted value. Accordingly, as discussed above, linear M-C criterion is too conservative if applied to the analysis of model holes. Many possible explanations have been proposed for this observed strengthening, including size effects, nonlinear material behaviour, plasticity, influence of the intermediate principal stress, definition of failure, and assumption of constant Young's modulus during failure.

As an alternative approach, Ewy (1999), proposed a modified Lade criterion for wellbore stability analysis, which is based on a three-dimensional failure criterion that is originally proposed for sands (Lade, 1977). The criterion could account for strengthening effects, if any, from the radial and axial stresses (minimum and intermediate principal stresses) that exist near the wall. The failure criterion has the form,

$$(I_1^{''})^3 / I_3^{''} = 27 + \eta \qquad (7.17)$$

where

$$\begin{aligned}
I_1^{''} &= (\sigma_1 + S_1 - p_o) + (\sigma_2 + S_1 - p_o) + (\sigma_3 + S_1 - p_o), \\
I_3^{''} &= (\sigma_1 + S_1 - p_o)(\sigma_2 + S_1 - p_o)(\sigma_3 + S_1 - p_o)
\end{aligned} \qquad (7.18)$$

S_1 and η are material constants, and p_o is pore pressure. He also propose that S_1 and η are functions of the cohesion and friction angle from triaxial tests as follows,

$$\begin{aligned}
S_1 &= c / \tan\varphi, \\
\eta &= 4\tan^2\varphi(9 - 7\sin\varphi)/(1-\sin\varphi)
\end{aligned} \qquad (7.19)$$

considering the values obtained for the cohesion and friction angle (Chapter 3) for both the M4 and M2, the S_1 and η values could be calculated from (7.19). These values are S_1=1.97 and 5.24 MPa and η= 50.6 and 19.2 for the M4 and M2, respectively. In our tests, p_o could be assumed zero, σ_3=0, and σ_2=0.47σ_1 at the hole wall. The invariants $I_1^{''}$ and $I_3^{''}$ in (7.18) could then be calculated as function of σ_1. These invariants could then be introduced in (7.17) and a value for σ_1 at failure is calculated. Applying this, predicted σ_1 values equal to 16.5 and 19.0 MPa were obtained for the M4 and M2, respectively. This is equal to σ_o values of 7.75 and 8.90 MPa, respectively. These values fail short to describe the expected collapse stresses of the hollow-cylinders (>40 MPa). However, considering the initial failure stresses of about 9 MPa, then the predictions from the criterion does reasonably represent the experiments.

Table 7.3: Outer-stress values from predictions using failure criterion and from experiments

Experimental / Model		Failure initiation (MPa)	Max. test stress (MPa)
Experimental	M4	8-10	35-40
	M2	7-10	35-40
Mohr-Coulomb	M4	4.20	
	M2	5.80	
Modified Lade	M4	7.75	
	M2	8.90	

In literature, it is frequently stated that a main hindrance to arrive at a conclusive judgement of the available wellbore/hollow-cylinder stability approaches (e.g. Mclean and Addis, 1990) is the size effect phenomenon. The size effect data obtained in this thesis could therefore contribute in validating/achieving such judgment. The analysis presented above is not intended to cover all aspects for hollow-cylinder stability or to perform an evaluation of the numerous constitutive models present in literature. Instead, an evaluation of rather simple approaches, with potential for practical application, is preformed. The aforementioned results suggest that if failure initiation (onset of nonlinearity) is considered, then linear-elasticity under-predicts hole stability, whereas a modified Lade criterion seems to reasonably predict the initiation stresses. On the other hand, if failure state is the target, then both approaches are conservative, with varying magnitudes (Table 7.3), and fail to predict the experimentally observed values. In the latter case, more sophisticated constitutive models should be exercised such as those based on bifurcation theories with Cosserat or higher-gradient plasticity models, which have shown success in describing failure and scale effects in hollow-cylinder tests (Sulem *et al.*, 1995).

7.3 FRACTURE PROCESS IN HOLLOW-CYLINDER FAILURE

The experimental results presented in Chapter 5 suggested that the initial fracture mechanism in both the M4 and M2 mixtures is by de-bonding (splitting) at grain boundaries. The fracture process as revealed is that firstly, small splitting cracks, mostly grain boundary cracks, initiate adjacent to the inner-wall in a nearly concentric pattern. Then, with stress increase, cracks start growing and seek coalescence, while new cracks could form deeper in from the wall. Mainly, inter-granular cracks were observed and occasionally intra-granular cracks, which probably depends on microstructural aspects such as grain size, grain stiffness with respect to orientation of crack propagation, and grain/ITZ/matrix strength ratio. In the M2, inter-granular cracking was more observed compared with the M4 mixture. This is thought due to the longer grain boundaries in the M2 that acts as stress concentrators and crack initiation sites. The obtained damage zone did not extend deep in the wall of the different sizes for both mixtures, which is believed due to a strengthening effect from the increase in radial stress away from the inner-wall. Therefore, stress gradients over the wall are seen crucial in determining the extent of damage in hollow-cylinders.
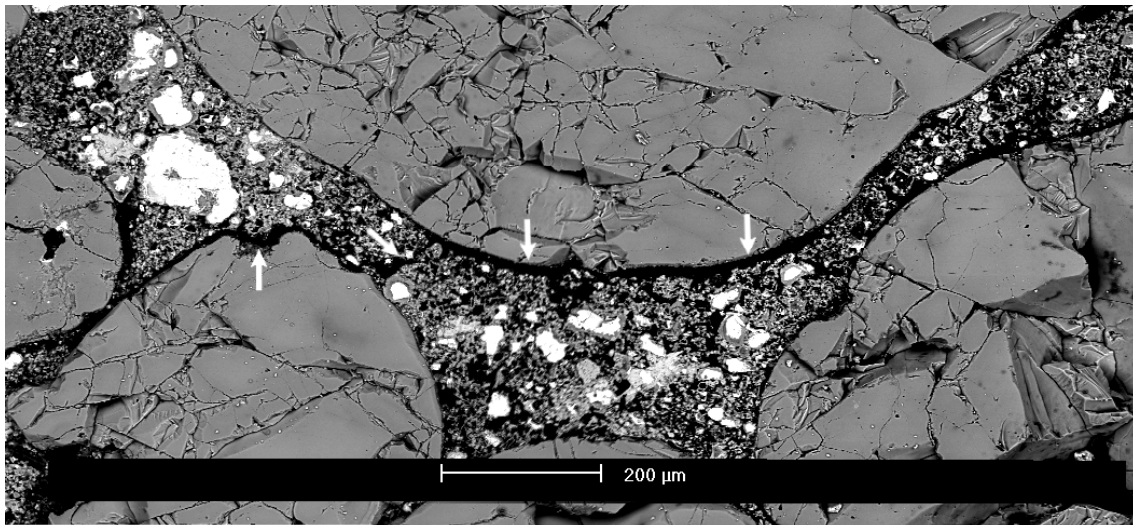
Figure 7.10: Juxtaposing of two micrographs showing grain boundary cracks in the M2 mixture at 5‰ strain. Direction of applied major principal stress is parallel to the long dimension of the image. White arrows in the image point to the crack path. Specimen surface is close to and parallel to the bottom edge of the image.

Observations from micrographs of polished sections, sliced perpendicular to the axisymmetric axis (axial axis), taken using BSE technique in ESEM, have revealed insight into the fracture process at different stages in the loading course. Figure 7.10, shows a crack pattern at 5‰ strain, which is believed close to crack initiation levels. The cracks (black lines of $\cong 20$ µm thickness) are observed along grain sides that are roughly parallel to the direction of major principal stress. Observed as well is crack coalescence through the cement matrix in the same direction, whereas long grain sides that are oblique to that direction with an angle of about 30° or more showed no visible signs of cracking. This conforms to the established view that under compressive loading, splitting type cracks initiate and grow parallel, or within a small inclination, to the major principal direction.

Cracking was noticed to begin either adjacent to the wall or within a close distance from it, which seems to depend on the layout of grains close to the surface. If several grains were aligned parallel to the wall with sufficient boundary lengths to enable crack formation, that develop afterwards to creation of spall slabs, then cracking begins adjacent to the wall with typical depths of 50-100 µm. Otherwise, cracks seemed to begin somewhat deeper in the wall where crack initiation was more favourable in terms of local stresses (Figure 7.10). When spalling occurred, a new stress free surface was created at this location and the aforementioned mechanisms seemed to recur.

Figure 7.11, shows a juxtaposing of two micrographs from a M2 specimen tested to 15‰ strain. The slab development (in two-dimensions in this case) is observed, which formed adjacent to the hole wall along grain boundaries that are aligned roughly parallel to the inner-wall, which is the direction of major principal stress. The cracks are seen to perfectly follow grain boundaries with a more or less fixed crack width in the order of 20-40 µm. These slabs were ready to detach and spall when their ends could meet the wall. This was possible when crack growth was arrested by either a steep inclination of the grain boundary away from the major principal stress direction or by a bulk, relatively stiff, cement matrix with no nearby possibilities for further crack linking or coalescence.

(a)

(b)
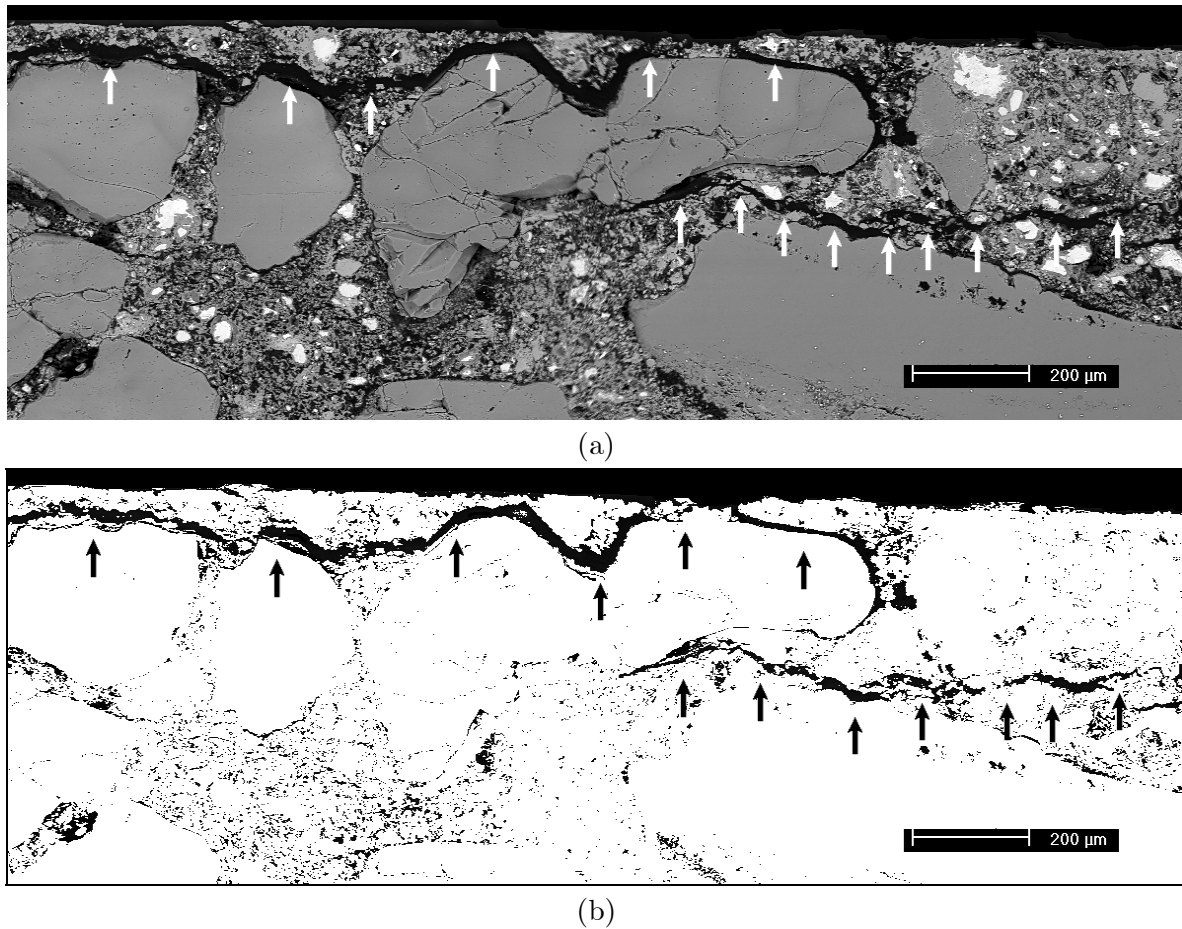
Figure 7.11: (a) Juxtaposing of two micrographs showing slab forming along grain boundaries in the M2 mixture at 15‰ strain. Direction of major principal stress is parallel to the long dimension of the image and inner-wall is located top in the image. (b) The same as in the previous after image processing to make cracks more visible. Black arrows guide crack path.

This mechanism is noticeable in the figure (middle right in the photo) with a crack initiating at grain boundary, and then shortly bridging the matrix to the nearby grain boundary. As the latter grain boundary extends with a steep inclination away from the σ_1 direction, the crack is set off the grain and propagates through the matrix in the direction of major principal stress. It should be noted, however, that it is expected under increasing σ_1 and low confinement that intra-granular cracks and the possibility to break through the cement matrix would increase. These higher loads are also favourable for spalling of the made ready slabs to take place.

An important result from the impregnation experiments was the observed dependence of failure behaviour on size. Figure 7.12, shows an image of a longitudinal cross-section in tested specimens of size A and C from the M4. Both specimens are tested to stress level 35-38 MPa before unloading. The damage depth and cracking pattern are visible and indicate that mesoscopic failure in specimen C is characterized by fracturing over several millimetres depth from the wall, whereas specimen A shows no destructive signs of failure. Intensive spalling activities took place for specimen C, which is not recognized in specimen A. This size effect in failure behaviour was consistently observed in all
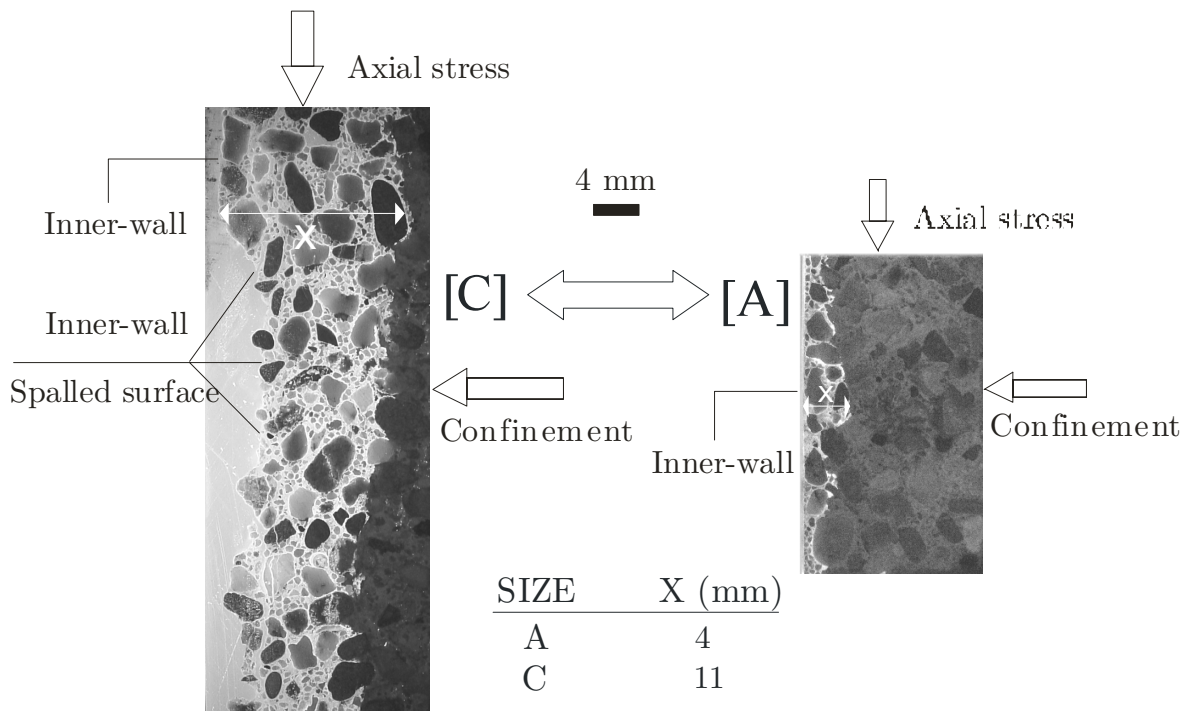
Figure 7.12: Comparison of damage depth and crack pattern for specimens A and C from the M4 mixture. The length X is the average impregnated depth measured over the length of the examined sample. Both specimens are tested to an outer-stress value of about 38 MPa.

performed tests on both mixtures. In general, specimens' size **A** did not show any signs of major damage characteristics during testing, but micro-cracks were detected in the ESEM. Specimens' size **B** showed damage in the form of spalling during testing and fracturing (Figure 5.17). The most damage was observed for specimens' type **C** characterized by intensive spalling and fracturing (Figure 5.19).

The intact state of specimens' size **A** after testing is probably due to a confining effect from the minimum principal stress, the radial stress, across the wall of the cylinder. A radial stress gradient acts across the wall concurrent with the tangential stress as discussed in § 7.1.2. This radial stress is equal to zero at the hole wall and increases gradually towards the outer-wall. Due to size effect, the rate of stress increase in smaller specimens is higher as compared with larger specimens. This means that at the same distance from a hole-wall, a higher confinement (radial stress) exists in the A size specimens as compared with the C size specimens. Therefore increased resistance develops against crack growth in the A size specimens, which contribute to the observed size dependent fracture behaviour. In addition to the confining effect from the radial stress, additional confinement arises owing to a geometrical effect from the curvature and surface area of the inner-hole. As the inner-hole size decreases and becomes proportionate in size with its neighbouring grains, the curvature of the inner-wall produces a confining and stabilizing effect. This pressure acts in the same manner as the radial stress hence counteracting tensile stress concentrations and increasing contact between surfaces of existing cracks. Surface area and volumetric effects were considered a source of size effect in hollow-cylinder tests by many researchers (e.g. Brown and Gonano, 1975).

7.4   PFC2D APPROACH TO SIZE EFFECT AND FRACTURE

In the numerical part of this study (Chapter 6), simulations were performed using the PFC2D discrete element program. Despite being a simplified approach to model complex material such as concrete, it showed plausible success in reproducing some of its failure characteristics and size behaviour. The model results were qualitatively comparable to experimental results rather than quantitative. This, however, could be attributed to e.g. limitations of using a two-dimensional model in describing three-dimensional nonlinear processes. Vonk (1993), notes that in numerical simulations of compression failure, the possibility of translating three-dimensional properties into two-dimensional ones to obtain a quantitatively correct description is a question which cannot be yet answered. Recently, Lilliu and Van Mier (2003), showed a marked difference between 2D and 3D lattice type simulations, particularly in the pre-peak region. Their 3D simulations resulted in increased nonlinearity in pre-peak and more ductility in the post-peak as compared with the frequently observed brittleness form 2D simulations. Another complicating factor witnessed during modelling was the optimization or calibration of the model parameters. Since a lack of ample understanding yet exists of the physical mechanisms during failure of materials such as concrete and rock under various modes, a lack arises of what constitutes a best and most relevant set of laboratory-scale properties to be used as calibration parameters. According to Potyondy and Autio (2001), the current understanding of the PFC calibration process is incomplete since e.g. it is not known how to construct a PFC material that reproduces a given biaxial strength envelope or that satisfies a given ratio of f_c/f_{spl}. This was also observed in the current analysis (§ 6.3.4) with f_c/f_{spl} values that are in the order of 3-4 as compared with $\cong$9 in the experiments. Also the gradient of the biaxial strength envelope (equals φ if M-C criterion is fitted to the results) was much less than in experiments. Effect of these factors on model results is not clear as well.

It was shown most important to include fracture patterns in the calibration process to ensure model objectivity and correctness in simulating the experiments. It appeared possible during sensitivity analysis and optimization to arrive at two different sets of model parameters that both satisfy a selected set of calibration parameters. One of them only, however, was able to produce comparable fracture behaviour as in the experiments. This was most pronounced in the hollow-cylinder simulations for its distinctive fracture pattern and failure process. It was also recognized that the calibration procedure could be sensitive to test type (applied stresses and specimen geometry). Individual calibration was necessary for the different tests since calibration parameters from uniaxial compression simulations resulted in what seemed fallacious results in hollow-cylinder simulations.

With regard to size effect, analyses were performed under different load modes (i.e. uniaxial compression, biaxial compression, Brazilian splitting, and hollow-cylinder test). The results showed the particle size in PFC2D to influence the simulations results, if scaling relations were not used of the type implemented in the FishTank of PFC. A dependency exists of results on a discretization parameter defined by the ratio between specimen dimension and average particle radius in the assembly ($L/\tilde{R}$). With respect to hollow-cylinder tests, results from size effect simulations presented qualitatively comparable trends to those obtained experimentally. In Brazilian splitting simulations, trends similar to those reported in literature were found. With regard to uniaxial and biaxial
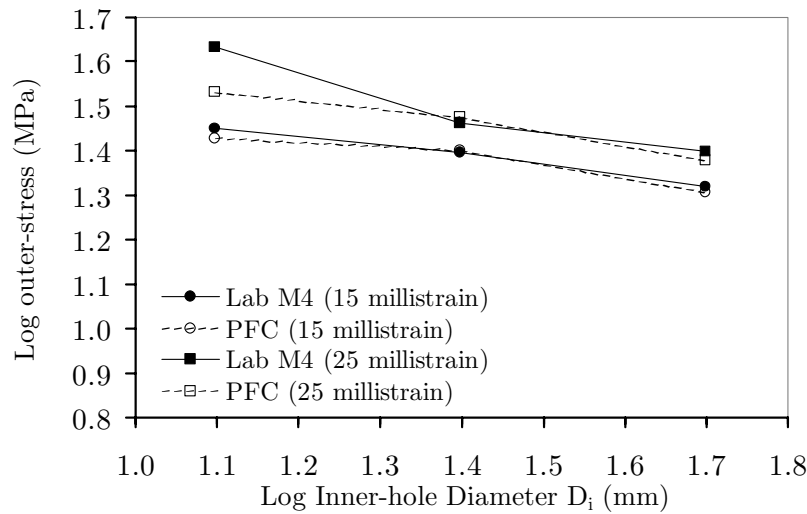
Figure 7.13: Comparison of size effect trends from PFC2D simulations and hollow-cylinder experiments at tangential strain levels of 15 and 25‰ strain.

compression simulations, there seem to be no obvious sight yet experimentally over their size effect behaviour due mainly to artefacts and influence of test boundary conditions. The simulations results from these tests were not evaluated or compared to experimental results and their outcome could, therefore, be argued as physically representative.

Figure 7.13, tentatively compares size effect trends at 15 and 25‰ strain from hollow-cylinder tests on the M4 and PFC simulations. A good agreement is observed for the 15‰ strain results and less comparable for the 25‰ strain, especially at the smallest size. This comparable trend behaviour was not attained for strain levels smaller than 10‰ strain (see Chapter 6) due to incompatibility of model's stress-strain behaviour with experiments. Possible explanations for such incompatibility are related to those abovementioned with regard to model limitations. Similarly, extrapolation of simulation results beyond the tested size range was not feasible. A major hindrance was differing failure behaviour observed at elevated stress levels, being more accelerated and pronounced in the simulations (Figure 7.14a). This caused flattening in their stress-strain response (Figure 6.19) as compared with the strain hardening behaviour in the experiments. This effect will be more marked for larger sizes, due to size effect, and the uncertainty would therefore increase. The differing damage behaviour under increased load could be understood from the simplified material structure in the model and suggests the need for more details to be included (e.g. cement matrix and interface). Since the cement-matrix phase is not represented in the model, all damage is forced to take place through contact failure and crack formation. The increased cracking could thus be an artefact due to this simplification. In real concrete, the matrix phase would inevitably contribute in the load-deformation response and processes within the matrix such as pore collapse and plastic sliding would redistribute local stresses and modify the energy balance during failure. 3D fracture processes in real specimens as compared to the simplified 2D simulations should not be overlooked as well.

The success of the model in capturing size effects is thought attributing to its discrete nature and heterogeneous structure. The discrete character provides free crack initiation and interaction possibilities and allows for their ensuing redistribution of local stresses.
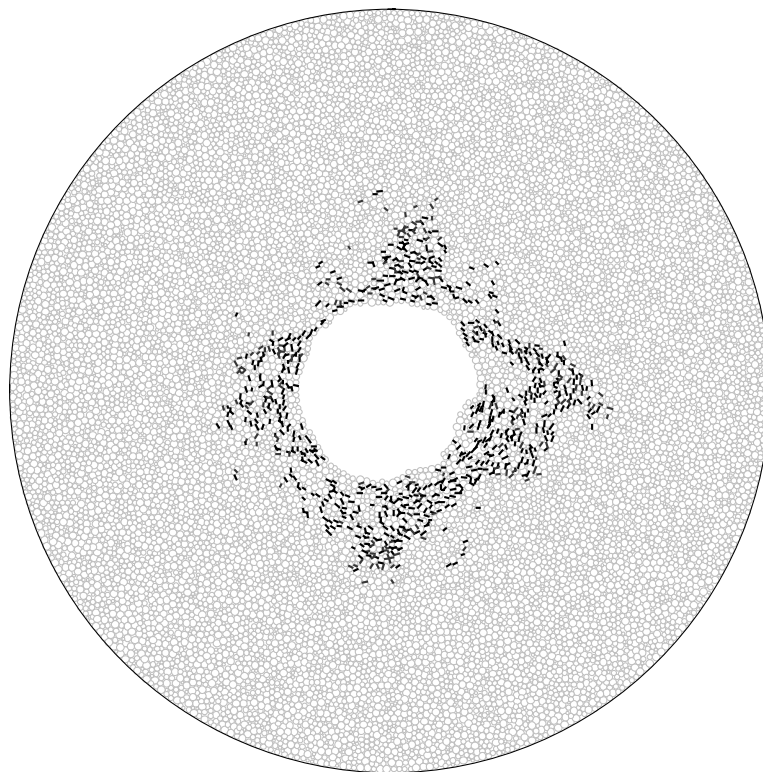
(a)
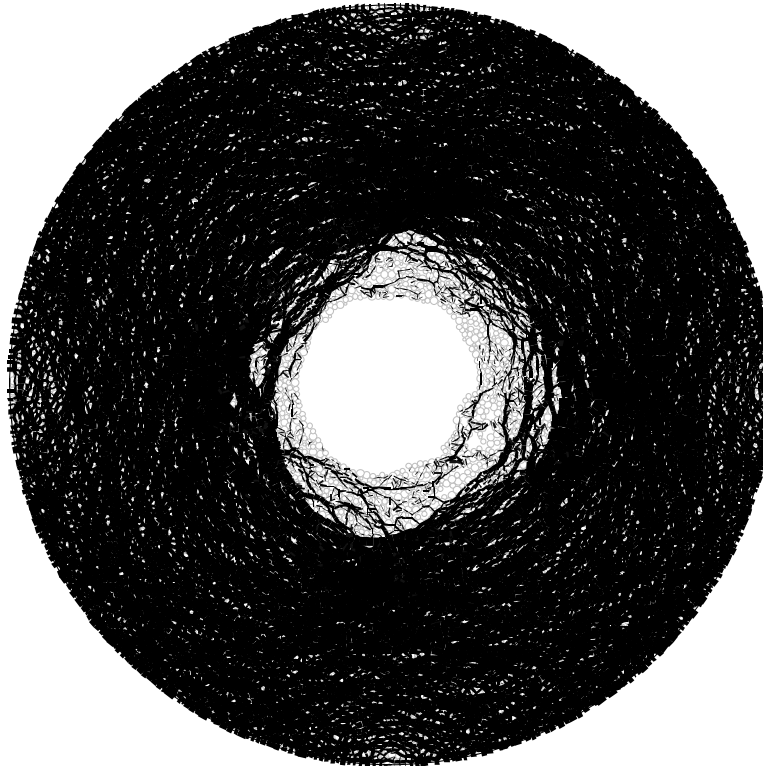
(b)

Figure 7.14: (a) Crack pattern and (b) contact force distribution in particle assembly from hollow-cylinder simulation for size C at tangential strain value of 6.8% and $\cong$26 MPa outer-stress.

This emphasises the role of heterogeneity in producing size effects in mechanical testing of composite materials such as concrete. Vonk (1993), successfully simulated fracture processes and shape effect in uniaxial compression tests on concrete using discrete elements. His model was more detailed since he described concrete as three-phase material—cement matrix, the ITZ, and angular shaped grains—and specified different properties to each phase raising accordingly the heterogeneity level in the model. Nevertheless, he recommends for more quantitative model results, extra heterogeneity and detail to be incorporated. In discrete simulations, raising heterogeneity levels and detail result in noticeably increased computational demand, which limits the applicability of the model for large-scale computations, such as those used for size effect analyses.

A noteworthy observation in Figure 7.14b is the redistribution of local contact forces (marked by black lines of thicknesses corresponding to the magnitude of the resultant contact force) due to cracking. This force relaxation mechanism shows the gradual development of damage from around the inner-hole towards the outer-wall. Higher force concentration is found adjacent to the inner-boundary with force chains that are sub-parallel to the hole wall, which coincides with the σ_1 direction. This agrees with the theoretical analysis of stresses inside a hollow-cylinder that suggests the major principal stress to be equal to the tangential stress.

A curious feature of the crack pattern in Figure 7.14a, is what appears as asymmetric crack behaviour with forming of V- or cusp-shaped failure zones. These shapes resemble borehole breakouts, in which the circular bore becomes modified to an elliptical form in response to the locally concentrated stress field around the borehole. A major difference with breakout formation, however, is that developed in the model in roughly two perpendicular directions, whereas in laboratory or filed breakout formations they are commonly observed oriented in one direction. The observed failure formation in the model, therefore, could better be regarded as indicative of localization at later stage in the fracture process. No clear and satisfactory explanation was found for this behaviour.

Concisely, the PFC2D model was experienced capable of qualitatively reproducing with reasonable success fracture features and size effect behaviour in concrete-like materials. In order to use the model for predicting such processes with quantitatively reproducible results, additional effort is needed. This could be achieved through increasing the level of detail and heterogeneity in the model, on the account of computational efficiency, or alternatively an enhancement of the calibration procedure could be accounted for. The latter is only achievable if fracture mechanisms are better understood and material parameters could be identified that are most relevant to failure and deformation processes under various load modes. In this case, different calibration parameters could be suggested depending on the test or loading type that are expected to present most representative simulations in this case. This calibration procedure should be always supplemented with experimentally observed fracture behaviour to guarantee the model objectivity.

Chapter 8

CONCLUSIONS AND RECOMMENDATIONS

8.1 GENERAL

The objective of this thesis was to investigate physically possible size effects on strength and fracture behaviour in hollow-cylinder tests using concrete specimens subject to external hydrostatic stress. For this purpose, 52 carefully designed hollow-cylinder experiments were performed on two-model concrete mixtures of 2 and 4 mm maximum aggregate size. The hollow-cylinder tests provide a multiaxial compressive stress condition and practically simulate stress situations around underground openings and deep boreholes. In addition, they offer the possibility for size effect investigation under three-dimensional scaling conditions.

For the experiments, a high-pressure test cell (maximum test pressures of 40 MPa) was developed and debugged that enables testing of hollow-cylinders with dimensions up to 200 mm outer-diameter and 300 mm length. The cell was equipped to accommodate smaller scaled specimens in a size range 1:4. The set-up was supplemented with novel measuring device for monitoring the deformations taking place inside the inner-hole, both in radial and axial directions. Further, two concrete mixtures were designed and characterized that model weak quasibrittle materials with uniaxial compressive strength in the order 10-15 MPa. All tested hollow-cylinder specimens were impregnated and obtained crack patterns and fracture mechanisms were examined.

Numerically, a distinct element program (PFC2D) was utilized to analyze the experimental outcome. The model belongs to the class of mesoscopic discrete models, which incorporate an internal length scale in their formulation. The model offers both large deformation capacity and unrestricted crack formation capabilities. The modelling took place through firstly, developing a numerically synthetic material that is calibrated for its (micro-) parameters using a set of laboratory mechanical tests. Afterwards, a model was developed to simulate the hollow-cylinder test in two-dimensions. Finally, analyses of the hollow-cylinder test and its size dependence using the simulated model material and test procedure were performed.

8.2   Size effect and fracture process

- Size effect was observed in the strength of hollow-cylinder concrete specimens in a scale range 1:4. A consistent decease of strength with size was recorded up to 32% and 44% for specimens with d_{max}=4 and 2 mm, respectively. At least six tests per size and for each mixture were conducted to account for scatter in the results. A scatter in the results in the range of 8 to 16% was marked for all sizes from both mixtures that are relatively low for concrete-like materials.

- Size effect in hollow-cylinder tests, as observed in the experiments conducted in this study and from the performed analyses, is a phenomenon and a process resulting from mutually and commensurate occurring processes and mechanisms. It could be stated that this size effect is a result of complex combination of structural factors (e.g. geometry imposed effects such as stress gradient and surface area and volumetric effects), mechanical processes of failure including deformation, and material characteristics in terms of heterogeneity and fabric. Existing theories, hypothesis, and concepts to explain size effect (statistical, energetic, or related to violation of similarity laws) are reasonable, but no theory seems to exist that encompasses these various factors and processes since it is not clear which factor has a prevailing influence, if any. This is more pronounced in compressive failure processes, being more complex, with most of the factors often act combined and hence emphasizing only one factor in a model or hypothesis and neglecting others brings an error to the model, which could be significant. The isolation of one of the factors to be independently studied experimentally is a difficult task and numerical simulations based on physical hypothesis could form a favourable supplement.

- Observed size effect was dependent on aggregate size, being stronger for the 2 mm mixture. A power relation could reasonably describe the average size effect trends, on a bi-logarithmic plot of size versus strength, with an exponent of –0.19 and –0.26 for the specimens with d_{max}=4 and 2 mm, respectively.

- Analysis of the results showed the onset of size effect in the experiments as linked to commencement of nonlinearity in the stress-tangential strain response. This took place at tangential strain levels in the order of 5‰ strain. At this strain level, microscopic examination of fracture processes showed small boundary cracks to exist with barely any crack interaction or propagation activities. This implies that material related factors contributing to onset of size effect should be linked to processes taking place at crack initiation. These are considered largely due to heterogeneity and distribution of defects in the material.

- Closed-form solution with stress-averaging functions showed stress gradients to noticeably contribute to the overall observed size effect. These stress gradients are imposed by the geometry of the hollow-cylinder and form a structural contribution to the observed size effects.

- The predicted size effect according to Weibull theory, with non-uniform triaxial stress considerations, described with reasonable success the obtained size effect trends near crack initiation levels.

- Both the SEL for compression and MFSL size effect models were able to fit the size effect data with close to one correlation coefficient. An assumption of material homogeneity in the SEL for compression, however, contradicts the experimental data in terms of material inhomogeneity and crack pattern. When these were taken into account, the model reverts to the form of LEFM and failed to fit the results.

- Microscopic examination of the fracture process revealed that failure initiated through small splitting cracks along grain-boundaries oriented parallel to the maximum principal stress. These cracks developed firstly close to the inner-hole and under increase of load have developed further deep in from the wall in a concentric pattern. They were observed to propagate either inter- or intra-granularly parallel to the principal stress direction and preferably along the spring-lines of the hole, but occasionally they turned to meet the surface of the inner-wall. Coalescence of these micro-cracks resulted in the formation of thin slabs, which then detached and started spalling into the hole. The fracture process seemed to sequentially repeat itself with new extensional cracks of small width forming behind the formed spall zones.

- The size of the damage zone, defined by the thickness of impregnation, was size dependent with a factor of nearly three in the tested scale range. The larger the size, the more intense and larger spread of damage was observed.

- Three-dimensional size effect experiments under complex geometric and loading conditions, as provided by the hollow cylinder test, appeared as a powerful tool for exploring and understanding fracture processes of quasibrittle materials and their size dependence. This would further assist in validating fracture models and identifying material parameters to describe material behaviour.

8.3 DISTINCT ELEMENT ANALYSIS

- Distinct Element simulations using PFC2D was found capable of qualitatively reproducing (with reasonable success) fracture features and size effect behaviour observed in the experiments. In order to use the model for predicting such processes with quantitatively reproducible results, additional model development is needed. A possibility is through increasing the level of detail and heterogeneity in the model, on the account of computational costs, or alternatively an enhancement of the calibration procedure could be accounted for. The latter is only achievable if fracture mechanisms are better understood and material parameters could be identified that are most relevant to failure and deformation processes under various load modes. Different calibration parameters could be suggested depending on the test or loading type that are expected to present most representative simulations in this case. This calibration procedure should be always supplemented with experimentally observed fracture behaviour to guarantee the objectivity of the model's outcome.

- The model showed pseudo-linear stress-tangential strain behaviour when compared with the hollow-cylinder experiments. The ratio f_c/f_{spl} from the calibrated specimens was lower than that obtained in the experiments. The model also under-predicted the biaxial strength envelope.

- Size effect simulations performed under different load modes (i.e. uniaxial and biaxial compression, Brazilian splitting tensile, and hollow-cylinder test) showed the model to depend on a discretization parameter defined by the ratio between specimen dimension and average particle radius in the assembly. Results from size effect hollow-cylinder simulations presented qualitatively comparable trends to those obtained experimentally. In the Brazilian splitting simulations, decreasing trends similar to those reported in literature were found. The compressive test simulations resulted in an increased strength with size for both uniaxial and biaxial compressive load conditions.

8.4 EXPERIMENTAL PROCEDURES

- Three-dimensional size effect experiments are highly demanding in terms of design, preparation, and application. Geometrically similar specimens needed to be prepared in the same manner and to be tested under the same boundary conditions. Verification tests combined with analytical and numerical analysis were performed to ensure that the assumptions and objectives made in the experimental design were satisfied. They were also used to investigate and quantify structural effects, which are possibly introduced during testing.

- The nature of the mixtures used (low strength, gap-graded, and high w/c ratio) showed a strong strength-time dependence and presented difficulties during casting and preparation of specimens for testing. The mixtures were sensitive for variations in the casting procedure (e.g. mixer type) and compaction process (vibration style and time). A consistent and well-defined specimen preparation procedure and test scheme was implemented throughout the experimental program, which resulted in a good quality control and managed to obtain a relatively low scatter in the experimental results.

- The application of a fluid pressure along the circumference of the cylinder is advantageous in terms of boundary restraint and load application procedure since it is almost unrestrained.

8.5 SUGGESTIONS FOR FUTURE WORK

Several aspects of the size effect and fracture phenomena in hollow-cylinder tests could be further investigated. These include:

- A theory that encompasses the various physical aspects contributing to size effect and failure in concrete under multiaxial compression loading is yet not available. The reason for this is the incomplete knowledge of these physical aspects and their role in the processes leading to the phenomena. Further efforts should take place in order to enhance this knowledge through physically based experimental and numerical work. This possibly applies to other loading modes as well such as uniaxial compression and mixed failure modes.

- Attention should be paid to the onset of size effect and the factors contributing to it in experimental studies of size effect under various loading modes. This can assist in understating the physical processes underlying the phenomenon.

- Size effect under various triaxial loading modes could be investigated using the hollow-cylinder test geometry, which would be advantageous in comprehending the phenomenon.

- Moisture and pore pressure effects are known to noticeably influence size effect and failure behaviour under various loading modes. A systematic study for their contribution in hollow-cylinder tests, similar to those performed in this study, would provide both more physical insight into the phenomena and an experimental data set useful for modelling purposes.

- For the problem of wellbore stability, it would be advantageous to extend and supplement the results obtained in this work with test results on natural rocks such as those encountered in underground reservoirs.

- Discrete element analysis appeared well suited to investigate size effect and fracture behaviour in heterogeneous disordered materials such as concrete. In order to get a better comparison with experiments, the analysis should be better extended to three-dimensional and the microstructure better be modelled in more detail through differentiating between the different material phases.

Bibliography

ANDREEV, G. E. (1995). Brittle failure of rock materials, A. A. Balkema, Rotterdam, p. 446.

ANTHEUNIS, D., VRIEZEN, P. B., SCHIPPER, B. A., and VLIS, A. C. VAN DER. (1976). Perforation collapse: Failure of perforated friable sandstones, *SPE-European spring meeting*, SPE 5750, Amsterdam, pp. 13.

BAARS, STEFAN VAN. (1996). Discrete element analysis of granular materials, Ph.D., Delft University of Technology, p. 133.

BAECHER, G.B., and EINSTEIN, H.H. (1981). Size effect in rock testing, *Geophysical Research Letters*, 8(7), pp. 671-674.

BATHURST, R.J., and ROTHENBURG, L. (1992). Investigation of Micromechanical Features of Idealized Granular Assemblies Using DEM, *Engineering Computations*, 9, pp. 199-210.

BAZANT, Z. P., and CEDOLIN, L. (1991). Stability of structures: elastic, inelastic, fracture, and damage theories, Oxford University Press, New York, p. 984.

BAZANT, Z. P., and PLANAS, J. (1998). Fracture and size effect in concrete and other quasibrittle materials, CRC Press, Boca Raton, p. 616.

BAZANT, Z. P. (2002). Scaling of structural strength, Hermes Penton, London, p. 280.

BAZANT, Z.P. (1984). Size effect in blunt fracture: Concrete, rock, metal, *Journal of Engineering Mechanics*, 110(4), pp. 518-535.

BAZANT, Z.P., LIN, F-B., and LIPPMANN, H. (1993). Fracture energy release and size effect in borehole breakout, *International Journal for numerical and analytical methods in Geomechanics*, 17, pp. 1-14.

BAZANT, Z.P., and XIANG, Y. (1997). Size effect in compression fracture: Splitting crack band propagation, *Journal of Engineering Mechanics*, 123(2), pp. 162-172.

BAZANT, Z.P. (1999). Size effect on structural strength: a review, *Archive of Applied Mechanics*, 69, pp. 703-725.

BIENIAWSKI, Z. T. (1967a). Mechanism of brittle fracture of rock: Part I-theory of the fracture process, *International Journal of Rock Mechanics and Mining Science & Geomechanics Abstracts*, 4(4), pp. 395-404.

BIENIAWSKI, Z. T. (1967b). Mechanism of brittle fracture of rock, CSIR, Pretoria, p.

BIENIAWSKI, Z. T. (1974). Estimating the strength of rock materials, *Journal of the South African Institute of Mining and Metallurgy*, 74, pp. 312-320.

BROWN, E. T., and GONANO, L.P. (1975). An analysis of size effect behaviour in brittle rock, *Proceedings Second Australia-New Zeeland Conference on Geomechanics*, National Conference Publication No 75/4, Brisbane, Australia, pp. 139-143.

BURLION, N., PIJAUDIER-CABOT, G., and DAHAN, N. (2001). Experimental analysis of compaction of concrete and mortar, *International Journal of Numerical and Analytical Methods in Geomechanics*, 25, pp. 1467-1486.

BURTSCHER, S. (2002). Size effect of concrete and sandstone in compression, Ph.D. thesis, Technical University of Vienna, Austria, p. 129.

CARPINTERI, A., and CHIAIA, B. (1995). Multifractal nature of concrete fracture surfaces and size effects on nominal fracture energy, *Materials and Structures (RILEM)*, 28, pp. 435-443.

CARPINTERI, A., CHIAIA, B., and FERRO, G. (1995). Multifractal scaling law: an extensive application to nominal strength size effect of concrete structures, (No. 51). Politecnico di Torino, Dipartimento di Ingegneria Strutturale, pp. 145.

CARPINTERI, A., FERRO, G., and MONETTO, I. (1999). Scale effects in uniaxially compressed concrete specimen, *Magazine of Concrete Research*, 51(3), pp. 217–225.

CARTER, B. J. (1992). Size and stress gradients effects on fracture around cavities, *Rock Mechanics and Rock Engineering*, 25(3), pp. 167-186.

COMMISSION ON SCALE EFFECTS IN ROCK MECHANICS, ISRM. (1995). Scale effects in the determination of rock mass properties, (No. Final Report). International Society for Rock Mechanics (ISRM), Tokyo, Japan, pp. 16.

CUNDALL, P.A. (1971). A computer model for simulating progressive, large scale movements in blocky rock systems, *International Symposium on Rock Fracture*, ISRM, Nancy, France, pp. II-8.

CUNDALL, P.A., and STRACK, O.D.L. (1979). A discrete numerical model for granular assemblies, *Geotechnique*(29), pp. 47-65.

CUNDALL, P.A. (1988). Formulation of a three-dimensional distinct element model — part I. A scheme to detect and represent contacts in a system composed of many polyhedral blocks., *International Journal of Rock Mechanics and Mining Science & Geomechanics Abstracts*, 25(3), pp. 107-116.

CUNDALL, P.A., and CARRANZA-TORRES, C. (2004). Micromechanical models for rock behavior, *International Journal of Rock Mechanics and Mining Sciences*, pp.???

DAEMEN, J.J.K., and FAIRHURST, C. (1971). Influence of failed rock properties on tunnel stability, *Proc. 12th U.S. Symposium on Rock Mechanics, Dynamic Rock Mechanics*, AIME, New York, pp. 855-875.

DIAMOND, S. (2004). The microstucture of cement paste and concrete-a visual primer, *Cement & Concrete Composites*, 26, pp. 919-933.

DIEDERICHS, M. S., KAISER, P. K., and EBERHARDT, E. (2004). Damage initiation and propagation in hard rock during tunnelling and the influence of near-face stress rotation, *International Journal of Rock Mechanics and Mining Sciences*, 41(5), pp. 785-812.

DOBEREINER, L., and DE FREITAS, M. H. (1986). Geotechnical properties of weak sandstones, *Géotechnique*, 36(1), pp. 79-94.

EBERHARDT, E., STIMPSON, B., and STEAD, D. (1999). Effects of grain size on the initiation and propagation thresholds of stress-induced brittle fractures, *Rock Mechanics and Rock Engineering*, 32(2), pp. 81-99.

EINSTEIN, H.H., and DERSHOWITZ, W.S. (1990). Tensile and shear fracturing in predominantly compressive stress fields - a review, *Engineering Geology*, 29, pp. 149-172.

EWY, R.T., COOK, N. G. W., and MYER, L.R. (1988). Hollow-cylinder tests for studying fracture around underground openings, *Key Questions in Rock Mechanics*, C. E. AL. (*ed.*), Balkema, Rotterdam, pp. 67-73.

EWY, R.T., and COOK, N.G.W. (1990a). Deformation and fracture around cylindrical openings in rock-II. Initiation, growth an dinteraction of fractures, *International Journal of Rock Mechanics and Mining Sciences & Geomechanics Abstracts*, 27(5), pp. 409-427.

EWY, R.T., and COOK, N.G.W. (1990b). Deformation and fracture around cylindrical openings in rock-I. Observations and analysis of deformations, *International Journal of Rock Mechanics and Mining Sciences & Geomechanics Abstracts*, 27(5), pp. 387-407.

EWY, R.T. (1999). Wellbore-stability prediction by use of a modified Lade criterion, *SPE Drilling & Completion*, 14(2), pp. 85-91.

GAY, N.C. (1973). Fracture growth around openings in thick-walled cylinders of rock subjected to hydrostatic compression, *International Journal of Rock Mechanics and Mining Sciences & Geomechanics Abstracts*, 10, pp. 209-233.

GOODMAN, R. E. (1980). Introduction to rock mechanics, Wiley, p. 576.

GOODMAN, RICHARD E. (1989). Introduction to rock mechanics, *2nd*, Wiley, p.

GRAMBERG, J. (1989). A non-conventional view on rock mechanics and fracture mechanics, Balkema, Rotterdam, p.

GUENOT, A. (1987). Constraintes et ruptures autour de forages petroliers, 6th cong. *ISRM*, Balkema, Rotterdam, Montreal, pp. 109-110.

GUENOT, A. (1989). General Report: Instability problems at great depth drilling boreholes and wells, *Rock at Great Depth*, MAURY and FOURMAINTRAUX (*eds.*), Balkema, Rotterdam, pp. 1277-1286.

HAIMSON, B.C., and HERRICK, C.G. (1989). Borehole breakouts and in situ stress, *Drilling Symposium*, J. C. ROWLEY (*ed.*), The Petroleum Division, ASME, Houston, Texas, USA, pp. 17-22.

HALLBAUER, D.K., WAGNER, H., and COOK, N. G. W. (1973). Some observations concerning microscopic and mechanical behavior of quartzite specimens in stiff, triaxial compression tests, *International Journal of Rock Mechanics and Mining Sciences*, 10(6), pp. 713.

HAZZARD, J.F., YOUNG, R.P., and MAXWELL, S.C. (2000). Micromechanical modeling of cracking and failure in brittle rocks, *Journal of Geophysical Research*, 105(B7), pp. 16,683-16,697.

HEATH, L.J. (1965). Variations in permeability and porosity of synthetic oil reservoir rock-methods of control, *Soc. Petrol. Engrs. J.,*, 5, pp. 329-332.

HOEK, E., and BROWN, E. T. (1982). Underground excavations in rock, *rev. ed.*, Institution of Mining and Metallurgy, London, p. 527.

HOEK, P. J. VAN DEN, SMIT, D. -J., KOOIJMAN, A. P., BREE, PH. DE, and KENTER, C. J. (1994). Size-dependency of hollow-cylinder stability, *EUROCK '94 - Rock Mechanics in Petroleum Engineering*, Delft, The Netherlands, pp. 191-197.

HOEK, P.J. VAN DEN , HERTOGH, G.M.M., KOOIJMAN, A.P., BREE, PH. DE, KENTER, C.J., and PAPAMICHOS, E. (2000). A new concept of sand production prediction: theory and laboratory experiments, *SPE Drill. & Completion*, 15(4), pp. 261-273.

HOSKINS, E.R. (1969). The Failure of Thick-Walled Hollow Cylinders of Isotropic Rock, *International Journal of Rock Mechanics & Mining Sciences*, 6, pp. 99-125.

HSU, T.T.C, SLATE, F.O., STURMAN, G.M., and WINTER, G. (1963). Microcracking of plain concrete and the shape of the stress-strain curve, *Journal of the American Concrete Institute*, 60, pp. 209.

HUANG, H. (1999). Discrete element modeling of tool-rock interaction, Ph.D. dissertation, University of Minnesota, Minneapolis, USA, p 131.

ISSA, S. A., ISLAM, M. S., YOUSIF, A. A., and ISSA, M. A. (2000). Specimen and aggregate size effect on concrete compressive strength, *Cement, Concrete, and Aggregates*, 22(2), pp. 103-115.

ITASCA CONSULTING GROUP, INC. (2003). "PFC^{2D} Particle Flow Code in 2 Dimensions", Itasca, Minneapolis.

JAEGER, J. C., and COOK, N. G. W. (1979). Fundamentals of Rock Mechanics, *3rd ed.*, Chapman and Hall, London, p. 593.

JAMET, P., MILLARD, A., and NAHAS, G. (1984). Triaxial behaviour of a micro-concrete complete stress-strain curves for confining pressures ranging from 0 to 100 MPa, *RILEM/CEB Symposium on concrete under multiaxial conditions*, Presses de l'Université Paul Sabatier, Toulouse, France, pp. 133-140.

KEMENY, J.M., and COOK, N. G. W. (1991). Micromechanics of deformation in rocks, *Toughening Mechanisms in Quasi-Brittle Materials*, S. P. SHAH (*ed.*), Kluwer Academic Publishers, pp. 155-181.

KOOIJMAN, A.P., VAN DEN ELZEN, M.G.A., and VEEKEN, C.A.M. (1991). Hollow-cylinder collapse: measurement of deformation and failure in an X-ray CT scanner, observation of size effect, *Rock Mechanics as a Multidisciplinary Science*, J. ROEIGERS (*ed.*), Balkema, Rotterdam, pp. 657-666.

KRANZ, R.L. (1983). Microcracks in rocks: a review, *Tectonophysics*, 100, pp. 449-480.

LADE, P.V. (1977). Elasto-plastic stress-strain theory for cohesionless soil with curved yield surfaces, *International journal of soilds and structures*, 13, pp. 1019-1035.

LILLIU, G., and VAN MIER, J.G.M. (1999). Analysis of crack growth in the Brazilian test, *Construction materials: Theory and applications (Hans-Wolf Reinhardt 60th Birthday commemorative volume)*, R. ELIGEHAUSEN (*ed.*), Ibidem-Verlag, Stuttgart, pp. 123-137.

LILLIU, G., and VAN MIER, J.G.M. (2003). 3D lattice type fracture model for concrete, *Engineering Fracture Mechanics*, 70, pp. 927-941.

MALONEY, S., and KAISER, P.K. (1989). Results of borehole breakout simulation tests, *Rock at Great Depth*, MAURY and FOURMAINTRAUX (*eds.*), Balkema, Rotterdam, pp. 745-752.

MCLEAN, M. R., and ADDIS, M. A. (1990). Wellbore stability analysis: A review of current methods of analysis and their field application, *IADC/SPE Drilling Conference*, Houston, Texas, USA, pp. 261-274.

MIER VAN, J. G. M. (1984). Strain softening of concrete under multiaxial loading conditions, Eindhoven University of Technology, Eindhoven, p. 349.

MINDESS, S., YOUNG, J. F., and DARWIN, D. (2003). Concrete, *Second*, Prentice-Hall, Upper saddle River, New Jersey, p. 644.

MOGI, K. (1967). Effect of the intermediate principal stress on rock failure, *Journal of Geophysical Research*, 72(20), pp. 5117-5131.

MÜHLHAUS, H.-B., and VARDOULAKIS, I. (1987). The thickness of shear bands in granular materials, *Geotechnique*, 37, pp. 271-283.

NEWMAN, J.B. (1979). Concrete under complex stress, *Developments in Concrete Technology*, F. D. LYDON, ed., Applied science publisher Ltd., London, pp. 151-220.

ORESKES, N., SHRADER-FRECHETTE, K., and BELITZ, K. (1994). Verification, validation, and confirmation of numerical models in the earth sciences, *Science*, 263, pp. 541-646.

PATERSON, M. S. (1978). Experimental Rock Deformation - The Brittle Field, Springer, Berlin, p. 254.

PERIE, P.-J., and GOODMAN, R.E. (1989). Evidence of new failure patterns in a thick-walled cylinder experiment, *Drilling Symposium*, J. C. ROWLEY (*ed.*), The Petroleum Division, ASME, Houston, Texas, USA, pp. 23-27.

POTYONDY, D. A., and CUNDALL, P. (1999). Modeling of notch formation in the URL mine-by tunnel: Phase IV - Enhancements to the PFC model of rock, (No. 06819-REP-01200-10002-R00), pp. 159.

POTYONDY, D.A., and AUTIO, J. (2001). Bonded-particle simulations of the in-situ failure test at Olkiluoto, *Rock mechanics in the national interest*, ELSWORTH, TINUCCI, and HEASLEY (*eds.*), Swets & Zeitlinger Lisse, pp. 1553-1560.

POTYONDY, D.A., and CUNDALL, P.A. (2004). A bonded-particle model for rock, *International Journal of Rock Mechanics & Mining Sciences*, 41, pp. 1329-1364.

RILEM, T. C. QUASIBRITTLE FRACTURE SCALING. (2004). Quasibrittle fracture scaling and size effect, *Materials and Structures*, 37, pp. 28.

RILEM TC-148. (2000). Strain softening of concrete-Test methods for compressive softening, test method for measurement of the strain-softening behaviour of concrete under uniaxial Compression, *Materials and Structures*, 33, pp. 347-351.

RINGSTAD, C., BREVIK, I, ADDIS, M.A., and SANTARELLI, J.F. (1993). Scale effects in hollow cylinder tests, *2nd workshop on Scale effects in rock masses*, P. DA CUNHA (*ed.*), Balkema, Rotterdam, Lisbon, Portugal, pp. 75-80.

ROBERTSON, E.C. (1955). Experimental study of the strength of rocks, *Bulletin of The Geological Society of America*, 1275-1314, pp. 1275-1314.

ROCCO, C., GUINEA, G.V., PLANAS, J., and ELICES, M. (1999). Size effect and boundary conditions in the Brazilian test: Experimental verification, *Materials and Structures (RILEM)*, 32, pp. 210-217.

ROUSCHOP, J., HELLER, H.K.J., and BAAREN, J.P. (1989). High pressure / temperature borehole simulator, (No. 13, Delft progress report). Delft University of Technology, Faculty of Mining and Petroleum Engineering, Delft, Netherlands, pp. 166-176.

SAHU, S., BADGER, N., THAULOW, N., and LEE, R.J. (2004). Determination of water-cement ratio of hardened concrete by scanning electron microscopy, *Cement & Concrete Composites*, 26, pp. 987-992.

SANTARELLI, J.F. (1987). Theoretical and experimental investigation of the stability of axisymmetric wellbore, Ph.D. dissertation, Imperial College, London, p. 472.

SCRIVENER, K.L. (2004). Backscattered electron imaging of cementitious microstructures: understanding and quantification, *Cement & Concrete Composites*, 26, pp. 935-945.

SHAH, S. P., CARPINTERI, A., and RILEM TECHNICAL COMMITTEE 89-FMT FRACTURE MECHANICS OF CONCRETE: TEST METHODS. (1991). Fracture mechanics test methods for concrete, Chapman and Hall, London, p. 287.

SINHA, B.P., GERSTLE, K.H., and TULIN, L.G. (1964). Stress-strain relations for concrete under cyclic loading, *Journal of the American Concrete Institute*, 61, pp. 195-211.

SLATE, F.O., and HOVER, K.C. (1984). Microcracking in concrete, *Fracrure mechanics of concrete: Material characterization and testing*, A. CARPINTERI and A. R. INGRAFFEA, eds., Martinus Nijhoff Publishers, pp. 137-159.

SLUYS, L.J. , and DE BORST, R. (1999). Computational methods in non-linear solid mechanics, (No. CTme5142). Delft University of Technology, Faculty of Civil Engineering and Geosciences, Delft, pp. 204.

SPOONER, D.C., POMEROY, C.D., and DOUGILL, J.W. (1976). Damage and energy dissipation in cement pastes in compression, *Magazine of Concrete Research*, 28, pp. 21-29.

STIMPSON, B. (1970). Modelling materials for engineering rock mechanics, *Int. J. Rock Mech. Min. Sci.*, 7, pp. 77-121.

SULEM, J., VARDOULAKIS, I., and PAPAMICHOS, E. (1995). Microstructure and scale effect in granular rocks, *Continuum models for materials with microstructure*, H.-B. MUHLHAUS, ed., John Wiley & Sons Ltd., pp. 201-237.

TAKAHASHI, M., and KOIDE, H. (1989). Effect of the intermediate principal stress on strength and deformation behaviour of sedimentary rocks at the depth shallower than 2000m, *Rock at Great Depth*, MAURY and FOURMAINTRAUX (*eds.*), Balkema, Rotterdam, pp. 19-26.

TASDEMIR, M.A., and KARIHALOO, B. L. (2001). effect of aggregate volume fraction on the fracture parameters of concrete: a meso-mechanical approach, *Magazine of Concrete Research*, 53(6), pp. 405-415.

TRONVOLL, J., MORITA, N., and SANTARELLI, F.J. (1992). Perforation cavity stability: comprehensive laboratory experiments and numerical analysis, *SPE 67th annual technical conference and exhibition*, Washington, DC, pp. 339-349.

TRONVOLL, J., and FJAER, E. (1994). Experimental study of sand production from perforation cavities, *International Journal of Rock Mechanics and Mining Science & Geomechanics Abstracts*, 31(5), pp. 393-410.

VAN DEN HOEK, P. J., KOOIJMAN, A.P., KENTER, C.J., KHODAVERDIAN, M., HYLAND, C.R., and MCLENNAN, J.D. (1992). Size-dependency of hollow cylinder collapse

strength, *SPE 67th annual technical conference and exhibition*, Washington, DC, pp. 351-360.

VAN DEN HOEK, P. J., SMIT, D. -J., KOOIJMAN, A. P., DE BREE, PH., and KENTER, C. J. (1994). Size-dependency of hollow-cylinder stability, *EUROCK '94 - Rock Mechanics in Petroleum Engineering*, Delft, The Netherlands, pp. 191-197.

VAN DEN HOEK, P.J., HERTOGH, G.M.M., KOOIJMAN, A.P., DE BREE, PH., KENTER, C.J., and PAPAMICHOS, E. (2000). A new concept of sand production prediction: theory and laboratory experiments, *SPE Drill. & Completion*, 15(4), pp. 261-273.

VAN MIER, J. G. M. (1984). Strain softening of concrete under multiaxial loading conditions, Eindhoven University of Technology, Eindhoven, p. 349.

VAN MIER , J.G.M. (1998). Failure of concerte under uniaxial compression: an overview, *FraMCoS-3*, AEDIFICATIO Publishers, Freiburg, Germany, pp. 1169-1182.

VAN MIER, J.G.M. (1997). Fracture processes of concrete, CRC Press, Boca Raton, p. 448.

VAN VLIET, M. R. A. (2000). Size effect in tensile fracture of concrete and rock, Ph.D., Delft University of Technology, Delft, p. 192.

VAN VLIET, M.R.A., and VAN MIER, J.G.M. (1995). Softening behaviour of concrete under uniaxial compression, *Fracture Mechanics of Concrete Structures, FraMCoS-2*, F. H. WITTMANN (*ed.*), AEDIFICATIO Publishers, Freiburg, pp. 383-396.

VAN VLIET, M.R.A., and VAN MIER, J.G.M. (2000). Experimental investigation of size effect in concrete and sandstone under uniaxial tension, *Engineering Fracture Mechanics*, 65, pp. 165-188.

VARDOULAKIS, I., and PAPANASTASIOU, P. (1988). Bifurcation analysis of deep boreholes: I. surface instabilities, *International Journal of Numerical and Analytical Methods in Geomechanics*, 12, pp. 379-399.

VARDOULAKIS, I., and SULEM, J. (1995). Bifurcation analysis in geomechanics, Blackie, London, p.

VONK, R. A. (1993). A micromechanical investigation of softening of concrete loaded in compression, *Heron*, 38(3), pp. 94.

WESTERGAARD, H.M. (1940). Plastic state of stress around a deep well, *J. of the Boston Soc. of Civil Engnrs*, XXVII(1), pp. 1-5.

WITTMANN, F. H., SADOUKI, H., and STEIGER, T. (1993). "Experimental and numerical study of effective properties of composite materials" Michromechanics of Concrete and Cementitious Materials, C. HUET, ed., Presses Polytechniques et Universitaires Romandes, Lausanne, 59-82.

WITTMANN, F.H. (1983). Structure of concrete with respect to crack formation, *Fracture Mechanics of Concrete*, F. H. WITTMANN (*ed.*), Elsevier, London, pp. 43.

WYGAL, R.J. (1963). Construction of models that simulate oil reservoirs, *Soc. Petrol. Engrs. J.,*, 3, pp. 281-286.

ZECH, B., and WITTMANN, F. H. (1978). A complex study on the reliability assessment of the containment of a PWR. Part II Probabilistic approach to describe the behaviour of materials, *Nuclear Engineering and Design*, 48(2-3), pp. 575-584.

ZERVOS, A., PAPANASTASIOU, P., and VARDOULAKIS, I. (2001). Modelling of of localization and scale effect in thick-walled cylinders with gradient elastoplasticity, *International journal of solids and structures*, 38(30-31), pp. 5081-5095.

Appendix A

Table A.1 gives an overview of the uniaxial compression tests, for both mixtures, and their outcome. The properties listed in the table are interpreted form the test results as follows:

- The uniaxial compressive strength f_c of the specimen was calculated by dividing the maximum load carried by the specimen during the test, at peak, by the original cross-sectional area.
- The axial Young's modulus E was calculated using tangent method at a stress level equal to 50% of the ultimate uniaxial compressive strength f_c.
- The Poisson's ratio ν was calculated as the ratio of the slope of axial stress-strain curve to the slope of diametric stress-strain curve at 50% of f_c.

Table A.1: Mechanical properties of materials from uniaxial-compression test results

Diameter mm	Length mm	f_c MPa	E-modulus GPa	Poisson's ratio ν^*	Mixture
60.13	120.00	9.64	7.99	NA	M4
60.10	120.25	8.20	8.16	0.15	M4
60.17	120.10	8.83	7.63	0.14	M4
60.18	121.40	10.2	7.90	0.15	M4
60.00	120.25	9.09	8.24	0.15	M4
60.03	121.10	8.85	6.51	0.15	M4
60.00	121.60	8.50	7.19	NA	M4
60.10	122.00	9.28	7.98	0.16	M4
54.02	107.00	11.6	7.58	NA	M2
54.20	106.90	16.3	6.78	0.11	M2
54.20	107.00	11.3	6.44	NA	M2
54.20	107.00	14.0	7.98	NA	M2
54.20	107.00	9.98	5.96	0.15	M2
54.20	107.00	12.2	5.90	0.11	M2

*NA=no lateral deformations were measured.

Appendix B

Table B.1 gives an overview of results from uniaxial compression tests, for both mixtures, and their outcome, which were used for verification of initial strength distribution in the hollow-cylinders. The properties listed in the table are interpreted form the test results as follows:

− The uniaxial compressive strength f_c of the specimen was calculated by dividing the maximum load carried by the specimen during the test, at peak, by the original cross-sectional area.

− The axial Young's modulus E was calculated using tangent method at a stress level equal to 50% of the ultimate uniaxial compressive strength f_c.

− The Poisson's ratio ν was calculated as the ratio of the slope of axial stress-strain curve to the slope of diametric stress-strain curve at 50% of f_c.

Table B.1: Test results from the verification series for strength homogeneity

Core No.	Location	E GPa	ν	f_c MPa
1	Top	14.30	---	18.10
2	Top	15.10	0.11	17.80
3	Top	14.10	0.11	19.50
4	Top	16.10	---	18.60
5	Middle	15.80	0.10	16.40
6	Middle	16.60	0.13	19.50
7	Middle	15.80	0.13	18.30
8	Middle	16.90	0.14	18.00
9	Middle	15.20	0.12	18.80
10	Middle	15.70	0.14	18.40
11	Bottom	11.60	---	14.50
12	Bottom	13.90	0.12	15.42
13	Bottom	13.30	0.09	16.10
14	Bottom	14.00	---	13.70

Appendix C

The problem is treated as double hollow-cylinder as considered earlier by (Ewy and Cook, 1990) for a hollow-cylinder jacketed with an outer steel casing. In our case, the inner cylinder represents the sample, which is surrounded by the outer rubber-sleeve.

The general plane strain solution for a finite hollow-cylinder is described as follows (Jaeger and Cook, 1979):

$$u = Ur + \frac{Y}{r} \tag{C.1}$$

where u is the displacement at the hole wall, r is the radius of the cylinder, and U and Y are constants. This solution holds for both the inner and outer hollow-cylinders with different constants for each. The boundary conditions for the problem are σ_r at $r_1 = \sigma_i = 0$, σ_r at $r_3 = \sigma_o$, and u and σ_r are continuous at the interface r_2 (see Figure C.1). Applying these conditions to (C.1) and the radial stress equation,

$$\sigma_r = (\lambda + 2G)\frac{du}{dr} + \lambda \frac{u}{r} \tag{C.2}$$

results in the full solution, which is found as:
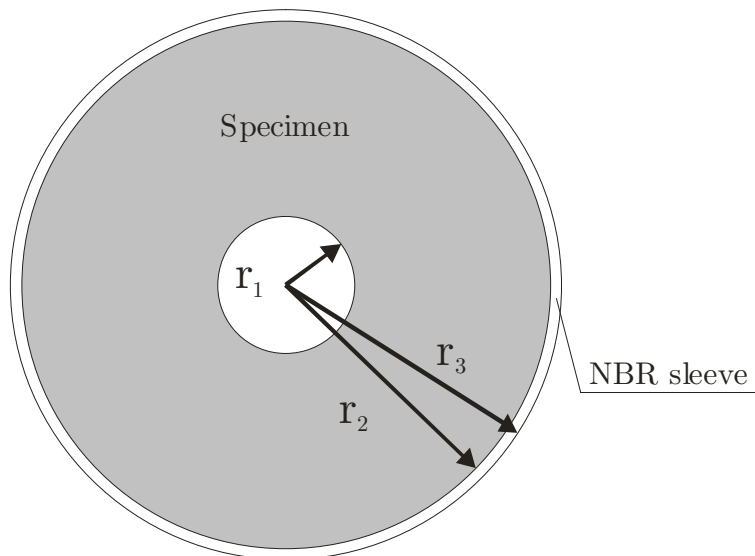
Figure C.1: Schematic representation for the double hollow-cylinder problem.

$$u = U_i r + \frac{Y_i}{r} \tag{C.3}$$

$$\sigma_r = 2(\lambda_i + G_i)U_i - \frac{2G_i Y_i}{r^2} \tag{C.4}$$

$$\sigma_\theta = 2(\lambda_i + G_i)U_i + \frac{2G_i Y_i}{r^2} \tag{C.5}$$

where i=1 or 2 for the region of interest and λ_i and G_i are the elastic constants. The constants U and Y could then be calculated using equations (C.3)-(C.5) and the boundary conditions. This results in the constants U and Y needed to calculate the stresses at the inner wall as:

$$U_1 = \frac{\sigma_o G_1(\lambda_2 + 2G_2) + \sigma_i \left\{ \frac{1}{2} \frac{r_1^2 \lambda_2 (G_2 - G_1)}{r_2^2 v_2} - \frac{r_1^2 G_2 \left(\frac{1}{2} \frac{\lambda_2}{v_2} + G_1 \right)}{r_3^2} \right\}}{\frac{G_1 \lambda_2 \left(1/2 \frac{\lambda_1}{v_1} + G_2 \right)}{v_2} - \frac{r_1^2 G_2 \lambda_1 \left(1/2 \frac{\lambda_2}{v_2} + G_1 \right)}{r_3^2 v_1} + \frac{r_1^2 \lambda_1 \lambda_2 \left(\frac{1}{2} G_2 - 1/2 G_1 \right)}{r_2^2 v_1 v_2} + \frac{r_2^2 G_1 G_2 \left(\frac{\lambda_1}{v_1} - \frac{\lambda_2}{v_2} \right)}{r_3^2}} \tag{C.6}$$

$$Y_1 = \frac{1}{2} \frac{\left[\frac{\sigma_o \lambda_1 (\lambda_2 + 2G_2)}{v_1} - \sigma_i \left\{ \frac{\lambda_2 \left(\frac{1}{2} \frac{\lambda_1}{v_1} + G_2 \right)}{v_2} + \frac{r_2^2 G_2 \left(\frac{\lambda_1}{v_1} - \frac{\lambda2}{v_2} \right)}{r_3^2} \right\} \right]}{\frac{G_1 \lambda_2 \left(\frac{1}{2} \frac{\lambda_1}{v_1} + G_2 \right)}{v_2} - \frac{r_1^2 G_2 \lambda_1 \left(\frac{1}{2} \frac{\lambda_2}{v_2} + G_1 \right)}{r_3^2 v_1} + \frac{r_1^2 \lambda_1 \lambda_2 \left(\frac{1}{2} G_2 - \frac{1}{2} G_1 \right)}{r_2^2 v_1 v_2} + \frac{r_2^2 G_1 G_2 \left(\frac{\lambda_1}{v_1} - \frac{\lambda_2}{v_2} \right)}{r_3^2}} \tag{C.7}$$

Knowing the material properties for the specimen and rubber used together with the applied stresses, it is possible from the above equations to calculate the tangential stress at the inner wall and its radial displacement (C.3)-(C.5). For the specimen, the parameters considered are E=7 GPa, ν=0.15, G=3 GPa, and λ=1305 MPa. For the NBR rubber, no tests have been performed and data from the supplier have been used, which is E=6 MPa, ν=0.45, G=2 MPa, and λ=18.6 MPa.

LIST OF FIGURES

161

LIST OF TABLES

SYMBOLS AND ABBREVIATIONS

SYMBOLS

§	—	section number
σ_1	MPa	maximum principal stress
σ_2	MPa	intermediate principal stress
σ_3	MPa	minimum principal stress
σ_m	MPa	non deviatoric stress component
σ_{dcv}	MPa	deviatoric stress component
$\bar{\sigma}$	MPa	The mean stress at failure
σ_N	MPa	Nominal material strength
$r,\ \theta,\ z$	—	cylindrical coordinates
σ_r	MPa	radial stress
σ_θ	MPa	tangential stress
σ_z	MPa	axial stress
ε_θ	—	tangential strain
ε_z	—	vertical strain
ε_r	—	radial strain
ε_v	—	volumetric strain
$\tau_{r\theta},\ \tau_{rz},$ and $\tau_{\theta z}$	MPa	shear stresses in cylindrical coordinates
σ_o	MPa	outer stress
σ_i	MPa	inner stress
f_c	MPa	uniaxial compressive strength
f_t	MPa	uniaxial tensile strength
f_{2c}	MPa	Biaxial strength
f_{spl}	MPa	Brazilian splitting strength
UCS	MPa	uniaxial compressive strength
w/c	—	water/cement ratio

$d_{\max}$	mm	maximum grain size
ε_1	—	maximum principal strain
ε_2	—	intermediate principal strain
ε_3	—	minimum principal strain
D_c	mm	characteristic dimension/size
A_{SEL}, B_{SEL}, C_{SEL}, and D_{SEL},	—	SEL size effect model constants
A_{MFSL}, B_{MFSL}, l_{ch}, and f_{MFSL},	—	MFSL size effect model constants
ρ	Kg/m³	material/particle assembly density
R_o	mm	outer radius
R_i	mm	inner radius
D_o	mm	outer-cylinder diameter
D_i	mm	inner-cylinder diameter
W	mm	wall thickness of hollow cylinder
u	mm	radial displacement at the inner-cylinder wall
w	mm	axial displacement of the hollow-cylinder
E	GPa	Young's modulus
ν	—	Poisson's ratio
λ and G	GPa	elastic constants
r	mm	radius of the cylinder between R_o and R_i
A_m-P_m	—	trial material mixtures developed in the study
M4	—	model mixture of 4 mm max. aggregate size
M2	—	model mixture of 2 mm max. aggregate size
2D	—	two dimensions
3D	—	three dimensions
p320, p500, and p1200	—	codes for fineness of sand papers
h	m	specimen height
d	m	specimen diameter
t	m	specimen thickness
500X	—	magnification factor
RH	—	relative humidity
T	°C	temperature

NX	mm	standard core size with 54.1 mm diameter
A	—	hollow-cylinder with inner diameter of 12.5 mm
B	—	hollow-cylinder with inner diameter of 25 mm
C	—	hollow-cylinder with inner diameter of 50 mm
D	—	hollow-cylinder with inner-hole diameter of 100 mm
A/D converter	—	Analogue/Digital converter
p_o	MPa	pore pressure
β	°	inclination of failure plane to maximum principal stress according to M-C failure criterion
c	MPa	cohesion
φ	°	internal friction angel
R^2	—	coefficient of determination
A_d	mm	Averaging distance
P_f	—	probability of failure of a specimen with volume V
V	m^3	volume
n_d	—	scale number in Weibull's theory
m	—	Weibull modulus
I_1'', I_3''	MPa	stress invariants in Lade criterion
S_1, η	—	constants of Lade criterion
k	—	constant
X	mm	average impregnated depth measured around the inner hole
$\tilde{R}$	mm	average particle radius
R_{min}	mm	minimum particle radius
R_{max}	mm	maximum particle radius
ϕ	—	porosity of particle assembly
k_n	GPa	normal stiffness
k_s	GPa	shear stiffness
k_n/k_s	GPa	stiffness ratio
T_n	MPa	normal strength
T_s	MPa	shear strength

$\bar{T}_{n,s}$	MPa	mean bond strength
μ	—	friction coefficient
F_n^i	N	normal component of the contact force
F_s^i	N	shear component of the contact force
U_n^i	mm	relative displacements between the contacting bodies in normal direction
U_s^i	mm	relative displacements between the contacting bodies in shear direction
n_i'	—	unit normal vector
$F_s^{\max}$	N	maximum allowable contact shear force
n	mm	contact overlap
L	mm	width of biaxial specimen/diameter of Brazilian specimen used in numerical simulations
H	mm	height of biaxial specimen/diameter of Brazilian specimen used in numerical simulations

ABBREVATIONS

ITZ	Interfacial Transition Zone
OPC	Ordinary Portland Cement
SD	Standard Deviation
LVDT	Linear Variable Differential Transducers
SEM	Scanning Electron Microscope
ESEM	Environmental Scan Electron Microscope
SE	Secondary Electron
BSE	Backscattered Electron
SEL	Size Effect Law
MFSL	Multifractal Scaling Law
LEFM	Linear Elastic Fracture Mechanics
M-C	Mohr-Coulomb
D-P	Drucker-Prager
PFC2D	Particle Flow Code in Two Dimensions
NBR	Nitrile-Butadiene Rubber
DIN	German Standards
PC	Personal Computer
NPT	National Pipe Thread
Teflon	Polytetrafluorethylene
FPZ	Fracture Process Zone
RVE	Representative Volume Element
DEM	Discrete/Distinct Element Method
FEM	Finite Element Method

ACKNOWLEDGEMENTS

During the evolution of this book I have accumulated many debts, only a proportion of which I have space to acknowledge here.

I am grateful to my supervisor and thesis advisor, Prof. dr. Jan van Mier, for giving me the opportunity to do this research, for the fruitful and constructive discussions through the years and for the insight and support he provided.

I am indebted to Ing. Gerard Timmers for the help he supplied in designing, constructing, and performing the experiments. His assistance was indispensable to accomplish this work. I would like to thank Andre Hoving and Jan Etienne from the Dietzlab for designing and debugging the pressure cell and for the guidance they provided in dealing with high-pressure tests and specimen preparation. The efforts by the concrete casting group of the Stevin Laboratory are highly appreciated. Thanks to our IT guru drs. Frank Everdij. I am especially thankful to Prof. dr. Bert Sluys who managed my project finance over the last three years and for his valuable scientific comments and interest in my work. I am appreciative to my friend, Dr. Mohamed Youssef, for his companionship, the tips and tricks with MS-Word and this thesis template, and for the interesting chats we had. Thanks are due to Dr. David Potyondy and Jitse Pruiksma for the useful feedback and PFC discussions. I would like to thank Dr. Max Hendriks for the Dutch translation. Thanks to the colleagues of the Microlab and Structural Mechanics groups for the pleasant atmosphere and friendly attitude.

Last but not least is my thanks and gratitude to my parents in Egypt for enduring my absence and for their continuous love, support, and prays. Special thanks and gratitude my wife, Buket, for her support, help, and patient understanding through the ups and downs despite her own PhD study duties and the responsibilities towards our toddler daughter Nur; accomplishing this work without her was not possible. I am appreciative and thankful to my in laws for their care and support. I would like to thank all my family and friends for their care and support, especially my uncle, Prof. Dr. Farouk Elkadi, who made it possible for me to come to the Netherlands to complete my M.Sc. studies and who introduced me to the interesting world of Civil Engineering.

CURRICULUM VITAE

Name:	Ahmed Said Kamal Elkadi
Birth Date:	26th March 1969, Tanzania
Nationality:	Egyptian
1986	High school diploma, science division, Cairo, Egypt
1991	B.Sc. in Civil Engineering, Structural Department, Faculty of Engineering, Ain Shams University, Cairo, Egypt
1991-1992	Military service, Egyptian Armed Forces
1992-1998	Geotechnical/structural consultant engineer, Nile Engineering Consulting Office, NECB, Cairo, Egypt
1998-2000	M.Sc. in Engineering Geology (with distinction), ITC, Enschede
2000-2005	Research Assistant, Microlab, Faculty of Civil Engineering and Geosciences, Delft University of Technology, Delft
Since May 2005	Civil Engineer, TNO DIANA BV, Delft

Publications from this thesis

Refereed Journals

Elkadi, A.S., & van Mier, 2005, Experimental observations of concrete behaviour under complex stresses: scaling and fracture processes, Special issue of the Engineering Fracture Mechanics. (Forthcoming)

Elkadi, A.S., & van Mier, 2005, Experimental investigation of size effect in concrete fracture under multiaxial compression, Special issue of the International Journal of Fracture. (In review)

Elkadi, A.S., van Mier, J.G.M., Sluys, L.J., 2005, Multiaxial failure of cohesive-frictional granular materials: fracture behaviour and size dependence, special issue of the Philosophical Magazine: Structure and Properties of Condensed Matter. (In press)

Conferences

Elkadi, A.S. & van Mier, J.G.M., Scaling of Multiaxial Compressive Fracture, 16th European Conference on Fracture ECF16, July 2006, Greece. (Forthcoming)

Elkadi, A.S. & van Mier, J.G.M., 2005, Size effect experiments on concrete under multiaxial compression, In proceedings 11th International Conference on Fracture, ICF-XI, Turin, Italy. (Extended abstract)

Elkadi, A.S. & van Mier, J.G.M., 2005, Size/scale effects in wellbore model tests, In proceedings EURO-Conference 2004 on Rock Physics and Geomechanics, Scaling Laws in Space and Time, 20-23 September 2004, Potsdam, Germany.

Elkadi, A.S. & van Mier, J.G.M., 2004, Scaling properties of mortar under complex stresses, In proceedings 5th International PhD conference in Civil Engineering PhDCE-5, Walraven et al. (eds.), 16-19 June 2004, Delft, Netherlands, Vol. 1, pp. 501-508.

Elkadi, A.S. & van Mier, J.G.M., 2004, Scaled hollow-cylinder tests for studying size effect in fracture processes of concrete, In proceedings 5th International conference on fracture mechanics of concrete and concrete structures FraMCoS-5, Li et al. (eds.), 12-16 April 2004, Vail, Colorado, USA, Vol. 1, pp. 229-236.

Elkadi, A.S., de Pater, C.J., van Mier, J.G.M., 2003, Stress-induced failure in hollow-cylinder tests and its size dependence, In proceedings 3rd International symposium on rock stress, 2-6 November, Kumamoto, Japan, pp.565-570.

Elkadi A.S., van Mier J.G.M., de Pater C.J., Development and behaviour of low-strength concrete, P. Schieβl et al. (eds.), Proceedings of 4th International Ph.D. symposium in Civil Engineering, September 2002, Munich, Germany, Vol. 1, pp. 135-142.